REPORT DOCUMENTATION PAGE

Form Approved
OMB No. 0704-0188

PLEASE DO NOT RETURN YOUR FORM TO THE ABOVE ADDRESS.

1. REPORT DATE *(DD-MM-YYYY)*	2. REPORT TYPE	3. DATES COVERED *(From - To)*
26-FEB-2008	Final Technical Report	From 13-APR-2004 To31-DEC-2007

4. TITLE AND SUBTITLE

Reliability Of Next generation Power Electronics Packaging Under Concurrent Vibration, Thermal and High Power Loads

5a. CONTRACT NUMBER

5b. GRANT NUMBER

N00014-04-1-0778

5c. PROGRAM ELEMENT NUMBER

6. AUTHOR(S)

Cemal Basaran

5d. PROJECT NUMBER

04PR13845-00

5e. TASK NUMBER

5f. WORK UNIT NUMBER

7. PERFORMING ORGANIZATION NAME(S) AND ADDRESS(ES)

The Research Foundation of the State University of New York DBA SUNY At Buffalo Sponsored Projects Services, 402 Crofts Hall, University at Buffalo, Buffalo, NY 14260

8. PERFORMING ORGANIZATION REPORT NUMBER

001

9. SPONSORING/MONITORING AGENCY NAME(S) AND ADDRESS(ES)

Terry S. Ericsen
Office Of Naval Research
875 North Randolph Street
Arlington, VA 22203-1995

10. SPONSOR/MONITOR'S ACRONYM(S)

ONR 331

11. SPONSOR/MONITOR'S REPORT NUMBER(S)

12. DISTRIBUTION/AVAILABILITY STATEMENT

Unlimited

13. SUPPLEMENTARY NOTES

14. ABSTRACT

This final report presents a study on predicting reliability of next generation power electronics packaging, under high power loads. The study entails computational simulation modeling of power electronics packaging under high current density, high temperature gradient, high temperature and mechanical loads. Computer simulations are used for various scenarios to predict life time to failure and predictions are compared against actual experimental field data to validate the models.

15. SUBJECT TERMS

16. SECURITY CLASSIFICATION OF:			17. LIMITATION OF ABSTRACT	18. NUMBER OF PAGES	19a. NAME OF RESPONSIBLE PERSON
a. REPORT	b. ABSTRACT	c. THIS PAGE			19b. TELEPHONE NUMBER *(Include area code)*
Unclassified	Unclassified	Unclassified	UU		

Final Technical Report

Award No: N00014-04-1-0778

Relibility of Next Generation Power Electronics Packaging Under Concurrent Vibration, Thermal and High Power Loads

Technical Representative:

Terry S. Ericsen,

ONR 331

875 North Randolph Street

Arlington, VA 22203-1995

Report Prepared By

Cemal Basaran

Electronic Packaging Laboratory

State University of New York at Buffalo

www.packaging.buffalo.edu

Table of Contents

List of Figures

List of Tables

Chapter 1 Background and Literature Survey

Equation Chapter 1 Section 1

1.1 Basics of Electromigration

Electromigration is a diffusion-controlled mass-transport phenomenon that takes place in metals and alloys. Under high current density atoms (ions) move in the same direction as electrons as a result of electron wind forces, which result in mass migration from the cathode side to anode side. Voids lead to electrical and mechanical failure of the electronic devices. Electromigration has not been a limiting factor for electronic devices up to this point because of relatively low current densities needed by the state-of-the-art electronic devices. In the next generation nanoelectronics and power electronics packaging current densities are expected to increase 2 or 3 orders of magnitude. Electromigration was identified as an integrated circuit failure cause by Blech et al in the 1960s (Blech and Sello 1965;Blech and Sello 1966). The works of Huntington and Fiks(Fiks 1959;Huntington and Grone 1961;Fiks 1964) has been the basis for the understanding of electromigration, and the understanding of physics of electromigration has been improved upon the subsequent studies(Bosvieux and Friedel 1962;Sorbello 1973;Das and Peierls 1973;Landauer 1975;Schaich 1976;Lodder and Brand 1984;Chu and Sorbello 1991).

1.1.1 Driving Forces of Electromigration

Regardless of complexity of electromigration in various materials, it is a diffusion controlled mass-transport phenomenon. The diffusion flux can be described based on Fick's laws :

$$J = \frac{ND}{kT} F \qquad [1\text{-}1]$$

in which N is the atomic concentration;

D is the diffusivity;

k is Boltzmann constant;

T is temperature (Kelvin)

F is the driving force.

There are four forces that drive or hinder electromigration process, they are;

1). Electron wind force

2) Stress gradient

3) Vacancy concentration gradient

4) Temperature gradient

In the following section these four forces will be briefly discussed.

1.1.1.1 Electron Wind Force

In the early 1950s, Seith and Wever used surface markers technique in the study of various Hume-Rothery alloys where they revealed a direct correlation

between the sign of the charge carriers and the direction of net mass motion (Seith and Wever 1953;Seith 1955;Wever and Seith 1955). Their hypothesis was, there is an effect of momentum exchange between the free electrons and the moving atoms (or ions; the terms "atom" and "ion" are used interchangeably), based on their observation. Such an electron wind force drives positive ions in the direction of the electron flow, which is opposite to the direction of the electrostatic force of the electric field. Figure 1 shows the schematic of electron wind force due to the momentum exchange (from collisions) between conducting electrons and diffusing metal atoms and direct electrostatic force exerted on the atoms in a metal conductor.

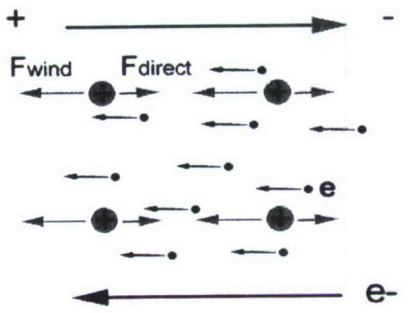

Figure 1 Kinematics of electromigration process (Ye 2004)

Therefore, the driving force exerted on an ion is then (Huntington 1972)

$$F = F_{wind} + F_{direct} = \left(Z_{wind} + Z_{el}\right)eE = Z^{*}e\rho j \qquad [1\text{-}2]$$

where Z_{wind} is the valence number arises from the electron wind force, Z_{el} is the nominal valence of an ion, Z^{*} is called effective valance (or effective charge number), which is combination of the electron wind force and electrostatic force, e

is electron charge, $\vec{E}$ is the macroscopic electric field, which is related to the electric potential ψ according to $\vec{E} = -\vec{\nabla}\psi$, ρ is resistivity, and $\vec{j}$ is current density. Z^* is commonly negative in metal conductors because of the influence of the "electron wind."

Among the various theoretical calculations of Z^*, the ballistic model is the most popular one developed independently by Fiks(Fiks 1959) and Huntington(Huntington and Grone 1961). For a complete review of the various theoretical models see (Sorbello 1991) and Ye(Ye 2004).

1.1.1.2 Spherical Stress Gradient and Vacancy Concentration Gradient

These two forces are thermodynamically interrelated and therefore they are put in the same section.

Ainslie et al (1972) first recognized that mechanical stress may play an important role in electromigration damage. They suggested that a spherical stress gradient may oppose electromigration flow and the spherical stress may affect the diffusivity. But they underestimated the possible stress level that can be obtained in thin film during electromigration. The importance of stress to electromigration was first demonstrated in experiments by Blech (Blech and Kinsbron 1975;Blech 1976;Blech and Herring 1976;Blech and Tai 1977). In a series of "drift" experiments, thin metal films were deposited onto a high-resistance, refractory

substrate. After running electric current through the thin film, the edge of the film closer to the cathode was observed to move towards the anode. It was discovered that the drift velocity was a function of the film length. Longer film showed a much higher drift velocity than short ones. He found that a threshold or critical film length exists for electromigration, under which no electromigration edge drift will occur (Figure 2).

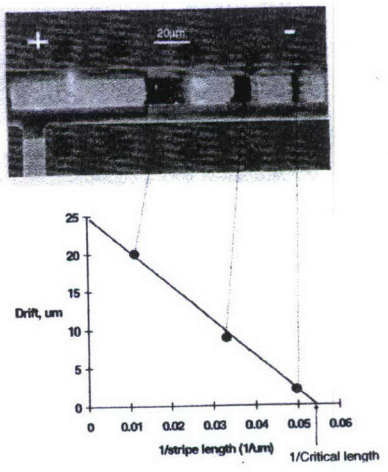

Figure 2 Drift of four aluminum strips with varying lengths (heat treated 350°C, 20h) after passage of $3.7\times10^5 A/cm^2$ (Blech 1976)

The experiments suggested that ions transported by the electromigration create a stress and/or concentration differences between the film ends causing a back flow that counteracts the electromigration. Under the critical length, a back flow created by pressure gradients balances the forward electromigration flow, thus eliminating any net flow. Based on the Fick's law flux due to stress gradient is given by

$$J = \frac{D}{kT}\nabla\sigma \qquad [1\text{-}3]$$

Where $\nabla\sigma$ is the spherical stress gradient.

Combining Equation [1-1] and [1-3], the driving force due to stress gradient can be identified as:

$$F = \frac{\nabla \sigma}{N} \qquad [1\text{-}4]$$

The critical length can be calculated from Equations [1-2] and [1-4] when the two forces are equal to each other.

Using transmission X-ray topography, Blech and Herring confirmed the stress gradient build-up in thin Al films during passage of electrical current (Blech and Herring 1976;Blech and Tai 1977).Ye was able to show the stress gradient in a solder joint using Moiré Interferometry (Ye 2004)

Mass diffusion due to atomic/vacancy concentration gradient can be described as

$$J = -D\nabla C \qquad [1\text{-}5]$$

where J is flux, D is diffusion coefficient and ∇C is concentration gradient.

It is worthwhile to point out that the vacancy concentration gradient and the stress gradient are not independent quantities. An increased tensile stress will have an increased vacancy concentration in thermal equilibrium status and the opposite for a compressive stress. Since the time needed for thermal equilibrium establishment is far shorter compared with relatively long period of time needed for solid diffusion, those two gradients are directly related to each other.

The experimental measurement of stress evolution are done mostly by x-ray microdiffraction techniques (Kuschke and Arzt 1994;Wang et al 1998;Wang 2001;Solak 2004) or other indirect techniques such as Raman spectroscopy and micro-topography (Wang 2000;Ma 2004). Indirect measurements have concentrated on measurement within substrate materials. Both direct and indirect measurements can not provide stress field values directly, because both methods can only measure strain field. Stress field must be deducted from strain field under a constitutive relation of the material and boundary conditions. With the advancing X-ray techniques such as advanced photon source and fresnel zone plates(x-ray optics), the decision and resolution of x-ray microdiffraction has been improving and are able to give real time strain field value under 10 micron resolution(Wang et al. 1998).

Several researchers proposed analytical or numerical models for stresses under electromigration(Ross 1991;Kirchheim 1992;Clement and Lloyd 1992;Korhonen et al 1993;Kirchheim 1993a;Clement and Thompson 1995).

In Kirchheim's approach(Kirchheim 1992), electromigration is described as a biased diffusion of vacancies. The vacancy flux and atomic flux must be equal in a vacancy controlled diffusion mechanism and 1-D vacancy flux in Kirchheim formulation is given by (Kirchheim 1992)

$$J = -D_v \frac{\partial c}{\partial x} + \frac{Dc}{kT} Z^* eE - \frac{D_v c}{kT} f\Omega \frac{\partial \sigma}{\partial x} \qquad [1\text{-}6]$$

where Z^*e is effective charge, j is current, D_v is vacancy diffusivity, f is

vacancy relaxation ratio (ratio of a volume of a vacancy to volume of an atom), $E = \rho j$, where ρ is resistivity and j is current density, Ω is atomic volume. A direct relationship between the rate of change of stress and the action of the vacancy source term is proposed as:

$$\frac{\partial \sigma}{\partial t} = Bf'\Omega \frac{\delta}{d} \frac{C_v - C_{ve}}{\tau_s} \qquad [1\text{-}7]$$

where *B* is the bulk modulus, $f' = 1 - f$, δ is grain boundary thickness, and *d* is grain size. Here Kirchheim only considered the diffusion in grain boundary since the grain boundary is the major path in diffusion of vacancies. This assumption is not true for bamboo structure, which a single grain occupies the whole lateral area. τ_s is characteristic time for generation or annihilation of vacancy and $\frac{C_v - C_{ve}}{\tau_s}$ is defined as vacancy generation/annihilation rate. It is proposed that vacancy will generate or annihilate in grain boundaries if their concentration deviates from the equilibrium value. C_v is vacancy concentration and C_{ve} is thermal equilibrium vacancy concentration. C_{ve} is defined by Kirchheim(Kirchheim 1992) as

$$C_{ve} = C_{v0} \exp(f'\Omega\sigma / kT) \qquad [1\text{-}8]$$

C_{v0} is the thermal equilibrium vacancy concentration at a stress-free state which is given by $C_{v0} = C_L \exp(-E_a^v / kT)$, where E_a^v is the activation energy for vacancy formation in the location of interest (lattice, grain boundary, or interface) and C_L is lattice concentration (Lloyd 1995).

In equation [1-7], Kirchheim directly relates stress change rate to the vacancy concentration recovery rate. It is pointed out by Sarychev (Sarychev and Zhinikov 1999) that if the rate change of vacancy concentration is considered another term which is the vacancy flux divergence should be also included. Kirchheim in his theory treats materials as elastic which is not true for most metals(Lin and Basaran 2004). But elasticity is a expedient assumption since it can dramatically simplify the solution. Elasticity assumption is used by most of the electromigration models in the literature. Finally the σ in Kirchheim formulations is spherical stress.

The conservation equation for vacancy concentration given by

$$\frac{\partial C_v}{\partial t} = -\frac{\partial J}{\partial x} - \frac{C_v - C_{ve}}{\tau_s} \qquad [1\text{-}9]$$

By solving the coupled differential equations [1-6] to [1-9], both the vacancy concentration evolution and transient spherical stress build-up in the one dimensional thin film conductor can be found.

Korhonen (1993) proposed another slightly different model than Kirchheim. In Korhonen's model the change of lattice sites per unit volume is used instead of vacancy change for the source of deformation. The same simplification of elasticity is used. To make problem more simpler, Korhonen assume thermal equilibrium of vacancy concentration is always maintained with the available sink/source of vacancy, thus

$$C_v = C_{ve} = C_{v0} \exp(\Omega\sigma / kT) \qquad [1\text{-}10]$$

Korhonen argued that because of the confinement by the surrounding in the metallization lines (integrated circuit) metallization, the change in lattice site will create stress in three major direction as σ_1, σ_2 and σ_3. Since the chemical potential in any cross section is constant at all boundary conditions, the deposition of atoms at the grain boundary does not have any preferred direction. Korhonen concluded that σ_1 must equal to σ_2 because of the reason stated above, where σ_1 σ_2 are in plane stress (integrated circuit plane). This conclusion comes directly from the constitutive model adopted by Korhonen. Korhonen used Eshelby theory of inclusions as the constitutive model. Eshelby theory gives the stress field due to inclusions in an infinite matrix which is not suitable for a thin film because it has limited dimension in thickness and width. But it is sufficient to provide a qualitative estimate of stress evolution during electromigration.

The constitutive equation between stress and vacancy concentrations is presented by Korhonen as follows

$$\frac{dC_L}{C_L} = \frac{-d\sigma}{B} \qquad [1\text{-}11]$$

where dC_L is the change of lattice site per unit volume and C_L is the lattice site concentration per unit volume, B is applicable bulk modulus which is related to aspect ratio and Young's modulus of specimen. Here the lattice site occupied

by atom or vacancy is treated as the same volume.

The conservation equation for lattice site is

$$-\frac{\partial J_a}{\partial x}=\frac{\partial C_v}{\partial t}+\frac{C_L}{B}\frac{\partial \sigma}{\partial t} \qquad [1\text{-}12]$$

where C_v is vacancy concentration. The lattice concentration is related to atomic concentration and vacancy concentration by: $C_L = C_a + C_v$. J_a is atomic flux which is defined as

$$J_a = -\frac{D_a C_a}{kT}\left(\nabla \mu + Eq^*\right) \qquad [1\text{-}13]$$

where D_a is atomic diffusivity, $\mu = \mu_0 - \Omega\sigma$ (Herring 1950;Herring 1971), is the chemical potential and μ_0 is chemical potential at stress free state, q^* is the effective charge, and E is electric field.

By further approximating that $C_L = C_a = 1/\Omega$ and $(C_v / C_L)B\Omega / kT \ll 1$, a one dimensional expression of stress evolution along the metal line during electromigration is derived as (Korhonen et al. 1993)

$$\frac{\partial \sigma}{\partial t}=\frac{\partial}{\partial x}\left[\frac{D_a B\Omega}{kT}\left(\frac{\partial \sigma}{\partial x}+\frac{Eq^*}{\Omega}\right)\right] \qquad [1\text{-}14]$$

Because of it's simplicity, Korhonen's model gained wide acceptance. By assuming that when the stress level reaches the yield stress, the material has failed, the solution of Equation [1-14] for blocking diffusion boundary conditions gives power of -2 dependence for time to failure versus current density relation which agrees with Black's experiments(Black 1969). The main advantage of Korhonen's model is that it only deals with a single differential equation rather than solving coupled differential equations which is proposed by Kirchheim,

Clement and Thompson (1995) re-examined the assumptions and approximations in the Korhonen treatment, and reformulated an analytic expression for the evolution of the stress in confined interconnect lines. In their approach, electromigration is described as a vacancy diffusion equation with a sink/source term:

$$\frac{\partial C_v}{\partial t} + \frac{\partial J_v}{\partial x} + \gamma = 0 \qquad [1\text{-}15]$$

where J_v is the vacancy flux and γ is the vacancy generation/annihilation rate. They expressed the sink/source term as $\gamma = -\frac{\partial C_L}{\partial t}$

Clement and Thompson used the same assumption as the Korhonen model that the vacancies are in equilibrium with stress and followed the stress-lattice concentration relationship developed in Korhonen model (Equation [1-11]) This model is later improved by Clement (Clement 1997) with the consideration of a ratio of the line cross sectional area to the area of the diffusion path, ε, in the vacancy sink/source term: $\gamma = -\varepsilon \frac{\partial C_L}{\partial t}$.

A more complicated model is proposed by Young-Joon Park et al(1996) based on the work of Korhonen and Clement. Park considered atomic diffusivity changing with spherical stress. A tensile stress increases the vacancy concentration aiding diffusion while a compressive stress will depress the vacancy concentration, hampering diffusion. Also the chemical potential term is more complicated in Park's model which is a polynomial term based on the work of Murray (Murray 1985). The same constitutive model is used for stress rate

change equation as Korhonen and Clement.

After reviewing the stress evolution model for thin film electromigration discussed above, several noticeable common weakness are in these models which need to be addressed for more complicated stress evolution that happens in solder alloy electromigration.

First, the mechanical constitutive models used in above models are all linear elastic, which is not true for most metals, especially for eutectic solder material (viscoplastic material with a low yield stress).

Second, the models discussed above can not consider various boundary and initial conditions, which can only be treated using a general finite element approach.

Third, due to elasticity simplification, these models all directly give equations which directly relate stress to vacancy concentration or lattice concentration, which prevents implementation of more complicated material constitutive models.

Sarychev (Sarychev and Zhinikov 1999) proposed a new model based on Kirchheim and Korhonen works., Sarychev improved Kirchheim's model by adding a direct contribution of the vacancy flux in the stress evolution to Kirchheim' model. More importantly, although Sarychev still used linear elastic constitutive relation in developing the model, they related stress and vacancy concentration through strain, thus allows implementation of complicated stress strain constitutive models. The result of Sarychev's model is a set of differential

equations in the form similar to Kirchheim's result. Because of the advantages of Sarychev and Zhinnikov's model, we will adopt their model as our bases for development of a general model for stress and damage evolution under electromigration. The details of Sarychev's model will be discussed in a latter chapter.

1.1.1.3 Thermomigration

The so called Soret diffusion is the atomic diffusion driven by thermal gradient(Huntington 1972). High current density in metal lines or solder joints cause self heating due to Joule effect which will create thermal gradient .inside the thin metal lines or solder connection. Due to the small dimension of electronic components, the thermal gradient can reach the order or $10^4\,^{\circ}C/cm$.

The driving force produced by a temperature gradient is described by the following equation:

$$F = -Q^{*}\nabla T / T \qquad [1\text{-}16]$$

where Q^{*} is the heat of transport, the isothermal heat transmitted by moving an atom in the process of jumping a lattice site less the intrinsic enthalpy. Since different mechanisms contribute to Q^{*}, both positive and negative values of Q^{*} have been found in the literature. For positive Q^{*} value, the atoms move from hot to cold zones. Some results(Van Gurp et al 1985;van Gurp and du Chatenier 1985) have demonstrated positive values in the case of indium, aluminum and

gold. For aluminum $Q^* \approx 0.03eV$, while a maximum estimate for the thermal gradient is $2\times10^3\,^\circ C/cm$. At $25^\circ C$ one calculates $F = 13eV/m$. This value is two orders of magnitude smaller than the electromigration driving force $F = 3000eV/m$ if we use $Z^* = -10$ and current density $j = 10^6 A/cm^2$. (Scorzoni et al 1991). So in thin film electromigration cases, the thermomigration can be omitted. Kirchheim(Kirchheim 1992) in his models also mentioned thermomigration and included it in his flux equation, but in latter formulation, he omitted the thermomigration term due to same reason above.

Although thermomigration may not be dominant compared to electromigration in thin film, it may not be omitted at other cases. For instance solder joints(Ye et al 2003e). This is mainly due to the micro structure of the solder joints. Several very thin layers of metallic mostly aluminum or copper above solder joint will generate a large amount of heat due to high current density(in the order of $10^7 A/cm^2$) which will create thermal gradient in the order of $10^4\,^\circ C/cm$. Consequently, reliability problems may arise due to thermomigration(Gupta 1997). Solder joint's dimension is in the order of $100\,\mu m$ which are much larger than thin film metal lines thickness, which makes the normal current density 2 order of magnitude smaller than metal lines, if the same temperature gradient existed and same order of magnitude of heat of transport adopted, the thermomigration driving force will be expected to be in the same order as electromigration (For eutectic solder joints the effective charge number is

in the same order of magnitude as aluminum). A reduced heat of transport $Q^* - h_f$ = 0.106±0.004 eV has been reported(Johns and Blackburn 1975) for thermomigration in pure lead at the temperature range of 595-475 K. The difficulty of considering thermomigration in solder joints is lack of available experimental data reporting heat of transport.

1.1.2 Diffusivity

Diffusivity is the material constant which represent the mobility of atoms or vacancies. In the general case diffusivity D is a tensor. Diffusivity usually obeys the following relationship:

$$D = D_0 \exp\left(-E_a / kT\right) \qquad [1\text{-}17]$$

where D_0 is a temperature-independent coefficient and E_a is the activation energy of the particular diffusion process. A number of diffusion mechanisms are known to act inside polycrystalline material. The kinetics of various mechanisms have been extensively studied and results indicate that the activation energy is closely related to the absolute melting temperature of the host medium.

1.1.2.1 Diffusion Mechanisms

Bulk/lattice diffusion, grain boundary diffusion and surface diffusion are three major diffusion mechanisms. Generally speaking surface diffusion is the fastest one and bulk/lattice diffusion slowest one. There are also other types of mechanisms for atom/vacancy diffusion such as grain boundary to bulk/lattice (which creates grain boundary segregation phenomenon). For aluminum, based

on Lloyd (Lloyd 1999) the activation energy for aluminum is 1.2 eV for bulk diffusion, 0.6-0.7eV for grain boundary diffusion and 0.8-1.0 eV for surface diffusion. For copper the activation energy for bulk diffusion is 2.3eV, for grain boundary diffusion is 1.2eV and 0.7-1.0 for surface diffusion. The difference in activation energy suggests that copper diffusion is slower than aluminum. The typical ULSI (Ultra Large Scale Integrated) circuit application operate at temperature of 373K, is about 40% of the aluminum melting point (933K) and 27.4% of the copper melting temperature (1357K). So the electromigration damage process in copper is expected to be slower than in aluminum. Also from above activation energies for different diffusion mechanisms for aluminum and copper, we can readily see that grain boundary diffusion is dominant in aluminum and with copper surface diffusion prevails. This is very important since it gives out different approaches to minimize the damage due to electromigration. For example, for aluminum narrow lines which have single grain along the width of lines (Bamboo structure) offer great advantage since it can reduces the grain boundary diffusion. But for copper the interface diffusion is dominant, the same approach can not be adopted since the narrow line will have the same surface area to cross section area ratio as wide lines(Li et al 2004a). We will further explore this issue at later sections.

For solder alloys, the surface area to cross section area ratio is much bigger than thin film due to the bulk structure of solder joints. Surface diffusion is

not significant compared to grain boundary diffusion. The melting temperatures of low tin solders (1-5wt% Sn) are in the range of 563K to 598K and those containing a near eutectic composition (62 wt% Sn) are in the 455K to 493K(Gupta et al 1998). In view of the low melting temperature of tin based solders, diffusion in lattice and in grain boundaries may occur simultaneously at the temperature of operation(Gupta 1997). The interplay of the two atomic diffusion processes is in polycrystalline materials is best described by the three kinetic regimes A, B and C due to Harrison(Harrison 1961) which are shown schematically in Figure 3.

Gupta (Gupta 1997) divided those three kinetics of diffusion according to the ratio of operating temperature to melting, that is, generally speaking when T/T_m is above 0.5, A-type kinetics which involve extensive lattice and grain boundary diffusion will be dominant. Consequently, the effective diffusivities (D_{eff}) have lower activation energy which can be described as:

$$D_{eff} = (1-f)D_l + fD_b \qquad [1\text{-}18]$$

where D_l is lattice diffusivity, D_b is grain boundary diffusivity and *f* is the fraction of atoms at the grain boundaries with respect to the grains so that $f = 4\delta/L$, where δ is the grain boundary width and L the grain diameter. For metals and most ceramic materials, the grain boundary width is assumed to have a constant value of *0.5nm*. If solute segregation (solute segregation means that the solute concentration is not continuous across the boundary condition) at the

grain boundaries is included, a segregation parameter $K = C_b / C_o$ must be included in equation [1-18], where C_b and C_o are the solute concentrations in the grain boundaries and the lattice respectively. Hence:

$$D_{eff} \square D_l + + \frac{4K\delta D_b}{L} \qquad [1\text{-}19]$$

In the temperature range of $0.3T_m < T < 0.5T_m$, B-type kinetics are operative as in Figure 3 (b). Here fast diffusion along the grain boundary is accompanied by leakage of the diffusant into the grains. At this type, the grain diameter L is consider to be a lot larger than the diffusion length $\sqrt{D_l t}$ where t is the time for diffusion. And below $0.3T_m$, lattice diffusion is almost frozen out so that only grain boundary diffusion prevails.. This is characterized by C-type kinetics shown in Figure 3(c). It requires $2\sqrt{D_l t} \square \delta$. For solder connections under accelerated life test for high current density , the temperature is normally at 373K which is above $0.5T_m$ so type-A or type B kinetics will be operative.

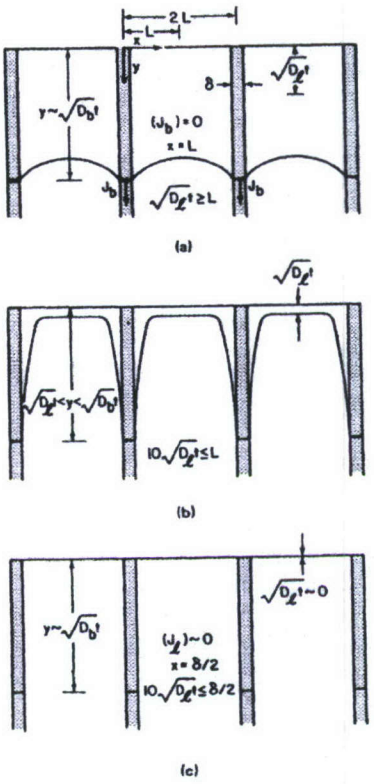

Figure 3 (a) Type-A (b) Type-B (c) Type-C kinetics

for grain boundary diffusion

the curved lines are isoconcentration contours

1.1.2.2 Measuring Diffusivity

The first direct proof of grain boundary diffusion was obtained in the early 1950s using autoradiography (Barnes 1950). The appearance of the famous Fisher model (Fisher 1951) of grain boundary diffusion and the development and extensive radiotracer serial sectioning technique makes the grain boundary diffusion quantitatively measurable.

Most grain boundary diffusion measurements are carried out using radio tracers and serial sectioning technique(Rothman 1984;Philbert 1991). After tracer deposition and diffusion anneal, thin layer of the material parallel to the

source surface are removed from the specimen (either mechanically or by ion sputtering) and radioactivity of each section is determined using a crystalline γ -detector or liquid scintillation counter. The quantity measured in such experiments is the average layered concentration of the diffusant, $\overline{c}$, as a function of the penetration depth y.(Mishin and Herzig 1999) This function, called a concentration (or penetration, or diffusion) profile, bears the information about the GB diffusion parameters. It is therefore subject to a mathematical treatment designed to extract that information.

1.1.2.3 Diffusivity Dependence

From equation [1-17], the temperature is obviously a very important factor which will great affect diffusivity. Also with the temperature change, the effective diffusivity will change since at higher temperature, the bulk diffusion may be operative along with grain boundary or surface diffusion.

Also material melting temperature is an important indication of diffusivity. There is a empirical correlations between GB diffusion data and melting temperature for three classes of metals (fcc,bcc and hcp) derived by Brown and Ashby(Brown and Ashby 1980) and Gust et al.(Gust et al 1985). Although the physical justification of such correlation is rather obscure, such correlations do work and are a very useful as a guide for the evaluation of new data.

	Brown and Ashby		Gust et al.	
Structure	δD_{b0} (m s^{-1})	E_b (J mol^{-1})	δD_{b0} (m^3 s^{-1})	E_b (J mol^{-1})
fcc	9.44×10^{-15}	$83.0T_m$	9.7×10^{-15}	$75.4T_m$
bcc	3.35×10^{-13}	$97.6T_m$	9.2×10^{-15}	$86.7T_m$
hcp	2.74×10^{-14}	$89.8T_m$	1.5×10^{-14}	$85.4T_m$

Figure 4 Empirical correlation between GB self-diffusion and the melting temperature

Microstructure changes also can greatly affect the diffusivity. Grain boundary diffusion is very sensitive to the grain boundary structure and the chemical deposition. In thin films, the alloying copper into aluminum has proven to significantly enhance aluminum interconnect electromigration through reducing grain boundary diffusivity(Lloyd and Clement 1995;Ogawa et al 2002). Also for eutectic solder, with the unstable lamella structure changes, the diffusion will change from interface diffusion to regular polycrystalline materials(Gupta et al. 1998).

Stress can also affect diffusivity. A tensile stress increases the vacancy concentration aiding diffusion while a compressive stress will depress the vacancy concentration, hampering diffusion. Not only does the stress state affect diffusivities through effects on the concentration of vacancies, but stress also affects the activation volume, increasing it and enhancing diffusion in tensile stress states, and decreasing it and suppressing diffusion in compressive stress states.

1.2 Electromigration Failure in Microelectronic Structure

Electromigration failure is very large scale integration interconnects has been studied since the early 1960s(Blech and Sello 1966;Blech and Sello 1967). Aluminum or aluminum alloy with 1-2% of copper has been under extensive study since aluminum has been interconnecting conductors in the microelectronic industry for the past 40 years. Due to the trend of miniaturization, however, the industry has turned to copper as the interconnect conductors for its low resistance-capacitance delay. The question of electromigration in copper metallization must be examined. Also since the system of interconnects in a device includes solder joints on one end that link to package circuits, electromigration in solder has also emerged as a concern in the industry. Compared to the research of electromigration in aluminum and copper, the study in electromigration in solder is rather immature.

When a high density current running through conductors, the electron wind force will cause the atom moving from cathode to anode and vacancy from anode to cathode. If the interface is diffusion barrier, such as aluminum interconnects with W vias, then the vacancy flux divergence near cathode will generate tension stress at interface of aluminum and W vias. On the opposite side, compression stress will build up at near anode side. The final failure at cathode side appears after the voids nucleate and coalesce, and eventually forming a open circuit

failure. On the opposite side, hillocks will generate due to compression stress and sometimes will cause short circuits failure. Voids and hillocks are the prominent two features of electromigration failure.

Blech (Blech and Kinsbron 1975;Blech 1976;Blech and Herring 1976;Blech and Tai 1977) showed that stress gradient play an important role. Also thermomigration can affect interconnects especially solder interconnection(Ye et al. 2003d). Current density distribution (current crowding) can affect voids preferable generation location(Tu et al 2000;Yeh and Tu 2000;Yeh et al 2002). Besides the driving force, diffusion mechanism will greatly affect material failure time. Also boundary condition and microstructure of interconnects are important factors too.

Experiments of electromigration are essential for investigating the failure mechanism and providing first hand data for further analysis. During the past 40 years, development of experimental technique furnished us more detail about electromigration failure. Also since electromigration is always coupled with thermal, electrical, and mechanical process, analytical tools are also needed to analyze the experimental data and systematically reveal the detail picture of electromigration failure. For a complete review for electromigration failure researches, readers are suggested to refer to (Scorzoni et al. 1991;Lloyd 1997;Ogawa et al. 2002;Tu 2003;Hau-Riege 2004;Li et al 2004b).

1.2.1 Black's Experiment and Time to Failure

EM can be studied using several test-structure types(Ogawa et al. 2002). In a given interconnect at some test temperature, electron flow is driven from its cathode-end into its anode. Testing at various temperatures, determining the failure rates, and testing structures with various width and thickness combinations permit the identification of the mechanism-types involved in the failure process. The most prominent type is a NIST(National Institute Standards and Technology) or stripe structure, which is essentially a long interconnect connected at its ends to contact bond pads. The structure is a 1-level structure and is much simpler to fabricate than a 2-level structure. The NIST structure is also useful for joule heating studies. Another type of structure is a "drift" or "Blech" structure(Blech 1976) , where the interconnect is deposited directly over a thin redundant layer of higher resistivity material such as "Al over titanium nitride" or "Cu over tungsten." The redundant layer is the level that is connected to external contact pads. When current is applied through it, the current preferentially flows through the lower resistivity metal. This is called a drift structure because the movement of material due to EM is visible from above, permitting measurement of a physical drift rate. When the rows of drift structures with various line lengths are serially arranged, one can measure the critical length or Blech effect where mass transport of interconnects with lengths shorter than a critical value fail to show evidence of

drift for a given current density. The drift structures are also useful because they do not possess a reservoir of material to annihilate the vacancies generated by EM as is the case for the 1-level NIST structures. 2-Level structures are also used(Hu et al 1993), where current into an interconnect lead is fed through a via placed above or below the ends of the lead. Usually, the via is made of a different material, e.g., tungsten, to form a flux-blocking boundary at the cathode and anode ends of the lead. This structure is useful for drift, resistance trace, kinetic, and critical current-length product studies. Passivation means that the metal conductor is completely surrounded by an insulating and protective barrier. Because EM mass transport can be affected by interfaces and the passivation has impact on the stress-levels attainable within the metal under EM driving force, this distinction is important in understanding the results in the literature.

James R. Black (Black 1967) was one of the pioneers in conducting research on the failure mechanisms of electromigration in thin metal conductors. He found that the lifetime of a thin metal conductor is inversely proportional to the square of the current density and has an Arrhenius component with activation energy consistent with grain boundary diffusion. He proposed the following median time to failure equation:

$$t_{50} = \frac{A}{j^2}\exp(\frac{E_a}{kT}) \qquad [1\text{-}20]$$

where t_{50}, median time to failure (MTTF), is defined as the time at which

50% of a large number of identical devices have failed, A is a empirical material constant, j is the current density, n is the current density exponent and is found to be 2 in Black's experiments, E_a is the activation energy, k is Boltzman's constant, and T is the absolute temperature. This equation is known as Black's Equation. Black's experiments suggest that grain boundary diffusion is the major diffusion mechanism and electromigration failure is controlled by grain boundary diffusion. The activation energy of time to failure coincides with the grain boundary diffusion activation energy. The single mode of distribution of aluminum thin film structure has been widely accepted. The current dependence of TTF of Black's equation has been under extensive research, numerous computational and analytical models have been proposed to explain the Black's equation. Main weakness of Black's Equation is the fact that it ignores the influence of thermal gradient across the specimen.

1.2.2 Voids Nucleation and Growth Locations

The driving force for void nucleation is the tensile stress at the local lattice sites(Gleixner and Nix 1996). Tensile stress is coming from the vacancy condensation due to local vacancy divergence flux. The usual locations for vacancy divergence flux are at the blocking boundaries of the interface. Current crowding(Yeh and Tu 2000;Yeh et al. 2002;Tu 2003) or stress concentration gradient due to the geometry can also cause vacancy flux divergence, where flux

divergence is $divJ = \nabla \square J$, J is flux.

The typical test structures for electromigration for aluminum and copper thin film interconnections are shown in Figure 5. Flip chip solder joint structure used for electromigration is shown in Figure 6. For aluminum test structure, the main flux divergence location is at the M2 layer and W via interface. For typical copper test structure, the maximum flux divergence location can either be at the interface of copper via and tantalum barrier due to the blocking boundary condition, or it could be at the upper corner of M2 line due to current and stress fields interaction. For solder joints, the interface of solder bump with the silicon die side is the most vulnerable location for void nucleation. The subsequent void growth depends on the diffusion mechanisms. In aluminum, the diffusion mechanism is well established to be grain boundary diffusion. So after voids nucleate at triple junction of grain boundaries or interface, the grain boundary provides a fast path for diffusion and voids grow till failure is reached

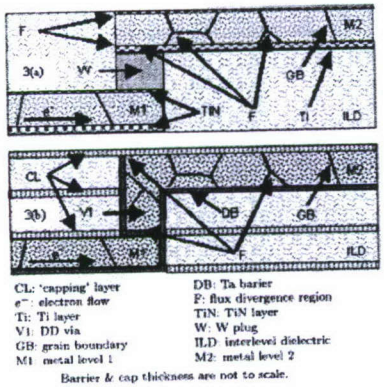

Figure 5 Idealized 2-level Al(Cu) (upper picture) or Cu Interconnections (lower picture)(Ogawa et al. 2002)

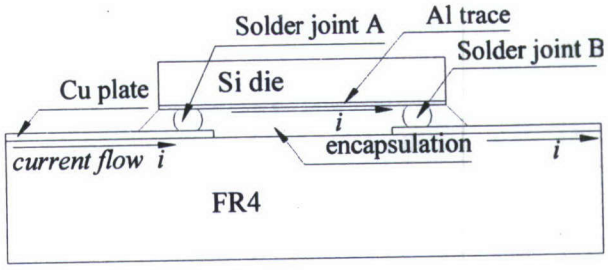

Figure 6 Flip Chip Solder Joints Test Structure(Ye Hua 2004)

Experimental observation of void nucleation and growth is usually done with SEM (Scanning Electronic Microscopy) and FIB (Focused Ion beam)(Hu et al 2002b;Liniger et al 2003;Hu et al 2003b). Also in-situ SEM technology(Meyer et al 2002;Zschech et al 2004) has also been developed to monitor the real time development of void nucleation and growth dynamics.

1.2.3 Time to Failure Statistical Analysis

Black's equation is widely used to extrapolate service life time for interconnections with the results obtained by MTF (median time to failure) technique. The standard approach to testing electromigration reliability is to stress a series of interconnect test structures at higher temperatures and current densities than would be seen during normal operation to accelerate the electromigration failure rate. These data are then used to estimate the maximum use current, j_{use}, where the chip will not fail prematurely from electromigration under a normal use temperature, e.g. 100 °C, over the lifetime of the chip. The j_{use} specification is used in the chip design. Traditionally, the cumulative percent

failure probability of an accelerated electromigration stress can be fitted using a cumulative lognormal function:

$$F = \int \frac{1}{\sqrt{2\pi}\sigma} e^{-\frac{(\ln\tau - \ln\tau_{50})^2}{2\sigma^2}} d\ln\tau \qquad [1\text{-}21]$$

The MTF of acceleration tests is then extrapolated according to Black's equation(Gignac et al 2003). Black's MTTF equations gives out -2 current density dependence of time to failure while Oates (Oates 1995).have reported different current density dependence value with respect to MTTF. This second order time dependence is analyzed by several models according to critical stress or critical concentration for void nucleation as failure criteria (Shatzkes and Lloyd 1986). In later section, we will give further review.

The single mode lognormal distribution adopted in small samples acceleration experiments means electromigration failure mechanism is mono mode, that is, only one failure mode is operative. The lognormal distribution is commonly used for general reliability analysis, cycles-to-failure in fatigue, material strengths and loading variables in probabilistic design (A random variable is lognormally distributed if the logarithm of the random variable is normally distributed). In order to extrapolate to service condition, it assume this failure mode under higher current and higher temperature under acceleration test is operative throughout the full temperature and current density range of service conditions. For single layer structure such as Aluminum (Cu) with W via or

Copper single damascene line, a log normal distribution can gives good fitting to experimental data. But for dual damascene or multi structure interconnection, a mono mode log normal distribution can not fit into data very well. Two mode or three mode log normal distributions are suggested for these structure and this implies more than one failure mechanisms are operative in these types of structures (Fischer et al ;Ueno et al ;Gill et al ;Lai et al ;Hu et al 2002a;Hu et al. 2002b;Gan et al 2003;Gignac et al. 2003;Liniger et al. 2003). Here a dual-damascene (DD) structure refer to the manufacturing process that only a single metal deposition step is used to simultaneously form the main metal lines and the metal in the via.

Two different methods are typically used for monitoring the electromigration time to failure. One is resistance change. Usually at the onset of current application, the resistance change is very small, and at the failure time the resistance will increase abruptly. The other one is to monitor the low frequencies changes. For resistance change, In order to detect the early stage of electromigration, due to the small resistance changes to be evaluated, a resolution of the order of 1×10^{-4} must be reached. Unfortunately, the resolution of conventional resistance measurements during electromigration is limited by thermal instabilities of the sample holder. In fact a typical temperature instability is of the order of $\pm0.2^{o}C$. This corresponds to $\Delta R/R \approx 4\times10^{-4}$ at 200 ^{o}C for aluminum films(Scorzoni et al. 1991). In order to compensate for temperature

changes and obtain a high resolution, an AC Wheatstone bridge(Lloyd and Koch 1988) was adopted, where the resistance of the conductor stripe undergoing high current density was compared to an unstressed monitor stripe. The measurement cycle was accomplished by introducing for a short period of high current density into both samples when the resistance of the stressed sample was measured. The duration of the stressing current in the reference sample was so small as to prevent an meaningful electromigration effect. This procedure ensured that the stressed and reference sample temperatures were identical.

The different failure criteria adopted in electromigration test can change the time to failure distribution. Liu et al (2004)used 1%, 50% and 60% of resistance change to study 0.23 μm wide copper dual-damascene lines connected to underlying W lines with a TaN/Ta liner and S_iN_x / S_iO_2 insulator. The results show that 1% resistance change at the test temperature is best described by a trimodal function which means three different failure mechanisms existed. However using 50% resistance increase as failure criteria, the lifetime of samples showed a bimodal behavior which means only two failure mechanisms existed.

The sampling size is important too in order to characterize the statistical nature of time to failure. It is impossible to test several million interconnect samples in an experimental approach. Only few studies have been performed which extended the test sample size beyond the typical number of several tens of failure units(Hoang et al 1989;Nogami et al 1995;Gall et al 2001). Due to the

amount of interconnects used in electronic industry, for example, a full-scale device such as a state-of-the-art microprocessor or memory chip can contain up to several million possible failure links. One weakest link fail can break down the whole system. Gall et al(Gall et al 1996;Gall et al 2000;Gall et al. 2001) used the weakest link approach tested more than 75000 interconnects with 480 interconnects connected together as a link. Then using statistical deconvolution they were able to show that for a single interconnect, the electromigration failure mechanism follows perfect log normal behavior down to the 4 sigma level (1×10^{-4}). The sample they used is Al(Cu).

1.2.4 Various Factors Affecting Electromigration Failures

Predicting the time to failure for electromigration damage is very complicated. During this process, conductors have electrical, thermal and mechanical field exist at the same time. Not only the conductor material's properties affect the time to failure, but also the non non-conductive and electrical connections surrounding it change the material electromigration life time. The researches on electromigration have focused on various conditions which will improve time to failure, or to prevent bad condition which will make material more vulnerable to electromigration. These research results give the industry guidance for reducing electromigration damage, also present insight to the failure mechanism of electromigration. Yet these empirical research results do not help

an engineer to do computational simulation on a next generation package that is in conceptual design phace

1.2.4.1 Effect of Microstructure on Electromigration

Here the microstructure means grain structure of a material. It is well known that in Al and Cu thin film grain boundary diffusion operate dominantly or together with surface diffusion. Hence the grain boundary, as a fast diffusion path, greatly affect the electromigration time to failure. Also the triple joints of grain boundaries (the intersection of three grain boundaries) can serve as center of atomic flux divergence lead to supersaturation of vacancies and become locations of void nucleation and growth near cathode(Tu 2003). Grain orientation and grain size also will affect time to failure(Onoda et al 1995). The so called bamboo structure also will greatly improve TTF of electromigration since it can reduce the effective diffusivity by greatly reducing the grain boundary as a fast path. Bamboo structure means that single grains are structured in a row in a very narrow stripe.

1.2.4.2 Effect of Solute on Electromigration

Adding a small percentage of Cu into Al thin film improve significantly electromigration life time(Ames et al 2000). In bulk alloys, certain solutes have the effect of retarding or enhancing solvent diffusion. In fact solute Cu in Al is known

to enhance the lattice diffusion of Al solvent atoms. As we are still not very clear about diffusion process in grain structure, it is still not clear why adding Cu into Al by 1% or so will greatly improve life of conductors under high current density. Several models have been proposed to explain this behavior(Morris et al 1996;Kim et al 1996;Liu et al 1998;Liu et al 1999b). Also by adding certain amount of Sn into Cu can improve copper interconnect electromigration performance(Gupta et al 1997).

1.2.4.3 Effect of Boundary Condition on Electromigration

The interconnections of electronic circuit are surrounded by non conducting and conducting materials. The non conducting materials such as S_iO_2 provide mechanical support and protection while conducting material such W (tungsten) via provide electrical and thermal connections. In copper dual-damascene structure, the liners which surround the copper thin film provide both mechanical protection and also as an electrical shunt layer. Here electrical shunt layer means it can also supply a path for electrical current. These conditions will greatly affect electromigration failure mechanism and time to failure. For detail of Al and Cu interconnection structure see Figure 5.

In copper damascene lines, studies have shown that the electromigration lifetime is mostly dependent on atomic diffusion along the interface between Cu and dielectric layer(Von Glasow et al ;Hu et al 1999;Hau-Riege and Thompson

2001). So the interfacial layer between capping and copper thin film will naturally affect electromigration. Different capping materials have been compared(Hu et al. 2002b;Lane et al 2003;Hu et al 2003a) with Cu dual damascene lines, the difference in selected capping layer material has proved to have a strong effect on electromigration life time of Cu lines. The activation energies for without capping is 0.87eV, with $S_iC_xH_yN_z$ capping it is 1.0eV, with Ta/TaN capping is 1.4eV and with CoWP capping it is1.9 eV (Hu et al. 2003a) . Other studies also show that TiN/Ti substrate on Al/Si/Cu alloy will improve electromigration reliability(Olowolafe et al 1993;Park and Lee 2001).

The diffusion barrier is another important boundary condition since it defines the flux divergence location near the blocking boundary. The W via under Al(Cu) alloy interconnection(see Figure 5) is an example for this blocking boundary condition. Another example is the TaN/Ta liner in Cu/SiO_2 interconnects structure. Liniger et al(Liniger et al. 2003) have shown that with a current density $<5mA/\mu m^2$ in the power line, the 6 nm liner thickness will give the best performance in mean time to failure. This can be attributed to the reason the thin liner will not prevent the Cu diffusion. Since the M1 layer of the structure is much wider than M2 layer, as a result it serves as a reservoir for diffusion according to Liniger. Other researches(Ueno et al. ;Hu et al 2001;Hu et al. 2002a) also showed this effect of liner thickness. The stress due to blocking boundary condition may play an important role here. With the thickness of liner increasing, the blocking

boundary condition will be fully established and stress gradient maybe the reason for the voids shown in Figure 7. Also when there is no liner, there will be no void formation at M1/Via interface since the Cu will form a continuous flow just like in Blech's drift test. But this require that the M2 layer must be a reservoir otherwise it will damage the M2 layer. Also the stress gradient won't build up and electromigration driving force will become larger since there is no stress gradient counter- balance force. The W via under Al(Cu) is relatively much thicker than the liner used in Cu interconnection, so it is a very good diffusion barrier for Al.

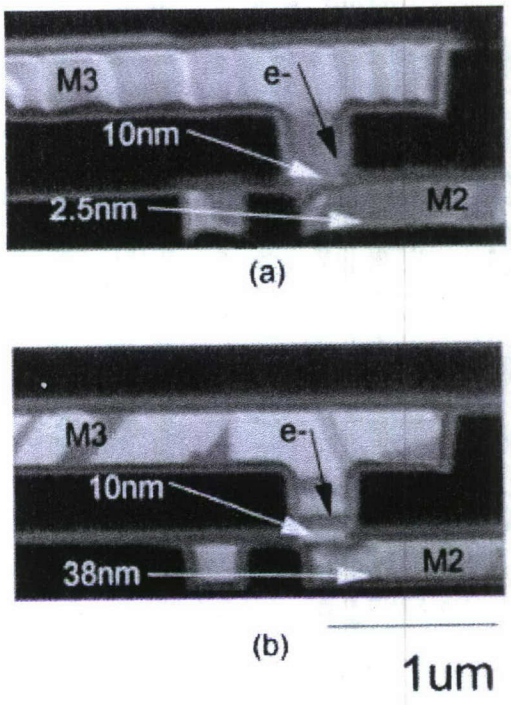

Figure 7 Focused Ion Beam Cross Section Images (Liniger et al. 2003)

1.2.5 Comparison of Electromigration Failure of Al and Cu versus Solder Alloys

The electromigration in solder(Liu et al 1999a;Liu et al 2000;Ye et al 2002;Choi et al 2002;Yeh et al. 2002;Gan et al 2002;Tu 2003;Nah et al 2003;Ye et al 2003a;Ye et al 2003b;Ye et al 2003c) is a relative new topic as compared to Al and Cu. A comparison is necessary for utilizing the researches on much matured Al and Cu electromigration research.

Tu (Tu 2003) compared diffusivity of Al, Cu and eutectic solder Pb/Sn at 373K and 350. °C. at 100 °C the lattice diffusivity of Cu and Al is significantly small, and the grain boundary diffusivity of Cu is three orders of magnitude smaller than the surface diffusivity of Cu. At 350 °C the difference between surface and grain boundary diffusivity of Cu is much less, indicating that we cannot ignore the latter. The lattice diffusivity of eutectic SnPb (not a face-centered-cubic metal) at 100 °C is given as an average value of tracer diffusivity of Pb and Sn in the alloy. It depends strongly on the lamellar microstructure of the eutectic sample. Since a solder joint has, typically, a few large grains, the smaller diffusivity is better for our consideration. To compare atomic fluxes transported by these three kinds of diffusion in a metal, we should multiply the diffusivity by their corresponding cross-sectional area of path of diffusion. But the outcome is the same.

Table I. Melting point and diffusivities of Cu, Al, and eutectic SnPb.				
	Melting point (K)	Temperature ratio 373 K/T m	Diffusivities at 100 °C (cm^2/s)	Diffusivities at 350 °C (cm^2/s)
Cu	1356	0.275	Lattice $D_l = 7\times10^{-28}$ Grain boundary $D_{gb} = 3\times10^{-15}$ Surface $D_s = 10^{-12}$	$D_l = 5\times10^{-17}$ $D_{gb} = 1.2\times10^{-9}$ $D_s = 10^{-8}$
Al	933	0.4	Lattice $D_l = 1.5\times10^{-19}$ Grain boundary $D_{gb} = 6\times10^{-11}$	$D_l = 10^{-11}$ $D_{gb} = 5\times10^{-7}$
Eutectic SnPb	456	0.82	Lattice $D_l = 2\times10^{-9}$–2×10^{-10}	Molten state $D_l > 10^{-5}$

Table 1 Diffusivities of Cu Al and eutectic solder(Tu 2003)

The low melting point eutectic solder and lead free solder alloys compared to aluminum and copper will show time dependent deformation which is called viscoplasticity. Under constant electrical current stressing, the solder is under stress due to the interaction between vacancy flux divergence and confined boundary. Because the vacancy flux divergence is determined by the blocking boundary condition and the electromigration driving force, the larger current density will increase stress faster than smaller current density. Thus the rate sensitivity of viscoplasticity will be different under different current densities.

The electromigration driving forces Pb/Sn solder, aluminum and copper are roughly at the same order. The solder joint dimension is at the order of 100

microns which is two orders of magnitude larger than copper and aluminum thin film. The electrical resistivity of aluminum and copper is one order of magnitude smaller than solder. The effective chargeness number reported in the literature is about one order of magnitude larger than copper and aluminum(Lee et al 2001;Huynh et al 2001;Ye Hua 2004). According to the electromigration driving force equation $F_e = z^* e \rho j$, we can see that they are in the same order of magnitude under the same applied current. Due to the smaller Young's modulus of solder joints compared with Al and Cu, the stress gradient counter force will be much smaller than Al and Cu. Thus the electromigration failure in solder joints will be a serious concern.

As a two phase material, there are two major diffusion species in Sn/Pb solder. This make the solder alloy diffusion more complicated than Cu and Al. At different temperature ranges, there seems to be different dominant diffusion mechanisms. experiments conducted at $150^{\circ}C$ that the diffusion of Pb is the dominant diffusion species(Lee et al. 2001). But at temperatures lower than $100^{\circ}C$ Sn instead of Pb is the dominant diffusion species(Liu et al. 2000). Due to the thermodynamically unstable nature of eutectic micro structure, microstructure changes affect the electromigration failure process. Thus annealing of the solder joint is very important. Before comparing different experiments reported in the literature the annealing temperature and time should be compared first.

Different composition of Sn and Pb makes solder alloy have different

electromigration failure resistance. This is partly due to the diffusivity caused by microstructural difference. Since Pb/Sn solder is a two phase system including Pb rich or Sn rich phase. But their grains are intertwined with each other inside each phase. This makes the diffusion path very complicated. If the main diffusion species is Sn, it will diffuse through Sn rich, Pb rich and also their interface boundaries. The diffusivity of Sn under various lattice structures is different(Gupta 1997;Gupta et al. 1997;Gupta et al. 1998) and the effective diffusivity which is a combination of these diffusivities is also different.

The typical flip chip package solder joint structure is shown in Figure 8. The current is passing through a thin layer of aluminum thin film deposited on silicon die side. Electroless Ni is another layer below Al thin film. The PCB side is usually consists of Cu/Ni/Au multilayer structure. As we know the noble element such as Ag, Ni and Cu will react with Sn to form various IMC (intermetalic compounds) during the reflow process and current driving. These IMC layers influence with the electromigration failure process compared to Al and Cu thin film structure.

The IMC formed at solder and metallization layer will makes the interface vulnerable for mechanical failure. The UBM (under bump metallization) of a flip chip has a large impact on the IMC formation and consequently on the solder joint durability. For eutectic SnPb solder with Ni/Au as UBM, continuous Ni_3Sn_4 and $AuSn_4$ IMC layers are often formed at the die/solder and substrate/solder interfaces during aging. With the increase of aging time, shear strength

degradation caused by the brittleness and weakness of the $AuSn_4$ IMC layer is observed, especially when the gold concentration in the solder joint is above 3 wt%. When Al/Ni(V)/Cu is used as the UBM, the formation of such a continuous $AuSn_4$ layer at the interfaces is suppressed by the formation of an η-Cu_6Sn_5 IMC layer with dissolution of nickel and gold, which shows better mechanical properties than $AuSn_4$(Duan et al 2003).

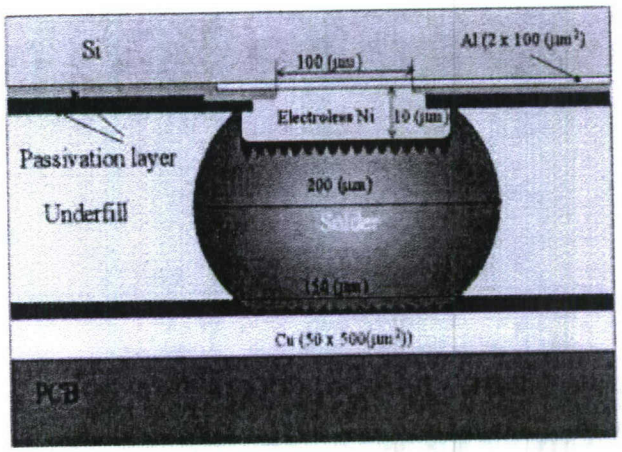

Figure 8 A typical solder connection structure(Lee et al. 2001)

The IMC layer will also affect the diffusion boundary. The IMC between Sn with Cu and Ni will form a blocking boundary condition to resist the consumption of thin film deposited on the solder interface. The IMC thickness is thus a very important factor in electromigration failure study since it has a direct impact on the boundary condition of diffusion flux. (Chen and Chen 2002) conducted experiments on Ni and Sn reaction under current loading. It was find out that different current direction will greatly affect the IMC thickness formed at the interface. When the electron direction is from Sn to Ni, the IMC layer thickness is

much larger than if the electron is passing from Ni to Sn. This may suggest that during the formation of IMC, the Sn atom flux is the dominant species.

1.3 Damage Modeling for Electromigration

The void nucleation and growth is the dominant damage mechanism in electromigration induced failure. The electromigration research efforts on prediction of damage failure have focused on void nucleation and growth. Usually the beginning of void nucleation is defined by means of critical stress level which is usually a spherical stress. Some researchers use critical atomic or vacancy concentration level as an criteria of nucleation of voids. The linear elastic stress evolution model is used to predict the stress level. The stress model is solved analytically for some simple 1-D or 2-D cases with ideal blocking boundary condition and initial stress-free state using linear elastic material assumption. Numerical method such as FEM is used to solve the diffusion equation. Void growth or void dynamics are also under extensive investigation. The driving force for void growth in electromigration is usually diffusion. There are some models in which researchers are trying to combine void nucleation and growth using numerical methods. The technical difficulty in these models is numerically singularities of free surface after the void nucleation and remeshing process. Since stress is usually induced by atomic flux divergence or vacancy flux divergence, some researchers directly use total atomic flux divergence or

vacancy flux divergence as an indication of void nucleation. In thin film technology, microstructure is a very important factor that affect damage evolution, especially grain structure of narrow thin film conductor. Some models incorporated microstructure in to the model when predicting damage. Due to the statistical nature of grain structure, the damage prediction is also statistical. In this sector, several typical models be reviewed and discussion regarding the pros and cons will be presented.

1.3.1 Analytical and semi-analytical failure models

The stress evolution model developed by Korhonen et al (1993) is widely used in the literature. The advantage of this model is that it established the direct relationship between spherical stress and atomic concentration. Thus it avoids a numerical procedure for solving coupled differential equations of displacement and diffusion. For a simple 1-D thin film structure with narrow width it is a quite reasonable assumption. The limitation of the model is also obvious that it can not be used to solve complicated boundary conditions and geometric features. Whether a model can be used to analyze an electromigration under irregular boundary conditions and irregular geometry determines if it is a numerical solution of the differential equations ot analytical solution. Semi-analytical models use FEM or other numerical tools but they do not include displacement boundary condition effects on the distribution of stress.

In order to explain exponent of 2 in Black's mean time to failure empirical equation, Shatzkes and Lloyd (1986) proposed an analytical solution for vacancy diffusion. The stress is omitted in their formulation. The vacancy continuity equation is given by

$$\frac{\partial C}{\partial t} = \frac{D\partial^2 C}{\partial x^2} - v\frac{\partial C}{\partial x} \qquad [1\text{-}22]$$

and the boundary and initial conditions are given by

$$C(-\infty, t) = C_0 \qquad [1\text{-}23]$$

$$J_v(0,t) = D\frac{\partial C}{\partial t} - vC = 0 \qquad [1\text{-}24]$$

where C is vacancy concentration ,

D is diffusivity,

$v = Z^* e\rho jD / kT$

Equation [1-22] is solved under blocking boundary condition and initial uniform vacancy distribution. By assuming a critical vacancy concentration as failure criteria, the time to failure is proportional to inverse of square of current density.

Shatzkes and Lloyd used vacancy as their primary variable; other researchers also use atomic concentration or hydrostatic stress as their primary variable(Ross 1991;Kirchheim 1992;Korhonen et al 1992;Kirchheim 1993b;Clement and Thompson 1995;Clement 1997). The damage metric for these models is critical stress or critical atomic concentration level. The exponent

of two dependence with current density and the time to failure have been verified by above listed researchers for specific cases. If vacancy is used instead of atoms in a model, since the vacancy does not follow conservation equation like atoms, the sink and source of vacancy are sometimes included into the equation set. Kirchheim(Kirchheim 1992) uses a rate equation to represent vacancy generation and annihilation which imply that vacancy and hydrostatic stress are in quasi static equilibrium anytime. If a vacancy and stress equilibrium can reach steady state fast, this sink and source term can then be ignored. This is controlled by the parameter called characteristic time. When this value is large, after the current is applied to conductors, the stress build up will be generally slow at the boundary for reaching maximum value since the stress build up process is mainly controlled by the diffusion process. If the characteristic time is small, stress build up at the boundary will be fast since now this process is controlled by vacancy-stress thermodynamic equation.

Grain structure is also considered by Knowlton et al (1997). A thin film near bamboo grain structure is shown in Figure 9. Author use the same stress evolution governing equation as Korhonen to predict the stress profile at different times which is also shown in Figure 9. The diffusivity of the bamboo section is set to be lower than the diffusivity of the multi grain section where effective diffusivity including grain boundary and bulk diffusion is calculated. Predicting the reliability of near-bamboo lines, therefore, requires a detailed understanding of the grain

structure of the interconnects, including the distribution of polygranular cluster lengths, the distribution of bamboo lengths, and the spatial distribution of clusters along the line length. Large populations of lines are generated in order to obtain meaningful failure time distributions for a variety of line characteristics and testing conditions. The stress distribution along the thin film line shown in Figure 9 is discontinuous. Based on mechanical equilibrium requirement, this stress profile therefore cannot be true. This proves that the limitation of ignoring the stress field boundary conditions and ignoring displacement continuity condition.

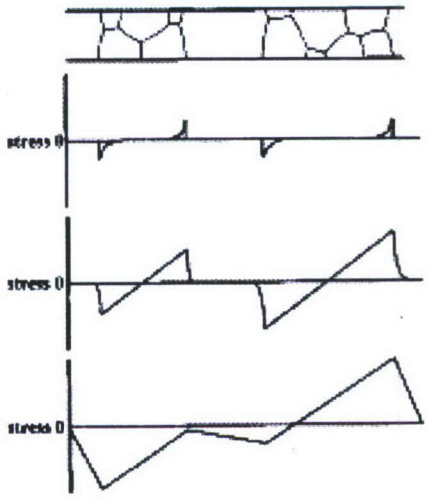

Figure 9 The microstructure and associated stress profile of a near bamboo structure as a function of position at (a) short (b) intermediate (c) long times(Knowlton et al. 1997)

A more complicated model based on atomic concentration is proposed by Park et al (1999) to include the atomic diffusivity dependence on hydrostatic stress. Finite volume method is used to calculate the stress evolution. Critical stress level is defined as a criterion of the onset of void nucleation. To considering

the void growth, the atoms removing from the void nucleation location which is atomic flux divergence is calculated. The stress relaxation after void nucleation is also considered in the model. But the stress relaxation effect is not a direct result of numerical calculation but rather defined by a constant relaxation length which is not clearly defined. Also the voids are considered to be occupying the whole width of the conductor which is obvious not true in a realistic situation.

Since electrical resistance change is often used as an indication in experiments for damage evolution, resistance change after void growth is also used as a parameter for damage evolution. Flippi et al(Filippi et al 1996) correlated resistance change with the void growth model based on very simple assumption of average strain. The voids in Flippi's model are assumed to be occupying the whole conductor intersection.

1.3.2 Numerical damage failure models

A general model for EM-induced voiding has been proposed and implemented by Sukharev et al (2004). Here temperature gradient, stress gradient, vacancy concentration gradient and electron wind force are all considered. The complete system of all related variables is considered which include Laplace's equation for electric field, Fourier's equation for thermal field, Navier's equation for displacement field and mass balance equation for diffusion process. It is not clear how the four coupled equations are solved from the paper

since it is a very complicated process. For thermal and electric field it will be stabilize very fast compared to diffusion process. The thermal field and electric field equations can be uncoupled from the system. A sequential analysis can then be performed before solving the coupled equations of diffusion and displacement field. The linear elastic assumption is used and a critical or threshold atomic concentration is defined. Once the critical atomic concentration is reached, the part will be occupied by an extending void. In order to avoid the numerical difficulties from the free surface created after the void nucleation, the void are defined through a method called phase field method. This method deals with modification of the material properties of the portion of conductor occupied by the growing void. Electrical conductivity, thermal conductivity, Young's modulus, etc. inside the void is reduced from the values corresponding to the considered metal to almost zero, which corresponds to vacuum.

1.3.3 Discussion and motivation

Void nucleation and growth is a complicated process even under only mechanical stress field. Void nucleation may depend on stress field, plastic strain accumulation, diffusion, microstructure evolution, preexisting second phase particles, and other factors. For different materials, void nucleation will obviously be controlled by different combination of above factors. Due to statistical nature of some conditions such as grain structure and preexisting second phase particle,

the simulation model must be stochastic in nature. A simple critical stress or critical vacancy concentration level is not enough to be used as an indication for material failure. A versatile damage metric is needed for different materials.

Although continuum mechanics can not deal with void growth modeling, void nucleation is usually a very good indicator for material damage. Void nucleation dominant failure is a good example. In this type of failure mechanism, once voids nucleate, material will fail very quickly. Due to the high residual stress level in embedded thin film structure and high plastic strain concentration in solder joints, the void nucleation is the most dominant failure mechanism. The incubation time for void nucleation in electromigration thus can be predicted using a general damage metric.

For simulating the damage process, initial thermal and electrical field are needed. The current field distribution sometimes is dominant feature and thermal mismatch will contribute to stress field also. Boundary conditions which include diffusion and displacement field need to be considered carefully. Blocking boundary conditions are usually being adopted for simulating the electromigration process in the literature. But blocking boundary conditions are not always present. Most of the models available do not considered displacement boundary conditions. The assumption is that thin film is under confinement of an infinite material and a simple bulk modulus is used to define the stress-strain relationship. In simple 1-D aluminum thin film, the simplicity of displacement boundary

conditions can allow such simplification. But in a little complicated geometric feature such as copper dual damascene structure, this assumption is not true. For 3-D solder joints, a coupled system is definitely needed to solve a displacement-diffusion problem.

Plasticity generally is not considered by the models available in the literature. The stress relaxation process due to plasticity or diffusion is discussed in the literature(Korhonen et al 1991;Singh et al 2005). The plastic strain accumulation is an important factor in void nucleation and growth process. The dislocations climb and glide accumulation at second hard phase particles is a source for void nucleation and growth. In order to accurately simulating the damage process the plasticity and viscoplasticity needs to be considered.

Chapter 2 Solution of Diffusion-Displacement Partial Differential Equations

Equation Chapter 2 Section 1

2.1 Introduction

In this chapter an electromigration induced strain-current density model is proposed and implemented in finite element procedure for solution of boundary/initial value problems. Plasticity including viscoplasticity model are also included. A user element for commercial software ABAQUS is created based on the model.

Electromigration is a mass diffusion process that happens as a result of an exchange of momentum between charge carriers(free electron) and the ions of the conductor(Huntington and Grone 1961). Electromigration became engineering interest since it was first observed as one of the primary failure mechanism in aluminum IC conductors. Due to insatiate demand for miniaturization of electronics, electromigration induced failure is becoming a concern for not only IC thin films but also for solder joints in microelectronic systems and power electronic packaging (Liu et al. 2000;Lee et al 2001b;Ye et al 2002a;Ye et al. 2002b;Ye et al 2002c;Ye et al 2002d;Ye et al 2002d;Ye et al. 2003a;Ye et al 2003a;Ye et al. 2003b;Ye et al 2003c;Ye et al. 2003d;Ye et al. 2003e). Under high current density electromigration, vacancy diffusion is driven

by four forces;

1) electrical current field forces, which is due to momentum exchange between moving electrons and host ions,
2) Stress gradient, due to localization of accumulation and depletion of mass,
3) Temperature gradient, due to Joule heating,
4) Vacancy concentration gradient.

Most of the published work ignored the influence of temperature gradient forces. Ye et al (2003e) was the first to observe that temperature gradient driving force can be as strong as other forces and under some instances it can be the dominant force.

Blech and Sello (1967) were the first to show that stress gradient can act as a counter force against electrical field driving force. As the mass moves from cathode side to anode side, compression on anode side and tension on cathode side will create a stress gradient. Black (1969) is the first to establish a relationship between mean time to failure (MTTF) with current density although he omitted many factors, hence his equation is applicable only to certain specific cases he tested.

Numerous experiments have already proved the existence of a strain gradient within the thin film conductor line using X-ray diffraction which can penetrate the passivation layer on top of thin film. (Wang 2001;Ma 2004;Solak 2004;Valek and Bravman 2004c) . Mechanical stress induced plastic deformation has been

verified by the obvious evidence of whisker or hillock at the anode side of metal conductors(Ye et al. 2002a;Ye et al. 2002c;Ye et al. 2002d;Ye et al. 2003a;Ye et al. 2003b;Ye et al. 2003e;Valek and Bravman 2004d). Plastic deformation also contributes to the main damage phenomenon, which is void nucleation at the cathode side. Plastic deformation by grain boundary sliding produces high stress localization when the slip band intersects with particles at grain boundary, which is a favorite site for void nucleation. Also when there is stress, void growth may occur within grains as it is governed by power law creep(Cocks 1982).Under high current density the damage is caused by several mechanisms including mechanical, thermal and electrical.

Physics literature is rich with empirical mean time to failure equations for thin films subject to electromigration. Yet these empirical and analytical equations can not be used for arbitrary boundary/initial value problems. Instead constitutive models that can be implemented in finite element method are needed(Trattles et al 1994;Sasagawa et al 2001;Ye et al. 2003c). Models proposed in the literature do not consider plastic deformation during electromigration process which can't be neglected. Also real interaction of vacancy flux and stress, which exists concurrently, needs to be solved together and not by a sequential method as it is conventionally done in the literature(Trattles et al. 1994), because of the coupled effect between stress evolution and atomic flux. In this chapter, a fully coupled model for simulation of mechanical stress and vacancy diffusion with inelastic

mechanical material property is proposed which has never been done before. The model accounts for vacancy flux due to electromigration, stress gradient, thermomigration and vacancy concentration gradient. It should be pointed out that earlier similar studies always assumed linear elastic material.

There are several electromigration stress evolution models proposed in the literature. Kirchheim (1992) proposed a stress model for electromigration in which generation of tensile and compressive stresses in grain boundaries during electromigration is caused by the transport, annihilation and generation of vacancies. Self-consistent equations were proposed describing vacancy migration through a grain boundary and the associated stress evolution. Another physical model was proposed by Korhonen et al. (1993) to describe the mechanical stresses arising due to electromigration in a confined thin film deposited on an oxidized silicon substrate and covered by a rigid dielectric passivation layer. While Kirchheim's model did not consider the direct contribution of the vacancy flux in the stress evolution; Korhonen's model's biggest disadvantages are that vacancy generation and annihilation effect was not taken into account and vacancy equilibrium was assumed. Also Kirchheim and Korhonen's model assumes a direct stress and vacancy/atom's flux divergence relationship based on certain boundary assumption. As a result, finite element solution implementation is not possible based on their models.

Sarychev(Sarychev and Zhinikov 1999) proposed another stress model which

takes into those factors. And he gave out several analytical solutions based on elastic material properties and special boundary conditions. It should be pointed out that none of the three models mentioned above include thermomigration, which cannot not be neglected under some circumstances as pointed out by Ye et al(Ye et al. 2003e). Also these models all assume that material is elastic. We base our constitutive modeling on Sarychev's stress evolution model. Because of Sarychev's model is based on vacancy concentration not atomic concentration, the flux in the later formulation is refer to vacancy flux instead of atomic flux. In this dissertation Sarychev and Zhinnikov's (1999) model is used.

2.2 Finite Element Formulation

The proposed model is implemented with ABAQUS general purpose finite element program using thermal-displacement analysis option. ABAQUS and other commercially available finite element codes do not have the capability to solve general electromigration problem directly. Thermal-displacement option is used simply because from mathematical point of view, diffusion process and thermal flux is governed by the same type of parabolic differential equations. With ABAQUS user element interface, we can embed the program into ABAQUS, where the temperature degree of freedom is utilized for normalized concentration of vacancy. An 8-node quadratic 2D element and a twenty-node 3D brick element have been established to simulate both 2D and 3D electromigration boundary

value problems.

In the following presentation of the model development, we adopt viscoplastic material behavior with kinematic and isotropic hardening which can accommodate most metal mechanical properties. The ultimate goal of this project is to study electromigration induced damage on microelectronics solder joints, which exhibit highly viscoplastic behavior with nonlinear kinematic/isotropic hardening. Ye et al (Ye et al. 2003a) have shown that solder joints under high current density exhibit significant viscoplastic behavior.

2.2.1 Governing equations

Electromigration is a diffusion controlled mass transport process. It is governed by the following vacancy conservation equation which is equivalent to mass conservation equation.

$$\int_{\mathbf{v}} (\mathbf{C}_{\mathbf{v0}} \frac{\partial c}{\partial t} + \nabla \bullet \mathbf{q} - G) dV = 0 \qquad [2\text{-}1]$$

where C_{v0} is equilibrium vacancy concentration in the absence of stress field,

c is normalized vacancy concentration and $c = \frac{C_v}{C_{v0}}$,

C_v is vacancy concentration,

t is time,

$\mathbf{q}$ is vacancy flux,

G is vacancy generation/annihilation rate.

Force equilibrium is governed by the following equation

$$\frac{\partial \sigma_{ij}}{\partial x_j} = 0 \qquad [2\text{-}2]$$

2.2.2 Constitutive equations

Assuming that driving forces of vacancy flux are vacancy concentration gradient, electrical field forces, stress gradient and thermal gradient, the vacancy flux is given by (Sarychev and Zhinikov 1999;Basaran et al 2003)

$$\mathbf{q} = -D_v C_{v0}(\nabla c + \frac{Z^* ec}{kT}(-\rho \mathbf{j}) + \frac{cf\Omega}{kT}\nabla \sigma_{spherical} + \frac{c}{kT^2}Q^* \nabla T) \qquad [2\text{-}3]$$

where D_v is vacancy diffusivity

C_{v0} is vacancy concentration at stress free state

c is normalized vacancy concentration

Z^* is vacancy effective charge number

e is electron charge

ρ is metal resistivity

j is current density (vector)

f is vacancy relaxation ratio, ratio of atomic volume to the volume of a vacancy

Ω is atomic volume

k is Boltzman's constant

T is absolute temperature

$\sigma_{spherical}$ is spherical part of stress tensor, $\sigma_{spherical} = trace(\sigma_{ij})/3$

Q^* is heat of transport, the isothermal heat transmitted by moving the atom in the process of jumping a lattice site less the intrinsic enthalpy.

The stress-vacancy relationship is represented by vacancy generation/annihilation rate which is given by(Sarychev and Zhinikov 1999)

$$G = -C_{v0}\frac{c - C_{ve}}{\tau_s} \qquad [2\text{-}4]$$

where $C_{ve} = e^{\frac{(1-f)\Omega\sigma_{spherical}}{kT}}$ is normalized thermodynamic equilibrium vacancy concentration.

τ_s is characteristic vacancy generation/annihilation time.

Stress is governed by

$$\sigma = \square\ \varepsilon \qquad [2\text{-}5]$$

where $\square$ is the tangential stiffness matrix.

2.2.3 Discretization for FEM Implementation

With equation [2-1] using weighted residuals method, we can write the following relationship,

$$\int_v \delta c\left[\mathbf{C}_{v0}\left(\frac{\partial c}{\partial t} + \nabla \bullet \mathbf{q} - G\right)\right] dV = 0 \qquad [2\text{-}6]$$

Using integration by parts and divergence theorem, we obtain

$$\int_v \delta c \cdot \nabla \bullet \mathbf{q} dV = -\int_v \frac{\partial \delta c}{\delta \mathbf{x}} \bullet \mathbf{q} dV + \int_S \delta c \cdot \mathbf{q} \bullet \mathbf{n} dS \qquad [2\text{-}7]$$

Substitute [2-7] into [2-6] and using normalized flux and vacancy generation rate to eliminate $\mathbf{C_{v0}}$

$$\int_v \delta c \cdot \frac{\partial c}{\partial t} dV - \int_v \frac{\partial \delta c}{\delta \mathbf{x}} \bullet \mathbf{q} dV = -\int_S \delta c \cdot \mathbf{q} \bullet \mathbf{n} dS + \int_v \delta c G dV \qquad [2\text{-}8]$$

If we assume blocking boundary condition for vacancy flux, $\mathbf{q} \bullet \mathbf{n} = 0$ then substituting constitutive equation[2-3] and [2-4] into[2-8], we obtain

$$\int_v \delta c \frac{\partial c}{\partial t} dV + \int_v \frac{\partial \delta c}{\delta \mathbf{x}} \bullet D \bullet \left(\nabla c + \frac{Z^* e}{kT}(-\rho \mathbf{j}) c + \frac{cf\Omega}{kT} \nabla \sigma_{spherical} + \frac{c}{kT^2} Q^* \nabla T \right) dV$$
$$- \int_v \delta c \cdot \frac{e^{\frac{(1-f)\Omega \sigma_{spherical}}{kT}} - c}{\tau_s} dV = 0$$

[2-9]

The Galerkin approach assumes that, the variational field, is interpolated by the same functions as weight functions used for method of weighted residuals.

$$\delta c = N^T \delta c \qquad [2\text{-}10]$$

$$\left[\int_v \frac{\partial N^T}{\delta \mathbf{x}} \bullet D \bullet \left(\nabla c + \frac{Z^* ec}{kT}(-\rho \mathbf{j}) + \frac{cf\Omega}{kT} \nabla \sigma_{spherical} + \frac{c}{kT^2} Q^* \nabla T \right) dV \right.$$
$$\left. - \int_v N^T \cdot \frac{e^{\frac{(1-f)\Omega \sigma_{spherical}}{kT}} - c}{\tau_s} dV + \int_v N^T \frac{\partial c}{\partial t} dV \right] \delta c = 0$$

[2-11]

Discretization of force equilibrium equation [2-2] can be found at any finite

element text book so it is omitted here.

It should emphasized that temperature gradient term in equation [2-11] can be obtained from a separate thermal analysis. Because thermal steady state is established much faster than vacancy diffusion process, steady state temperature gradient from thermal analysis can be used for this purpose.

2.2.4 Integration Algorithm

The complexity of this problem comes from coupling terms between diffusion governing partial differential equation and force equilibrium governing partial differential equation. In order to determine Jacobian contributions (stiffness matrix contribution) material constitutive equation is needed. Because of the nonlinear behavior of the material (viscoplasticity), a local integration scheme is also needed, here return mapping algorithm (Simo and Hughes 2001) is used. In the following derivation current step means at step n+1, the state variables at previous step n are known.

The stress-strain constitutive equation is established as,

$$\sigma = \square\ (\varepsilon_{total} - \varepsilon_{visoplastic} - \varepsilon_{electromigration} - \varepsilon_{thermal}) \qquad [2\text{-}12]$$

where $\square = \kappa \mathbf{1} \otimes \mathbf{1} + 2\mu(\mathbf{I} - \frac{1}{3}\mathbf{1} \otimes \mathbf{1})$ and κ is bulk modulus, μ is shear modulus; and

$$\mathbf{I}=\begin{bmatrix}1&0&0&0&0&0\\0&1&0&0&0&0\\0&0&1&0&0&0\\0&0&0&0&0&0\\0&0&0&0&0&0\\0&0&0&0&0&0\end{bmatrix},\quad \mathbf{1}=\begin{bmatrix}1\\1\\1\\0\\0\\0\end{bmatrix}$$

$$\varepsilon_{electromigration}=\tfrac{1}{3}\mathbf{1}\cdot\varepsilon^{trace}_{electromigration}$$

Thermal strain is not included as a field variable in current formulation but it can be added into the model from the results of an independent thermal-displacement analysis. Compared to mass diffusion, thermal transport process is a rapid process, so there is no need to solve thermal degree of freedom concurrently with diffusion process, thus a sequential analysis is enough for solving the problem.

Itemized strain components,

$$\varepsilon_{total}=\tfrac{1}{3}\varepsilon^{trace}_{total}\cdot\mathbf{1}+\varepsilon^{dev}_{total} \qquad [2\text{-}13]$$

$$\varepsilon_{viscoplastic}=\tfrac{1}{3}\varepsilon^{trace}_{viscoplastic}\cdot\mathbf{1}+\varepsilon^{dev}_{viscoplastic}=\varepsilon^{dev}_{viscoplastic} \qquad [2\text{-}14]$$

$$\varepsilon_{electromigration}=\tfrac{1}{3}\varepsilon^{trace}_{electromigration}\cdot\mathbf{1}+\varepsilon^{dev}_{electromigration}=\tfrac{1}{3}\varepsilon^{trace}_{electromigration}\cdot\mathbf{1} \qquad [2\text{-}15]$$

where in Equation [2-15], $\varepsilon^{dev}_{electromigration}$ is zero since in mass diffusion only volumetric deformation is considered.

Substitute equation[2-13],[2-14] and [2-15] into equation[2-12], we obtain

$$\sigma=\kappa\cdot(\varepsilon^{trace}_{total}-\varepsilon^{trace}_{electromigration})\mathbf{1}+2\mu(\varepsilon^{dev}_{total}-\varepsilon_{viscoplastic}) \qquad [2\text{-}16]$$

where $\varepsilon^{trace}_{electromigration}$ is described by following equation (Sarychev and Zhinikov

1999)

$$\frac{\partial \varepsilon_{electromigration}^{trace}}{\partial t} = \Omega C_{v0}(f \nabla \mathbf{q} + f^{'} G)$$

[2-17]

$$f^{'} = 1 - f$$

According to equation[2-17], it is assumed that when an atom is replaced by a vacancy there is a local spherical strain introduced at that lattice site due to difference between the volume of an atom and volume of a vacancy. Electromigration introduced strain happens due to

1) vacancy flux divergence

2) vacancy generation

Using equation[2-1], we can transform equation [2-17] into

$$\frac{\partial \varepsilon_{electromigration}^{trace}}{\partial t} = \Omega C_{v0}(G - f\frac{\partial c}{\partial t}) = \Omega C_{v0}(\frac{e^{\frac{(1-f)\Omega\sigma_{spherical}}{kT}} - c}{\tau_s} - f\frac{\partial c}{\partial t})$$ [2-18]

Equations [2-16] and [2-18] plus plasticity theory all combined together yield the constitutive material behavior.

Now we perform a local integration scheme to determine the stiffness matrix $\frac{\partial \sigma_{n+1}}{\partial \varepsilon_{n+1}}$ and update the plastic strain and other related state variables.

First, we establish a trial state which we assume elastic behavior at current step n+1 is given by

$$s_{n+1}^{trial} = 2\mu \cdot (\mathbf{I} - \tfrac{1}{3}\mathbf{1} \otimes \mathbf{1})(\varepsilon_{n+1}^{dev} - \varepsilon_n^{vp})$$ [2-19]

where s is the deviatoric stress. And viscoplastic flow is described by flow rule as

$$\dot{\varepsilon}^{vp} = \gamma \mathbf{n} \qquad [2\text{-}20]$$

with $\mathbf{n} = \dfrac{\partial F}{\partial \sigma}$ which is normal to the yield surface

where γ is the consistency parameter.

Consider kinematic hardening, we define relative effective stress as

$$\xi_{n+1}^{trial} = \mathbf{s}_{n+1}^{trial} - \mathbf{X}_n \qquad [2\text{-}21]$$

where $\mathbf{X}_n$ is back stress tensor and $\mathbf{X}_n$ is described as

$$\frac{\partial \mathbf{X}}{\partial t} = \gamma \tfrac{2}{3} H'(\alpha) \frac{\xi}{\|\xi\|} \qquad [2\text{-}22]$$

$$\dot{\alpha} = \sqrt{\frac{2}{3}}\gamma \qquad [2\text{-}23]$$

where $H'(\alpha)$ is kinematic hardening modulus

α is equivalent plastic strain given by $\int \sqrt{\tfrac{2}{3}\dot{\varepsilon}_{ij}^{p}\dot{\varepsilon}_{ij}^{p}}\,dt$

Yield function is defined by,

$$f_{n+1} = \left\|\xi_{n+1}\right\| - \sqrt{\tfrac{2}{3}}K(\alpha_n) \qquad [2\text{-}24]$$

The trial yield function is defined as

$$f_{n+1}^{trial} = \left\|\xi_{n+1}^{trial}\right\| - \sqrt{\tfrac{2}{3}}K(\alpha_n) \qquad [2\text{-}25]$$

$K(\alpha)$ represents the isotropic hardening component defining the radius of the yield surface in stress space. It is a function of the hardening parameter α with an evolution given by equation[2-23].

For a rate independent material model γ obeys the so-called loading/unloading and consistency condition

$$\gamma \geq 0 \text{ and } F(\sigma,\alpha) \leq 0 \qquad [2\text{-}26]$$

$$\gamma \dot{F}(\sigma,\alpha) = 0 \qquad [2\text{-}27]$$

For a rate dependent material model conditions [2-26] and [2-27] are replaced by a constitutive equation of the form (where η represents a viscosity material parameter).

$$\gamma = \frac{\langle \phi(F) \rangle}{\eta} \qquad [2\text{-}28]$$

Equation [2-28] can be transformed as:

$$F = \Theta\left(\frac{\Delta\gamma\eta}{\Delta t}\right) \qquad [2\text{-}29]$$

where $\Theta\left(\frac{\Delta\gamma\eta}{\Delta t}\right) = \phi^{-1}\left(\frac{\Delta\gamma\eta}{\Delta t}\right)$.

and $\Delta\gamma = \gamma_{n+1}\Delta t$, which is based on implicit backward difference scheme.

Tang et al(Tang and Basaran 2001) developed viscoplastic flow rule for solder alloys based on Kashyap and Murty(Kashyap and Murty 1981) model, where grain boundary sliding is the dominant mechanism, primary and steady state creep can be given by

$$\dot{\varepsilon}_{ij}^{vp} = \frac{AD_0Eb}{k\theta}\left(\frac{\langle F \rangle}{E}\right)^n \left(\frac{b}{d}\right)^p e^{-Q/R\theta} \frac{\partial F}{\partial \sigma_{ij}} \qquad [2\text{-}30]$$

where the material parameters are defined as follows,

A: a dimensionless material parameter to describe the strain rate sensitivity.

$D_0 e^{\left(\frac{Q}{R\theta}\right)}$ is a diffusion coefficient where

D_0 is a frequency factor

Q is the creep activation energy for plastic flow

R is the universal gas constant = 8.314 J/K.mol = 8.314 N.mm/K.mol

θ: absolute temperature in Kelvin

E: Young's modulus

b: characteristic length of crystal dislocation (magnitude of Burger's vector)

k: Boltzmann's constant

d: average phase size

p: grain size exponent

n: stress exponent for plastic deformation rate, where 1/n indicates strain rate sensitivity.

From [2-20], [2-28] and [2-30], we can identify,

$$\langle \phi(F) \rangle = \langle F \rangle^n \qquad [2\text{-}31]$$

$$\frac{1}{\eta} = \frac{AD_0 Eb}{k\theta}\left(\frac{1}{E}\right)^n \left(\frac{b}{d}\right)^p e^{-Q/R\theta} \qquad [2\text{-}32]$$

If $f_{n+1}^{trial} \leq 0$ then set $s_{n+1}^{trial} = s_{n+1}$; Otherwise there is plastic strain at current step, using flow rule equation [2-20], $\mathbf{S}_{n+1}$ and ξ_{n+1} can be obtained as follows:

$$\mathbf{S}_{n+1} = \mathbf{S}^{tr}_{n+1} - \Delta\gamma 2\mu \mathbf{n}_{n+1} \qquad [2\text{-}33]$$

$$\left\|\xi_{n+1}\right\| + \left\{\Delta\gamma 2\mu + \sqrt{\frac{2}{3}}\Delta H\right\} = \left\|\xi^{tr}_{n+1}\right\| \qquad [2\text{-}34]$$

where

$$\mathbf{n}_{n+1} = \frac{\xi^{tr}_{n+1}}{\left\|\xi^{tr}_{n+1}\right\|} \qquad [2\text{-}35]$$

Using [2-24] for the rate independent case or [2-29] for the rate dependent case we have the following nonlinear scalar equation for the consistency parameter which can be solved by a local Newton method(Simo and Hughes 2001), where $g(\Delta\gamma)$ is a scalar equation with the only unknown $\Delta\gamma$,

$$g(\Delta\gamma) = -\sqrt{\frac{2}{3}}K(\alpha) + \left\|\xi^{Tr}_{n+1}\right\| - \left[\Delta\gamma 2\mu + \sqrt{\frac{2}{3}}\Delta H_{n+1}\right] - \Theta\left(\frac{\Delta\gamma\eta}{\Delta t}\right) = 0 \qquad [2\text{-}36]$$

Once [2-36] is solved for $\Delta\gamma$ using the following updating scheme (Simo and Hughes 2001)

$$\alpha_{n+1} = \alpha_n + \sqrt{2/3}\Delta\gamma \qquad [2\text{-}37]$$

$$\varepsilon^{VP}_{n+1} = \varepsilon^{VP}_n + \Delta\gamma \mathbf{n}_{n+1} \qquad [2\text{-}38]$$

$$\mathbf{X}^D_{n+1} = \mathbf{X}^D_n + \frac{2}{3}H'(\alpha_{n+1})\Delta\gamma \mathbf{n}_{n+1} \qquad [2\text{-}39]$$

$$\xi^D_{n+1} = R(\alpha_{n+1})\mathbf{n}_{n+1} \qquad [2\text{-}40]$$

$$\mathbf{S}_{n+1} = \xi^D_{n+1} + \mathbf{X}^D_{n+1} \qquad [2\text{-}41]$$

$$\sigma_{n+1} = \mathbf{S}_{n+1} + \frac{1}{3} Tr(\sigma_{n+1})\mathbf{I} = \mathbf{S}_{n+1} + \sigma_{n+1}^{spherical}\ \mathbf{I} \qquad [2\text{-}42]$$

$\sigma_{n+1}^{spherical}$ is determined as follow equation

$$\sigma_{n+1}^{spherical} = \sigma_{n}^{spherical} + \kappa(Tr(\Delta\varepsilon_{n+1}^{total}) - Tr(\Delta\varepsilon_{n+1}^{electromigration})) \qquad [2\text{-}43]$$

According to rate equation of [2-17],

$$Tr(\Delta\varepsilon_{n+1}^{electromigration}) = \Omega C_{v0}\left(\Delta t \frac{e^{\frac{(1-f)\Omega\sigma_{n+1}^{spherical}}{kT}} - c_{n+1}}{\tau_s} - f\Delta c\right) \qquad [2\text{-}44]$$

Substitute [2-44] into [2-43] and after some manipulation we can get

$$\sigma_{n+1}^{spherical} - \sigma_{n}^{spherical} - \kappa\left[Tr(\Delta\varepsilon_{n+1}^{total}) - \Omega C_{v0}\left(\Delta t \frac{e^{\frac{(1-f)\Omega\sigma_{n+1}^{spherical}}{kT}} - c_{n+1}}{\tau_s} - f\Delta c\right)\right] = 0$$

[2-45]

Iterating above scalar equation we get updated spherical stress and substitute updated spherical stress into[2-42], we obtain updated stress at step n+1.

2.2.5 Jacobian contribution

Now we can determine consistent stiffness matrix through linearization of equation [2-16], with differentiating both side of the equation:

$$\mathrm{k}_{n+1} = \kappa \cdot (\mathbf{1} \otimes \mathbf{1} - \frac{\partial \varepsilon^{trace}_{electromigration} \cdot \mathbf{1}}{\partial \varepsilon_{n+1}}) + 2\mu \cdot \frac{\partial (\varepsilon^{dev}_{total,n+1} - \varepsilon^{vp}_{n+1})}{\partial \varepsilon_{n+1}} \qquad [2\text{-}46]$$

with some basic manipulation and noting that $\frac{\partial \varepsilon^{dev}_{total,n+1}}{\partial \varepsilon_{n+1}} = (\mathbf{I} - \frac{1}{3}\mathbf{1} \otimes \mathbf{1})$ and $\frac{\partial \varepsilon^{vp}_{n+1}}{\partial \varepsilon_{n+1}} = \frac{\partial \Delta \varepsilon^{vp}_{n+1}}{\partial \varepsilon_{n+1}}$, the second part of equation [2-46] can be described as (Simo and Hughes 2001)

$$\mathrm{k}'_{n+1} = 2\mu(\mathbf{I} - \tfrac{1}{3}\mathbf{1} \otimes \mathbf{1}) + 2\mu \cdot \frac{\partial \Delta \varepsilon^{p}_{n+1}}{\partial \varepsilon_{n+1}} = 2\mu(\mathbf{I} - \tfrac{1}{3}\mathbf{1} \otimes \mathbf{1}) + 2\mu \cdot \frac{\partial \Delta\gamma \mathbf{n}_{n+1}}{\partial \varepsilon_{n+1}} \quad [2\text{-}47]$$

With

$$\frac{\partial \Delta\gamma}{\partial \varepsilon_{n+1}} = \frac{\mathbf{n}_{n+1}}{\frac{1}{2\mu}\frac{\partial \Theta}{\partial \Delta\gamma} + \frac{K'(\alpha_{n+1}) + H'(\alpha_{n+1})}{3\mu}} \quad [2\text{-}48]$$

and

$$\frac{\partial \mathbf{n}_{n+1}}{\partial \varepsilon_{n+1}} = \frac{2\mu}{\left\| \xi^{D,Tr}_{n+1} \right\|} \left(\mathbf{I} - \frac{1}{3}\mathbf{1} \otimes \mathbf{1} - \mathbf{n}_{n+1} \otimes \mathbf{n}_{n+1} \right) \qquad [2\text{-}49]$$

The integration detail for equation [2-47] is given by Simo and Hughes(Simo and Hughes 2001)

Substitute [2-48] and [2-49] into [2-47],

$$\mathrm{k}'_{n+1} = 2\mu(\theta_{n+1}(\mathbf{I} - \frac{1}{3}\mathbf{1} \otimes \mathbf{1}) - \bar{\theta}_{n+1}\mathbf{n}_{n+1} \otimes \mathbf{n}_{n+1}) \qquad [2\text{-}50]$$

with

$$\theta_{n+1} = 1 - \frac{\Delta\gamma 2\mu}{\left\| \xi^{Tr}_{n+1} \right\|}$$

[2-51]

and

$$\bar{\theta}_{n+1} = \frac{\mathbf{n}_{n+1}}{\frac{1}{2\mu}\frac{\partial\Theta}{\partial\Delta\gamma} + \frac{K'(\alpha_{n+1}) + H'(\alpha_{n+1})}{3\mu}} - \frac{\Delta\gamma 2\mu}{\left\|\xi^{Tr}_{n+1}\right\|} \qquad [2\text{-}52]$$

Now we return to equation[2-46] to determine consistent stiffness matrix at step n+1, with equation[2-43] and [2-44], we can get nine equations with nine unknowns as follow

$$\mathrm{k}^{ij}_{m+1} = \kappa(1 - \Omega\Delta t\Xi\sum_{k=1}^{3}\mathrm{k}^{kj}_{m+1}) + \mathrm{k}'^{ij}_{m+1}$$

[2-53]

where $\Xi = \dfrac{C_{v0}\frac{(1-f)\Omega}{kT}e^{\frac{(1-f)\Omega\sigma^{spherical}_{n+1}}{kT}}}{3\tau_s}$

Solve above symmetric equation to obtain final form of the stiffness matrix

$$\mathrm{k}^{ij}_{m+1} = \kappa\left[1 - \Omega\Delta t\Xi\left(3\kappa - \kappa\Omega\Delta t\Xi\frac{9\kappa + \mathrm{k}'_{total}}{1 + 3\kappa\Omega\Delta t\Xi} + \sum_{k=1}^{3}\mathrm{k}'^{,kj}_{m+1}\right)\right] + \mathrm{k}'^{ij}_{m+1} \quad [2\text{-}54]$$

where $\mathrm{k}'_{total} = \sum_{i,j=1}^{3}\mathrm{k}'^{,ij}_{total}$ for i,j=1,3

for other terms of k^{ij}_{m+1} is defined by

$$\mathrm{k}^{ij}_{m+1} = \mathrm{k}'^{,ij}_{m+1} \qquad [2\text{-}55]$$

for i,j =4,6

Other terms of constitutive equations needed for final total Jacobian matrix can be derived from k_{m+1}. We will derive those as follows,

Based on equation[2-16] and [2-18] we can get

$$\frac{\partial \sigma}{\partial c_{n+1}} = \kappa C_{v0} \Omega \delta_{ij} (\Delta t \frac{\partial G}{\partial c_{n+1}} - \frac{f \partial \Delta c_{n+1}}{\partial c_{n+1}}) \qquad [2\text{-}56]$$

Substitute G and notice that $\frac{\partial \Delta c_{n+1}}{\partial c_{n+1}} = \frac{\partial (c_{n+1} - c_n)}{\partial c_{n+1}} = 1$, we can obtain three equations with three unknowns ($\delta_{ij} \frac{\partial \sigma_{n+1}^{ij}}{\partial c_{n+1}}\Big|_{i,j=1,3}$)

$$\frac{\partial \sigma_{n+1}^{ij}}{\partial c_{n+1}} = -\delta_{ij} \kappa \Omega C_{v0} (\frac{\Delta t}{\tau_s} - f) + \delta_{ij} \kappa \Omega C_{v0} \Delta t \frac{(1-f)\Omega}{3kT\tau_s} e^{\frac{(1-f)\Omega \sigma_{n+1}^{spherical}}{kT}} (\sum_{i,j}^{1,3} \delta_{ij} \sigma_{n+1}^{ij}) \qquad [2\text{-}57]$$

We solve above equations to obtain

$$\frac{\partial \sigma_{n+1}^{ij}}{\partial c_{n+1}} = \frac{\kappa \Omega C_{v0} (\frac{\Delta t}{\tau_s} - f)}{1 + 3\kappa \Omega C_{v0} \Delta t \frac{(1-f)\Omega}{3kT\tau_s} e^{\frac{(1-f)\Omega \sigma_{n+1}^{spherical}}{kT}}} \qquad [2\text{-}58]$$

By using equation [2-3], we can get

$$\frac{\partial \mathbf{q}_{n+1}}{\partial c_{n+1}} = -D\left(\frac{\partial}{\partial \mathbf{x}} + \frac{Z^* e}{kT}(-\rho \mathbf{j}) + \frac{f \Omega \nabla \sigma_{n+1}^{spherical}}{kT} + \frac{f \Omega c}{kT} \frac{\partial \nabla \sigma_{n+1}^{spherical}}{\partial c_{n+1}} + \frac{Q^* \nabla T}{kT^2} \right) \qquad [2\text{-}59]$$

Where all terms are known except for the term $\frac{\partial \nabla \sigma_{n+1}^{spherical}}{\partial c_{n+1}}$, which can be calculated using finite difference scheme at local material points. Then it can be reformed as

$$\frac{\partial \nabla \sigma_{n+1}^{spherical}}{\partial c_{n+1}} = \frac{\partial}{\partial \mathbf{x}} \left(\frac{\partial \sigma_{n+1}^{spherical}}{\partial c_{n+1}} \right) \qquad [2\text{-}60]$$

where $\frac{\partial \sigma_{n+1}^{spherical}}{\partial c_{n+1}}$ can be calculated from [2-58].

Also we can derive the following relation from equation [2-3]

$$\frac{\partial \mathbf{q}_{n+1}}{\partial \varepsilon_{n+1}} = -D\frac{cf\Omega}{kT}\frac{\partial}{\partial \mathbf{x}}\left(\frac{\partial \sigma_{n+1}^{spherical}}{\partial \varepsilon_{n+1}}\right) \qquad [2\text{-}61]$$

where $\left(\frac{\partial \sigma_{n+1}^{spherical}}{\partial \varepsilon_{n+1}}\right)$ can be determined through equation [2-54].

From equation [2-4], we can obtain

$$\frac{\partial G_{n+1}}{\partial c_{n+1}} = \frac{\left(e^{\frac{(1-f)\Omega\sigma_{n+1}^{trial}}{kT}}\frac{(1-f)\Omega}{kT}\frac{\partial \sigma_{n+1}^{spherical}}{\partial c_{n+1}} - 1\right)}{\tau_s} \qquad [2\text{-}62]$$

where $\frac{\partial \sigma_{n+1}^{spherical}}{\partial c_{n+1}}$ is given out through equation [2-58]

Also from equation [2-4], we can obtain

$$\frac{\partial G_{n+1}}{\partial \varepsilon_{n+1}} = e^{\frac{(1-f)\Omega\sigma_{n+1}^{trial}}{kT}}\frac{(1-f)\Omega}{kT}\frac{\partial \sigma_{n+1}^{spherical}}{\partial \varepsilon_{n+1}} \qquad [2\text{-}63]$$

With equations [2-54], [2-55], [2-58], [2-59], [2-60], [2-61], [2-62] and [2-63], we have got all the terms needed for calculating the final Jacobian terms at current step n+1.

First taking derivative with respect to c for equation [2-11], we obtain

$$\mathrm{k}_{cc}^{1} = \iiint_V N^T \frac{1}{\Delta t} N \, dV \qquad [2\text{-}64]$$

$$\mathrm{k}_{cc}^{2} = \iiint_V \frac{\partial N^T}{\partial \mathbf{x}} D \left(\begin{array}{l} \dfrac{\partial N}{\partial \mathbf{x}} - \dfrac{Z^* e}{kT}(\rho \mathbf{j}) N + \dfrac{f\Omega}{kT} \nabla \sigma_{n+1}^{spherical} N \\ + \dfrac{f\Omega c_{n+1}}{kT} \dfrac{\partial}{\partial \mathbf{x}} \left(\dfrac{\partial \sigma_{n+1}^{spherical}}{\partial c_{n+1}} \right) N + \dfrac{Q^* \nabla T}{kT^2} N \end{array} \right) dV$$

[2-65]

$$\mathrm{k}_{cc}^{3} = \iiint_v -N^T \left(\frac{\dfrac{(1-f)\Omega}{kT} e^{\frac{(1-f)\Omega\sigma_{n+1}^{spherical}}{kT}} \dfrac{\partial \sigma_{n+1}^{spherical}}{\partial c_{n+1}} - 1}{\tau_s} \right) N \, dV \qquad [2\text{-}66]$$

and we have

$$\mathrm{k}_{cc}^{n+1} = \mathrm{k}_{cc}^{1} + \mathrm{k}_{cc}^{2} + \mathrm{k}_{cc}^{3} \qquad [2\text{-}67]$$

Also we can take derivative with respect to u^M for equation [2-11], we obtain

$$\mathrm{k}_{cu}^{1} = \iiint_V D \frac{\partial N^T}{\partial \mathbf{x}} \frac{c_{n+1} f\Omega}{kT} \frac{\partial}{\partial \mathbf{x}} \left(\frac{\partial \sigma_{n+1}^{spherical}}{\partial \varepsilon_{n+1}} \right) \mathrm{B} dV \qquad [2\text{-}68]$$

where $\varepsilon_{n+1}^{M} = \mathrm{B} \otimes \mathbf{u}^{\mathbf{M}}$

$$\mathrm{k}_{cu}^{2} = \iiint_V -N^T \frac{(1-f)\Omega}{kT} \frac{e^{\frac{(1-f)\Omega\sigma_{n+1}^{spherical}}{kT}}}{\tau_s} \frac{\partial \sigma_{n+1}^{spherical}}{\partial \varepsilon_{n+1}} \mathrm{B} dV \qquad [2\text{-}69]$$

and

$$\mathrm{k}_{cu}^{n+1} = \mathrm{k}_{cu}^{1} + \mathrm{k}_{cu}^{2} \qquad [2\text{-}70]$$

At the same time, we can also take derivative with regard to the discretized displacement governing equation, we obtain:

$$\mathrm{k}_{uu}^{n+1} = \iiint_V \mathrm{B}^T \otimes \mathrm{k}_{n+1} \otimes \mathrm{B} dV \qquad [2\text{-}71]$$

$$\mathrm{k}_{uc}^{n+1} = \iiint_V \mathrm{B}^T \otimes \frac{\partial \sigma_{n+1}^{spherical}}{\partial \varepsilon} \otimes N dV \qquad [2\text{-}72]$$

Finally, we have our final Jacobian matrix as (where subscript *c* represents vacancy concentration and *u* represents displacement)

$$\mathrm{K}_{n+1} = \left[\begin{pmatrix} \mathrm{k}_{cc}^{n+1} & \mathrm{k}_{cu}^{n+1} \\ \mathrm{k}_{uc}^{n+1} & \mathrm{k}_{uu}^{n+1} \end{pmatrix} \right] \qquad [2\text{-}73]$$

2.3 Nonlinear kinematic damage coupled formulation

Above formulation is only for linear kinematic hardening formulation, the integration scheme is called radial return method. The radial return method presented is based on Simo and Hughes (1997), but Simo and Hughes formulation did not include nonlinear kinematic hardening. Armstrong-Frederic evolution of the back stress with radial return method is presented by Lubarda and Benson(Lubarda and Benson 2002). But Lubarda did not specify stiffness matrix updating procedure in his paper. Based on Lubarda's paper, the stiffness matrix updating scheme is presented here. Also damage will be coupled into the formulation for the convenience of implementation. Some equations that are similar to the previous sections are also presented for the convenience of the readers.

2.3.1 Rate Dependent Combined Isotropic/Kinematic Hardening Model.

Consider the following classical Von Mises plasticity model:

Hooke's law

$$\dot{\boldsymbol{\sigma}} = \mathbf{C} : (\dot{\boldsymbol{\varepsilon}} - \dot{\boldsymbol{\varepsilon}}^{p}) \qquad [2\text{-}74]$$

Yield function

$$F = \|\mathbf{S} - \mathbf{X}\| - \sqrt{\frac{2}{3}} K(\alpha) \qquad [2\text{-}75]$$

Flow rule

$$\dot{\boldsymbol{\varepsilon}}^{P} = \gamma \hat{\underline{\mathbf{n}}} \qquad [2\text{-}76]$$

with $\hat{\underline{\mathbf{n}}} = \dfrac{\partial F}{\partial \boldsymbol{\sigma}}$ (normal to the yield surface)

Hardening laws

Isotropic hardening $\dot{\alpha} = \sqrt{\dfrac{2}{3}}\gamma$ [2-77]

Kinematic hardening $\dot{\mathbf{X}} = c_1 \dot{\boldsymbol{\varepsilon}}_{\mathbf{ij}}^{\mathbf{p}} - c_2 \mathbf{X} \dot{\alpha}$ [2-78]

where c_1 is linear kinematic hardening constant

c_2 is nonlinear kinematic hardening constant.

$\mathbf{S} = \boldsymbol{\sigma} - \dfrac{1}{3} Tr(\boldsymbol{\sigma}) \mathbf{1}$

$\mathbf{X}$ is a back stress tensor defining the displacement of the center of the yield surface in the deviatoric stress space.

$K(\alpha)$ represents the isotropic hardening component defining the radius of the yield surface in stress space. It is a function of the hardening parameter α.

$$K(\alpha)=\sqrt{\frac{2}{3}}Y_0+R_\infty\left[1-e^{-c\alpha}\right] \qquad [2\text{-}79]$$

where Y_0 is initial yield stress at uniaxial tension,

R_∞ is isotropic hardening saturation value,

c is isotropic hardening rate.

γ Is a non-negative plasticity (consistency) parameter

$F(\sigma,\alpha)$ is a yield function separating the elastic from the inelastic domain. In the case of a rate dependent material on the other hand, the magnitude of the viscoplastic flow is proportional to the distance of the stress state to the surface defined by $F(\sigma,\alpha)=0$. Using this fact we have for a time step Δt and using (8) that the following relation can be established

$$F=\Theta\left(\frac{\Delta\gamma\eta}{\Delta t}\right) \qquad [2\text{-}80]$$

where $\Theta\left(\frac{\Delta\gamma\eta}{\Delta t}\right)=\phi^{-1}\left(\frac{\Delta\gamma\eta}{\Delta t}\right)$.

and $\Delta\gamma=\gamma_{n+1}\Delta t$, which is based on implicit backward difference scheme.

Tang et al(Tang and Basaran 2001) developed viscoplastic flow rule for solder alloys based on Kashyap and Murty(Kashyap and Murty 1981) model, where grain boundary sliding is the dominant mechanism, primary and steady state creep can be given by

$$\dot{\varepsilon}_{ij}^{vp} = \frac{AD_0Eb}{k\theta}\left(\frac{\langle F\rangle}{E}\right)^n\left(\frac{b}{d}\right)^p e^{-Q/R\theta}\frac{\partial F}{\partial \sigma_{ij}} \qquad [2\text{-}81]$$

we can identify,

$$\langle \phi(F)\rangle = \langle F\rangle^n \qquad [2\text{-}82]$$

$$\frac{1}{\eta} = \frac{AD_0Eb}{k\theta}\left(\frac{1}{E}\right)^n\left(\frac{b}{d}\right)^p e^{-Q/R\theta}$$

2.3.2 Damage coupled constitutive model

Making use of the strain equivalence principle we can write in the usual form

$$\dot{\boldsymbol{\sigma}} = (1-D)\mathbf{C} : (\dot{\boldsymbol{\varepsilon}} - \dot{\boldsymbol{\varepsilon}}^p) \qquad [2\text{-}83]$$

where D is a damage parameter,

$$F = \|\mathbf{S} - \mathbf{X}\| - (1-D)\sqrt{\frac{2}{3}}K(\alpha) \qquad [2\text{-}84]$$

$$\dot{\mathbf{X}} = (1-D)(c_1\dot{\boldsymbol{\varepsilon}}_{\mathbf{ij}}^{\mathbf{p}} - c_2\mathbf{X}\dot{\alpha}) \qquad [2\text{-}85]$$

2.3.3 Return mapping algorithm

Consider the following trial (elastic predictor) state.

$$\mathbf{S}_{\mathbf{n+1}}^{\mathbf{tr}} = \mathbf{S}_{\mathbf{n}} + (1-D)2\mu\Delta\mathbf{e}_{\mathbf{n+1}} \qquad [2\text{-}86]$$

where $\Delta\mathbf{e}_{\mathbf{n+1}}$ is deviatoric strain increment at current time

The increment of the back stress will be computed from [2-85]

$$d\mathbf{X}_{n+1} = (1-D)\left[c_1 d\boldsymbol{\varepsilon}^{p}_{n+1} - c_2^{'}\Delta\gamma\left[\theta\mathbf{X}_n + (1-\theta)\mathbf{X}_{n+1}\right]\right], 0 \le \theta \le 1 \qquad [2\text{-}87]$$

where $c_2^{'} = \sqrt{\frac{2}{3}}c_2$

The generalized midpoint rule where $\theta = 1/2$ is used for the recall term, the value $\theta = 0$ and $\theta = 1$ corresponding to the backward and forward Euler time integration schemes, respectively.

Equation [2-75] and [2-76] define flow rule in algorithmic formulation for plastic strain increment

$$d\boldsymbol{\varepsilon}^{p}_{n+1} = \Delta\gamma \frac{\mathbf{S}_{n+1} - \mathbf{X}_{n+1}}{\left\|\mathbf{S}_{n+1} - \mathbf{X}_{n+1}\right\|} \qquad [2\text{-}88]$$

Substitution of equation [2-88] and $X_{n+1} = X_n + dX_{n+1}$ into equation [2-87] gives

$$d\mathbf{X}_{n+1} = a_{n+1}\Delta\gamma\left(\frac{\mathbf{S}_{n+1} - \mathbf{X}_{n+1}}{\left\|\mathbf{S}_{n+1} - \mathbf{X}_{n+1}\right\|} - \frac{c_2^{'}}{c_1}\mathbf{X}_n\right) \qquad [2\text{-}89]$$

where $a_{n+1} = \dfrac{c_1(1-D)}{1 + c_2^{'}(1-D)(1-\theta)\Delta\gamma}$

then using the flow rule [2-88], equation [2-86] can be rewritten as

$$S_{n+1} = S^{tr}_{n+1} - \Delta\gamma(1-D)2\mu\frac{\mathbf{S}_{n+1} - \mathbf{X}_{n+1}}{\left\|\mathbf{S}_{n+1} - \mathbf{X}_{n+1}\right\|} \qquad [2\text{-}90]$$

and introducing the relative stress $\xi^{D}_{n+1} = S_{n+1} - X^{D}_{n+1}$ with equation [2-90] we have

$$\xi^{D}_{n+1} = \mathbf{S}_{n+1} - \mathbf{X}^{D}_{n+1} = \mathbf{S}^{tr}_{n+1} - \Delta\gamma(1-D)2\mu \frac{\mathbf{S}_{n+1} - \mathbf{X}_{n+1}}{\left\|\mathbf{S}_{n+1} - \mathbf{X}_{n+1}\right\|} - \mathbf{X}_{n} - d\mathbf{X}_{n+1} \qquad [2\text{-}91]$$

Substitution equation [2-89] into equation [2-91] gives

$$\mathbf{S}_{n+1} - \mathbf{X}_{n+1} + \Delta\gamma((1-D)2\mu + a_{n+1}) \frac{\mathbf{S}_{n+1} - \mathbf{X}_{n+1}}{\left\|\mathbf{S}_{n+1} - \mathbf{X}_{n+1}\right\|} = \mathbf{B}_{n} \qquad [2\text{-}92]$$

where $\mathbf{B}_{n} = \mathbf{S}^{tr}_{n+1} - \mathbf{X}_{n} + b_{n+1}\Delta\gamma\mathbf{X}_{n}$

and $b_{n+1} = \frac{c_2'}{c_1} a_{n+1}$

Also from equation [2-92], one can identify following relationship,

$$\mathbf{n}_{n+1} = \frac{\mathbf{S}_{n+1} - \mathbf{X}_{n+1}}{\left\|\mathbf{S}_{n+1} - \mathbf{X}_{n+1}\right\|} = \frac{\mathbf{B}_{n}}{\left\|\mathbf{B}_{n}\right\|} \qquad [2\text{-}93]$$

which is used for updating plastic strain using [2-88] once $\Delta\gamma$ is known.

We take a trace product of equation [2-92] with itself, which gives

$$\left\|\mathbf{S}_{n+1} - \mathbf{X}_{n+1}\right\| + \Delta\gamma((1-D)2\mu + a_{n+1}) =$$
$$\left[\left\|\mathbf{S}_{n} - \mathbf{X}_{n}\right\|^2 + \left\|(1-D)2\mu\Delta\mathbf{e}_{n+1} + b_{n+1}\Delta\gamma\mathbf{X}_{n}\right\|^2 + 2\left(\mathbf{S}_{n} - \mathbf{X}_{n}\right) : \left((1-D)2\mu\Delta\mathbf{e}_{n+1} + b_{n+1}\Delta\gamma\mathbf{X}_{n}\right)\right]^{1/2}$$

[2-94]

In view of equation [2-84] for rate independent case or using equation [2-80] for rate dependent case, equation [2-94] can be rewritten as

$$F(\Delta\gamma) = (1-D)\sqrt{\frac{2}{3}}K\left(\alpha_n + \sqrt{\frac{2}{3}}\Delta\gamma\right) + \Delta\gamma((1-D)2\mu + a_{n+1}) - \Theta\left(\frac{\Delta\gamma\eta}{\Delta t}\right)$$

$$-\left[\left\|\mathbf{S}_n - \mathbf{X}_n\right\|^2 + \left\|(1-D)2\mu\Delta\mathbf{e}_{n+1} + b_{n+1}\Delta\gamma\mathbf{X}_n\right\|^2 + 2\left(\mathbf{S}_n - \mathbf{X}_n\right):\left((1-D)2\mu\Delta\mathbf{e}_{n+1} + b_{n+1}\Delta\gamma\mathbf{X}_n\right)\right]^{1/2}$$

[2-95]

Newton's iterative method is employed to solve above equation [2-95] to obtain $\Delta\gamma$

Once [2-95] is solved for $\Delta\gamma$ the following updating scheme can be used

$$\alpha_{n+1} = \alpha_n + \sqrt{2/3}\Delta\gamma \qquad [2\text{-}96]$$

$$\boldsymbol{\varepsilon}^{\mathbf{P}}_{\mathbf{n+1}} = \boldsymbol{\varepsilon}^{\mathbf{P}}_{\mathbf{n}} + \Delta\gamma\frac{\mathbf{B_n}}{\|\mathbf{B_n}\|} \qquad [2\text{-}97]$$

$$\mathbf{X}_{\mathbf{n+1}} = \mathbf{X}_{\mathbf{n}} + a_{n+1}\Delta\gamma\left(\frac{\mathbf{S_{n+1}} - \mathbf{X_{n+1}}}{\|\mathbf{S_{n+1}} - \mathbf{X_{n+1}}\|} - \frac{c_2'}{c_1}\mathbf{X_n}\right) \qquad [2\text{-}98]$$

$$\xi^{\mathbf{D}}_{\mathbf{n+1}} = (1-D)K(\alpha_{n+1})\frac{\mathbf{B_n}}{\|\mathbf{B_n}\|} \qquad [2\text{-}99]$$

$$\mathbf{S_{n+1}} = \xi^{\mathbf{D}}_{\mathbf{n+1}} + \mathbf{X}^{\mathbf{D}}_{\mathbf{n+1}} \qquad [2\text{-}100]$$

$$\boldsymbol{\sigma}_{\mathbf{n+1}} = \kappa(1-D)\left(tr\left[\boldsymbol{\varepsilon}_{\mathbf{n+1}}\right]\right)\mathbf{1} + 2\mu\left(1-D\right)(\mathbf{e_{n+1}} - \boldsymbol{\varepsilon}^{\mathbf{p}}_{\mathbf{n}} - \gamma_{n+1}\frac{\mathbf{B_n}}{\|\mathbf{B_n}\|})$$

[2-101]

2.3.4 Linearization (Consistent Jacobian)

By differentiating equation [2-101] with respect to total strain for stress tensor, one obtains

$$d\boldsymbol{\sigma}_{n+1} = (1-D)\left[\mathbf{C} - 2\mu\mathbf{n}_{n+1} \otimes \frac{\partial \Delta\gamma}{\partial \boldsymbol{\varepsilon}_{n+1}} - 2\mu\Delta\gamma \otimes \frac{\partial \mathbf{n}_{n+1}}{\partial \boldsymbol{\varepsilon}_{n+1}}\right] : \mathbf{d}\boldsymbol{\varepsilon}_{n+1} \qquad [2\text{-}102]$$

were $\mathbf{C} = \kappa \mathbf{1} \otimes \mathbf{1} + 2\mu\left(\mathbf{I} - \frac{1}{3}\mathbf{1} \otimes \mathbf{1}\right)$ is the elastic tensor.

By differentiating equation [2-94] with respect to $\boldsymbol{\varepsilon}_{n+1}$, after some mathematical manipulation one can obtain

$$\frac{\partial \Delta\gamma}{\partial \boldsymbol{\varepsilon}_{n+1}} = \frac{2\mu(1-D)\mathbf{B}_n}{\mathrm{A}\Phi_2 - \mathbf{B}_n : \boldsymbol{\Phi}_1} \qquad [2\text{-}103]$$

where

$$\boldsymbol{\Phi}_1 = (b'_{n+1}\Delta\gamma + b_{n+1})\mathbf{X}_n$$

$$\Phi_2 = \frac{2}{3}(1-D)K'(\alpha_{n+1}) + 2\mu(1-D) + a_{n+1} + \Delta\gamma a'_{n+1}$$

$$\mathrm{A} = \left(\left\|\mathbf{S}_n - \mathbf{X}_n\right\|^2 + \left\|2\mu(1-D)\mathbf{de} + b_{n+1}\Delta\gamma\mathbf{X}_n\right\| + 2(\mathbf{S}_n - \mathbf{X}_n) : (2\mu(1-D)\mathbf{de} + b_{n+1}\Delta\gamma\mathbf{X}_n)\right)^{1/2}$$

Utilizing equation [2-93], one can obtain

$$\frac{\partial \mathbf{n}_{n+1}}{\partial \boldsymbol{\varepsilon}_{n+1}} = \frac{\partial \mathbf{n}_{n+1}}{\partial \mathbf{B}_n}\frac{\partial \mathbf{B}_n}{\partial \boldsymbol{\varepsilon}_{n+1}} = \frac{1}{\|\mathbf{B}_n\|}\left[\mathbf{I} - \mathbf{n}_{n+1} \otimes \mathbf{n}_{n+1}\right] : \frac{\partial \mathbf{B}_n}{\partial \boldsymbol{\varepsilon}_{n+1}} \qquad [2\text{-}104]$$

where $\frac{\partial \mathbf{B}_n}{\partial \boldsymbol{\varepsilon}_{n+1}} = 2\mu(1-D)\left(\mathbf{I} - \frac{1}{3}\mathbf{1}\otimes\mathbf{1}\right) + (b'_{n+1}\Delta\gamma + b_{n+1})\mathbf{X}_n \otimes \frac{\partial \Delta\gamma}{\partial \boldsymbol{\varepsilon}_{n+1}}$

Substitute equation [2-103] [2-104] into equation [2-102], one obtains Consistent Jacobian for the current step.

2.4 Viscoplastic Nonlinear Kinematic/Isotropic hardening Verification

The complexity of nonlinear kinematic and isotropic hardening viscoplastic models presented above need to be verified before implemented into the displacement-diffusion coupled problem. For that purpose, a user material is built for ABAQUS and implemented. The comparison will prove the robustness and accuracy of the algorithm.

2.4.1 Isoerror Map

The purpose of isoerror map is to test the accuracy of the integration algorithm, although this technique can not replace rigorous mathematical stability and accuracy analysis.

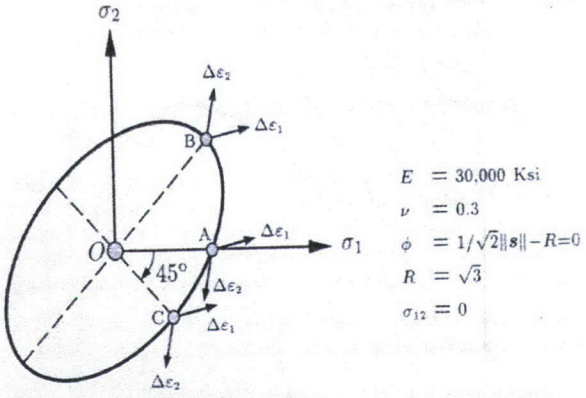

FIGURE 3-3. Plane-stress yield surface. Points for isoerror maps.

Figure 10 Points on Yield Surface(Simo and Hughes 2001)

Figure 10 shows three points on the yield surface. A strain increment at each point is applied. Then the stresses are computed by applying the integration algorithm. The error is represented by,

$$\delta = \frac{\sqrt{(\boldsymbol{\sigma} - \boldsymbol{\sigma}^*) : (\boldsymbol{\sigma} - \boldsymbol{\sigma}^*)}}{\sqrt{\boldsymbol{\sigma}^* : \boldsymbol{\sigma}^*}} \times 100 \qquad [2\text{-}105]$$

Here $\boldsymbol{\sigma}$ is the result obtained by applying the algorithm, whereas $\boldsymbol{\sigma}^*$ is the exact solution corresponding to the specified strain increments. The exact solution is obtained by repeatedly applying the algorithm with increasing number of sub increments until no significant change in solution. A special program is written to generate isoerror map using Fortran 90. The final results are shown in Figure 11 respectively for points A, B and C. Good accuracy (within five percent) is obtained for strain increments of the order of the characteristic yield strains. In

Figure 11 x, and y axis represent strain increment normalized by yield strain of material at x and y direction.

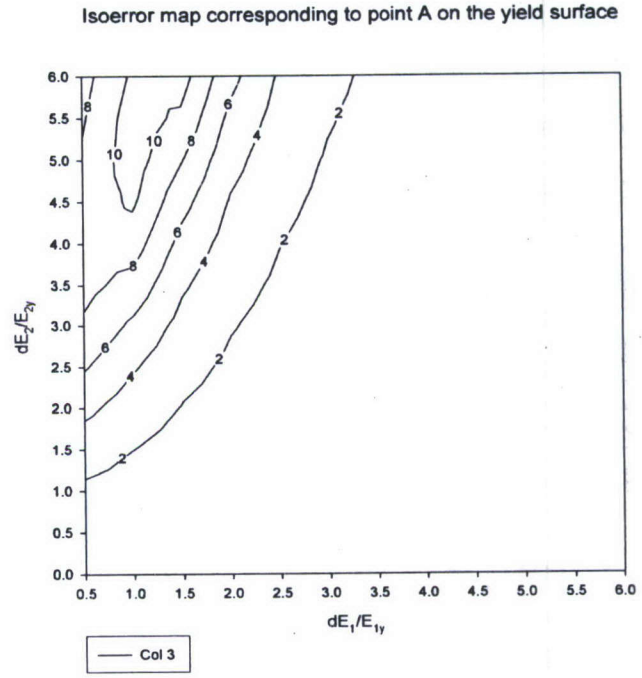

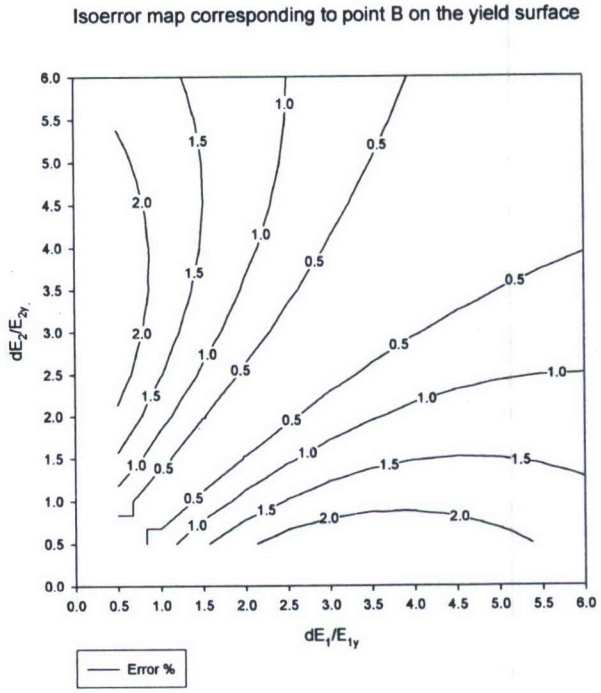

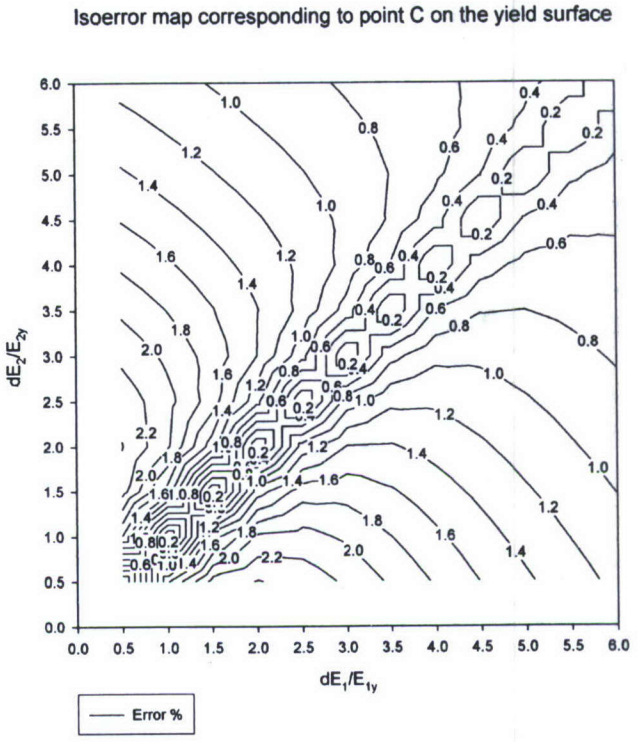

Figure 11 Isoerror Maps for Points A, B and C

2.4.2 Comparison with Abaqus

In order to further verify the constitutive model, a number of direct comparisons with Abaqus are performed. These comparisons are conducted with a single element by applying uniaxial and shear displacement boundary condition.

The following material properties are from Tang et al (2001). Temperature dependent shear modulus and Young's modulus are respectively,

$$G(T) = 19.44 - 0.0395\ T(K) \qquad [2\text{-}106]$$

$$E(T) = 52.10 - 0.1059\ T(K) \qquad [2\text{-}107]$$

The initial yield stress is measured for Pb37/Sn63 solder, and given by:

$$\sigma_Y(T) = 60.069 - 0.140T(K) \qquad [2\text{-}108]$$

The parameters for strain hardening are given in Table 2.

Table 2 Hardening Parameters

Parameter	Value
c_1 (MPa)	2040
c_2 (MPa)	180
c	383.3
R_∞ (MPa)	37.47 – 0.0748 T (K)

The analysis results for uniaxial and shear are shown in Figure 12 and Figure 13 respectively. The user material modeling gives out exactly same numbers as Abaqus. Since Abaqus does not have viscoplastic model like we defined, we did not take viscoplastic effect into consideration, and used rate independent material properties. 4 nodes element is used in analysis.

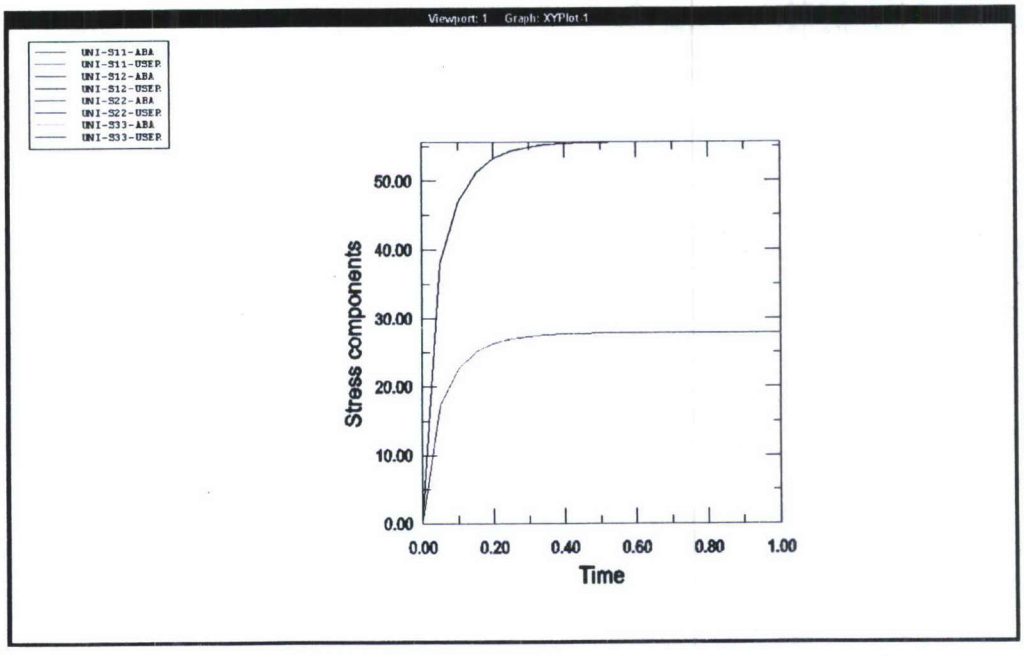

Figure 12 Uniaxial Tension Analysis Results Comparison for User Material Model and Abaqus

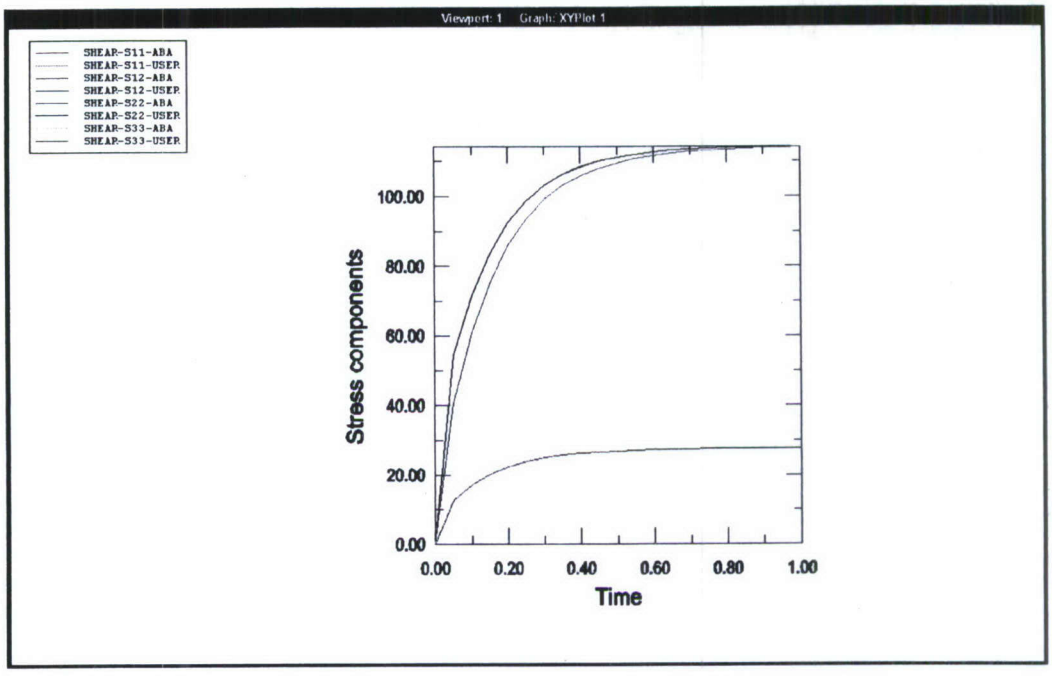

Figure 13 Shear Analysis Results Comparison for User Material Model and Abaqus

Since Abaqus uses Ziegler's model instead of Prager's model for nonlinear kinematic hardening, Abaqus yields different back stress value than our model if there is a spherical stress. This is verified by comparing shear and tension back stress evolution. Abaqus gives out the same back stress for shear but not for tension. In order to test this effect, a cyclic loading of uniaxial tension and compression is performed with Abaqus built-in model and user defined material model. The result is shown at Figure 14. The stresses evolutions for both cases are almost overlapped each other. Here only the stress in the applied tension and

compression direction is shown.

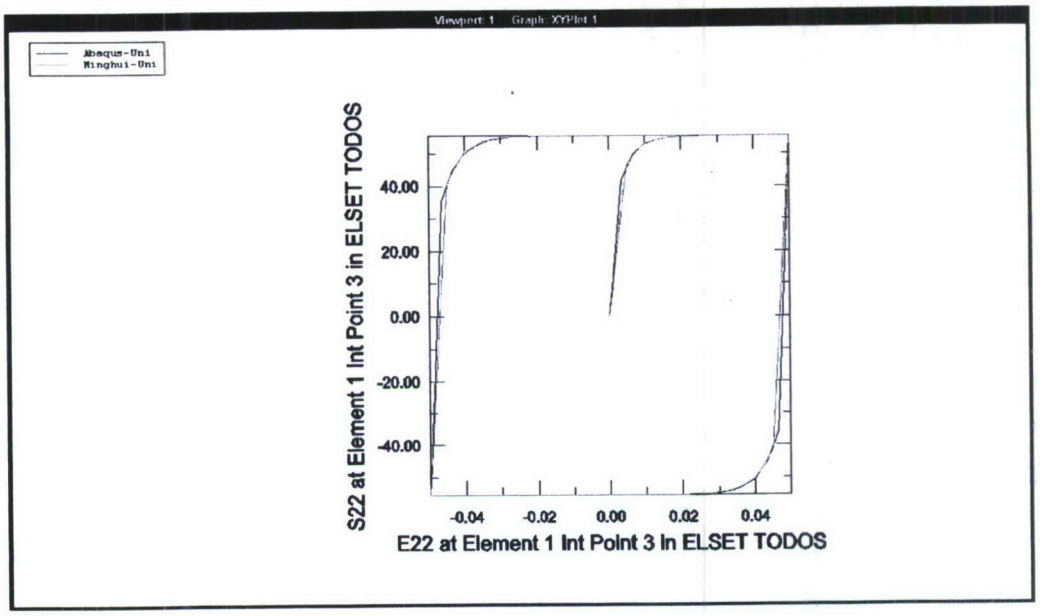

Figure 14 Cyclic Uniaxial Analysis Results From Abaqus Built-in model and User defined Material Model

2.4.3 Strain Rate Sensitivity

Since Abaqus does not have our viscoplastic flow model, direct comparison with Abaqus is not possible. In order to verify viscoplastic model, a strain rate sensitivity analysis is performed. The material parameters for viscoplastic flow function are listed in Table 3. Several loading with different strain rate are applied to a plate with a hole in the middle shown in Figure 15. The applied loadings are displacement at the free edge of plate. The other edge of plate is fixed according to symmetry properties of the problem. The analysis results are shown in Figure 16. In Figure 16 the reaction force of the fixed edge is shown under different strain rate. For very high strain rate, material exhibits hardening since material does not

have enough time for viscoplastic flow which causes stress relaxation.

Table 3 Viscoplastic Flow Parameters

Parameter	*Value*
$D_0(cm^2/s)$	0.488
$b(\mathring{A})$	3.18
$d(\mu m)$	10.6
N	1.67
P	3.34
Q(KJ/mole)	44.7
A	7.6×10^9

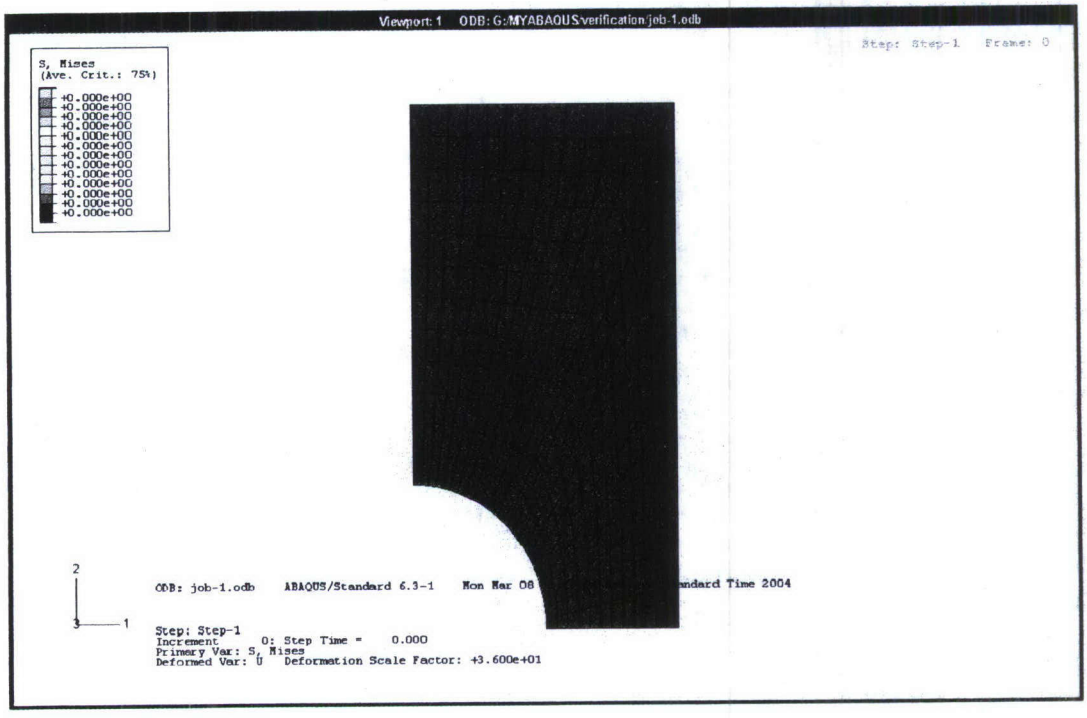

Figure 15 Plate with a Hole

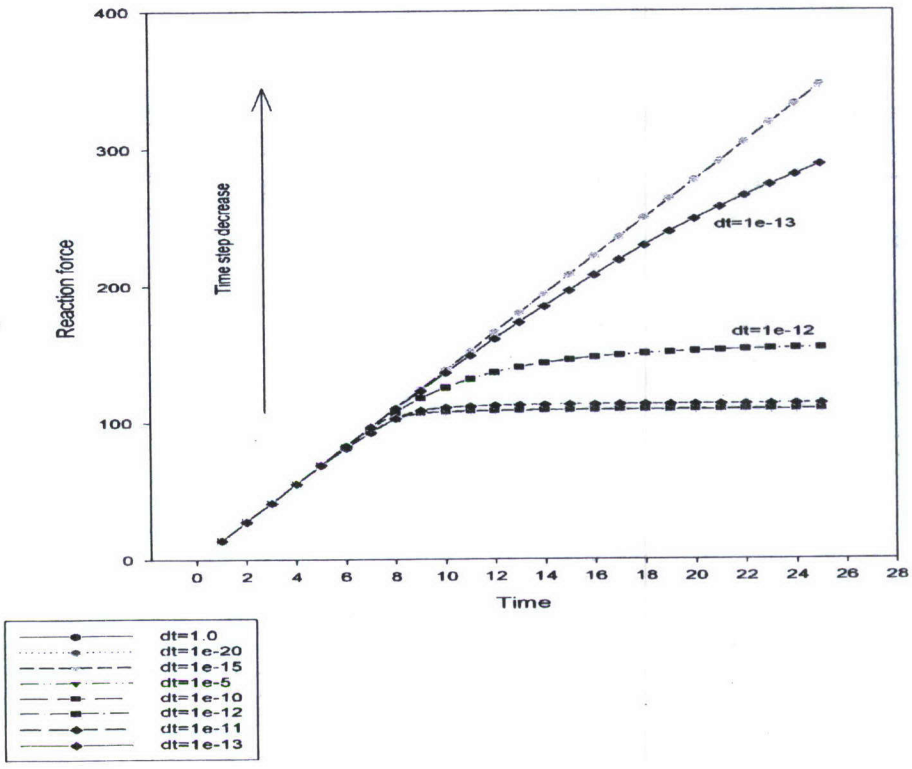

Figure 16 Strain Rate Sensitivity Analysis

2.4.4 Cyclic loading

After verification of the model, a number of cyclic loading analyses for different plastic strain ranges are performed to compare with experimental results. The tests are performed by Tang with a thin layer of solder sandwiched between two copper plates (Figure 17) (Tang and Basaran 2001). Shear displacement deformation is applied to the samples. The testing temperature is $22^{0}C$. The parameters for the analysis are listed in Table 2 and Table 3. For strain rate of $1.67\times10^{-3}/s$, analysis results are shown in Figure 18 and Figure 19 for plastic range of 0.022 and 0.004 respectively. The results for analyses deviate from

experimental results. The main reason is believed to be the difference of Young's modulus.

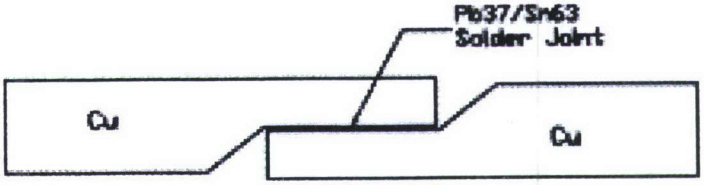

Figure 17 Specimen for fatigue shear testing for Pb37/Sn63 thin layer solder joints

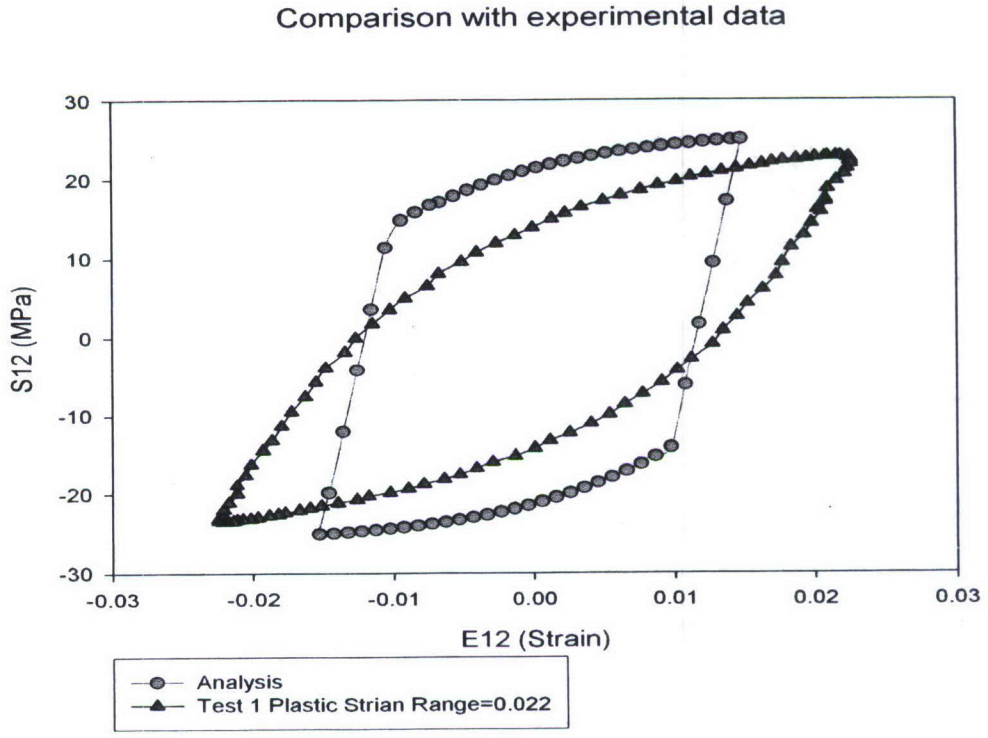

Figure 18 A Comparison of Analysis and Experiment Results for Plastic Range 0.022

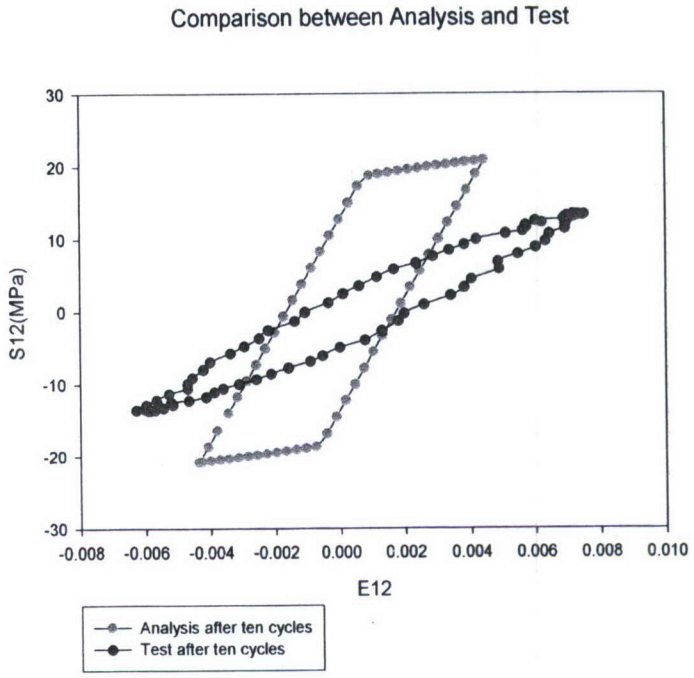

Figure 19 A Comparison of analysis and Experiment for Plastic Range 0.004

After the cyclic loading simulation, two analyses with damage are performed. The results are shown in Figure 20 for plastic range of 0.022 and 0.004. The damage evolution is within the expected range. For the detail of damage formulation please refer to the paper by (Tang and Basaran 2001;Basaran and Tang 2003;Basaran et al. 2003).

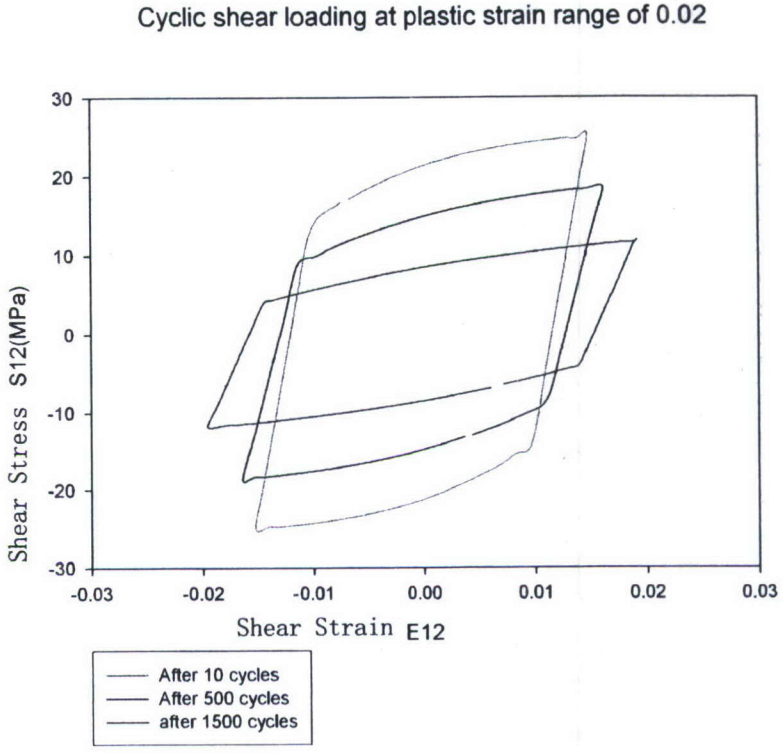

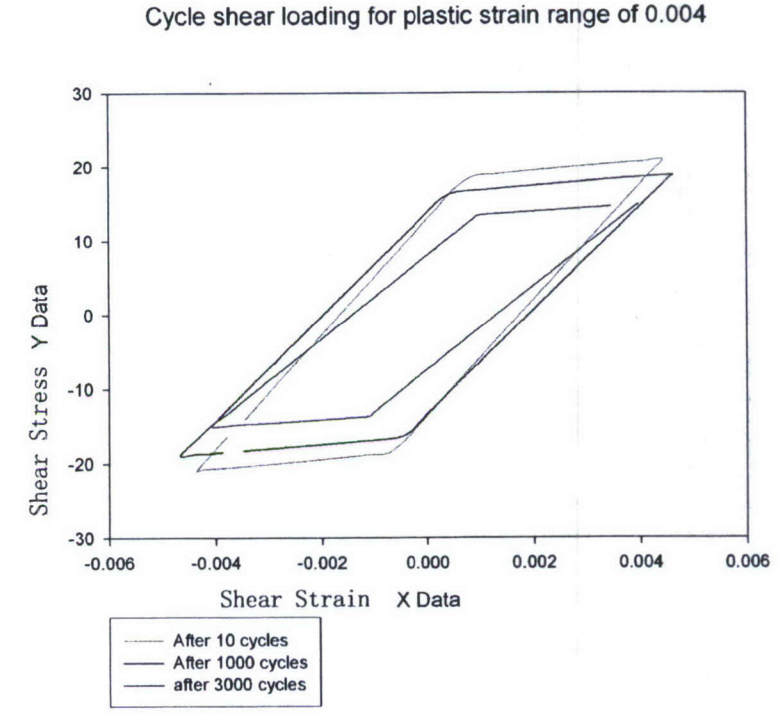

Figure 20 Cyclic Loading Simulation with Damage Coupled Viscoplastic Model for Different Plastic Strain Ranges

2.5. Conclusions

A general diffusion displacement finite element formulation is presented in this chapter. The material plasticity including nonlinear kinematic isotropic hardening rate dependent formulation is also formulated and successfully implemented and verified. Thus the formulation enables us to simulate stress and diffusion coupled system with various material properties including very complicated solder alloy material properties. Using the commercially available ABAQUS, user defined element and user defined material are programmed using FORTRAN 90. In the next several chapters, these programs will be used to simulate various electromigration processes for different material and boundary conditions.

Chapter 3 Finite Element Simulations

Equation Chapter 3 Section 1

In this chapter, the finite element formulation developed in the second chapter will be used for simulation in aluminum thin film, dual damascene copper interconnects and lead free solder connections. The main purpose of simulaiton is to investigate the model behavior under various boundary conditions and different material properties. Comparison with experimental results and other models presented in the literature are conducted. Damage is not formulated explicitly in the model, but some damage prediction will be conducted using various damage metrics presented in the literature. The numerical results prove the robustness of the program. Also it reveals some important factors during damage prediction. Basically, this chapter is for verification purpose and it will pave the road for the next chapter's damage formulation and implementation.

3.1 Simulation for Aluminum thin film

3.1.1 Mesh sensitivity

There are many experiments reported in the literature calculating stress based

on elastic strain measurement during electromigration. In order to eliminate thermal stress contribution, we choose Valek's(Valek and Bravman 2004c) experiment to verify our model because it reports the deviatoric stress which eliminates thermal stress influence. Valek uses scanning white beam x-ray microdiffraction, which allows for mapping the complete orientation and deviatoric strain tensor of micron-scale grains within a passivated thin film interconnect line.

The geometry of Valek's experiment is an aluminum thin film of 4.1 micron of width, 30 micron in length and 0.75 micron in thickness. It is passivated by 0.7 micron of SiO_2 on both sides. Current was ramped up to 30mA (j= $0.98\times10^6 A/cm^2$) over the course of 24 hours with increments of 10mA, then turn off for 12 hours. The material used for samples is sputtered Al (0.5wt%Cu). During the experiment the temperature is controlled at $205°C$. Because of the geometry of sample, plane strain element is used to simulate the process. Current direction is from left to right. Also diffusion along boundaries is considered to be blocking boundary condition. The displacement boundary conditions are assumed to be fixed at all boundaries, because both ends are connected through via for electrical connection and top and bottom boundaries are confined by passivated layers.

Before we proceed to compare our simulation results with Valek's experiment, a mesh sensitivity analysis is performed to show the robustness of our model. Two meshes are generated using ABAQUS CAE; A coarser mesh with 40

elements and a finer mesh with 180 elements; both elements are 8-node elements. The coordinates are set to be as x along length, y along thickness and z is along width. The meshes are shown on Figure 21. The geometric dimension of the model is identical to Valek's specimen.

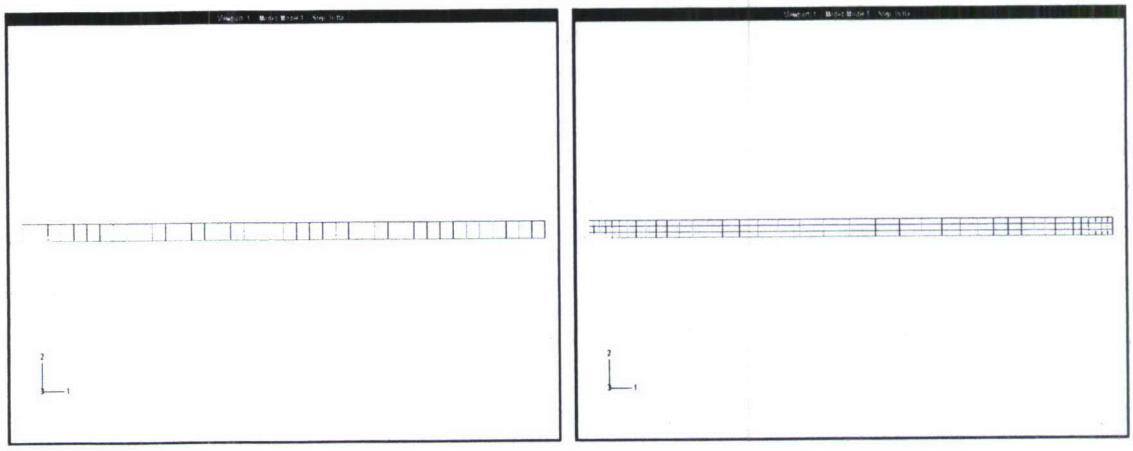

Figure 21 Mesh generated by Abaqus CAE

Material properties used in analysis are listed in Table 4. For this study we use perfect elastic-perfect plasticity material model for Aluminum. So there are no hardening effects.

Table 4 Other Material Properties

T, temperature(K)	*477*	*(Valek and Bravman 2004b)*
k, Boltzman's constant(J/K)	1.38×10^{-23}	(Ye et al 2003b)
E Young's modulus(GPa)	62	(Ma 2004)
v, Poission ratio	0.33	(Ma 2004)
Yield stress(MPa)	72	(Ma 2004)
Equilibrium Vacancy concentration at a stress free state at 473K($/cm^3$)	6.02×10^{15}	(Korhonen et al 1993)
Atomic volume($/cm^3$)	1.66×10^{-23}	(Ye et al. 2003b)
Vacancy relaxation time(s)	0.0018	(Sarychev and Zhinikov 1999)
f, average vacancy relaxation ratio	0.6	(Sarychev and Zhinikov 1999)
Effective charge number	4	(Tu 1992)
Resisitivity ohm.cm	2.07×10^{-7}	(Ye et al. 2003b)

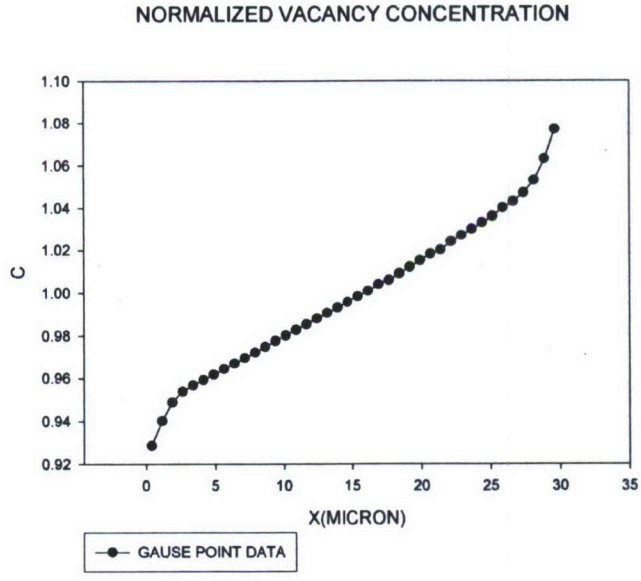

(a) Normalized Vacancy Concentration Distribution along the Thin Film

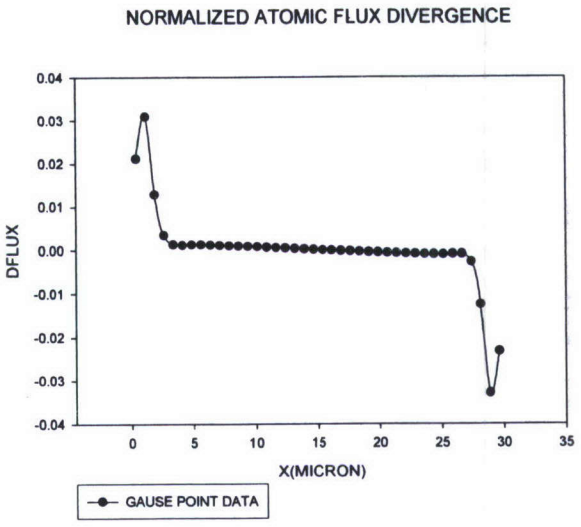

(b) Normalized Atomic Flux Divergence Distribution along the Thin Film

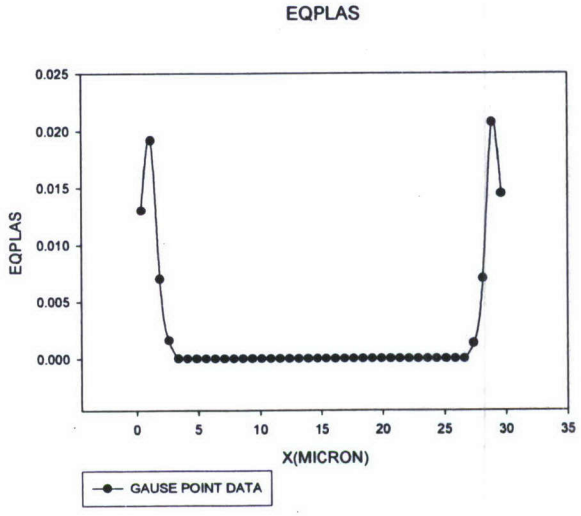

(c) Equivalent Plastic Strain Distribution along the Thin Film

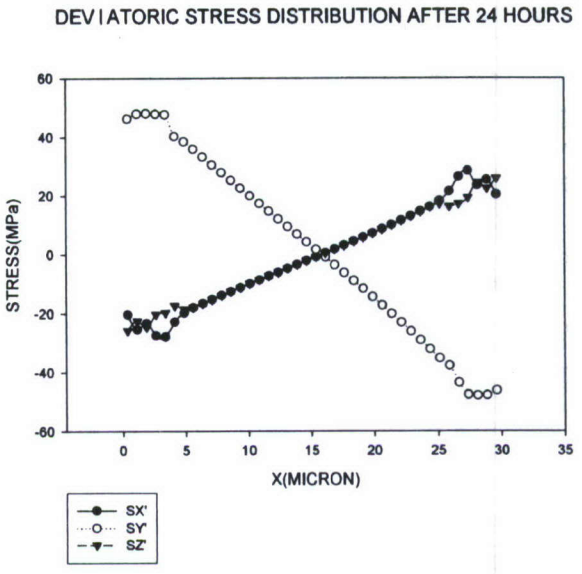

(d) Deviatoric Stress Components Distribution along the Thin Film

Figure 22 (a-d) Results for coarser mesh after 24h current stressing

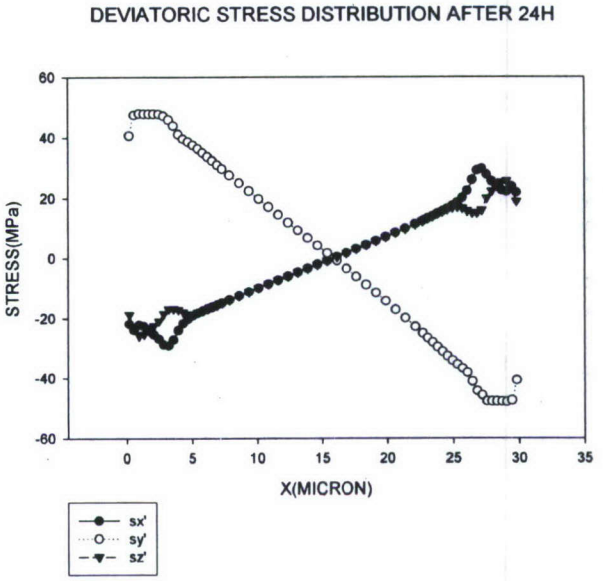

(a) Deviatoric Stress Distribution along Thin Film

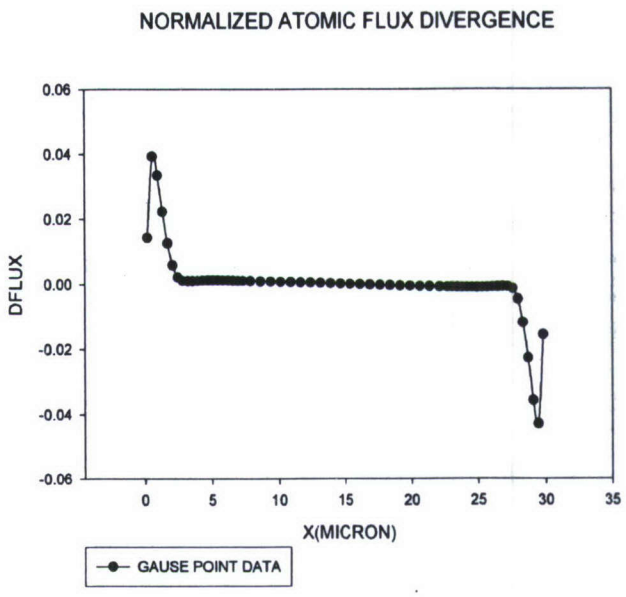

(b) Normalized Atomic Flux Divergence Distribution along Thin Film

Figure 23 Deviatoric stress and flux divergence for finer mesh after 24 hours

The computational results shown in Figure 22 are normalized vacancy concentration, normalized atomic flux divergence, equivalent plastic strain and deviatoric stress distribution. Peak near the end in all figures is due to blocking boundary condition where transported flux is zero. Atomic flux divergence is calculated based on vacancy flux divergence and $C_v / C_a = 1 \times 10^{-7}$, where C_v is vacancy concentration gradient and C_a is atomic concentration, unchanged throughout the process. Atomic flux divergence simply represents the percentage of mass transported out or in to the unit volume throughout the whole process. This variable is used to represent damage by many researches such as Sasagawa (Sasagawa et al 2001). Results shown in Figure 22 indicate that even if there is no current crowding effects, atomic divergence can still happen because

of the blocking boundary condition. Because of the discontinuity of vacancy flux at both ends, flux divergence and equivalent plastic strain distribution exhibit abrupt decrease near the boundary. Figure 22 (a-d) Results for coarser mesh after 24h current stressing also shows that vacancy flux is on the same direction as current direction which will cause tension at right hand side (cathode) and compression at left hand side (anode), which is in accordance with equation [2-3].The counter diffusion caused by stress gradient and vacancy concentration is at the opposite direction of current direction. Plastic deformation takes place at two ends which propagates towards middle of line until reaching steady state.

The results for finer mesh are shown at Figure 23. Compared with coarser mesh we can see finer mesh gives out same distribution as coarser mesh, maximum atomic flux divergence and deviatoric stresses for finer mesh result are very close to the values of coarser mesh. Therefore we conclude that there is no mesh sensitivity.

3.1.2 Comparison with Valek's Experimental Data

The experimental result reported by Valek is shown below. The stress shown in Figure 24 is deviatoric stress, where *X* is in the axial direction of the thin film line, *Y* is across the line, and *Z* is normal to the sample surface. So Valek's z direction is y direction in our numerical analysis.

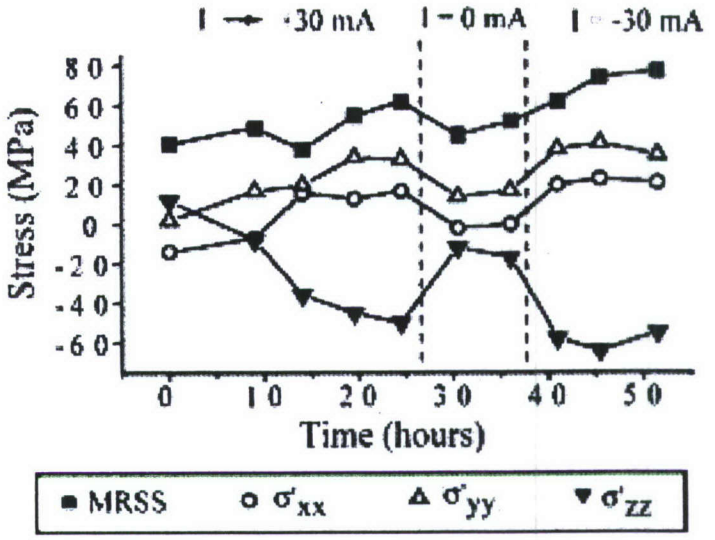

Figure 24 Deviatoric stress distribution(Valek and Bravman 2004a)

It should be pointed out that initial deviatoric stress must be considered during comparison. The experimental results show that maximum change in deviatoric stress along x direction is 30 MPa, along y direction is 35 MPa and along z direction is 60 MPa. Valek calculates stresses as average value for grains [we believe] in the near right [or left] ends since they are maximum stress locations. Inspecting Figure 23 we see that deviatoric stresses along x, y, z direction are 30, 50 and 25 MPa respectively from numerical simulation. There is a good match between computational simulation and experimental data for deviatoric stresses.

In order to prove the necessity of plasticity in electromigration modeling, another simulation is performed using exactly same material properties and loading except this time we set yield stress to a much higher value, 200GPa. Then we will have elastic mechanical response in the model. The simulation

results are shown at Figure 25. With elastic material properties, we predict a much higher stress near two ends which is almost three times bigger than experimental result.

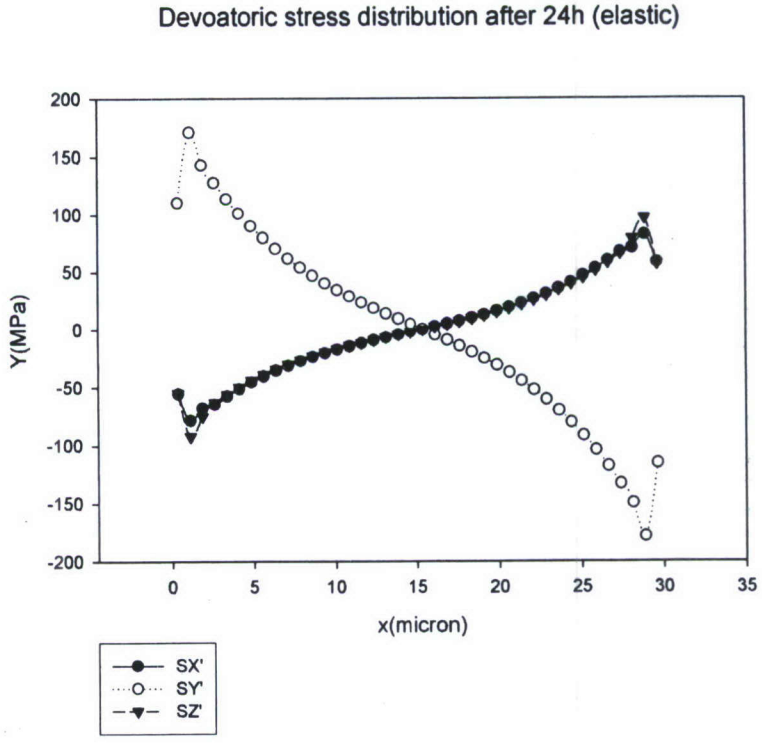

Figure 25 Elastic model result

After 24 hours of current stressing, we set current to be zero for another 12 hours. The simulation results shown at Figure 26 compare vacancy distribution for finer mesh after 24 hours and 36 hours, respectively. The flux is, as expected, to flow in the opposite direction after we turned off the current. Figure 27 depicts deviatoric stress distribution after 36 hours. The stress relaxation is observed as expected with the comparison of Figure 27 with Figure 22 (d) and Figure 23 (b). .

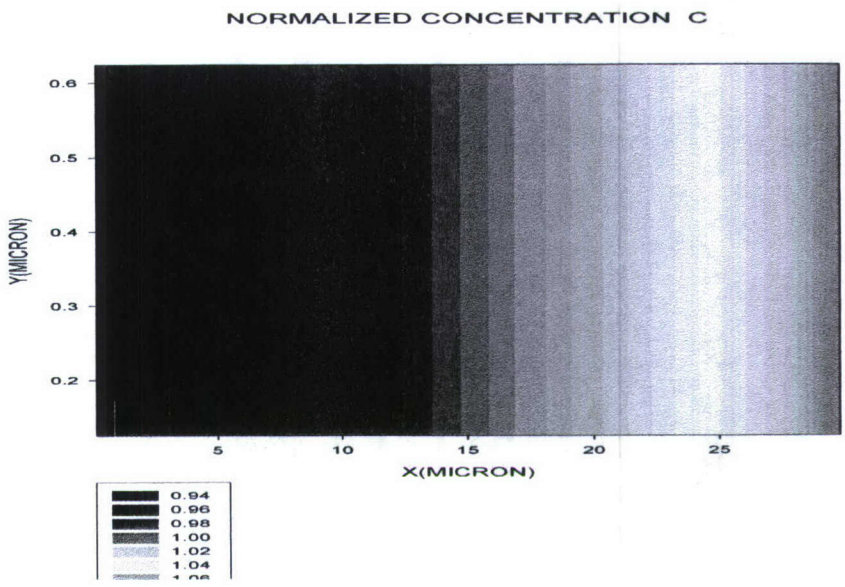

(a) After 24 Hours

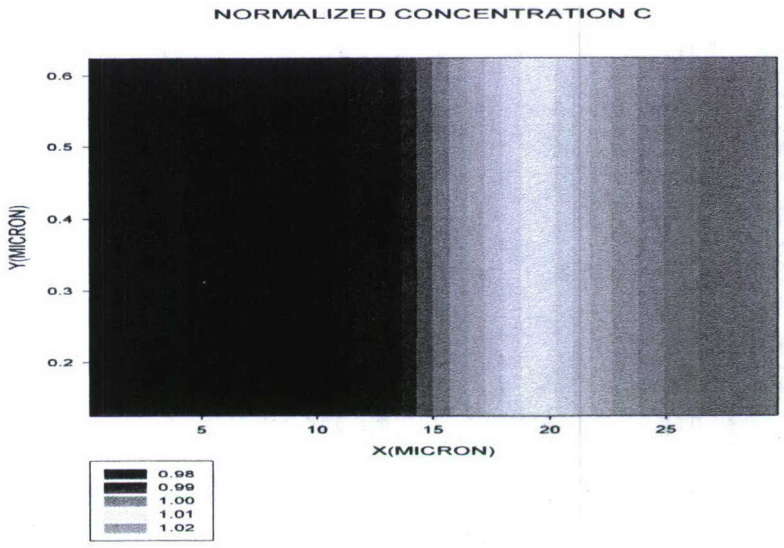

(b) After 36 Hours

Figure 26 Vacancy concentration distribution for 24h and 36h

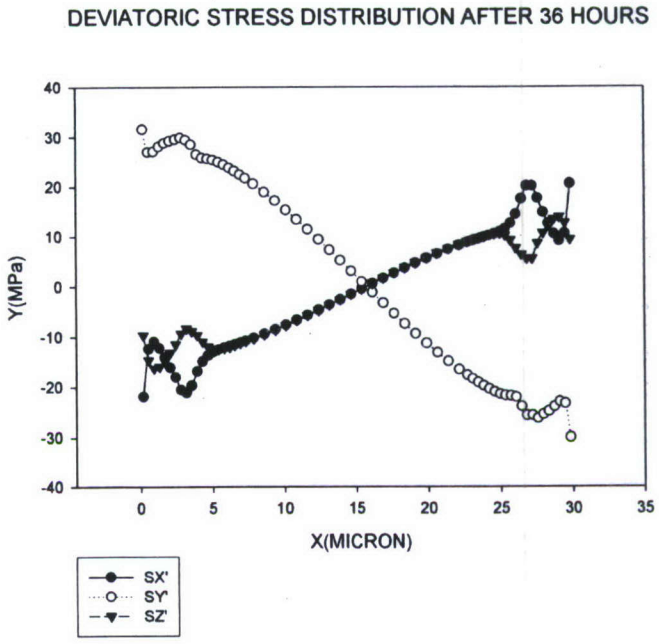

Figure 27 Deviatoric stress distribution at 36h (12 hours after unloading)

To better illustrate the evolution of deviatoric stress and atomic flux divergence, an evolution history is given out completely for 36 hours of analysis at Figure 28. Here the data is collected from largest atomic flux divergence and equivalent plastic strain position, which is the second element from the left end of the mesh.

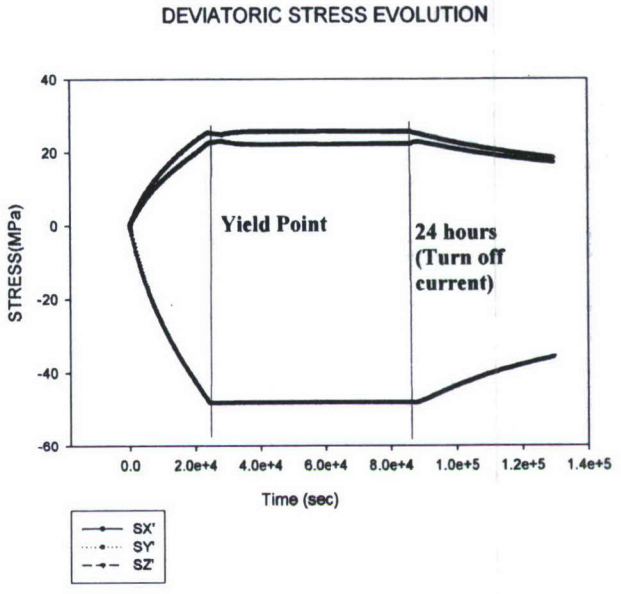
DEVIATORIC STRESS EVOLUTION
STRESS(MPa)
40
20
0
-20
-40
-60
Yield Point
24 hours
(Turn off
current)
0.0
2.0e+4
4.0e+4
6.0e+4
8.0e+4
1.0e+5
1.2e+5
1.4e+5
Time (sec)
SX'
SY'
SZ'

(a)

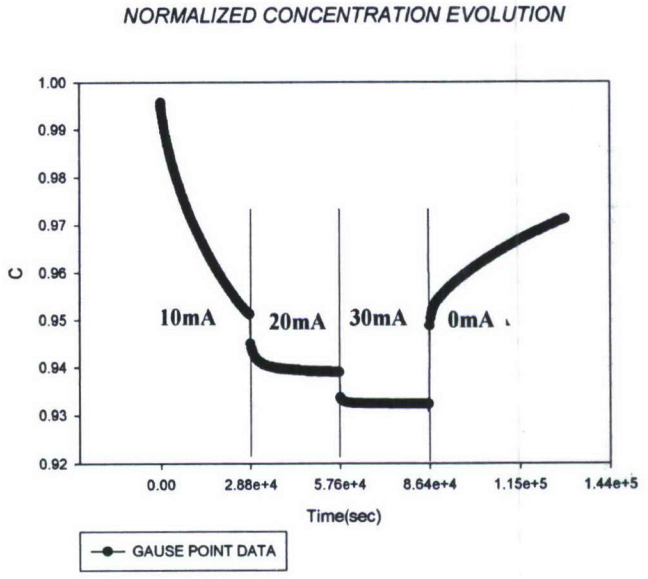
NORMALIZED CONCENTRATION EVOLUTION
C
1.00
0.99
0.98
0.97
0.96
0.95
0.94
0.93
0.92
10mA
20mA
30mA
0mA
0.00
2.88e+4
5.76e+4
8.64e+4
1.15e+5
1.44e+5
Time(sec)
GAUSE POINT DATA

(b)

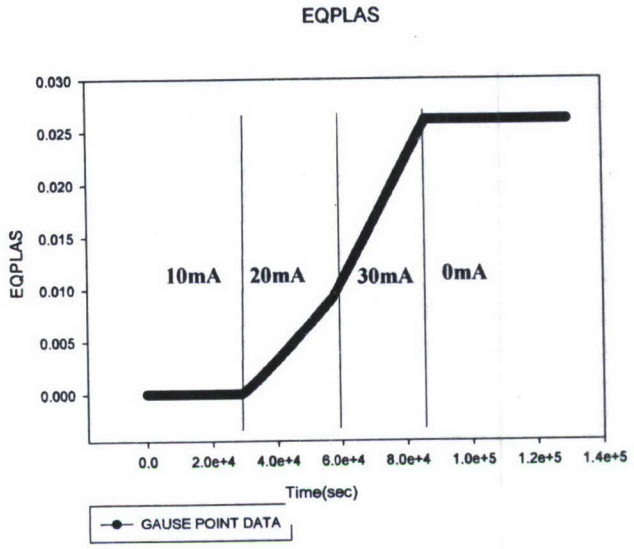

(c)

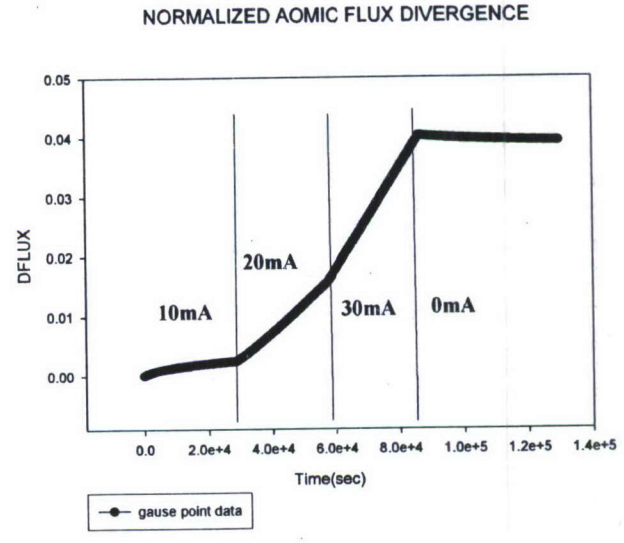

(d)

Figure 28 Stress, vacancy concentration,
equivalent plastic strain and flux divergence evolution history

Figure 28 clearly shows that plasticity has significant influence. From equivalent plastic strain and deviatoric stress history, we can see that after plastic deformation takes place, deviatoric stress will cease to grow which is in

accordance with our perfectly plastic material model. After turning off the current, three components of the deviatoric stresses decrease in accordance with Valek's experiment. The most important feature of time evolution history of Figure 28 is that both atomic flux divergence and equivalent plastic strain increase rate is much bigger after we increase the current. This is importance because atomic flux divergence and equivalent plastic strain are both very important features for material degradation. Both will contribute to nucleation and growth process of voids.

3.1.3 Comparison with Korhonen's Model

For thin films, for its simplicity, Korhonen's (1993) analytical model is widely used for one dimensional analysis. To prove effectiveness of our model, a simple analysis is performed to compare with Korhonen's model. Wang, et al (2000) performed an experiment on a 200 micron long and 0.5 micron aluminum thin film with a current density of $2.5\times10^4 A/cm^2$, also Wang derived an analytical solution using Korhonen' model. The results of Wang's experimental and analytical solution are shown in Figure 29; Simulation results using the proposed model for Wang's test are shown in Figure 30. The results shown in Figure 29 and Figure 30 are spherical stress distribution along the specimen length. In Figure 29 EM stress is spherical stress. It should be pointed out our tensile stress is positive

while in Korhonen's model, tensile stress is on negative sign. From Figure 30, we can see that the proposed model produce similar trend as Korhonen's model as well as experimental result. Also at this current density, material is still in elastic range. Because Wang did not give units of stress in his paper, numerical comparison is not possible at this time. We realize that amplitude of our simulation results for stresses are twice the data provided by Wang. Because Wang does not provide the units, a quantitative comparison is not possible. Yet qualitatively, simulation and experimental data are very similar. In the paper by Wang, he also mentioned that a stress localization behavior near 90 micron from cathode side, which he explained that may be caused by local microstructure irregularities. It is suggested by Wang that in order to simulate that locality effect, a local parameter which can represent initial defects should be included.

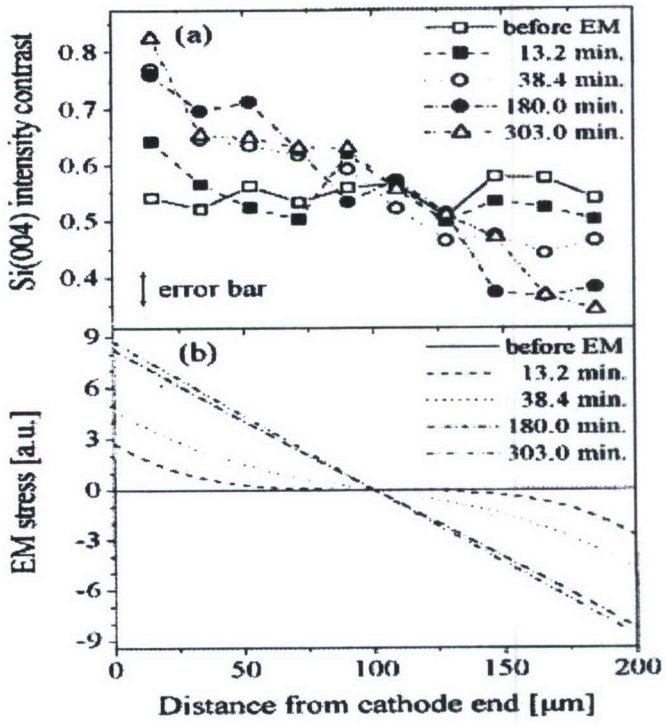

Figure 29 Wang's experimental and analytical result (P.-C.Wang 2000)

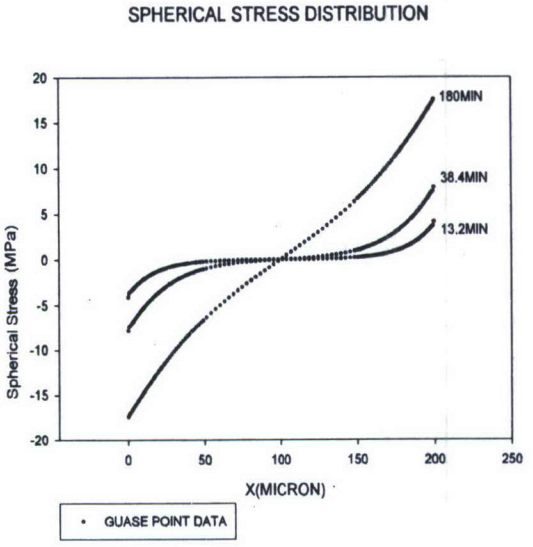

Figure 30 Proposed model simulation results

3.1.4 **Comparison with Black's equation**

Black's (Black 1969) equation, which is the most commonly used mean time to failure equation(MTTF), gives out MTTF proportional to inverse square of current density. To illustrate relation between the current density with material degradation, several analysis are performed with the same condition as Valek's experiment but with different current density values ranging from $1\times10^4 A/cm^2$ to $1\times10^6 A/cm^2$. The result is shown in Figure 31. In Figure 31, atomic divergence is divided into two separate graphs for different magnitudes of current density. With the smaller current density, there is no plastic deformation occurring. If we just take atomic flux divergence as a damage parameter which is analogous to void ratio, then we can define a critical flux divergence as a failure

criteria. Figure 31 shows the limitation of Black's equation. For lower current density it can never reach critical flux divergence no matter how long the current loading duration is. Also plasticity will have an effect on damage process when larger current density is applied which is not presented in Black's formulation. This finding is also supported by Ye (Hua Ye 2004), his dissertation show that Black's equation cannot be used to predict MTTF when temperature gradient, stress gradient or vacancy gradient are present.

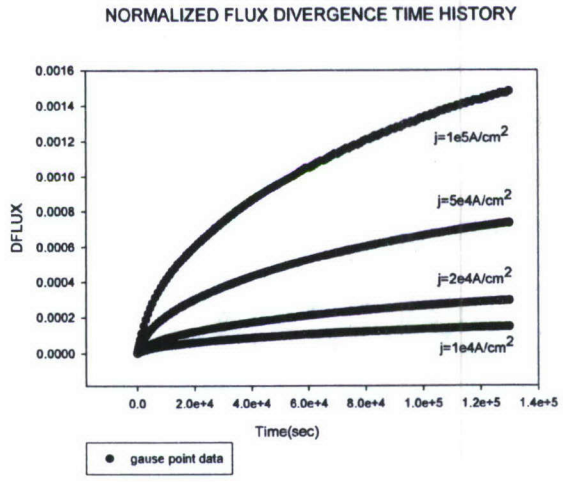

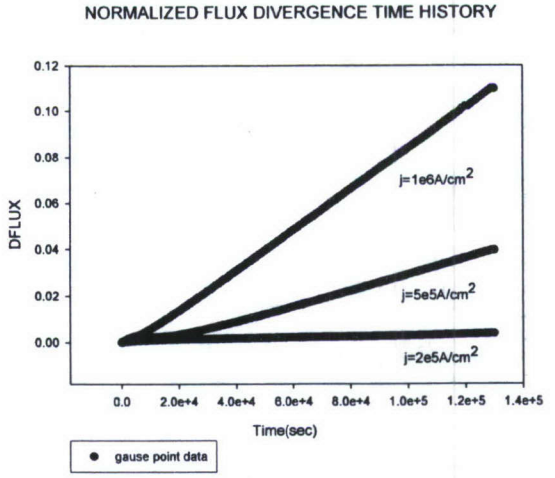

(a) Normalized Flux Divergence Time History with Different Current Densities

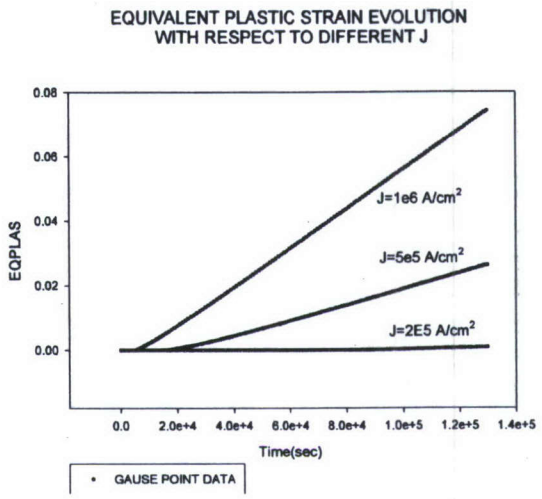

(b) Equivalent Plastic Strain Evolution with Different Current Densities

Figure 31 Atomic flux divergence and equivalent plastic strain with respect to different current density

3.1.5. Conclusions

A fully coupled diffusion-displacement analysis using inelastic mechanical material properties with regard to electromigration process is presented. The analysis yields good correlation between experimental and computational simulation results. The simulation results exhibit importance of inelastic mechanical behavior in electrical current loading which is neglected in the state of art research work, until very recently.

A very important finding is that it shows that Black's MTTF equation may only valid for the test data and current range used to come up with the empirical model. The advantage of the model proposed in this dissertation is that it uses implicit formulation which is not limited by time step. This will decrease real time

simulation computation time to a great extent. For a 2-D problem as it is shown above, it will take only a little of more than one hundred of increments to finish a simulation for 36 hours of real time and wall clock time consumed is on the order of minutes.

Third, the material integration scheme at each gause point adopted return mapping algorithm which is quadratic in convergence. That also speeded up the computation.

Finally, a fully coupled model is included to precisely illustrate interaction between diffusion field and displacement field.

Other features of this proposed model include:

(1). Accommodating variable current profiles,

(2). Dealing with different geometry including 3-D modeling

(3). Being able to incorporate various mechanical material properties, including most metals.

(4). Being able to handle different boundary conditions, including displacement boundary conditions and flux boundary conditions.

(5). The model enables us to simulate pre existing void inside a conductor material.

(6). The model allows consideration of pre existing stress field influence.

(7). The model utilizes widely used commercial software Abaqus with its strong modeling capability and powerful nonlinear solution solver.

3.2 Simulation for dual damascene copper thin film

Copper has been chosen to replace Al for IC interconnects to reduce the resistance-capacitance delay. Different integration process, geometry and material brings new challenges to the reliability of copper interconnects. Among those reliability issues electromigration under high current density is a major concern for IC industry. Based on a general computational damage mechanics model which is capable of simulating electromigration and stress coupled evolution, several dual damascene copper structure simulations have been performed to investigate the behavior of electromigration damage. Different diffusion boundary condition including blocking and non blocking boundary condition, current crowding effects, interface diffusion effects and material plasticity have been considered. Different damage criteria are used for quantifying material damage. Simulation results fit well with experimental findings and the model is proved as a useful tool for further quantifying the damage process.

Due to its better resistance capacitance delay properties, copper has been chosen to replace aluminum for IC interconnects. Electromigration research has increased during past several years on copper interconnects. Comparing with the research of aluminum electromigration, copper electromigration study is a rather immature and its damage process is not well understood as aluminum

electromigration. The different material properties, integration technique and geometry of copper with aluminum thin films bring new challenge to the investigation of copper electromigration damage.

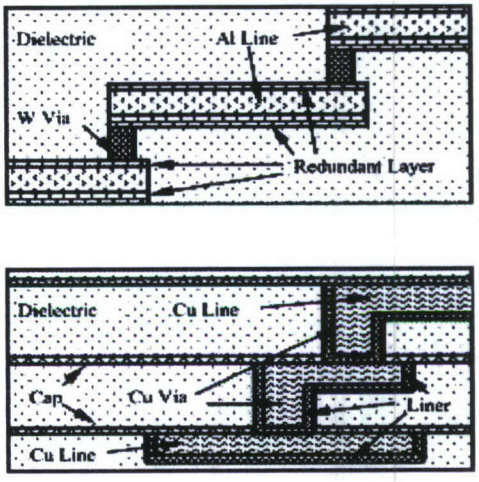

Figure 32 Cross Section of a aluminum interconnect (top) and a copper interconnect (bottom)(Li et al 2004)

A typical structure of aluminum and copper interconnects are shown on Figure 32. The critical damage location(void nucleation) for aluminum is at the upper edge of left W via if the current direction is from left to right due to the blocking boundary condition provided by W via. For copper interconnects, the critical points is at the bottom of Cu via or left upper edge of Cu M2 layer if the current density is from left to right. (M2 is the middle layer of copper in bottom figure of Figure 32) The void nucleation at bottom of via usually shows slit like void nucleation according to Liniger (Liniger et al 2003) which represents early failure mode. The void appearing at the upper edge of Cu M2 layer is usually large 3-D voids and is sometimes combined with slit like void at the base of void. According

to Liniger, this is the second mode of damage when the blocking boundary condition is presented due to underlying Ta/TaN liner. The feature of multiple voids nucleation may be the reason for statistical multi-mode nature of MTF (median time to failure) of copper interconnects while aluminum interconnect MTF is well represented by a single mode log normal distribution. Surface migration is considered in copper interconnects as a fast diffusion path. In copper different surface coating will brings different MTF distribution(Hu et al 2002) which shows that the surface migration might be an important factor.

The thickness of liner will also affect the failure time distribution. Different thicknesses of liners have been used from 10 nm to no liner to investigate the effects(Liniger et al. 2003). When the liner thickness is decreasing below 10 nm the copper interconnects shows increasing life time but when further reducing it below 1.4 nm, the life time of copper interconnect decreases. This is also reported by Hu et al.(Hu et al 2001). Different boundary conditions are taken into account for the simulations.

Current crowding is also considered as an important factor by Tu (2002). Tu suggested that current density gradient is the reason for void nucleated at the upper edge of M2 layer where very small current density distribution exists. The current density gradient driving force is used to explain the vacancy build up and void nucleation. At this chapter, current density distribution is included to investigate the damage distribution.

In simulations copper is modeled as a elastic perfect plastic material.

Several methods are used to calculate the damage of copper interconnects, total atomic flux divergence (integrated over time and local volume) is calculated according to the relationship between vacancy flux and atomic flux, which is equal to each other. Also we can use local vacancy concentration and spherical stress level as critical damage value. Yield stress is also used to be a critical value for damage simulation. These different damage criteria will be compared and discussed during the simulations.

3.2.1 Finite Element Modeling

8-nodes higher order user defined elements are used to mesh the geometry. A 50 μm and a 300 μm long lines are simulated. The line thickness is 1 μm and via height is 2 μm. The displacement boundary conditions are considered to be fixed along the copper interconnects. Different vacancy flux boundary conditions are considered for several cases. The mesh and boundary conditions (Left and right edge) are shown in Figure 33. Six watch points are labeled in Figure 33 from a to f, these elements are potential points for void nucleation. Also a thin layer of Ta/TaN liner is modeled at the bottom of the via and above the left end of copper which are used to define vacancy flux boundary condition. In Ta/TaN layer, outer surface are fixed at vacancy concentration degree of freedom to be value of 1 which is initial normalized vacancy concentration at stress free state. If a blocking boundary condition is considered, then flux diffusivity of this

layer will be 30 orders of magnitude smaller than vacancy flux diffusivity in copper grain boundary. Different diffusivity number will generate various flux boundary conditions from non blocking boundary conditions to fully blocking boundary conditions.

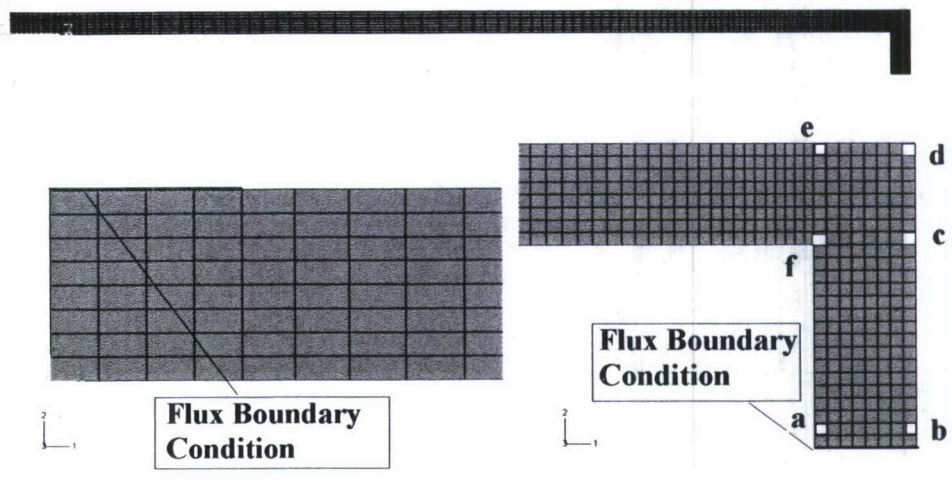

Figure 33 Finite element mesh

3.2.2 Material Properties Determination

Material parameters are summarized in this section, the Young's modulus of copper is set to be 120 GPa and Possoin ratio is set to be 0.3. Temperature is 473K. $D_{gb} = 1.2 \times 10^{-9} cm^2/s$ and $D_s = 1.0 \times 10^{-8} cm^2/s$ (Tu 2003). Ignoring surface diffusivity (which will be taken into account later), the effective atomic diffusivity can be calculated as

$$D_{eff} = \frac{\delta D_{gb}}{d} \qquad [3\text{-}1]$$

where $\delta(0.5nm)$ is the grain boundary width and d is average grain boundary

diameter which is estimated to be 0.5 μm. Since in this formulation, vacancy diffusivity instead of atomic diffusivity is used, we need to use the relationship of vacancy and atomic flux as

$$D_a C_a = D_v C_v \qquad [3\text{-}2]$$

to calculate effective vacancy diffusivity. In the calculation assumption of $\frac{C_v}{C_a} = 1 \times 10^{-7}$ is used. The effective vacancy diffusivity is calculated to be $1.2 \times 10^{-5} cm^2 / s$. Effective charge number Z^* is 0.7 according to Ogawa(2002). Other parameters are listed below:

Electric resistivity of copper is $1.6730 \mu ohm \cdot s \cdot cm$, atomic volume is $1.1887 \times 10^{-11} \mu m^3$, initial stress free state vacancy concentration is $8.413 \times 10^{15} / cm^3$.

3.2.3 Current Density Distribution Simulation

In order to consider current density distribution, a separate electrical field analysis is performed using the ABAQUS. The current direction is from left to right. The current is considered to be uniform at the bottom of via with the magnitude of $4.5 \times 10^5 A / cm^2$ and electrical potential at the right upper edge is set to be 0. The current density concentrated on the via-line corner as expected which is shown in Figure 34. In Figure 34, two meshes are shown with the same current density load. The maximum current density in finer mesh which is of course at the corner of via-copper is $1.636 \times 10^6 A / cm^2$ and with coarser mesh the maximum density is

$1.217\times10^{6}\,A/cm^{2}$. The current density distribution along the line AB is shown in Figure 35. This shows the current density distribution is mesh dependent around the corner. This is expected since the corner is a numerical singular point and analytical solution for the density is infinite at the corner. So if we want to utilize the current density distribution as our initial field input, we need to consider if the mesh dependence will affect the final solution. To investigate the latter, the current density distribution shown in Figure 34 are both used as input for stress and vacancy coupled analysis with the same boundary condition and material parameters. The results after 10 hours of simulation which are shown in Figure 36 show small difference. Due to data processing difficulties, only the via and copper above the via are shown in Figure 36. This analysis proved that the current singularity is localized and there is no mesh dependence effect. Also we can see from Figure 36, the spherical stress distribution is corresponding to the current distribution and shows a turning point around the corner of via-copper line.

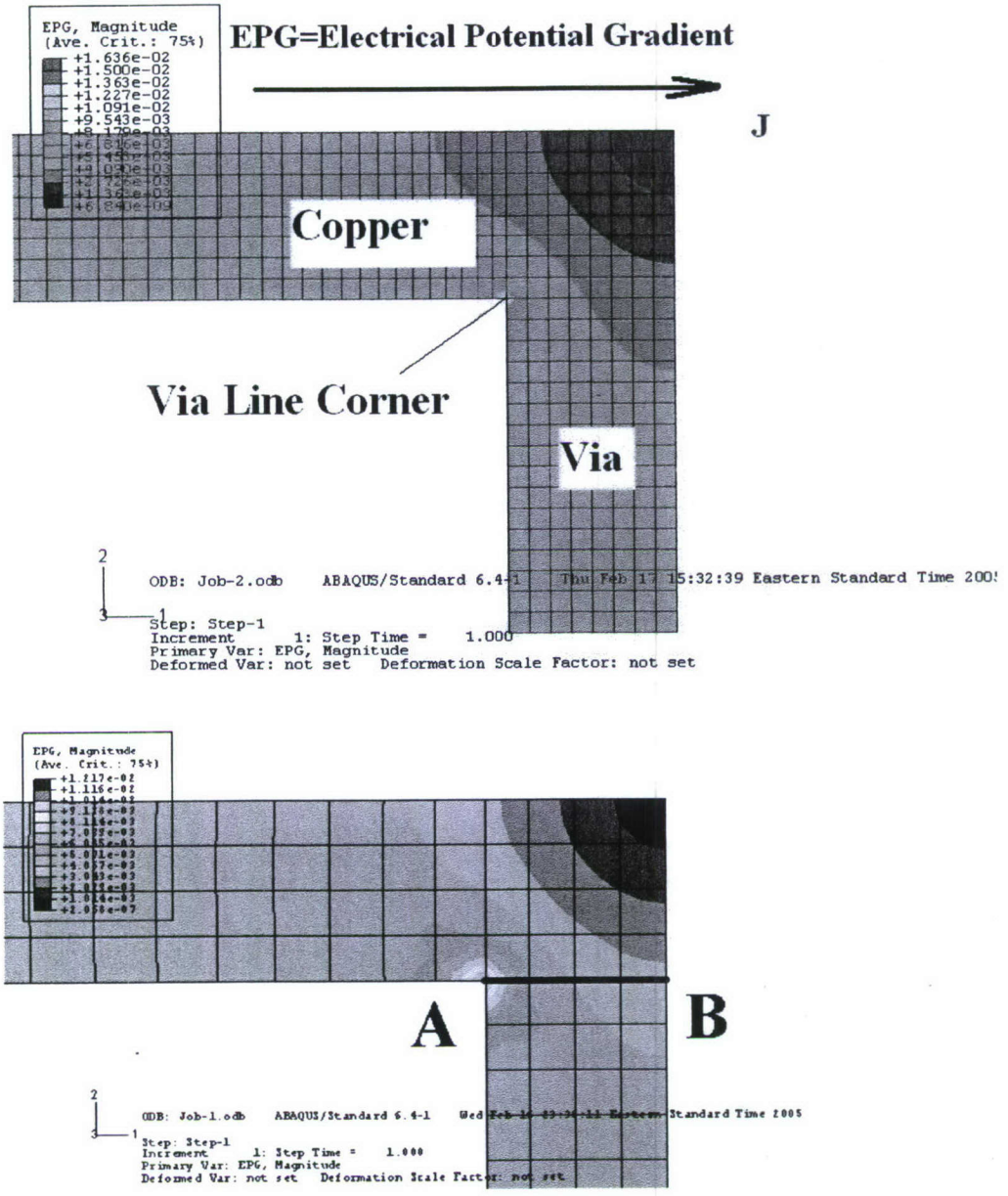

Figure 34 Current Density Distribution

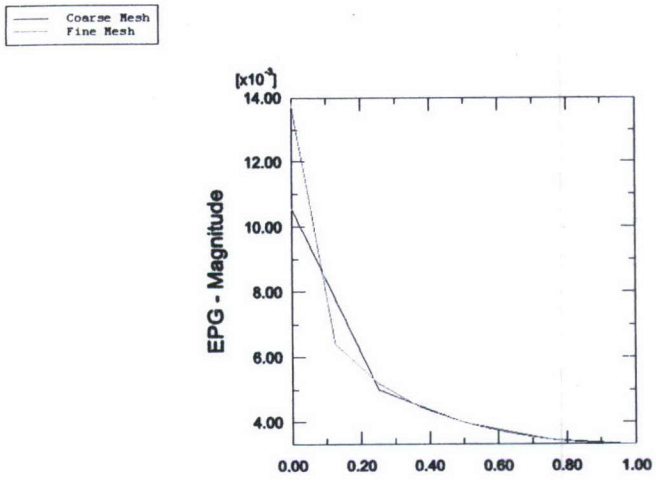

Figure 35 Current Density Distribution Along Line AB

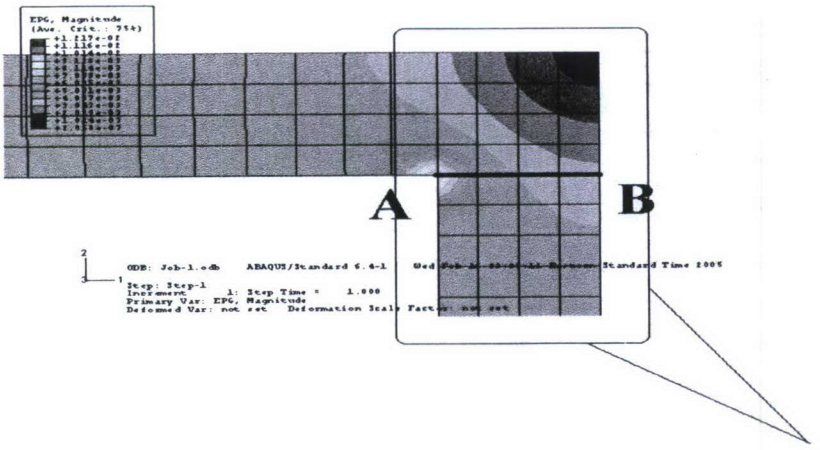

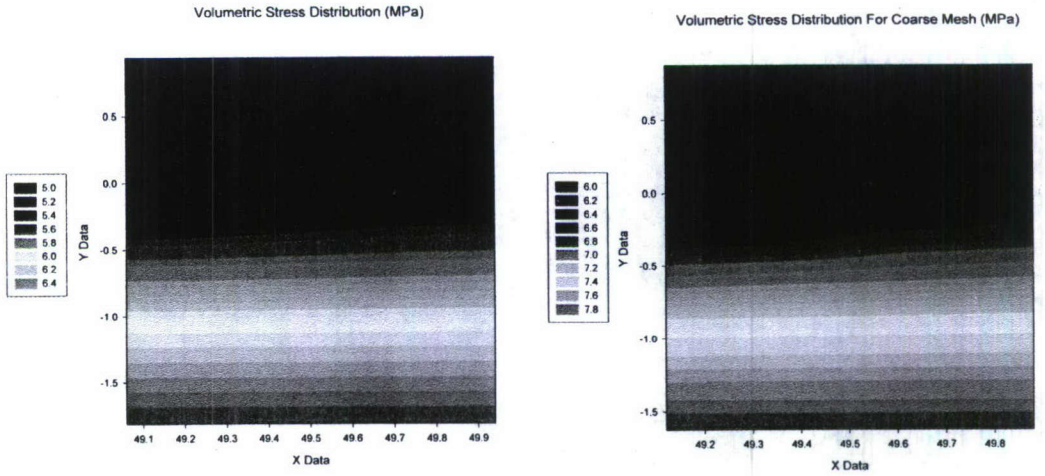

Figure 36 Spherical Stress Distribution for Fine(Left) and Coarse(right) Mesh after 10 Hours

3.2.4 Simulation Case Study1

A 50 μm long thin film with copper via is modeled. The copper thickness is 1 μm. According to Hu et al (1999) in such a thickness, the diffusion path is a mixture of grain boundary and surface diffusion, in this case, pure grain boundary diffusion will be used and mixture of diffusion path will be considered in later case. All the displacement boundary conditions are considered to be fixed. The flux

boundary conditions are defined as blocking boundary condition as stated in previous part. Current loading is $4.5\times10^5 A/cm^2$ and the direction of current is from left to right. The current density distribution is mapped into the initial field of the second displacement-vacancy coupled analysis. A fine mesh with typical element length of $0.125\,\mu m$ will be used. The simulation duration is 100 hours. Material plasticity is not considered in case 1.

The results at six watch points defined in Figure 33 are presented in Figure 37. Normalized vacancy concentration evolution in Figure 37 (a) shows that inside the via or above the via the normalized vacancy concentrations are very close to each other among 6 points. Point a and point f are closest to blocking boundary and they are the maximum vacancy concentration location. Same trend is shown in spherical stress and total atomic flux divergence result which are shown in Figure 37 (b) and (c). Although the current density at point f is the highest, the vacancy concentration and flux divergence at point f is still smaller than point a and b. Also at point d the current density is very small compared to other points, the vacancy concentration and flux divergence is still very close to other points. Current crowding effects are used by Tu(Tu et al 2000) to explain the void formation at no current region where the point d is located. Tu proposed that current density gradient is the reason for vacancy build up in no current region. Since vacancy flux is proportional to current density, at current concentration area, more vacancy will moves out than moves in, if there is current crowding. This is

one source of vacancy flux divergence. But the analysis shows a different picture. If the current crowding is the main reason for void in no current region, then we will expect that point d and f will have big difference in flux divergence or vacancy concentration since the current density at these two points are the highest and lowest respectively. From the analysis results we can see for points c, d ,e and f, the vacancy flux divergence and vacancy concentration are very close to each other.

There is another source for vacancy flux divergence, which is the blocking boundary condition. Due to length of copper is much longer that the via height, the blocking boundary at right and bottom of the via is dominant compared to the current density gradient. Thus the vacancy concentration is mainly determined by the horizontal distance from the blocking boundaries of the points. Point a and b have relatively larger vacancy concentration and flux divergence, this is because of the blocking boundary condition at the bottom of the via.

In Figure 37 (d) shear stress at six points are shown. Shear stress at point a and point b are much larger than other points. This is caused by the interaction of volumetric strain at local points and displacement boundary condition. Due the vacancy build-up at points a and b, the material will shrink but this shrink is constrained by via-Ta/TaN interface since the Ta/.TaN is a material with much smaller vacancy diffusivity than bulk copper. Points c and e shear stress are in the second place and shear stress in points d and f is the minimum. Liniger et al

(2003) pointed out that under blocking boundary condition, slit like voids under the via is the major void type for early failure. Shear stress concentration located at the bottom of via in this simulation can well explain the slit like void nucleation in early failure. Once the interface bonding strength or yield strength of copper is reached at the bottom of via, void nucleated at bottom of via will soon propagate under the shear stress. This is the dominant failure mode. The failure time is solely determined by void nucleation time. At later case plasticity will be incorporated into model and the time needed to reach yield stress will gives a estimation of the time to failure.

For points at e and c shear stress are much smaller than the bottom of via. In this region, the spherical stress is very high (tension stress is positive). Gleixner et al (1996) pointed out at such high spherical stress, void nucleation rate is still too slow to be responsible for void nucleation according to classical void nucleation theory. In Gleixner paper, an upper limit of 2 GPa of spherical stress is used and we can see from Figure 37 (b) spherical stress in this analysis is much smaller than 2 GPa. Gleixner pointed out that interface defect combined with high spherical stress may dramatically reduce the critical stress level for void nucleation. This can explain why large 3-D voids will appear in the upper surface of the copper lines where there is small current density. Since the shear stress level here is relatively low, void growth in this region is totally determined by the flux divergence rate and is relatively slow than stress assisted void growth at the

bottom of the via. This type of failure is described by Liniger (2003) as the second mode of failure. Total atomic flux divergence in Figure 37 (c) can be also considered as an important damage criteria since it represents the decreasing in atomic concentration level. In this analysis, since the steady state is reached, the change in atomic concentration level is relatively small.

In Figure 37 (e), vacancy flux at horizontal direction (which is the major flux direction) of element at the middle point of copper line is shown. Flux is reaching zero after 100 hours of time which means that steady state is reached. Figure 37 (f) shows the shear stress distribution in the via and copper interconnection above the via, the shear stress is concentrated at two sides of via bottom. Since the current density distribution is assumed to be uniform at the bottom, the shear stress concentration at both corners of interface are equal. In real interconnects, current density will concentrated on right corner if we taken into account M-1 layer in current field analysis. Thus the right corner will be the most critical point. M-1 layer is located at the bottom the via (Figure 32).

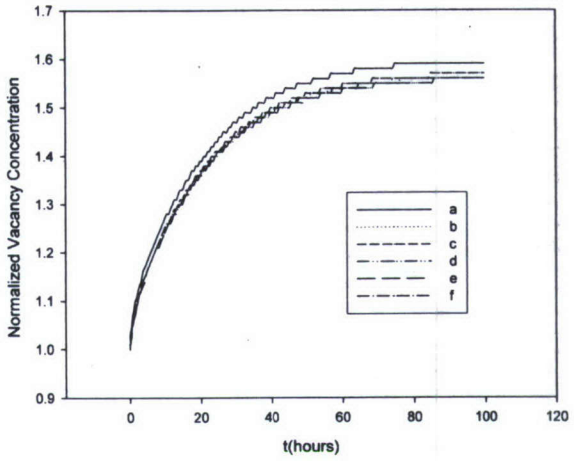
Normalized Vacancy Concentration
1.7
1.6
1.5
1.4
1.3
1.2
1.1
1.0
0.9
0
20
40
60
80
100
120
t(hours)
a
b
c
d
e
f

(a)

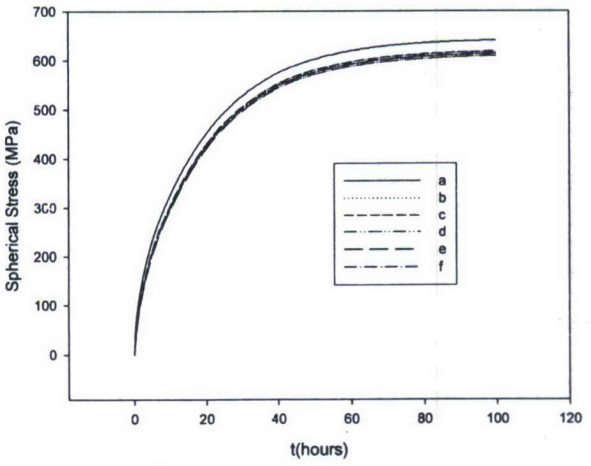
Spherical Stress (MPa)
700
600
500
400
300
200
100
0
0
20
40
60
80
100
120
t(hours)
a
b
c
d
e
f

(b)

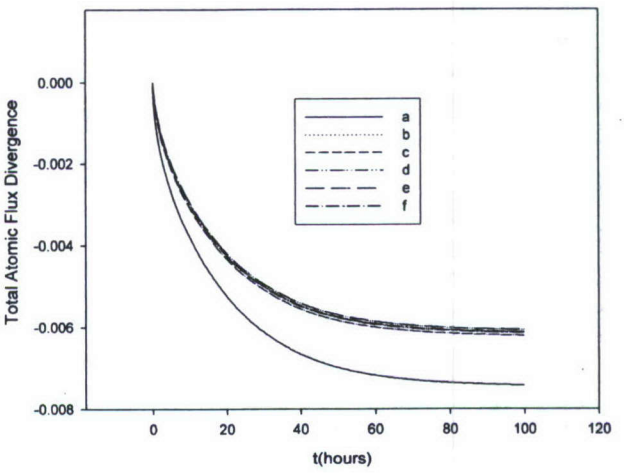
Total Atomic Flux Divergence
0.000
-0.002
-0.004
-0.006
-0.008
0
20
40
60
80
100
120
t(hours)
a
b
c
d
e
f

(c)

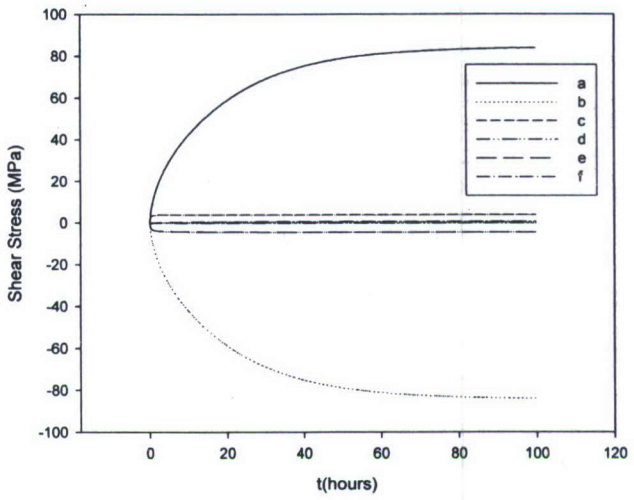

(d)

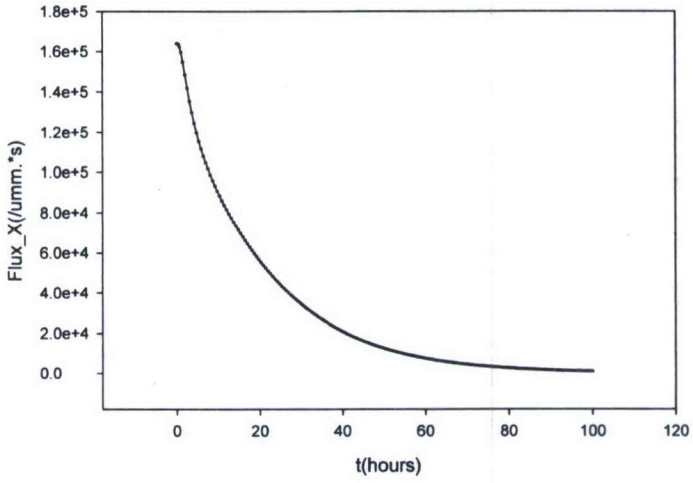

(e)

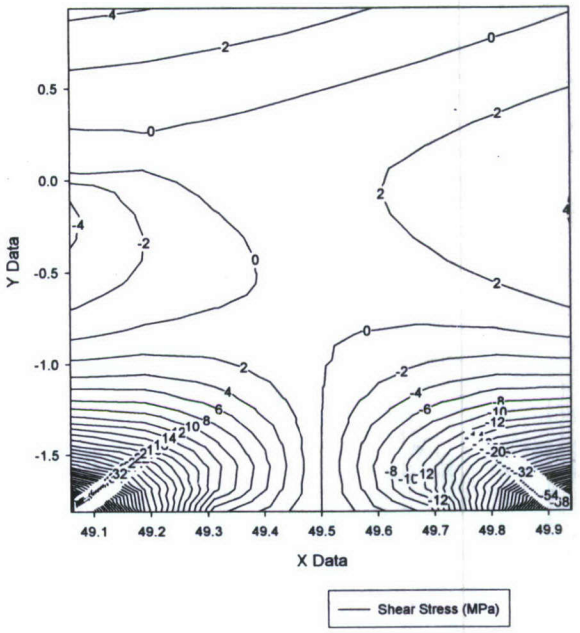

(f)

Figure 37 Time history of (a) Normalized Vacancy Concentration (b) Spherical Stress (c) Total Atomic Flux Divergence (d) Shear Stress at Six Watch Points (e) Vacancy Flux at Horizontal Direction at Middle of Line (f) Shear Stress Distribution in Via

3.2.5 Simulation Case Study 2

To investigate different flux boundary condition, the diffusivity in Ta/TaN layer (at the bottom of the via) is set to be just one order of magnitude smaller than copper diffusivity. With the same current distribution input and same displacement boundary condition as in case 1, case 2 is simulated for 100 hours. The partial results at watch points are shown in Figure 38. The spherical stress is very small compared to case 1 where blocking boundary condition was used for Ta/TaN layer.Also the total atomic divergence and the shear stress are very small. This is expected since the flux divergence source is controlled by blocking boundary condition. Under non blocking boundary condition, at the steady state, although

the divergence flux is reaching zero, vacancy flux is still at very high level. MTF in this interconnects will be very long if there is a huge vacancy reservoir at the bottom of via. If we include M-1 layer into the simulation, damage will focus in M-1 layer since the vacancy source in M-1 layer can not be infinite. The experimental results(Liniger et al. 2003) are in accordance with the simulation result.

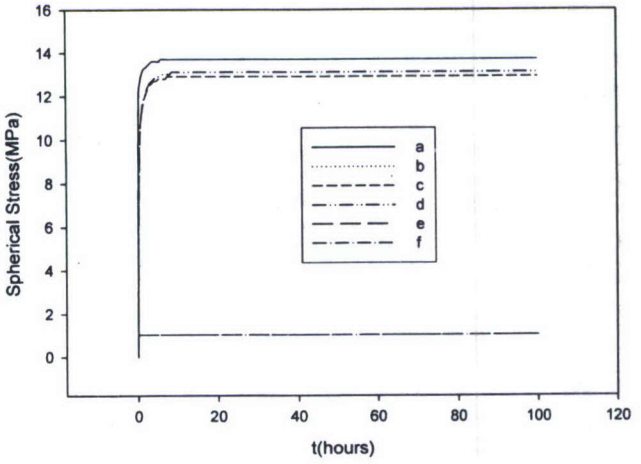

(a)

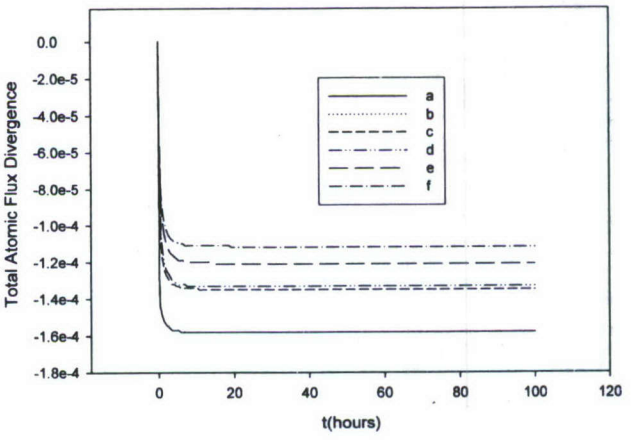

(b)

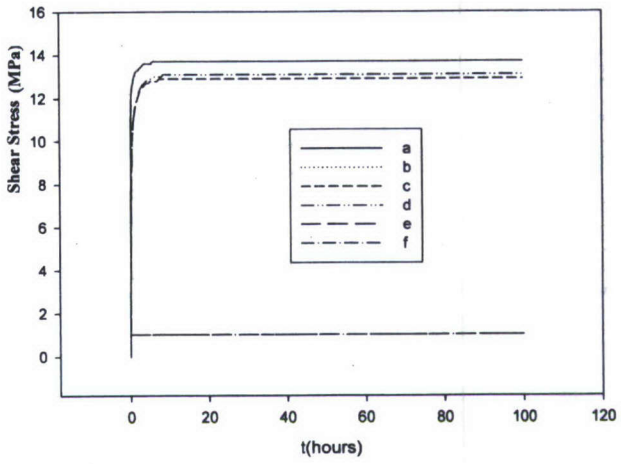

(c)

Figure 38 Time history of (a) Spherical Stress (b) Total Atomic Flux Divergence (c) Shear Stress at Six Watch Points

3.2.6 Simulation Case Study 3

Since the shear stress concentration at the two corners of via bottom, the yield stress here can be reached and plastic strain accumulation here will further assist void nucleation. A plastic material model with yield stress at 69 MPa and no hardening is considered in this case study. Blocking boundary condition is considered. Other material parameters are the same with case 1. The simulation results are shown in Figure 39. Figure 39 (a) shows the equivalent plastic strain accumulation evolution at six watch points. Points (a) and (b) has the same plastic strain and other points have no plastic strain accumulation. The time to reach yield at points a and b is roughly 4.75 hours. If the yield stress is defined as a critical points as void nucleation, the time to failure will be around 5 hours which is in the same order of magnitude as the MTF of first failure mode reported by

Liniger (2003). Spherical stress results are very close to case 1 which is shown in Figure 39 (b). Figure 39 (c) shows the shear stress distribution at six watch points. For all points but points a and b, shear stress is very close to simulation case 1. For points a and b shear stress level is much smaller than case 1. And after reaching yield points, shear stress in points (a) and (b) decrease a little and finally reaching steady state. The softening is due to the stress relaxation with plastic strain in local region. In order to investigate the influence of plastic strain, the normalized vacancy concentration and total atomic flux divergence are compared in Figure 40 for point a. These results are very close to each other which show that the plastic strain does not have strong influence on results.

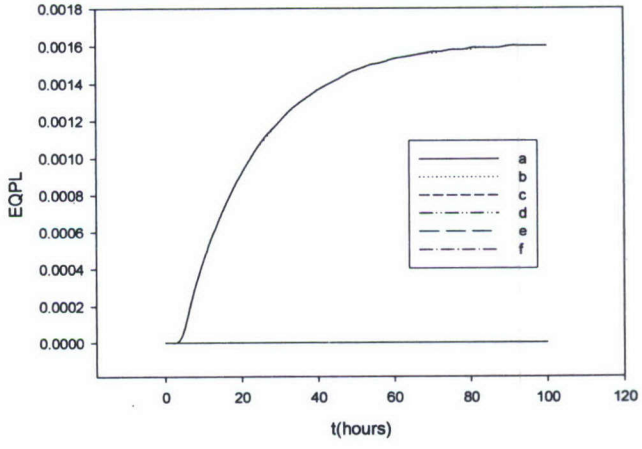

(a)

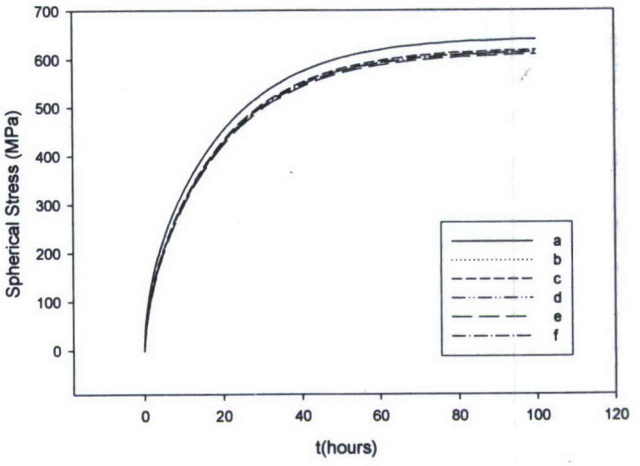

(b)

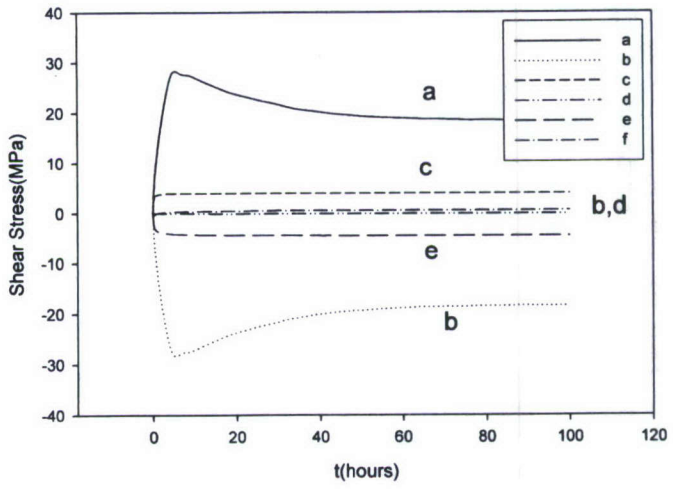

(c)

Figure 39 Time history of (a) Equivalent Plastic Strain (b) Spherical stress (c) Shear Stress at Six Watch Points

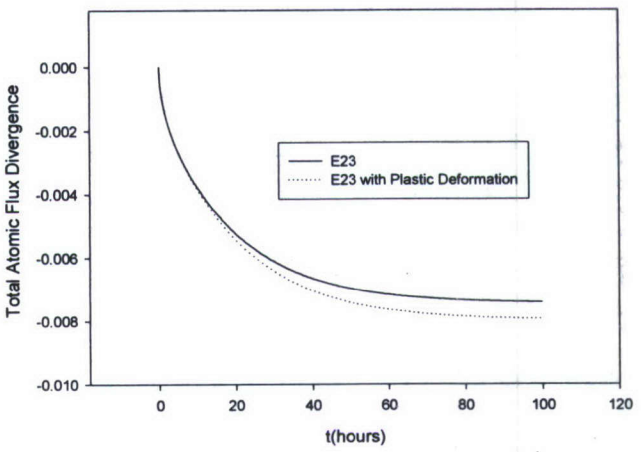

(a)

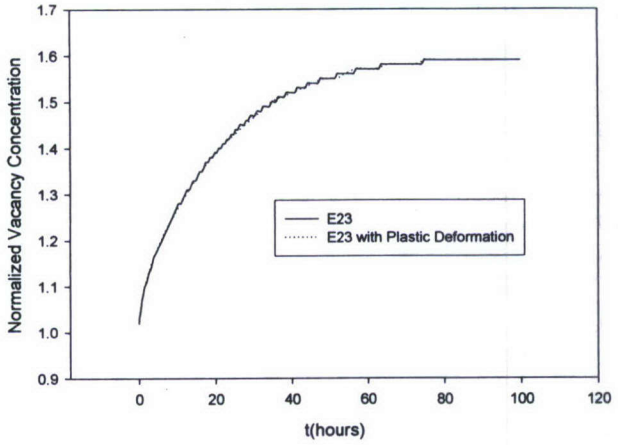

(b)

Figure 40 Comparing between Case 1 and Case 3 in Point A (a) Total Atomic Flux Divergence (b) Normalized Vacancy Concentration

3.2.7 Simulation Case Study 4

A 300 μm long copper line is simulated in case study 4. All the material parameters and boundary conditions are the same as in case 1 except the length of copper line. Results of simulation are shown in Figure 41. Figure 41 (a) shows the normalized vacancy concentration evolution history in 100 hours simulation. Six watch points normal vacancy concentration are very close to each other with

points a and b the largest vacancy concentration. Flux divergence and spherical stress results are in the same trend as case 1 but with bigger values. This further verifies that with longer length, horizontal direction vacancy flux is more dominant and current crowding effect in via is very small. Shear stress distributions for six watch points are shown in Figure 41 (d). Shear stress at points a and b are much larger than case 1 and this is expected since the deformation caused by vacancy build up is much larger. Figure 41 (e) shows the vacancy flux evolution at horizontal direction which is the major direction at the middle of line. We can see from Figure 41 (e) that steady state is not reached.

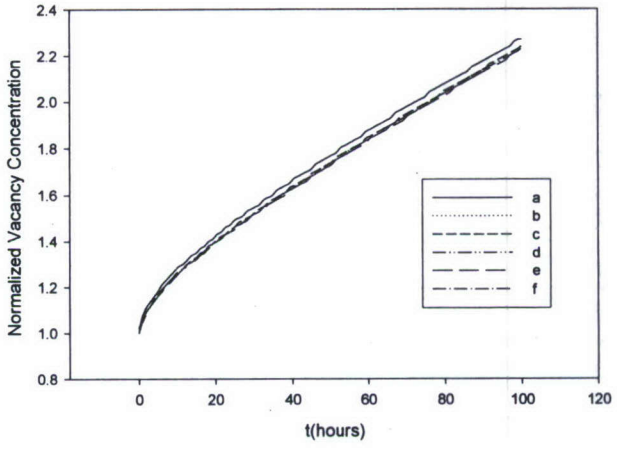

(a)

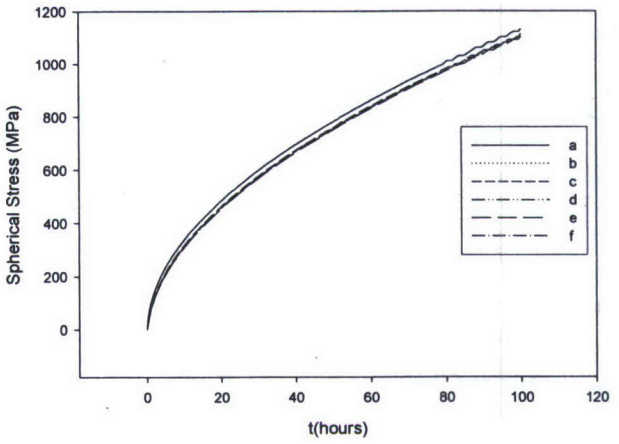
Spherical Stress (MPa)
1200
1000
800
600
400
200
0
0
20
40
60
80
100
120
t(hours)
a
b
c
d
e
f

(b)

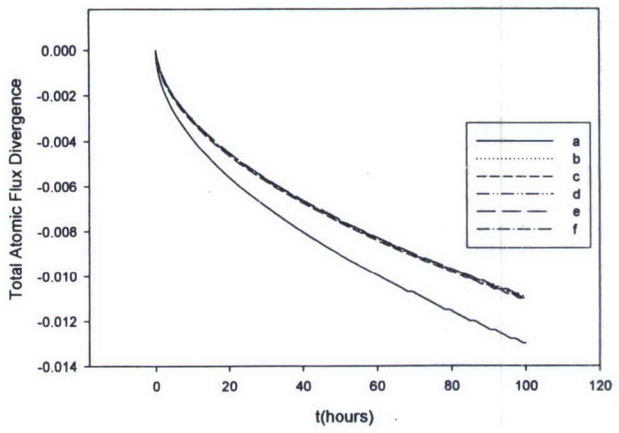
Total Atomic Flux Divergence
0.000
-0.002
-0.004
-0.006
-0.008
-0.010
-0.012
-0.014
0
20
40
60
80
100
120
t(hours)
a
b
c
d
e
f

(c)

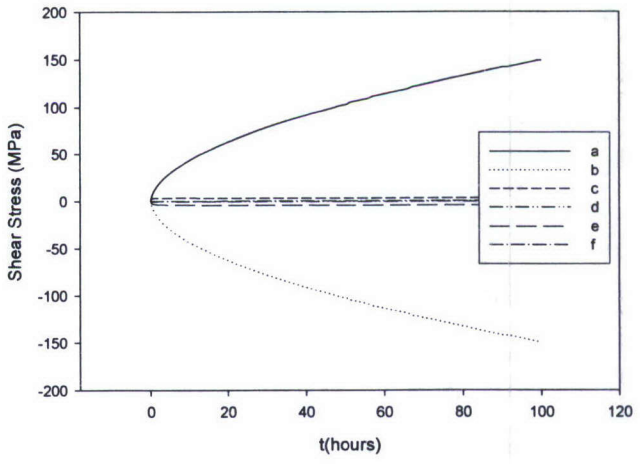
Shear Stress (MPa)
200
150
100
50
0
-50
-100
-150
-200
0
20
40
60
80
100
120
t(hours)
a
b
c
d
e
f

(d)

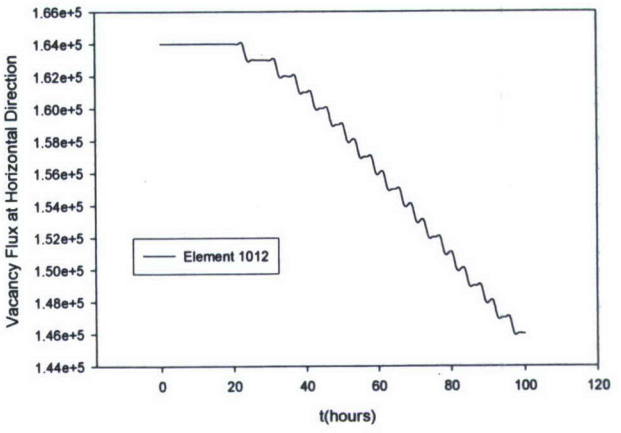

(e)

Figure 41 Time history of (a) Normalized Vacancy Concentration (b) Spherical Stress (c) Total Atomic Flux Divergence (d) Shear Stress at Six Watch Points (e) Vacancy Flux at Horizontal Direction at Middle of Line

A detailed comparison between case 1 and case 4 are shown in Figure 42and Figure 43. Figure 42 compares the shear stress and spherical stress evolution at point a. Shear stress and spherical stress of case 4 at point a are both much higher than case 1. The time to reach yield point is controlled by shear stress and from the results shown in Figure 42, the time needed to reach the yield stress for longer line is the same as in the shorter line. Although in case 1 a plasticity model is not included, we can still compare the time need to reaching the yield stress. Shear stress evolution comparison for point e is also shown in Figure 43. At point e shear stress is very small although vacancy concentration in case 4 is much higher than in case 1. The results verified that major source of shear stress is due to different diffusivity of via and liners.

According to the above analysis, with the longer length, time to reach critical

shear stress at the bottom of via interface is the same for shorter line if we use yield point as the critical point. This is by no means that line length do not have effect on MTF, this only means that beyond certain length, the effect of line length to MTF become trivial. On the other hand it is obvious from Figure 42 (a) Shear Stress and (b) Spherical Stress Evolution for Point a in Case 1 and Case 4that, in longer line stresses continue to increase in long line on the other hand, they reach asymptotic state in shoter line. The second failure mode which is the large 3-D voids at corner of the copper lines is much stronger than shorter lines since the vacancy concentration and flux divergence are much larger than in case 1. This trend is based on this analysis only and need to be further verified by tests.

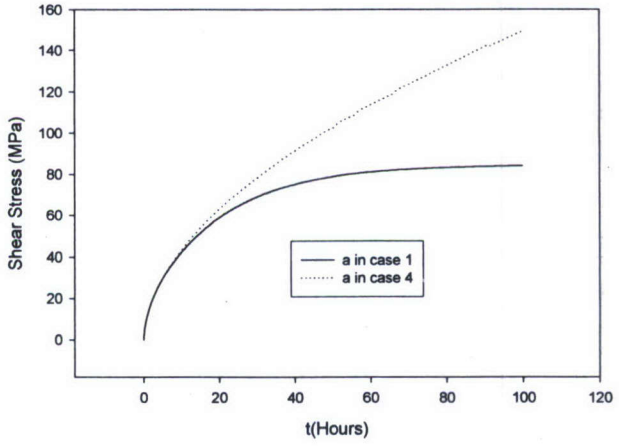

(a)

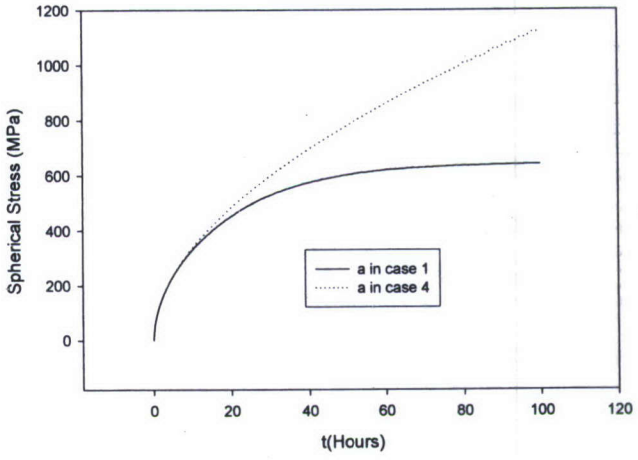

(b)

Figure 42 (a) Shear Stress and (b) Spherical Stress Evolution for Point a in Case 1 and Case 4

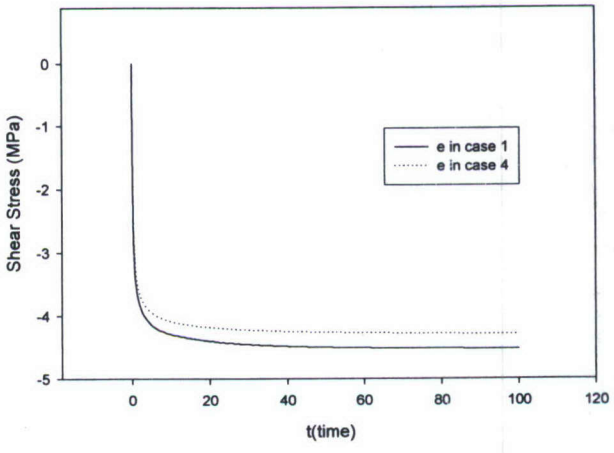

Figure 43 Shear Stress Evolution for Point e

3.2.8 Simulation Case Study 5

The interface diffusion at the top of copper thin film (the interface between capping layer and copper thin film (Figure 32) is considered a fast diffusion path by most researchers(Hu et al. 2002). To investigate on this, a fast diffusion path was created on the top of the surface. The diffusivity along this interface is set to be

one order of magnitude larger than vacancy diffusivity in the copper layer. All the other simulation parameters are the same as in case 1. The simulation results are shown in Figure 44. Figure 44 (a) and (b) show the vacancy concentration and spherical stress for 6 watch points, and we can see the fast diffusion path did not separate those six points evolution, in spite of the fact that points d and e are closer to the fast diffusion path. The shear stress distribution also shows the same pattern as vacancy concentration and spherical stress. To further investigate on this fast diffusion path, a two order of magnitude increase in interface diffusivity is used for another simulation case. The results are shown in Figure 45. Still there is no separation for vacancy concentration, spherical stress or shear stress evolution for six watch points. This can be explained by the dimension of copper thickness and via is very small compared to the copper length, although a fast diffusion path can favor those points which are close to it, this trend can not be distinguished since the distance between those six points are too small. The detail comparison at point a among simulation case 1 and two fast path simulation cases are shown in Figure 46. The evolution of normalized vacancy concentration, total atomic flux divergence and shear stress are much faster with fast diffusion path. Experimental study by Hu et al (2002) also showed by using a capping layer on the top of copper interconnect surface can dramatically increase the MTF of copper interconnect line.

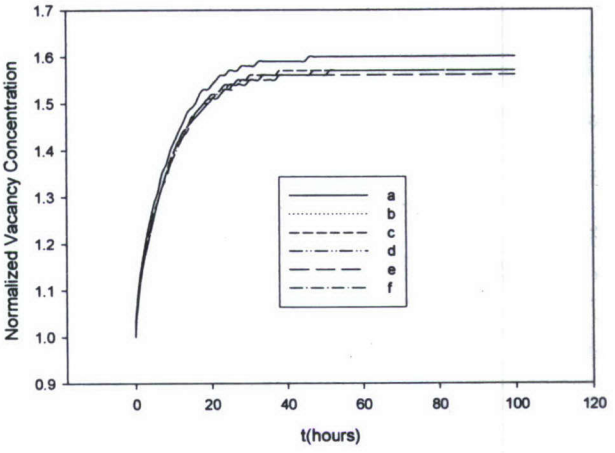
Normalized Vacancy Concentration
1.7
1.6
1.5
1.4
1.3
1.2
1.1
1.0
0.9
0
20
40
60
80
100
120
t(hours)
a
b
c
d
e
f

(a)

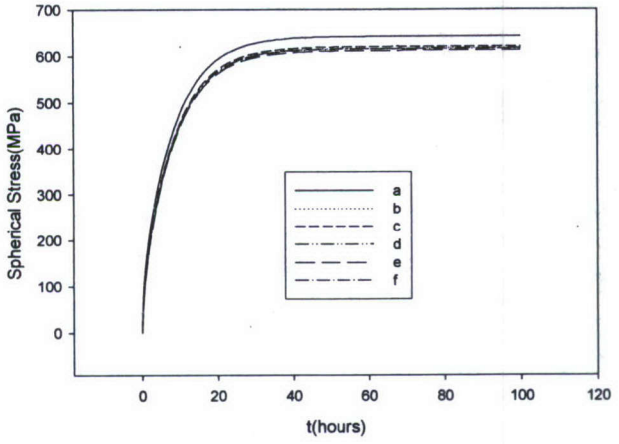
Spherical Stress(MPa)
700
600
500
400
300
200
100
0
0
20
40
60
80
100
120
t(hours)
a
b
c
d
e
f

(b)

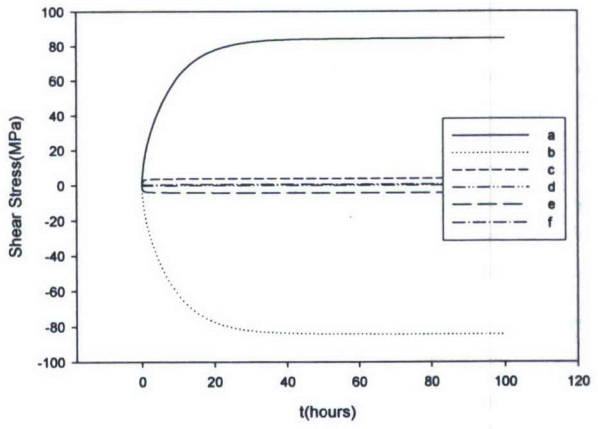
Shear Stress(MPa)
100
80
60
40
20
0
-20
-40
-60
-80
-100
0
20
40
60
80
100
120
t(hours)
a
b
c
d
e
f

(c)

Figure 44 Time History of (a) Normalized Vacancy Concentration (b) Spherical Stress (c) Shear Stress at Six Watch Points

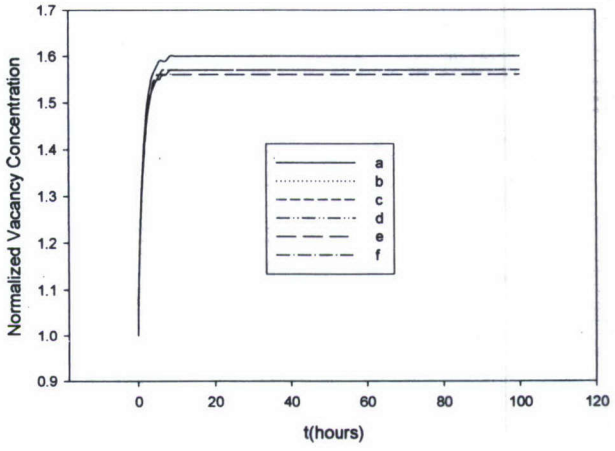

(a)

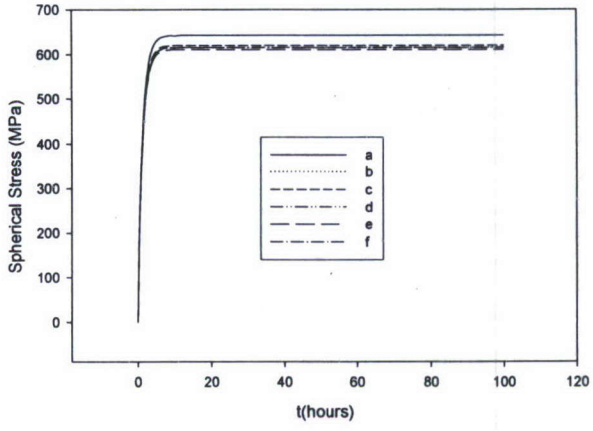

(b)

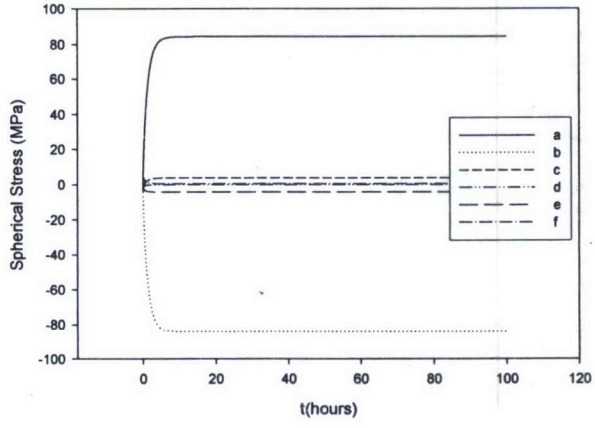

(c)

Figure 45 Time History of (a) Normalized Vacancy Concentration (b) Spherical Stress (c) Shear Stress at Six Watch Points

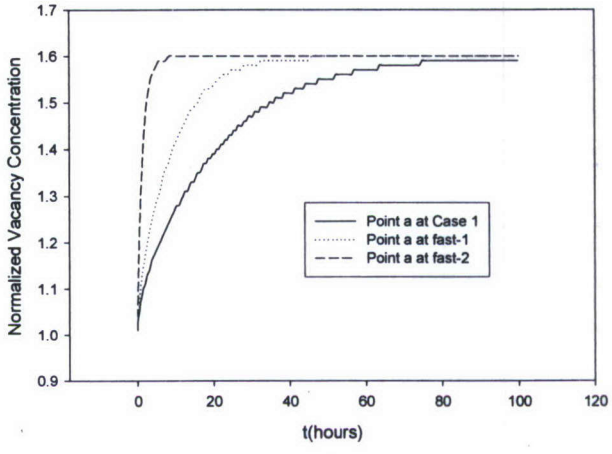

(a)

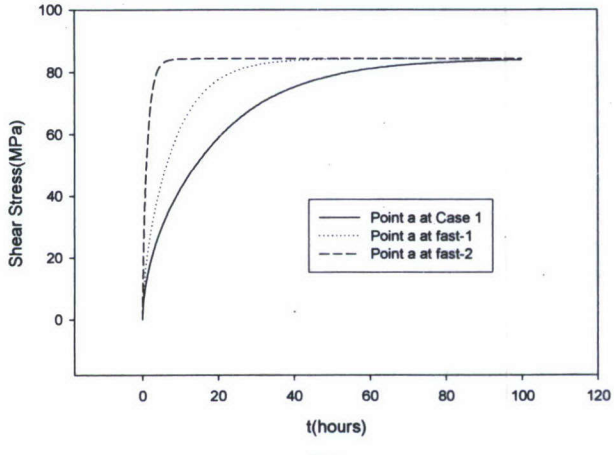

(b)

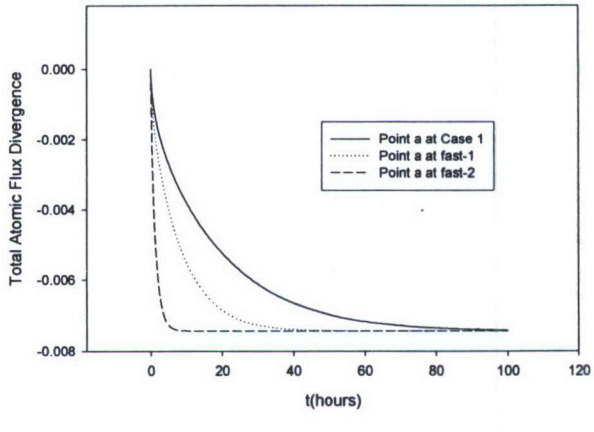

(c)

Figure 46 Time History of (a) Normalized Vacancy Concentration (b) Shear Stress (c) Total Atomic Flux Divergence at Watch Point a

3.2.9 Conclusions and discussion

Based on the simulation results, two failure mechanisms are observed. One is the shear stress controlled failure at the bottom of via at blocking boundary condition. The other one is interfacial failure and void growth controlled failure at the end of copper line. Eliminating the fast diffusion path can greatly increase MTF. Also changing the blocking boundary to partial blocking boundary can also increase MTF. If totally non blocking boundary condition is used, MTF for the layer M-2 which is the simulated one in above cases will increase greatly but that is achieved by using underlying M-1 as a vacancy reservoir. So a balanced solution is to use partial blocking boundary condition which can be determined by including M01 layer into the FEM simulation. Current density distribution is considered and the analysis shows that the current concentration at the corner is not a major factor compared to blocking boundary conditions. Also material plasticity is considered and plastic strain accumulation is calculated. The stress relaxation after plasticity is also observed in this analysis. For non blocking boundary conditions, the flux divergence at copper interconnect line is very small but vacancy flux is very large. The failure at non blocking boundary condition is controlled by mass depletion at other layer of copper interconnect lines.

From the simulation analysis above, to extend MTF of copper interconnect,

there are several methods can be adopted. First it is very obviously, to reduce the effective diffusivity of the material. Second, boundary conditions are very important. A partially blocking boundary condition needed to be determined from analysis for best performance. Also, a soft material with small Young's modulus as a liner will benefit the reliability at the interface thus increase the MTF.

3.3 Simulation for lead-free solder connection

Electromigration is becoming a reliability concern for electronic packaging with miniaturization to nanoscale. This is especially true for solder joints at 10 microns range which are expected to be used for nanoelectronics packaging. Since February 13, 2003, the use of lead free solder joint has been a law in European Union (EU). The implementation day is July 1, 2006. That means after July 1st, electronic products containing lead free solder can not be made or shipped to EU. Recently, packages such as PBGA (plastic ball grid array), CSP (chip scale package), and WLCSP (wafer level chip scale package) have been very popular for consumer, computer, communication, optoelectronic, and optical MEMS (micro-electromechanical system) products. Lead free solder are used as their interconnects. In order to investigate electromigration failure in solder joints, some efforts have been made to model and simulate stress evolution due to electromigration, which include some analytical solutions and numerical method implementations(Korhonen et al. 1993;Sarychev and Zhinikov 1999;Park et al

1999;Ye et al. 2003b). A big disadvantage of those models is that they treat materials as linear elastic for simplification although material such as aluminum, copper and solder exhibit plasticity. In this dissertation a fully coupled displacement-diffusion model with nonlinear mechanical material properties (viscoplasticity) is implemented with finite element method. The simulation results are compared with experimental Moiré Interferometry results. The comparison validated the model and paves the way for further development of damage prediction model.

The FEM formulation is already presented in previous chapter. Lead free solder viscoplasticity model is developed by Neu et al(Neu et al 2000). The viscoplastic flow rule for Sn-Ag lead free solder alloys based on McDowell's (McDowell 1992) Unified Creep Plasticity (UCP) model,

$$\dot{\varepsilon}_{ij}^{vp} = A\left(\frac{\langle F\rangle}{Dr}\right)^{n} \exp\left[\left(\frac{\langle F\rangle}{Dr}\right)^{n+1}\right] e^{-Q/R\theta}\frac{\partial F}{\partial \sigma_{ij}} \qquad (3)$$

where the material parameters are defined as follows,

A: a dimensionless material parameter to describe the strain rate sensitivity.

$e^{\left(\frac{-Q}{R\theta}\right)}$ is a Arrhenius exponential for temperature dependency, where

Q is the creep activation energy for plastic flow

R is the universal gas constant = 8.314 J/K.mol = 8.314 N.mm/K.mol

θ: absolute temperature in Kelvin

Dr: Drag Strength

F: Over stress defined as $F = \|\boldsymbol{\sigma} - \mathbf{X}\| - K(\alpha)$

n: stress exponent for plastic deformation rate,

Neu (2000) used a very complicated back stress evolution model, after simplification, the following hardening evolution can be obtained. Here we ignore the term in long range back stress evolution function which is negligible compared with other terms. As a result we obtain a kinematic hardening function similar to the one proposed by Armstrong (Armstrong and Frederick 1966) and Chaboche (Chaboche 1989).

$$\dot{\alpha} = \sqrt{\frac{2}{3}}\dot{\gamma} \tag{4}$$

$$\dot{\mathbf{X}} = c_1 \dot{\boldsymbol{\varepsilon}}_{ij}^{p} - c_2 \mathbf{X}\dot{\alpha} \tag{5}$$

where c_1 is linear kinematic hardening constant

c_2 is nonlinear kinematic hardening constant.

$\dot{\boldsymbol{\varepsilon}}_{ij}^{p}$ is plastic strain rate tensor

γ is the plastic strain trajectory.

$$\mathbf{S} = \boldsymbol{\sigma} - \frac{1}{3} Tr(\boldsymbol{\sigma})\mathbf{1}$$

$\mathbf{X}$ is a back stress tensor defining the displacement of the center of the yield surface in the deviatoric stress space.

$K(\alpha)$ represents the isotropic hardening component defining the radius of the yield surface in stress space. $K(\alpha)$ is constant for lead free solder according

to Neu et al (2000).

The test data we have used in this work was provided by Ye et al (2003a). Using the Moiré Interferometry technique, in-situ displacement fields were measured during the electrical current loading process. The Moiré Interferometry results and finite element simulation results are compared for displacement and strain fields.

3.3.1 Samples Structure and Modeling

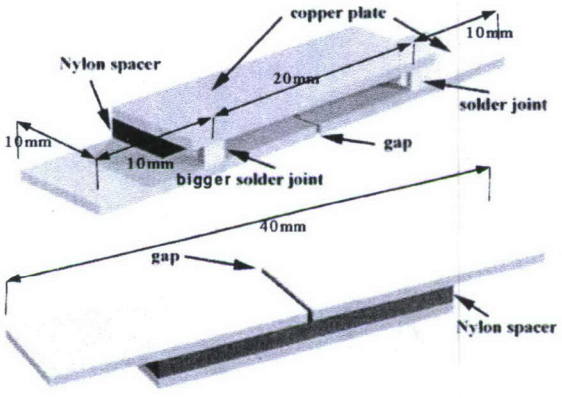

Figure 47 Test Sample Detail (Ye 2004)

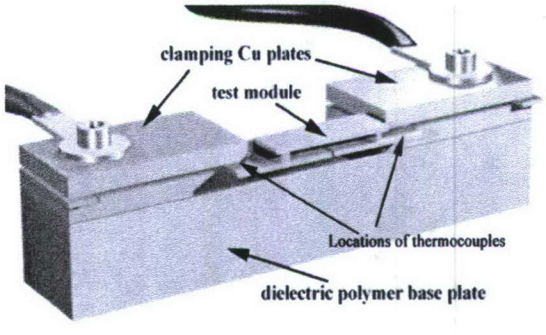

Figure 48 Electrical Connection for Test Sample (Ye 2004)

Test sample details are shown on Figure 47 and Figure 48, where the optical

table under the specimen is not shown. By means of optical diffraction grating attached on the surface of solder joints the images of the fringes are recorded in-situ throughout the whole current stressing process. The temperature fluctuation is controlled within 4 degrees (Ye 2004).

Finite element model established as shown in Figure 49 based on the sample structure shown in Figure 47. Copper Plates and Solder are taken into consideration. 8 nodes plain strain elements with thickness are used to mesh the solder and copper parts.

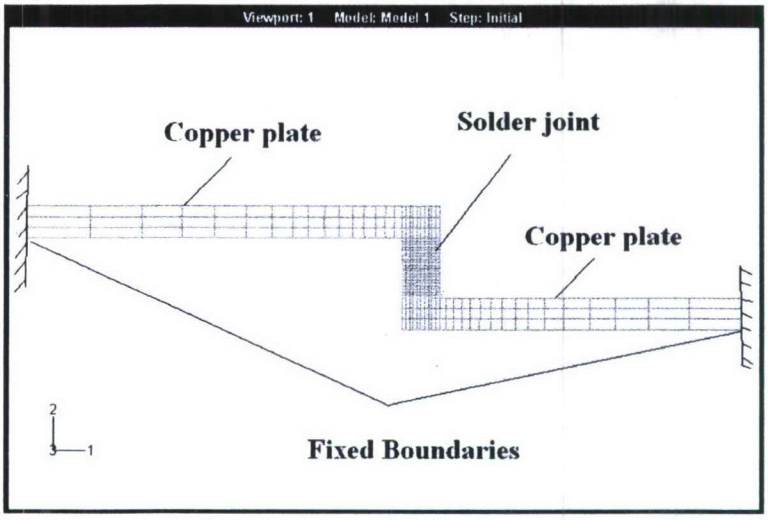

Figure 49 Finite Element Mesh for Copper Plates and Solder Joint

Copper plate thickness is 40 times of solder joint's thickness. The left and right ends of copper plate are fixed in both x and y directions with respect to displacement boundary conditions. The diffusion boundary conditions between copper and solder are considered to be free. This means copper and solder can inter diffuse into each other. This assumption will be discussed further in the later

part of the paper.

3.3.2 Determination of Material Properties

94Sn/4Ag lead free solder alloy is used in the tests. Sn is considered to be main diffusion specie(Ye et al. 2003a).

For lead free solder, the mechanical material properties are obtained from Neu et al (2000). Young's modulus and shear modulus are respectively:

$$E(T) = 45.0\text{-}9.0 \tanh [0.028(T(k)\text{-}298)] \text{ GPa}$$

$$\text{Poisson Ratio}=0.4$$

where T is temperature in Kevin.

The yield stress in uniaxial tension is:

$$\sigma_{Y0} = 3.0MPa$$

Kinematic hardening parameters are shown in Table 5. Viscoplastic flow function parameters are shown in

Table 6.

Table 5 Kinematic Hardening Parameters for 94Sn/4Ag lead frees solders

Parameter	Value
c_1 (MPa)	9626.5
c_2	725.1

Table 6 Flow Function Parameters for 94Sn/4Ag lead frees solders

Parameter	*Value*
D_r	3.0MPa
N	3
Q(KJ/mole)	50.0
A	0.55

The material properties of copper are follows

E=117GPa

Poisson Ratio=0.33

The atomic volume, □, of tin is 16.3cm^3/mol or 2.71×$10^{-23}cm^3/atom$. The atomic concentration, C_a, of tin is 3.69×$10^{22}/cm^3$. The equilibrium vacancy concentration at a stress free state is reported as $C_{v0}/C_a = 3\times10^{-5}$ (Balzer and Sigvaldason 1979), or C_{v0}=1.11×$10^{18}/cm^3$.

Pure Tin grain boundary diffusivity is found (Prabjit and Milton 1984) by assuming a grain boundary width of 0.5nm:

$$D_{gb} = (4.9^{+15.6}_{-3.7})\exp[-(11700\pm840 cal/mol)/RT]cm^2/s$$

where R = 8.3145J/mol=1.987cal/mol, is gas constant, and T is absolute temperature. Diffusivity at grain boundary for Tin is larger than lattice diffusivity by an order of magnitude, therefore in this simulation, the grain boundary diffusion is

assumed to be the main diffusion mechanism in electromigration. By assuming an average grain size of d=300nm (Prabjit and Milton 1984), the effective atomic diffusivity is thus:

$$D_a = \frac{\delta}{d} D_{gb} = \frac{0.5nm}{300nm} \times 4.9 \times \exp(-11700cal/RT) cm^2/s$$

At 300K , D_a is calculated to be $2.97\times10^{-11} cm^2/s$. The vacancy diffusivity is calculated from the relation (Clement and Thompson 1995), $D_aC_a=D_vC_v$, at the stress free state. By assuming $C_{v0}/C_a = 3\times10^{-5}$ (Balzer and Sigvaldason 1979), $D_v=D_a/(3\times10^{-5})=1\times10^{-6} cm^2/s$ is derived and used in the following simulations.

The effective charge number of lead-free solder is given by (Prabjit and Milton 1984) -10 at 30°C (measured stressing temperature). This negative effective charge number is for the atoms in the solder, indicating that the atoms are actually migrating in the opposite direction of electric current. Since the vacancy migrates in the opposite direction of the moving atom, the effective charge number for the vacancy is positive. Therefore, in the simulation the effective charge number of vacancy is taken as 10. Other material parameters are listed as,

T=303K, temperature (assumed as uniformly distributed in the solder joint).

$K=8.62\times10^{-5} eV/K=1.38\times10^{-23} J/K$, Boltzman's constant.

$t_s=1.8\times10^{-3} s$, vacancy relaxation time ((Sarychev and Zhinikov 1999)).

f=0.6, average vacancy relaxation ratio ((Sarychev and Zhinikov 1999)).

ρ =1.15×10^{-5}□·*cm*, electrical resistivity.

All the material parameters regarding to diffusion are summarized in Table 7.

Table 7 Diffusion Materials Parameters

Temperature	*303K*
Vacancy relaxation time (TS)	1.8E-3 s (Sarychev and Zhinikov 1999)
Diffusity (D)	100.0 $\mu m^2 s^{-1}$
Effective charge number (Z*)	10
Resistivity (ρ)	1.15E11 $\mu m^3 s^{-3} A^{-2} kg$
Average vacancy relaxation ratio (f)	0.6(Sarychev and Zhinikov 1999)
Atomic volume of tin (Ω)	2.71E-11 μm^3
Initial vacancy concentration (C_{v0})	1.11E6 μm^{-3} (Balzer and Sigvaldason 1979)
Boltzman constant (AK)	1.38E-11 $\mu m^2 s^{-2} K^{-1} kg$
Universal gas constant	8.314E6 $\mu m.s^{-2} kg.Mole^{-1}.K^{-1}$

3.3.3 Numerical simulation Case 1

The only loading considered in the analysis is electrical current, the thermal loading is considered to be irrelevant based on small fluctuation of temperature, although our model has the ability of taking into account thermal loading. For case 1, the electrical current density is $1.12\times10^4 A/cm^2$. The current input is about 28

A and current direction is from top to bottom. Since the solder joint has non uniform thickness, the current density is not constant along the height of solder joint. This is taken into consideration in the numerical simulation and it turns out to be an essential part of loading condition. Non uniform thickness of solder joint-1 is shown in Figure 50.

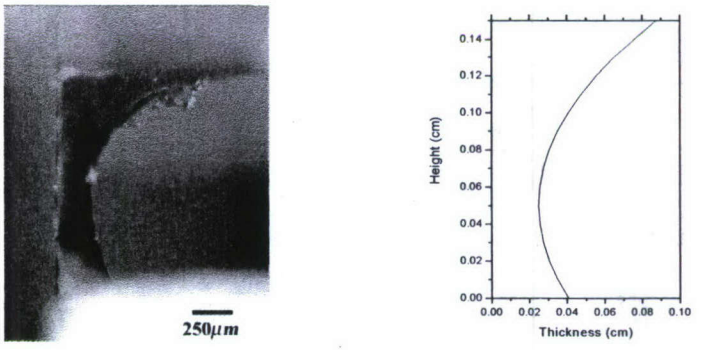

Figure 50 (a) Optical microscopic image of the solder joint (b) Thickness variation along the height of the solder joint used in the simulation (Ye et al(Ye et al))

The variation of the thickness of solder joint-1along its height can be formulated as

$$W_{thickness} = 0.025 \times [1 + 2.5 \times (\frac{y - 0.05}{0.1})^2]$$

where y is the distance from the bottom of the solder joint. The current density of solder joint-1 distribution along y direction is then

$$j = 1.12 \times 10^4 / [1 + 2.5 \times (\frac{y - 0.05}{0.1})^2] \, (A / cm^2)$$

To further prove the current distribution formulation, a 3-D electrical analysis is performed using Abaqus to simulate current density distribution. The steady state result of electrical potential is shown in Figure 51. The analysis verified the

current density distribution given above is close to real distribution.

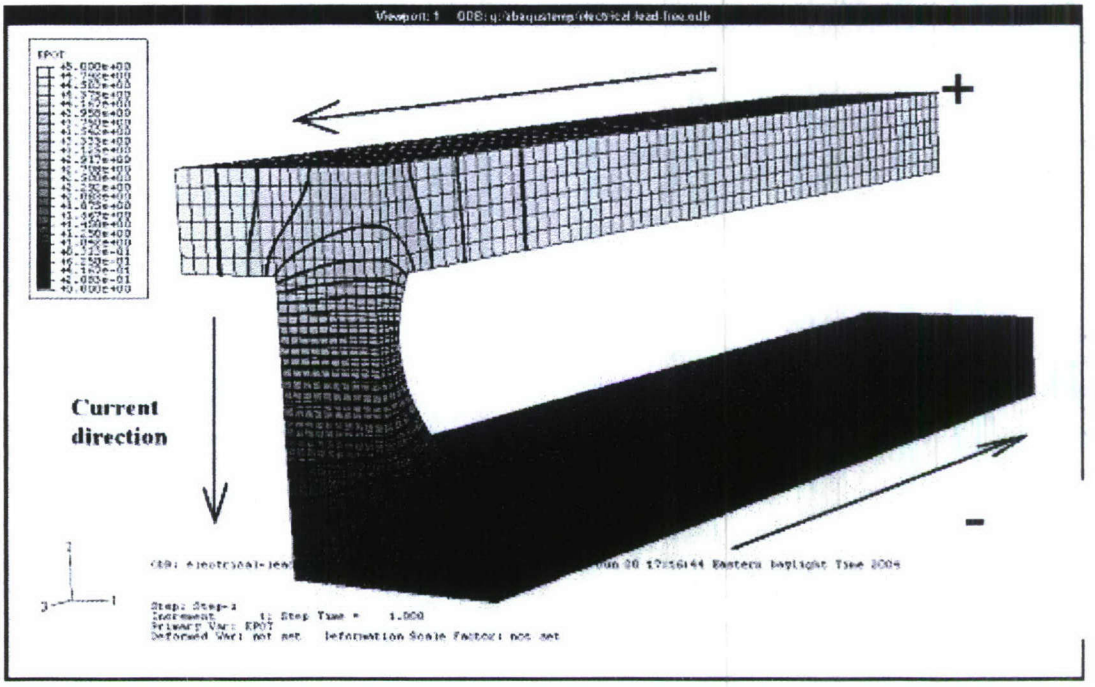

Figure 51 Steady State Electrical Potential Distribution for Solder Joint

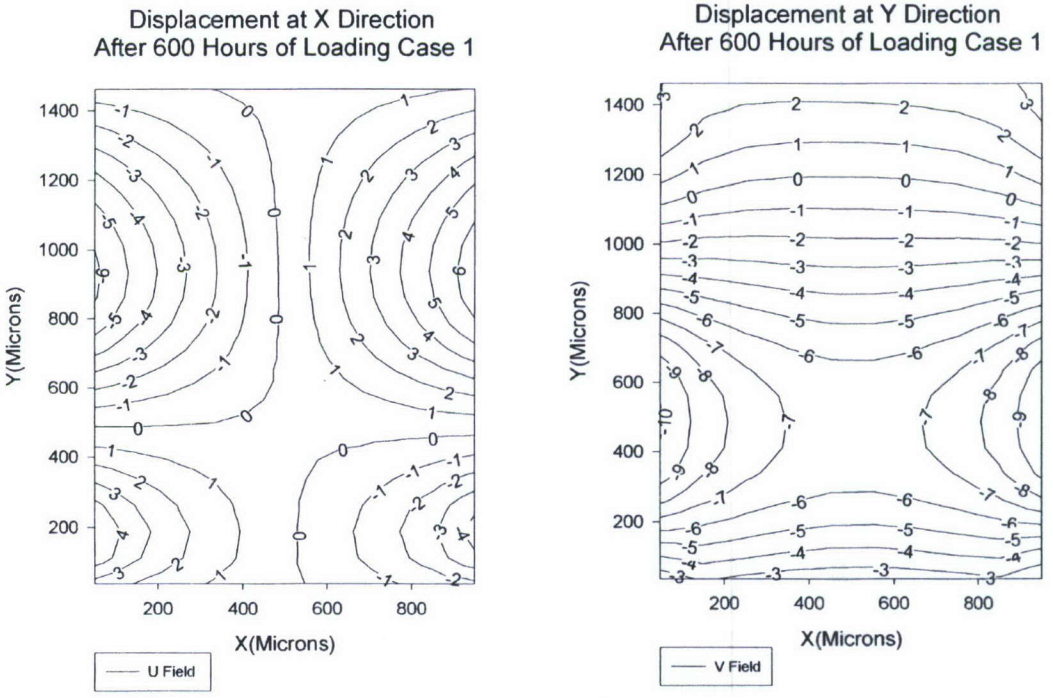

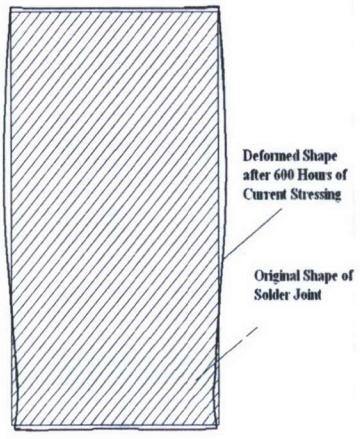

(c)

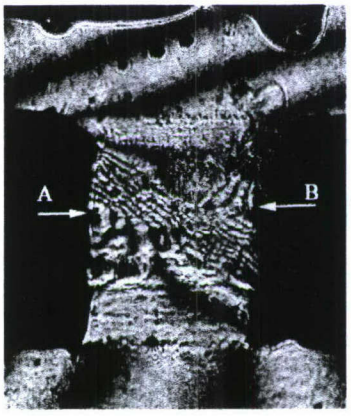

(d)(Ye et al.)

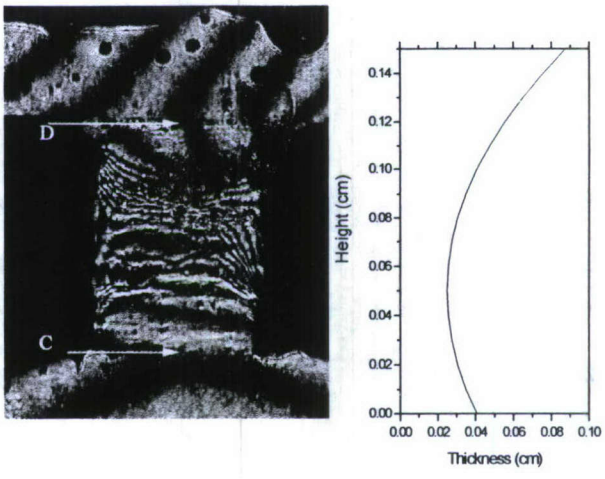

(e) (Ye et al.)

Figure 52 (a) X-direction displacement field after 600 hours (b) Y-direction displacement field after 600 hours (c) Simulated Deformed Shape after 600 hours (d) U-Field Moiré Interferometry Fringe (e) V-Field Test Moiré Interferometry Fringe After 600 Hours

The simulation is performed for 1000 hours. Moiré Interferometry technique is used for measuring displacement field time history. The displacement field in the solder joint is represented by the fringe numbers shown is Figure 52 (d) and (e). Figure 52 shows the displacement fields and deformation result for both test

and numerical simulation after 600 hours of current testing. The displacement field predicted by numerical analysis and test data are close to each other. From the deformation of solder shown in Figure 52 (c), the upper part of solder is in expansion and lower part of solder is in contraction. This can be explained by looking at the current density distribution which is in correspondence with solder thickness distribution shown in Figure 50 (b). From Figure 50, on the upper part of solder joint, current density is increasing and reach maximum value around the axis of y=0.5 mm. Since vacancy flux is proportional to current density, the vacancy flux is also increasing and reach maximum value around the axis of y=0.5 mm. Pick any unit cell A at the upper part of solder, the vacancy flux at the upper boundary of cell A is smaller than vacancy flux at the lower boundary of cell A. since the vacancy flow is in the same direction as current direction (from top to bottom), this means more vacancy is leaving out cell A than coming in and there exists a positive vacancy flux divergence at cell A. The mass accumulation at cell A and the whole upper part of solder joint will results in expansion. The opposite is happens for the lower part of solder. In this simulation, since the vacancy flux boundary conditions of solder joint and copper plates are set up to allow for vacancy inter diffusion, the main deformation is not determined by the blocking boundary conditions , instead it is determined by current density gradient or so-called current crowding effect (Tu 2003).

Relative displacements along y direction (V field) between Points C and D

(points shown in Figure 52 (e)) are shown in Figure 53. The simulation gives good prediction for V field evolution and distribution. Also simulation gives close prediction result for strain at y direction as shown in Figure 54. The black triangles in Figure 53 and Figure 54 are from Moiré results.

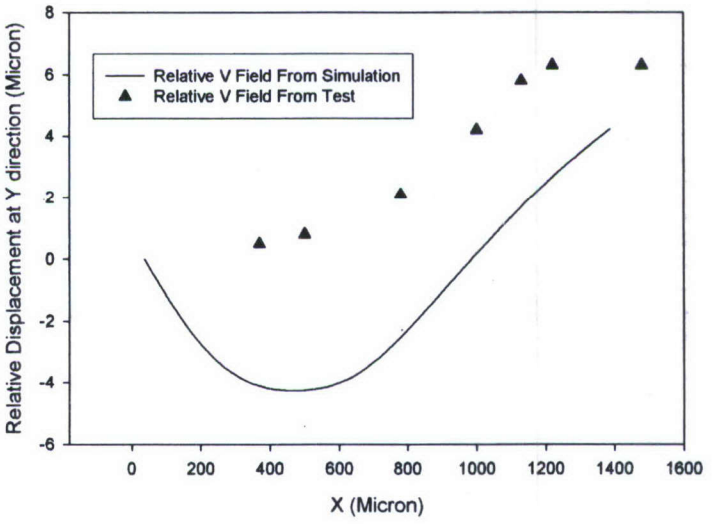

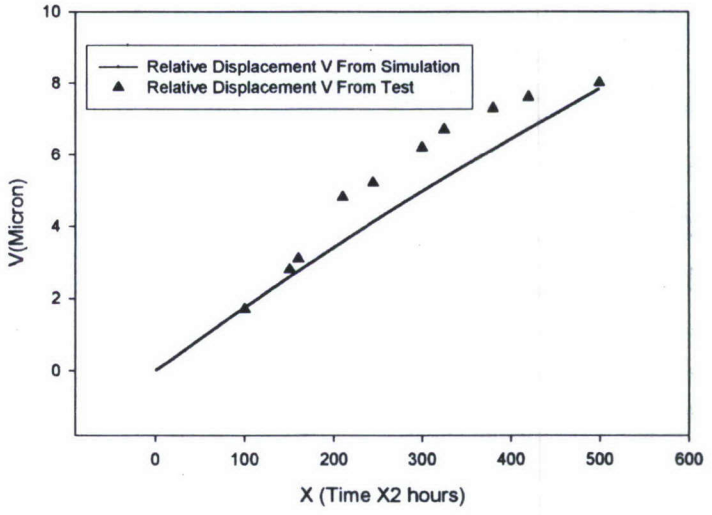

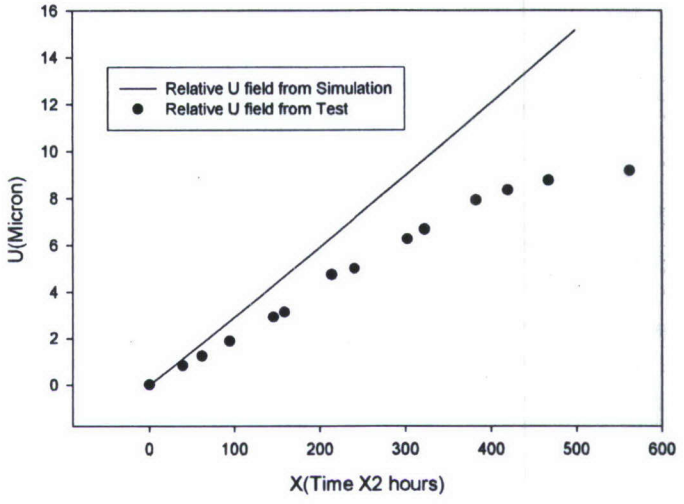

Figure 53 (a) Relative V Field Distribution along Y Axis between Points D and C after 600 hours

(b) Relative V Field Displacement Evolution between Points D and C

(c) Relative U Field Displacement Evolution between Points A and B

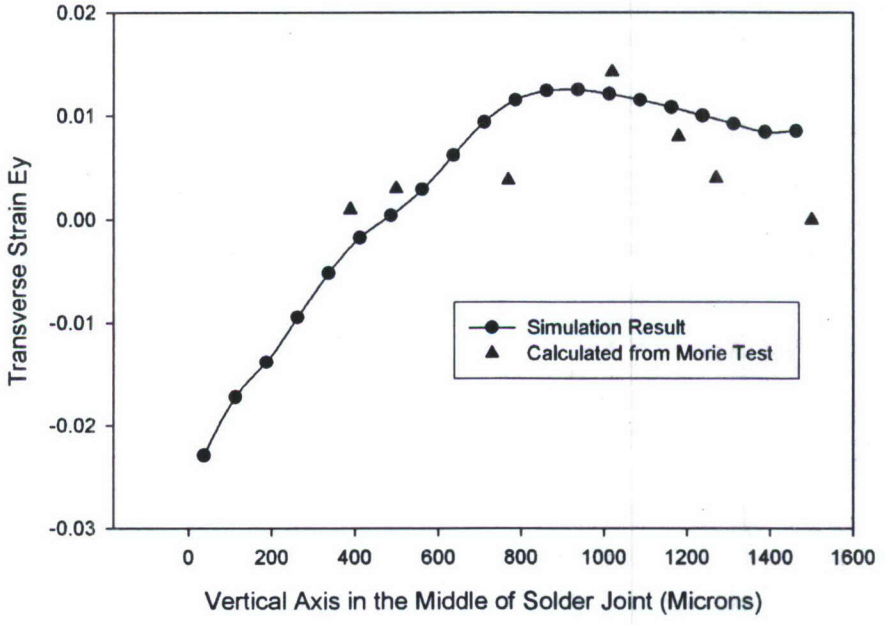

Figure 54 Strain_Y Distribution Along Line CD after 600 Hours

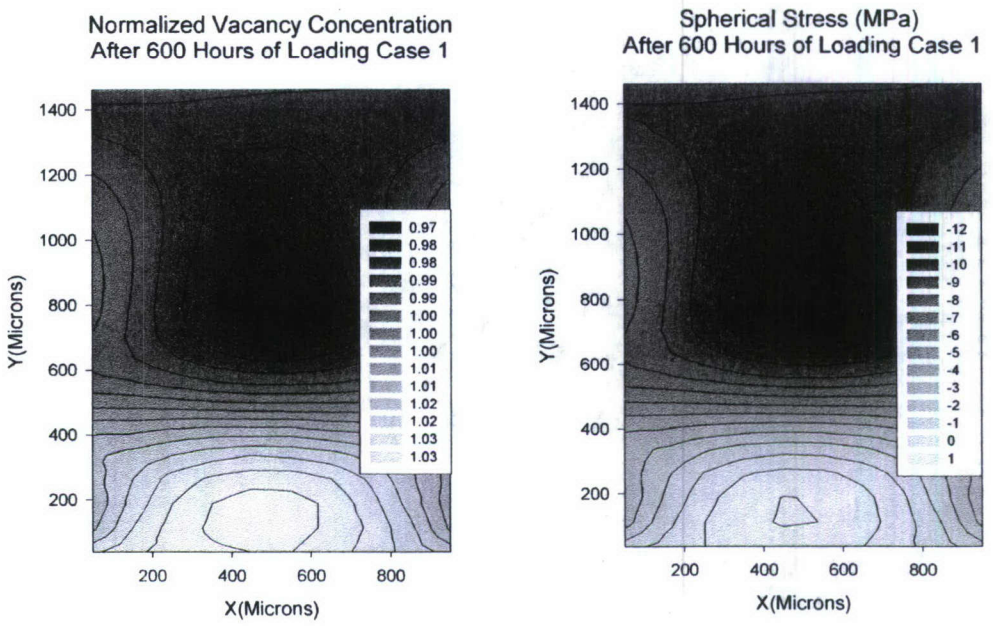

Figure 55 Normalized Vacancy Concentration and Spherical Stress Simulation Results after 600 Hours

Blech (1976) was the first to prove the existence of counter vacancy flow by spherical stress and vacancy gradient during electromigration. From Figure 55 the direction of vacancy gradient and spherical stress gradient can be extracted directly, which are in the opposite direction of electrical current driving force. In order to estimate the magnitude generated by those three factors (vacancy concentration gradient, stress gradient and electrical current driving force), a simple calculation is performed to calculate the mean forces. The gradients are calculated based on the data provided by Figure 55 as follows:

Vacancy concentration gradient force; $\nabla c = \frac{1.03 - 0.90}{-1500} = -8.67 \times 10^{-5} (1/\mu m)$

Stress gradient force $\frac{cf\Omega}{kT} \nabla \sigma_{spherical} = \frac{1.0 \square 0.6 \square 2.71 \times 10^{-11}}{1.38 \times 10^{-11} \square 300} \frac{1-(-12)}{-1500 \mu m} = -3.405 \times 10^{-5} (1/\mu m)$

Electrical current field force $\frac{Z^* e}{kT}(-\rho \mathbf{j})c = \frac{10 \square 1.602 \times 10^{-19}}{1.38 \times 10^{-11} \square 300} \square 1.15 \times 10^{11} \square 1.12 \times 10^{-4} \square 1.0$

$= 4.984 \times 10^{-3} (1/\mu m)$

The counter flow of concentration gradient and spherical stress gradient is only 2.4 percent of electrical current driving force according to above calculations. This is because of the dimension of the solder joint is large compared to 100 microns diameter found in flip chip solder joints. Diffusion in the bigger solder joints takes a much longer time and also the gradient depends on height of the solder joint. Moreover the non blocking boundary conditions contribute to this small gradient of force and vacancy concentration. So the critical stress points as stated in Blech's paper can not be reached in this system. But this does not mean that steady state can not be reached, the solder joints will reach a steady state once all the diffusion caused deformations cease to grow inside the solder. At the steady state although vacancy flux still exists, the vacancy flux divergence is zero everywhere.

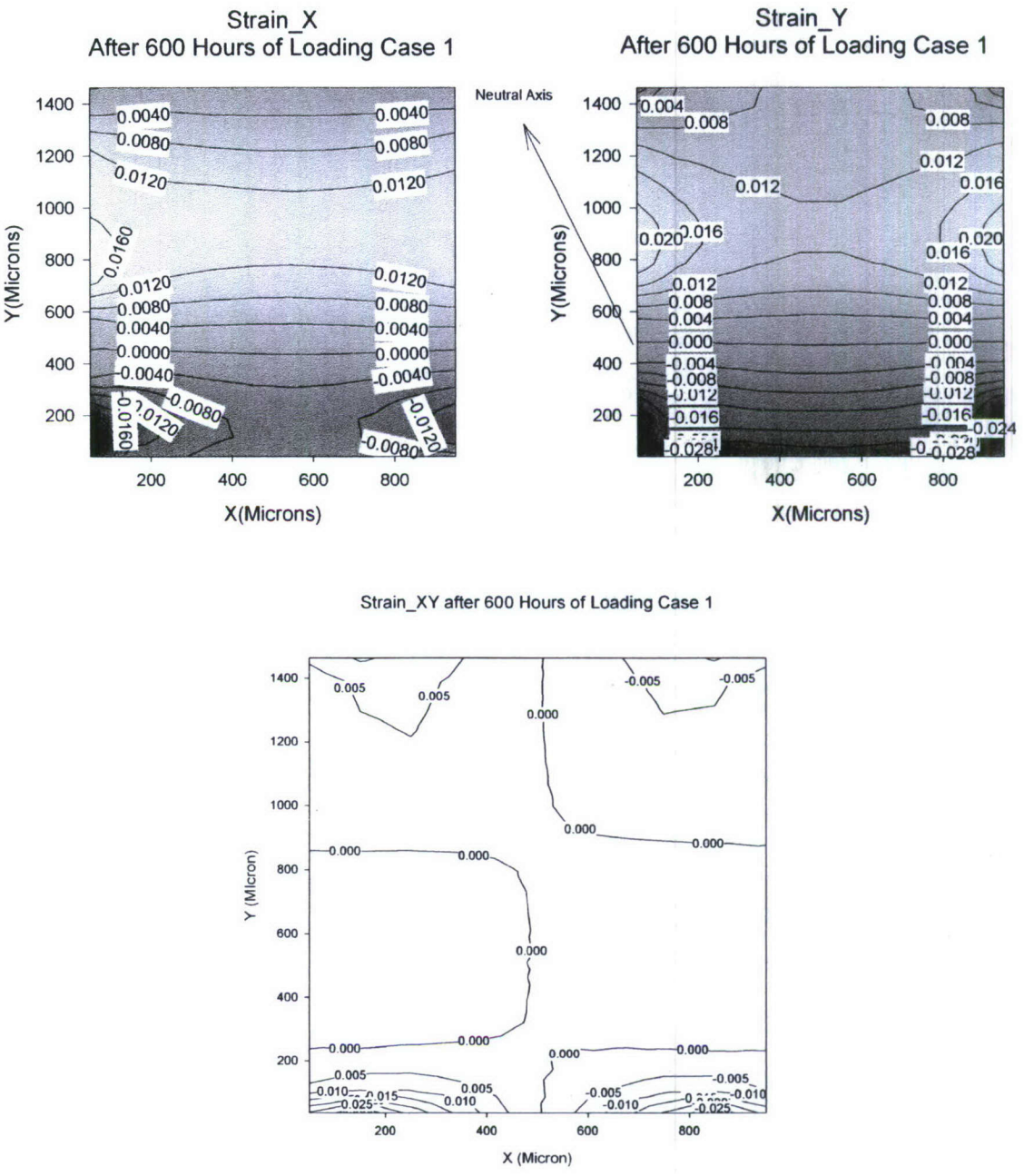

Figure 56 Total Strain Field Distributions after 600 Hours of Current Stressing

Figure 56 shows the normal strain field in X and Y direction as well as the shear strain field. Shear strain is highly localize at the corners of solder joints and is very small at other part of solder joint.

In Figure 56, the location where the strains at X and Y direction both equal to zero is shown as neutral axis. This corresponds to y=0.5 mm where current density gradient is zero. This again proves that the deformation in this case primary due to current density gradient

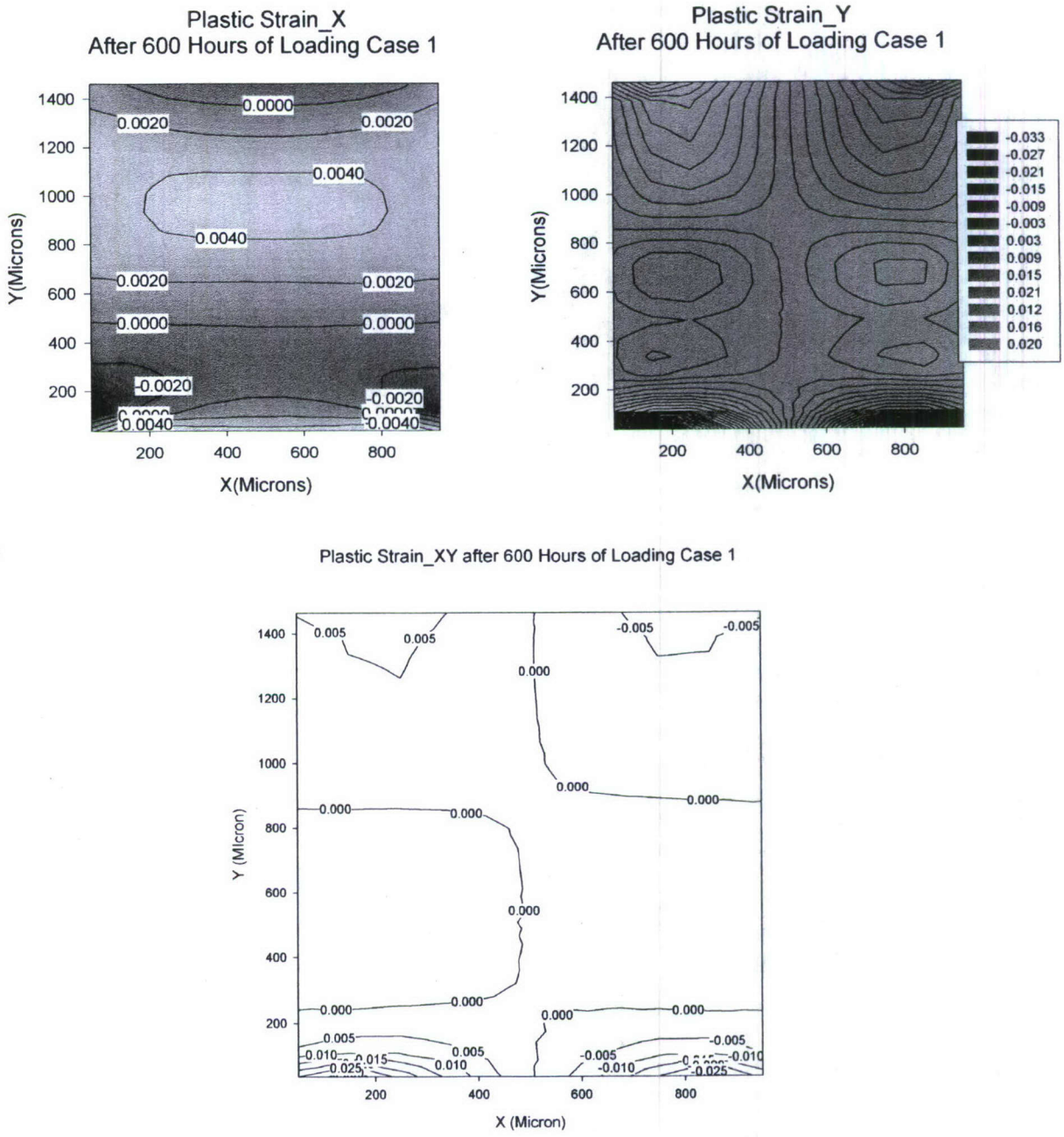

Figure 57 Plastic Strain Deformation Fields after 600 Hours

The biggest advantage of the proposed model is taking into accounts inelastic material behavior. Figure 57 shows the plastic strain at X, Y direction and plastic shear strain. The major plastic strain direction is on Y direction which corresponds to major loading direction. The maximum plastic strain of Y is on the order of 3.3 percent. Plastic shear strain appears to be highly localized.

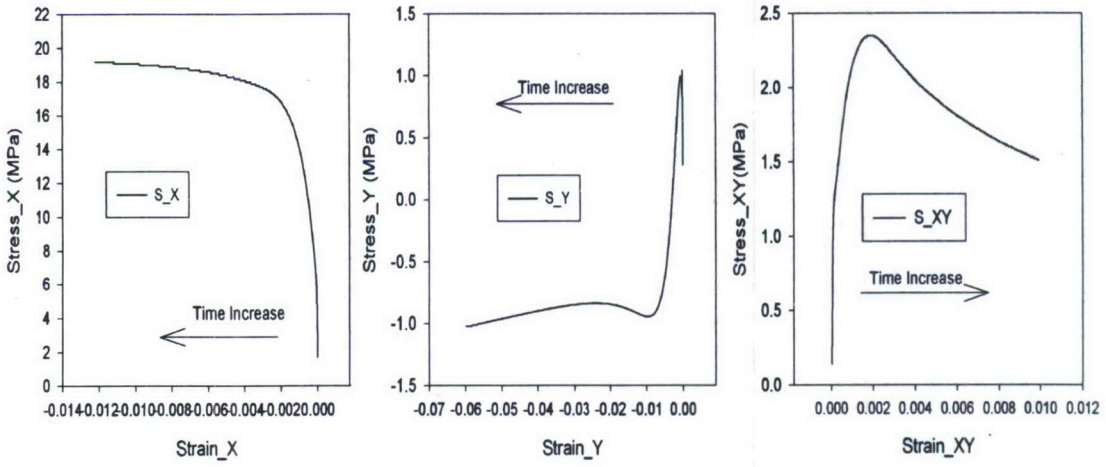

Figure 58 Strain-Stress Evolutions for 1000 Hours Simulation

Using viscoplastic constitutive model stress and strain evolution was simulated for 1000 hours. The results are shown in Figure 58. The stress and strain data shown in Figure 58 is for point C at Figure 52. Here tension stress is positive and compression is negative. Mass depletion happens at point C due to current direction and current crowding. Since the confinement of copper plate in X direction is very strong, the stress in X direction is major force here and it resists the contraction of solder and appears as tension force. Stress in Y direction

appears tension first due to the confinement at Y direction then it turns into compression. This can be explained as follows. Two copper plates can be viewed as two cantilever beams, on Y direction, it allows the solder to deform vertically but horizontal they provide much stronger confinement. As time evolves, eventually stress in Y direction is dominated by the stress in X direction due to Poisson effect and appears compression. The stress at X direction is one order of magnitude larger than stress at Y direction from Figure 58. Shear stress strain curve appears softening due the viscoplastic nature of stress relaxation.

3.3.4 Numerical Simulation Case 2

In order to further verify the numerical model, another simulation is performed based on the test sample configuration. The current density in case 2 is smaller than case 1 and the current crowding effect is weaker than case 1. The current loading profile for loading case 2 is as follows;

The thickness distribution along Y axis is

$$W_{thickness} = 0.025 \times (1 + 0.5 \times (\frac{y - 0.1}{0.1})^2)$$

average current density is 6000 A/cm^2. The current density distribution is

$$j = 0.6 \times 10^4 / (1 + 0.5 \times (\frac{y - 0.1}{0.1})^2) \, (A / cm^2)$$

The neutral axis is around y=1mm from the bottom of the solder joint.

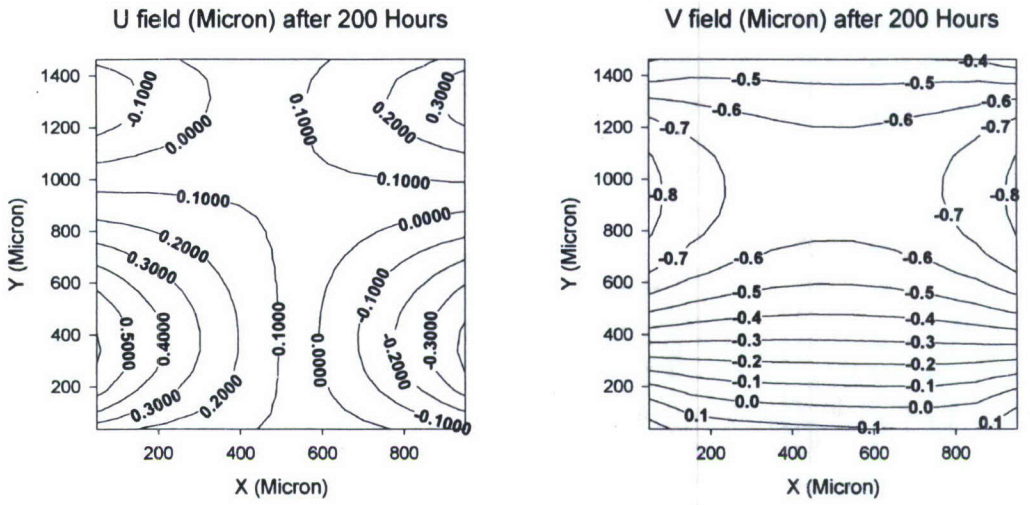

Figure 59 Displacement Fields Distribution for Solder Joint 2 after 200 Hours

The displacement field shown in Figure 59 shows similar shape as solder joint 1, the upper part of solder joint (anode) is in expansion and lower part of solder joint (cathode) is in contraction at X direction. The relative displacement between points C and D after 200 hours (points are shown in Figure 52) is 0.5360 μm from simulation results and Moiré measurement is 0.834 μm . Relative displacement between points A and B is 0.5233 μm and Moiré measurement value is 0.834 μm . Since precision of Moiré Interferometry limited by the frequency of the diffraction grating (1200 lines/mm) which is 0.417 μm per fringe order, the discrepancy between test and simulation is within the error range of moiré interferometry technique. The displacement in case 2 is smaller than case 1 because of current density and current density gradient are both smaller than case 1.

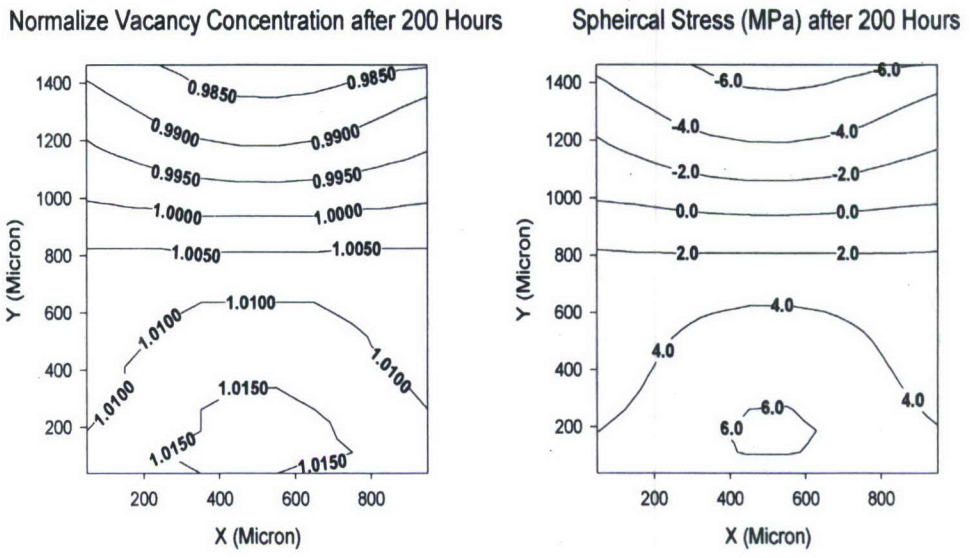

Figure 60 Normalize Vacancy Concentration and Spherical Stress for Solder 2 after 200 Hours

Normalized vacancy concentration and spherical stress distributions after 200 hours of current stressing for case 2 are shown in Figure 60. The driving forces by spherical stress gradient and vacancy gradient are on the opposite direction of current driving forces as expected. Figure 61 shows the strain field including total strains and plastic strains for solder 2 after 200 hours. Around y=1mm horizontal line, strains are zero as expected since at this location the gradient of current density is zero. The order of plastic strain and shear strain are in the range of 1×10^{-4}. The total strain fields except shear plastic strain are on the order of 1×10^{-3}.

Figure 62 shows the total strain and stress evolution curves of solder 2 for 250 hours of current loading. All three components of stresses exhibit the same

hardening behavior after yielding. The mechanical behavior of lead free solder joints shown in Figure 58 with Figure 62 exhibit consistency.

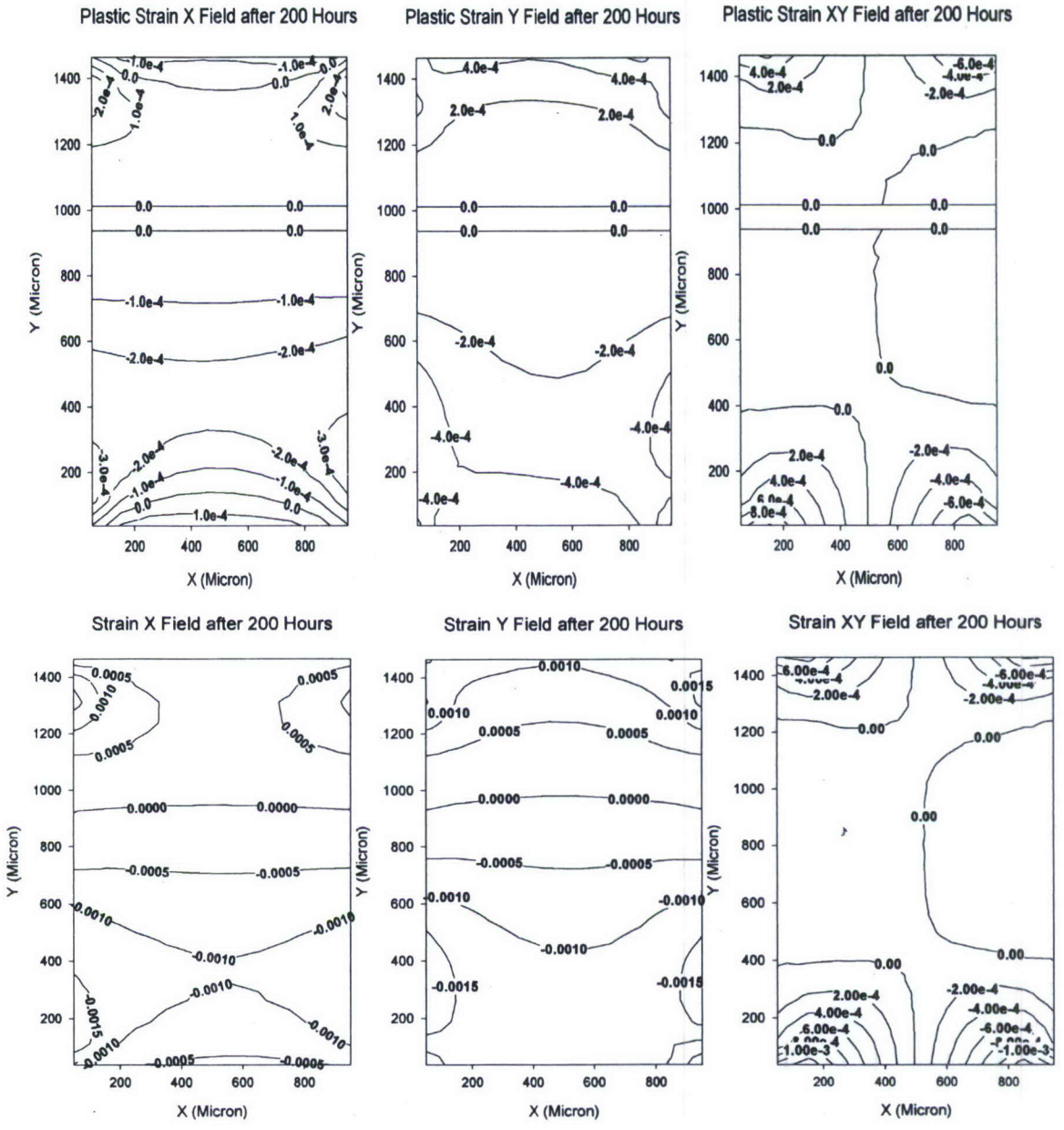

Figure 61 Strain Fields Distribution after 200 Hours for Solder 2

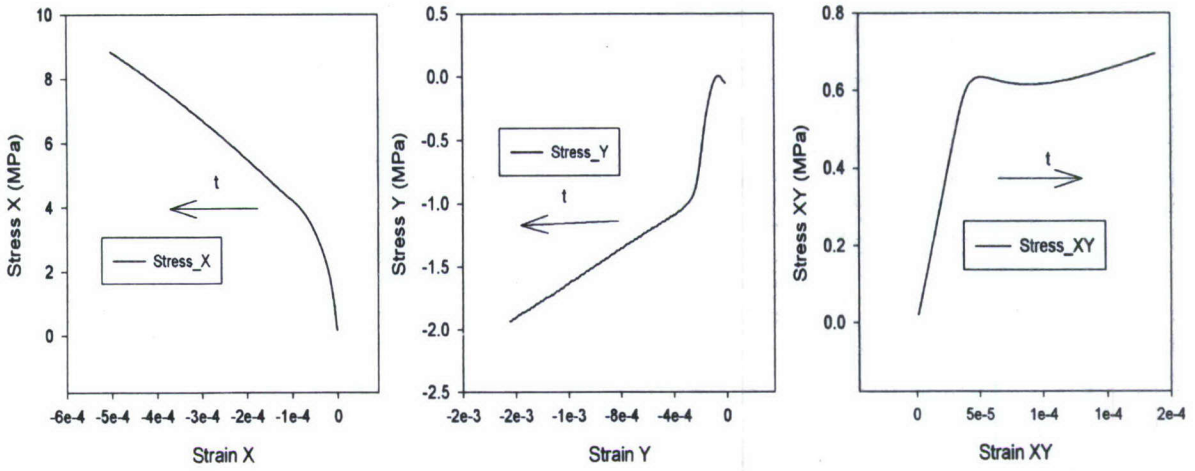

Figure 62 Stress-Strain Evolution of Solder 2 for 250 Hours Current Loading

3.3.5 Conclusions

FEM simulations for electromigration induced deformation for lead free solder are performed. By incorporating viscoplasticity into electromigration model, the model has the capability to simulate proper mechanical response under electromigration. The assumption of linear elasticity material behavior is not true for most of the cases under electromigration.

Two cases of lead free joints under different current density profiles are simulated and results are compared with experimental moiré interferometry results. The comparisons indicate that there is a very good match between simulation and test results. The simulation confirmed that current density gradient (current crowding) is the major source of flux divergence under non blocking boundary conditions. A 3-D electrical steady state analysis is performed to verify the current density profile.

With the proper consideration for material mechanical behavior, the stress

and vacancy distribution can be simulated with a high degree of confidence. This will improve the electromigration simulation accuracy and gives us a tool for prediction and verification of certain material properties related to electromigration, for example, the determination of effective charge number. Parametric study can be utilized to obtain value of effective charge number to match up with experimental observation.

The simulation of plastic strain and stress behavior also reveals material damage evolution process. Both stress and plastic strain are related to degradation of material. The simulation thus can be utilized to simulate material degradation process with certain damage criteria (Basaran et al 2003).

Numerical analysis error in this analysis may come from several aspects

1) Material parameters, like diffusivity and effective charge number values vary a lot in the literature. This can be improved by comparing more test and simulation cases to reach certain confidence in material parameters. Unfortunately there is very little data, if any, on electromigration at lead free solder joints.

2) Structural modeling, using plain strain idealization with thickness brings some degree of error. A 3-D analysis would improve the results, but it is time consuming.

3) Numerical error inherited in finite element simulation, which can be improved with finer mesh but also requires more computational time. This is verified by mesh sensitivity analysis conducted for aluminum electromigration cases.(Lin and

Basaran 2004)

4) Microstructure evolution and its influence are not taken into account in the current model.

Chapter 4 Thermodynamic Damage Formulation and Implementation

Equation Chapter 4 Section 1

4.1 Introduction

Electromigration failure has been under great attention since 1960s for thin film interconnection. With the downscaling of IC structure and Flip-Chip technology, solder joint failure caused by electromigration is expected to become a concern for the nanoelectronics. There are two types of failures within electromigration. On the anode side, the mass accumulation causes local compression and eventually mass will be squeezed out of material surface to form protrusions called hillocks. When the protrusions contact with circuit nearby, it causes short circuit failure. While on the cathode side, mass depletion causes tension and vacancy accumulation. Voids which nucleate under tension stress will grow and coalesce until causing circuit failure. The second failure mechanism is the main failure phenomenon and under extensive research.

Electromigration is a major concern for solder joints in microelectronics even when the current density level at solder joints is two orders of magnitude smaller than what is in VLSI interconnects. If we consider electromigration driving force

$F_{em} = Z^* e \rho j$, where Z^* is the effective charge number of electromigration, e is the charge of an electron , ρ is resistivity and j is current density, the effective charge number and resistivity of solder are both one order of magnitude larger than Al and Cu thin film(Callister 1996). Thus the electromigration in solder joints has the same amount of driving force as in thin film. Besides that, melting temperature of solder (approximately $200^{\circ}C$) is much smaller than Cu and Al and exhibits viscoplastic effect under service condition, this means the contribution of stress gradient counter balance force is smaller in solder joints and also plastic strain accumulation in solder is much larger than thin film.

In reliability prediction Black's equation is used for extrapolating accelerated experimental results to service condition. Black's (Black 1967) equations gives the relationship between Median Time to Failure (MTF) and current density as $MTF \propto j^{-2}$ and it also defines the activation energy. Other researchers proposed different current density exponent values ranging from 1 to 15(Shatzkes and Lloyd 1986) according to their own experimental. Joule heating effects is believed to be one cause of such discrepancy. While grasping the essence of electromigration failure by defining most critical parameters temperature and current density, Black's equation leaves out many important factors such as material mechanical properties, boundary condition, geometrical details and current crowding. As an empirical equation, Black's equation also can not show the different failure mechanism presented with different materials and boundary

conditions. Since Black's equation can only used as a general guide for failure prediction. In order to investigate different material behavior under various boundary conditions, Computational simulation of damage process is needed. This damage formulation will be embedded into a general finite element simulation for coupled displacement-diffusion process.

Although driving force for void growth is well understood, the void nucleation has received very little attention (Gleixner et al 1997). Void nucleation is a complex process and due to its inherent stochastic nature, the numerical simulation of void nucleation is still quantitatively difficult. Gleixner used thermodynamics and kinematic theory to calculate void nucleation rate (Gleixner and Nix 1996;Gleixner et al. 1997). Gleixner shows that void nucleation due to vacancy condensation is not expected to occur in passivated aluminum line unless there are other mechanisms which have extremely low barrier energy. One possibility as pointed out by Gleixner is flaws at metal/passivation interface. In Gleixner's calculation, spherical stress is estimated and void nucleation rate is calculated based on spherical stress value.

The void nucleation not only depends on spherical stress but also depends on effective stress which is von-Mises stress for metal. The most commonly used continuum model for void nucleation is due to Argon(Argon et al 1975), The decohesion critical stress is defined as a critical combination of two stresses:

$$\sigma_c = \sigma_m + \sigma_e \qquad (4\text{-}1)$$

where σ_e is the effective stress, given by

$$\sigma_e = \sqrt{1/2}\left[(\sigma_1 - \sigma_2)^2 + (\sigma_2 - \sigma_3)^2 + (\sigma_1 - \sigma_3)^2\right]^{1/2} \qquad (4\text{-}2)$$

and σ_m is mean spherical stress. For void growth, Rice and Tracey (1969) showed that rate of change of void under triaxial stress is related to principle strain rate. Above formulations that relate void nucleation and growth are based on fracture mechanics under remote stress fields. Moreover, Argon(1975) and Rice and Tracy(1969) assume that there is no diffusion in the solid. Their definition of void formation is strictly for thermomechanical forces, which differ greatly from electromigration.

The stress field under electromigration process due to the interaction between diffusion and confined boundary condition is the real driving force for void nucleation. If there is no confinement of boundaries, such as in the 'drift velocity' measurement in Blech's(Blech 1976) experiments, there is no void nucleation, since there is no stress field created due to lack of confinement. Spherical stress level and vacancy concentration level are used as an index for void nucleation because of the confining boundary condition, but we should also include Von-mises stress since it is another indication for void nucleation. Plastic strain plays an important role in void nucleation. As pointed out by Goods and Brown (1978), there exists a critical strain for cavity nucleation. As a direct result

of grain boundary sliding and material hardening, a local stress concentration will decrease incubation time for void nucleation thus accelerate damage process.

In computational simulations, various damage parameters are used to indicate material degradation for electromigration failure. Since spherical stress is closely related to void nucleation, the choice of critical spherical stress value as an indication of void nucleation is natural. This is adopted by Shatzkes(1986), (Trattles et al 1994) and Park(1999). The usage of critical vacancy concentration is the same as spherical stress since vacancy concentration and spherical stress are corresponding to each other through thermodynamics equilibrium. Sasagawa(2001) instead used atomic flux divergence as an damage parameter.

A thermodynamic based damage formulation was originally proposed by Basaran et al(1998), Basaran and Tang(2002), Nie and Basaran(2006) and was successfully implemented in low cycle fatigue failure predictions. Based on thermodynamics and continuum damage mechanics, this model has its unique advantage. A further development of this model to include electromigration effect into this general damage model is natural choice. The new model will unify electrical, mechanical, thermal field damage based on thermodynamics basic theory. In the mean time, this damage model will include the most important features which will affect material damage process including stress, plastic strain, diffusion, boundary conditions, etc. The model will be coupled into the FEM simulation presented in previous chapter and compared with experimental result

for verification.

4.2 Damage Mechanics Formulation

Before developing damage formulation, a brief review of the electromigration basic flux equation is necessary.

$$\frac{\partial C_v}{\partial t} = -\vec{\nabla} \cdot \vec{q} + G \qquad (4\text{-}3)$$

$$\vec{q} = -D_v[\vec{\nabla} C_v + \frac{C_v Z^* e}{kT}(-\rho \vec{j}) - \frac{C_v}{kT}(-f\Omega)\vec{\nabla}\sigma + \frac{C_v Q^*}{kT}\frac{\vec{\nabla} T}{T}] \qquad (4\text{-}4)$$

combined these two equations yield

$$\frac{\partial C_v}{\partial t} = D_v[\nabla^2 C_v - \frac{Z^* e \rho}{kT}\vec{\nabla} \bullet (C_v \vec{j}) + \frac{f\Omega}{kT}\vec{\nabla} \bullet (C_v \vec{\nabla}\sigma) + \frac{Q^*}{kT^2}\vec{\nabla}(C_v \nabla T)] + G \qquad (4\text{-}5)$$

where

C_v, vacancy concentration

D_v, vacancy diffusivity

$\vec{q}$, vacancy flux vector

Z^*, vacancy effective charge number

e, electron charge

ρ, metal resistivity

$\vec{j}$, current density vector

f, vacancy relaxation ratio, the ratio of the volume of an atom and the volume of a vacancy

Ω , atomic volume

Q^* heat of transport, the isothermal heat transmitted by moving the atom in the process of jumping a lattice site less the intrinsic enthalpy

k, Boltzman's constant

T, absolute temperature

$\sigma = trace(\sigma_{ij})/3$, hydrostatic or spherical part of the stress tensor, (Sarychev and Zhinikov 1999)

G, vacancy generation rate,

$$G = -\frac{C_v - C_{ve}}{\tau_s},$$

C_{ev} , thermodynamic equilibrium vacancy concentration

$$C_{ve} = C_{v0} e^{\frac{(1-f)\Omega\sigma}{kT}}$$

C_{v0} , equilibrium vacancy concentration in the absence of stress

τ_s , characteristic vacancy generation/annihilation time

If we define $C \equiv C_v / C_{v0}$ as the normalized concentration, then the vacancy diffusion equation could be re-written as

$$\frac{\partial C_v}{\partial t} = D_v[\nabla^2 C - \frac{Z^* e\rho}{kT}\vec{\nabla}\bullet(C\vec{j}) + \frac{f\Omega}{kT}\vec{\nabla}\bullet(C\vec{\nabla}\sigma) + \frac{Q^*}{kT^2}\vec{\nabla}(C\vec{\nabla}T)] + \frac{G}{C_{vo}} \quad (4\text{-}6)$$

where, initially, $C = 1 (\text{or } C_v = C_{v0})$.

The vacancy can be considered as a substitutional species at the lattice site with a smaller relaxed volume than the volume of an atom. When a vacancy switches lattice site with an atom or a vacancy is generated/annihilated at a grain

boundary local volumetric strain occurs. Proposed by Sarychev (1999), the vacancy causes volumetric strain in the metal, because the volume of the vacancy is different than the volume of the atom. This volumetric strain is composed of two parts, ε_{ij}^{m}, the volumetric strain due to vacancy flux divergence, and ε_{ij}^{g}, the volumetric strain due to vacancy generation. Since diffusion is a time dependent process, these volumetric strains are naturally expressed in the form of strain rates,

$$\dot{\varepsilon}_{ij}^{m} = \frac{1}{3} f \Omega \vec{\nabla} \cdot \vec{q} \delta_{ij} \qquad (4\text{-}7)$$

$$\dot{\varepsilon}_{ij}^{g} = \frac{1}{3}(1-f)\Omega G \delta_{ij} \qquad (4\text{-}8)$$

where δ_{ij} is the Kronecker's delta.

Thus, the combined volumetric strain rate due to current stressing is:

$$\dot{\varepsilon}_{ij}^{elec} = \dot{\varepsilon}_{ij}^{m} + \dot{\varepsilon}_{ij}^{g} = \frac{\Omega}{3}[f\vec{\nabla} \cdot \vec{q} + (1-f)G]\delta_{ij} \qquad (4\text{-}9)$$

The total volumetric strain rate due to current stressing is then:

$$\dot{\varepsilon}^{elec} = \Omega[f\vec{\nabla} \cdot \vec{q} + (1-f)G] \qquad (4\text{-}10)$$

By analogy to thermal strain (which is the volumetric strain caused by temperature variation), the volumetric strain caused by the current stressing is superimposed onto the strains tensor with strains due to other loadings, thus total strain can be given by:

$$\varepsilon_{ij}^{total} = \varepsilon_{ij}^{mech} + \varepsilon_{ij}^{therm} + \varepsilon_{ij}^{elec} \qquad (4\text{-}11)$$

where ε_{ij}^{total} is the total strain tensor, ε_{ij}^{mech} is the strain due to mechanical

loading, ε_{ij}^{therm} is the strain due to thermal load, and ε_{ij}^{elec} is the volumetric strain due to electromigration.

Thermodynamics of Damage Evolution Due to Electromigration

Statistical mechanics gave a precise meaning to disorder and established the connection between disorder and entropy by the following relation:

$$s = k \ln W \qquad (4\text{-}12)$$

Where s *is* the entropy of the system, *k* is the Boltzmann's constant and *W* is the disorder parameter, which is the probability that the system will exist in the state it is relative to all the possible states it could be in.

The entropy of a unit volume then can be given as:

$$s = N_0 k \ln W \qquad (4\text{-}13)$$

From the above equation, we can write:

$$W = e^{s/N_0 k} \qquad (4\text{-}14)$$

If we select an initial reference state of the solid body with disorder W_0; then the change in disorder at any arbitrary time with respect to the initial reference state is given by $\Delta W = W - W_0 = -(e^{s_0/N_0 k} - e^{s/N_0 k})$ (4-15)

Let us define a variable *D* as the ratio of the change in disorder parameter to the

original reference state disorder parameter defined as follows:

$$D = D_{cr}\left(\frac{\Delta W}{W_0}\right) = D_{cr}\left(1 - e^{(\frac{s_0}{N_0 k} - \frac{s}{N_0 k})}\right) \qquad (4\text{-}16)$$

D_{cr} is the critical damage parameter used to define the failure point. It can also be used in a function form to correlate entropy production with specific mechanical property degradation. But in this work it is only used as critical damage parameter.

Expanding the exponent term in this equation to Taylor's series, and ignoring the higher order terms, yields the following simplification:

$$D = D_{cr}\left[1 - e^{\frac{-\Delta s}{N_0 k}}\right] \qquad (4\text{-}17)$$

Using principles of continuum damage mechanics (4-17) can be implemented in stress-strain relations by, Lemaitre and Chaboche (Lemaitre 1996)

$$d\sigma = (1 - D)\, C\, d\varepsilon \qquad (4\text{-}18)$$

where $d\sigma$. is the incremental effective stress tensor, C is the tangential material constitutive tensor, and $d\varepsilon$. is the incremental total strain tensor.

According to the hypothesis in equation (4-17) when change in entropy Δs is equal to zero the material is at original state hence D is equal to zero. In this state there is no additional disorder with respect to the original state. When Δs is equal

to infinity material must fail according to the second law of thermodynamics and D will be equal to D_{cr}. In reality material fails (or considered to be failed) long before entropy change becomes infinity. In most engineering applications failure point is defined at a stage long before actual collapse of the structure occurs. There is always a factor safety. In traditional damage mechanics D value ranges between zero (at initial state) and one (at final collapse state). Actually failure definition can vary from application to application, owing to the fact that the factor of safety value is different in each engineering application. In Equation (4-17) D_{cr} allows defining failure point with respect to the problem at hand.

Equation (4-17) provides an evolution criterion for degradation of the system with respect to the intrinsic state variable entropy, which is defined at macro level. In the finite element formulation entropy is computed at each Gauss point, and the virtual work equation is written for the entire system not for a discreet lattice point, entropy is a variable that bridges micro behavior (atomic flux) with macro response (effective stress). Traditionally Weibul function is used by the dislocation mechanics community and damage potential surface is used by the researchers who belong to phenomenological modeling school of thought. Based on our laboratory experience, Basaran and Tang [5], both Weibull function and damage potential surface are unattractive for engineering use due to extensive testing needed to find the necessary constants. The proposed model

does not require a potential surface, there are no curve fitting material parameters involved just the entropy production rate.

At this point we need to answer the fundamental question, which is, does all entropy change contribute to damage? If we inspect the traditional entropy production equation, we can see that entropy change happens in two categories, one is caused by the entropy flowing into the system and the other one is due to the internal entropy production. We may argue that only the internal entropy production leads to degradation of the system, which we call as damage. The relation between entropy production rate and entropy can be given by,

$$\Delta s = \int_{t_0}^{t} \gamma dt \qquad (4\text{-}19)$$

Entropy Production for an Irreversible Process

In this section the entropy production rate function will be derived in a way appropriate for implementation in equation(4-19). In this section for the sake of completeness, and clarity, some obvious thermodynamics relations are stated.

According to the second law of thermodynamics for any macroscopic system the entropy, S, of the system is a state function.

The variation of the entropy, dS, may be written as the sum of two terms

$$dS = dS_e + dS_i \qquad (4\text{-}20)$$

Where dS_e is the entropy supplied to the system and dS_i is the entropy

produced inside the system. The second law of thermodynamics states that dS_i must be equal to zero for reversible and positive for irreversible processes.

$$dS_i \geq 0 \qquad (4\text{-}21)$$

Classical thermodynamics deals with the reversible process for which the internal entropy production is zero. In the thermodynamics of irreversible processes, the objective is to relate the internal entropy production to the various irreversible phenomena within a solid continuum. For this purpose, we need to establish the local form of entropy, as

$$S = \int_V \rho s dV \qquad (4\text{-}22)$$

$$\frac{dS_e}{dt} = -\int_\Omega \mathbf{J}_{s,tot} \bullet d\Omega \qquad (4\text{-}23)$$

$$\frac{dS_i}{dt} = \int_V \gamma dV \qquad (4\text{-}24)$$

Where s is the entropy per unit mass, $\mathbf{J}_{s,tot}$ is the total entropy flow per unit area and unit time, and γ the entropy source strength or entropy production per unit volume per unit time.

Using the local form of entropy, we can get the local form of the variation of entropy as follows,

$$\frac{\partial \rho s}{\partial t} = -div\mathbf{J}_{s,tot} + \gamma \qquad (4\text{-}25)$$

$$\gamma \geq 0 \qquad (4\text{-}26)$$

With the help of the material time derivative of the volume integral, which is given by

$$\frac{d}{dt} = \frac{\partial}{\partial t} + \mathrm{v} \bullet \mathrm{grad} \qquad (4\text{-}27)$$

equation (4-25) can be rewritten in a slightly different form as :

$$\rho \frac{ds}{dt} = -div\mathbf{J}_s + \gamma \qquad (4\text{-}28)$$

where the entropy flux, J_s, is the difference between the total entropy flux and a convective term:

$$\mathbf{J}_s = \mathbf{J}_{s,tot} - \rho s\mathbf{v} \qquad (4\text{-}29)$$

In obtaining (4-26) and (4-28), we have assumed that the definition given by equations (4-20) and (4-21) also hold for infinitesimally small parts of the system. This assumption is in agreement with the Boltzman relation where the entropy state is related to the disorder parameter via Boltzmann constant using statistical mechanics,

Entropy Balance equations:

Based on above definitions, the change in the mechanical properties (such as degradation) of the system can be related to the rate of change of the entropy. This will enable us to obtain more explicit expressions for the entropy flux and internal entropy production rate.

With the assumption of a caloric equation of state, Helmoltz free energy □in differential formcan be written as:

$$d\Psi = du - Tds - sdT \qquad (4\text{-}30)$$

where u is internal energy, T is temperature

(Here we use upper case Ψ to distinguish from the potential ϕ

Rearranging leads to

$$Tds = du - d\Psi - sdT \qquad (4\text{-}31)$$

in order to get the expression for free energy, we need to specify a function with a scalar value concave with respect to temperature T and convex with respect to other variables. Here we use:

$$\Psi = \Psi(\varepsilon, \varepsilon^e, \varepsilon^p, T, V_k) \qquad (4\text{-}32)$$

where V_k can be any internal variable determined by the specific application at hand and physical processes.

In small strain theory, the strain can be written in the form of their additive decomposition

$$\varepsilon - \varepsilon^p = \varepsilon^e \qquad (4\text{-}33)$$

so that:

$$\Psi = \Psi((\varepsilon - \varepsilon^p), T, V_k) = \Psi(\varepsilon^e, T, V_k) \qquad (4\text{-}34)$$

time derivative of the free energy is given by,

$$\frac{d\Psi}{dt} = \frac{\partial \Psi}{\partial \varepsilon^e} : \frac{d\varepsilon^e}{dt} + \frac{\partial \Psi}{\partial T} : \frac{dT}{dt} + \frac{\partial \Psi}{\partial V_k} : \frac{dV_k}{dt} \qquad (4\text{-}35)$$

From equation (4-31), we obtain:

$$T\frac{ds}{dt} = \frac{du}{dt} - \frac{d\Psi}{dt} - s\frac{dT}{dt} \qquad (4\text{-}36)$$

Using the first principle of thermodynamics the conservation of energy equation can be given by,

$$\rho\frac{du}{dt} = -div\mathbf{J}_q + \sigma : \mathbf{Grad}(\mathbf{v}) + \sum_k \mathbf{J}_k \bullet \mathbf{F}_k \qquad (4\text{-}37)$$

u is the total internal energy, $\mathbf{J_q}$ is the heat flux, □is the stress tensor, v is the rate of deformation, $\mathbf{J_k}$ is the diffusional flux of component k and F_k is the body force acting on the mass of component k.

Using the conservation of energy equation in the form given by Equation (4-37) and Eqs. (4-28) and (4-29), we can write the rate of change of entropy density as follows,

$$\rho\frac{ds}{dt}=\frac{1}{T}(-div\mathbf{J_q}+\sigma:\mathbf{Grad(v)}+\sum_k\mathbf{J}_k\bullet\mathbf{F}_k-\rho(\frac{\partial\Psi}{\partial\varepsilon^e}:\frac{d\varepsilon^e}{dt}+\frac{\partial\Psi}{\partial T}:\frac{dT}{dt}+\frac{\partial\Psi}{\partial V_k}:\frac{dV_k}{dt}-s\frac{dT}{dt}) \tag{4-38}$$

where

$$\sigma:\mathbf{Grad(v)}=\sigma:(\mathbf{D}+\mathbf{W}) \tag{4-39}$$

and **D** (symmetric) and **W** (skew symmetric) are the rate of deformation tensor and spin tensor, respectively.

Due to the symmetry of σ

$$\sigma:(D+W)=\sigma:D \tag{4-40}$$

For small deformation, we can make the following assumption

$$\sigma:\mathbf{D}=\sigma:\frac{d\varepsilon}{dt}=\sigma:(\frac{d\varepsilon^e}{dt}+\frac{d\varepsilon^p}{dt}) \tag{4-41}$$

Rearrange equation (4-38) and comparing with (4-28) we can get $\mathbf{J_s}=\frac{1}{T}\mathbf{J_q}$ and the following entropy production rate term

$$\gamma = -\frac{1}{T^2}\mathbf{J_q} \bullet Grad(T) + \frac{1}{T}\sum_k \mathbf{J}_k \bullet \mathbf{F}_k + \frac{1}{T}\sigma : \frac{d\varepsilon^p}{dt} + \frac{1}{T}(\sigma : \frac{d\varepsilon^e}{dt} - \rho\frac{\partial\Psi}{\partial\varepsilon^e} : \frac{d\varepsilon^e}{dt})$$
$$+ \frac{\rho}{T}(s + \frac{\partial\Psi}{\partial T})\frac{dT}{t} - \frac{\rho}{T}\frac{\partial\Psi}{\partial V_k} : \frac{dV_k}{dt}$$

(4-42)

In solids with internal friction all deformations cause positive entropy production rate $\gamma \geq 0$. (the Classius-Duhem Inequality)

Using the following relations,

$$\sigma = \rho(\partial\Psi/\partial\varepsilon^e) \qquad (4\text{-}43)$$

$$s = -\frac{\partial\Psi}{\partial T} \qquad (4\text{-}44)$$

we can simplify Equation (4-42) as follows,

$$\gamma = -\frac{1}{T^2}\mathbf{J_q} \bullet Grad(T) + \frac{1}{T}\sum_k \mathbf{J}_k \bullet \mathbf{F}_k + \frac{1}{T}\sigma : \dot{\varepsilon}^p - \frac{\rho}{T}\frac{\partial\Psi}{\partial V_k} : \frac{dV_k}{dt} \qquad (4\text{-}45)$$

or if the heat flux term J_q is replaced by

$$J_q = \frac{1}{T^2}C\left|Grad(T)\right|^2 \qquad (4\text{-}46)$$

where is C is the thermal conductivity tensor, the entropy production rate can be given by

$$\gamma = -\frac{1}{T^2}C\left|Grad(T)\right|^2 + \frac{1}{T}\sum_k \mathbf{J}_k \bullet \mathbf{F}_k + \frac{1}{T}\sigma : \dot{\varepsilon}^p - \frac{\rho}{T}\frac{\partial\Psi}{\partial V_k} : \frac{dV_k}{dt} \qquad (4\text{-}47)$$

We identify J_k in Equation (4-47) as $\vec{q}$ in Equation (2) and the effective driving force terms F_k as

$$F_k = \left[Z^* ej\rho + (-f\Omega)\vec{\nabla}\sigma - \frac{Q}{T}\vec{\nabla}T - \frac{kT}{C}\vec{\nabla}C \right] \qquad (4\text{-}48)$$

From equation (4-47), we can see that the irreversible dissipation includes two parts, the first term is called heat dissipation caused by conduction inside the system, while the second, third and fourth terms account for other irreversible processes in the system, we will call it intrinsic dissipation.

According to second law of thermodynamics all systems must fail when entropy is at maximum and the production rate is at minimum. Based on this law, entropy production rate given in the form shown in Equation (4-47) allows accounting for electromigration induced entropy production in the system. Because electromigration is an irreversible process and leads to failure of the system, we assume that it must fall within the laws of thermodynamics. Entropy production rate given in Equation (4-47) could be written in many different forms, but this form of this equation is the most appropriate for our purpose.

With the help of equations (4-47), and (4-48), we can write equation (4-17) as:

$$\Delta s = \int_{t_0}^{t} (\frac{1}{T^2} C \left| Grad(T) \right|^2 + \frac{C_v D_{effective}}{kT^2} (Z_l^* e \rho j - f \Omega \nabla \sigma + \frac{Q \vec{\nabla} T}{T} + \frac{kT}{C} \vec{\nabla} C)^2 + \frac{1}{T} \sigma : \varepsilon^p - \frac{\rho}{T} \frac{\partial \Psi}{\partial V_k} : \frac{dV_k}{dt}) dt$$

(4-49)

If we only consider the damage caused by electrical driving forces and disregard other factors such as stress gradient, temperature gradient, atomic vacancy concentration the damage evolution formula can be given by

$$D = D_{cr}\left[1 - e^{\frac{\int_{t_0}^{t} \frac{C_v D_{effective}}{kT^2}(Z^* e\rho j)^2 dt}{N_0 k}}\right] \qquad (4\text{-}50)$$

we assume that the solder joint has failed when the degradation reaches some critical value (e.g. it is 5% drop in electrical resistance of a solder joint in the U.S. microelectronics industry), defined as D_{cr}, the time required to reach the failure can be obtained from Equation (4-50) as:

$$t = \frac{N_0 T^2 k^2}{C_v D_{effective}(Z^* e\kappa j)^2} \ln \frac{1}{(1 - D_{cr})} \qquad (4\text{-}51)$$

From equation (4-50), we observe that the dependence on temperature is to the power of two. One may wonder why the time to failure is larger when the temperature is larger. The fact is that the diffusivity is going to change with temperature too. The relationship between the temperature and the diffusivity is represented by Arrnhenius function,

$$D_{effective} = D_0 e^{-\frac{Q}{kT}} \qquad (4\text{-}52)$$

Inserting the equation (4-52) into equation (4-50), we can get:

$$t = \frac{N_0 T^2 k^2}{N_l D_0 (Z_l^* e\kappa j)^2} (\ln \frac{1}{(1 - D_{cr})}) e^{\frac{Q}{kT}} \qquad (4\text{-}53)$$

The last term (exponent) dominates the temperature effect so the time to failure

decreases with temperature as expected.

Comparison with other models in the literature:

Equation (4-53) indicates that damage evolution in electromigration is related to the square of the current density, which was first proposed by Black(Black 1977):

$$t = \frac{wh}{Aj^2}\exp\frac{Q}{kT} \qquad (4\text{-}54)$$

where t is mean time to failure, w is the conductor width and h is the film thickness, Q is the activation energy, k is Boltzman constant and T is temperature, and the constant A is related to several factors such as,

1) the volume resistivity of the metal
2) the electron-free time between collisions or the electron free path and average velocity
3) the effective ionic scattering cross section for electrons
4) the frequency factor for self diffusion (e.g. aluminum in aluminum)

Shatzkes and Lloyd(Shatzkes and Lloyd 1986) , starting with following atomic flux assumption equation

$$J = D\left(\frac{Z^* e \kappa j}{kT} C_v - \frac{\partial C_v}{\partial x}\right) \qquad (4\text{-}55)$$

For a blocking boundary condition with the assumption of the time to failure is the time to achieve a specific vacancy concentration, they proposed the following time to failure equation:

$$t_f = \frac{2C_f k^2 T^2}{D_0 (Z^* e \rho j)^2} e^{\frac{\Delta H}{kT}} \qquad (4\text{-}56)$$

For thin films, Korhonen et al (Korhonen et al 1992) considered the stress gradient as counter force to electrical field forces, starting with the following atomic flux equation

$$J = \frac{C_v D}{kT} (\nabla(\sigma\Omega) + Z^*(\rho j)) \qquad (4\text{-}57)$$

They defined failure as the time to reach a critical hydrostatic stress value, "yield stress" for initiation of a void, for a blocking boundary condition, they proposed the following time to failure equation,

$$t_f = \frac{\pi \Omega k T}{4DB(\rho j Z^* e)^2} \qquad (4\text{-}58)$$

where B is applicable modulus, which depends on the elastic properties and the aspect ratio of the cross-section, other variables have the usual meaning as before.

It should be pointed out that these time to failure equations, may be able to predict the time to failure for thin films on thick substrate, yet these empirical equations cannot be used for solution of a boundary value or initial value problem

using finite element (or similar) method. Comparing (4-53) with (4-56), dependence of the mean time to failure on temperature and current density is the same, the difference is that (4-56) has a N_f term which is the critical vacancy concentration and while (4-53) has a critical damage term. In classical continuum damage mechanics the damage variable is defined by (Lemaitre 1996)

$$D = \frac{\delta S_d}{S} \qquad (4\text{-}59)$$

where δS_d is the void area on the principle surface and S is the original total surface area. If we treat the voids (accumulated atomic vacancies) as damaged area, we can see that the critical damage is related to critical vacancy concentration (if assuming that the void nucleation is caused by critical vacancy concentration) as it appeared in the equation (4-55).

Comparing equation (4-58) with equation (4-53), we can observe that the main difference is that the mean time to failure dependence on temperature is to the first power in equation (4-58). Korhonen et al (Korhonen et al. 1992) assumed that in confined metal line the lattice site vacancy concentration is related to stress change by the following relation

$$\frac{dC_v}{C_c} = \frac{-d\sigma}{B} \qquad (4\text{-}60)$$

As the stress reaches the critical value (yield stress), the atomic concentration also reaches a critical value and which can then be directly related to the critical

damage value (assuming that a critical vacancy concentration value need to be reached for void nucleation). It can be interpreted that critical damage value in the proposed model corresponds to critical vacancy concentration in Shatzkeyes and Lloyd model and critical stress in Korhonen model.

4.3 FEM Implementation

A general damage model based on thermodynamics is proposed and implemented in finite element method.

$$D = 1 - e^{\frac{-\Delta s}{N_0 k}} \qquad (4\text{-}61)$$

where

$$\Delta s = \int_{t_0}^{t} \left\{ \frac{1}{T^2} C \left| Grad(T) \right|^2 + \frac{C_v D_{effective}}{kT^2} \left[Z_l^* e \rho j - f \Omega \nabla \sigma + \frac{Q \vec{\nabla} T}{T} + \frac{kT}{C} \vec{\nabla} C \right]^2 + \frac{1}{T} \boldsymbol{\sigma} : \boldsymbol{\varepsilon}^{\mathrm{p}} \right\} dt \qquad (4\text{-}62)$$

and N_0 is unit molar volume and k is Boltzmann constant

C_v, vacancy concentration

D_v, vacancy diffusivity

Z^*, vacancy effective charge number

e, electron charge

ρ, metal resistivity

$\vec{j}$, current density vector

f, vacancy relaxation ratio, the ratio of the volume of an atom and the volume of a vacancy

Ω , atomic volume

T, absolute temperature

$\sigma = trace(\sigma_{ij})/3$,

$\boldsymbol{\sigma}$ is stress tensor and $\dot{\boldsymbol{\varepsilon}}_{\mathbf{p}}$ is plastic strain rate tensor.

This damage model has been successfully implemented to simulate cyclic temperature failure of solder joints and we have extended this model to simulate failure process of electromigration. The damage formulation accounts for damages from different processes. A finite element coupled diffusion-displacement analysis with nonlinear material properties is proposed by (Lin and Basaran 2004). In this section damage is coupled into the finite element formulation and simulation results are compared with experimental results.

4.3.1 Finite element formulation

The finite element formulation is presented in the precious chapter. The usage of nonlinear kinematic/isotropic hardening in this section will make formulation very lengthy and interested reader can obtain detail material integration formulation with regard to nonlinear kinematic/isotropic hardening from (Lubarda and Benson 2002). In simulation of strain caused by electromigration, Sarychev's physical model is used(Sarychev and Zhinikov 1999) .

4.3.1.1 Governing equations:

Electromigration is diffusion controlled mass transport process. It is governed by the following vacancy conservation equation which is equivalent to mass conservation equation.

$$\int_{v}(\mathbf{C_{v0}}\frac{\partial c}{\partial t}+\nabla\bullet\mathbf{q}-G)dV=0 \qquad (4\text{-}63)$$

where C_{v0} is equilibrium vacancy concentration in the absence of stress field,

c is normalized vacancy concentration and $c=\frac{C_v}{C_{v0}}$,

C_v is vacancy concentration,

t is time,

$\mathbf{q}$ is vacancy flux,

G is vacancy generation/annihilation rate.

Assuming that driving forces of vacancy flux are vacancy concentration gradient, electrical field forces, stress gradient and thermal gradient, the vacancy flux is given by (Sarychev and Zhinikov 1999;Basaran et al 2003)

$$\mathbf{q}=-D_vC_{v0}(\nabla c+\frac{Z^*e}{kT}(-\rho\mathbf{j})c+\frac{cf\Omega}{kT}\nabla\sigma_{spherical}+\frac{c}{kT^2}Q^*\nabla T) \qquad (4\text{-}64)$$

where D_v is vacancy diffusivity

$\sigma_{spherical}$ is spherical part of stress tensor, $\sigma_{spherical}=trace(\sigma_{ij})/3$

Q^* is heat of transport, the isothermal heat transmitted by moving the atom in the process of jumping a lattice site less the intrinsic enthalpy.

The stress-vacancy relationship is represented by vacancy generation/annihilation rate which is given by(Sarychev and Zhinikov 1999)

$$G = -C_{v0}\frac{c - C_{ve}}{\tau_s} \tag{4-65}$$

where $C_{ve} = e^{\frac{(1-f)\Omega\sigma_{spherical}}{kT}}$ is normalized thermodynamic equilibrium vacancy concentration.

τ_s is characteristic vacancy generation/annihilation time.

4.3.1.2 Viscoplastic Constitutive Model:

Tang et al(Tang and Basaran 2001) developed viscoplastic flow rule for solder alloys based on Kashyap and Murty(Kashyap and Murty 1981) model, where grain boundary sliding is the dominant mechanism, primary and steady state creep can be given by

$$\dot{\varepsilon}_{ij}^{vp} = \frac{AD_0Eb}{k\theta}\left(\frac{\langle F\rangle}{E}\right)^n\left(\frac{b}{d}\right)^p e^{-Q/R\theta}\frac{\partial F}{\partial\sigma_{ij}} \tag{4-66}$$

where the material parameters are defined as follows,

A: a dimensionless material parameter to describe the strain rate sensitivity.

$D_0e^{\left(\frac{-Q}{R\theta}\right)}$ is a diffusion coefficient where

D_0 is a frequency factor

Q is the creep activation energy for plastic flow

R is the universal gas constant = 8.314 J/K.mol = 8.314 N.mm/K.mol

θ: absolute temperature in Kelvin

E: Young's modulus

b: characteristic length of crystal dislocation (magnitude of Burger's vector)

k: Boltzmann's constant

d: average phase size

p: grain size exponent

n: stress exponent for plastic deformation rate, where 1/n indicates strain rate sensitivity.

Hardening laws

$$\dot{\alpha} = \sqrt{\frac{2}{3}}\gamma \qquad (4\text{-}67)$$

$$\dot{\mathbf{X}} = c_1 \dot{\boldsymbol{\varepsilon}}_{\mathbf{ij}}^{\mathbf{p}} - c_2 \mathbf{X}\dot{\alpha} \qquad (4\text{-}68)$$

where c_1 is linear kinematic hardening constant

c_2 is nonlinear kinematic hardening constant.

$$\mathbf{S} = \boldsymbol{\sigma} - \frac{1}{3} Tr(\boldsymbol{\sigma})\mathbf{1}$$

$\mathbf{X}$ is a back stress tensor defining the displacement of the center of the yield surface in the deviatoric stress space.

$K(\alpha)$ represents the isotropic hardening component defining the radius of the yield surface in stress space. It is a function of the hardening parameter α.

$$K(\alpha) = \sqrt{\frac{2}{3}} Y_0 + R_\infty \left[1 - e^{-c\alpha}\right] \qquad (4\text{-}69)$$

where Y_0 is initial yield stress,

R_∞ is isotropic hardening saturation value,

c is isotropic hardening rate.

4.3.2 Pb37/Sn63 Solder Alloy Material Parameters Determination

4.3.2.1 Mechanical material properties

Young's modulus and shear modulus are respectively(Basaran and Tang 2003):

$$G(T) = 24.28\text{-}0.029\ T(K) \qquad (4\text{-}70)$$

$$E(T) = 62.00 - 0.067T(K) \qquad (4\text{-}71)$$

The yield stress is measured for Pb37/Sn63 solder, and given by:

$$\sigma_Y(T) = 60.069 - 0.140T(K) \qquad (4\text{-}72)$$

Table 8 Kinematic and Isotropic Hardening Parameters

Parameter	Value
c_1 (MPa)	13.6
c_2	457.9
c	383.3
R_∞ (MPa)	37.47 – 0.0748 T (K)

Table 9 Flow Function Parameters

Parameter	Value
$D_0(cm^2/s)$	0.488

$b(\mathring{A})$	3.18
$d(\mu m)$	10.6
n	1.67
p	3.34
Q(KJ/mole)	44.7
A	$7.6x10^9$

Table 10 Other Materials Parameters

Temperature	373K
Vacancy relaxation time (Ts)	1.8E-3 s (Sarychev and Zhinikov 1999)
Diffusivity (D)	62.4 $\mu m^2 s^{-1}$
Effective charge number (Z*)	10
Resistivity (ρ)	1.450E11 $\mu m^3 s^{-3} A^{-2} kg$ (Pecht et al 1998)
Average vacancy relaxation ratio (f)	0.6(Sarychev and Zhinikov 1999)
Atomic volume of tin (Ω)	2.71E-11 μm^3
Initial vacancy concentration (C_{v0})	1.11E6 μm^{-3} (Balzer and Sigvaldason 1979)
Thickness	1 μm
Boltzmann constant (AK)	1.38E-11 $\mu m^2 s^{-2} K^{-1} kg$
Universal gas constant	8.314E6 $\mu m.s^{-2} kg.Mole^{-1}.K^{-1}$
Avogadro's number	6.02E23 $Mole^{-1}$
Atomic weight	20.14E12 $\mu m^3.Mole^{-1}$

4.3.2.2 Diffusivity and effective charge number determination:

Lattice diffusivity and grain boundary diffusivities for Pb38/Sn62 are given out by (Gupta et al 1998), (Mehrer and Seeger 1972) and (Decker et al 1977) as follows

Diffusant	$D_l^0 (10^{-5}\ m^2/s)$	$Q_l (kJ/mol)$	$\delta D_{i/b}^0 (10^{-15}\ m^3/s)$	$Q_{i/b} (kJ/mol)$
Pb	1.5	100	7000	77.0
Sn	4.1	99	700,000	84.8

Where D_l^0 is lattice diffusivity

$D_{i/b}^0$ is interface/grain boundary diffusivity

δ is grain boundary width, for most metals it is assumed to be 0.5nm(Gupta 1997),

Q_l is lattice diffusion activation energy

$Q_{i/b}$ is interface/grain diffusion activation energy.

According to (Gupta 1997), effective diffusivity is determined by

$$D_{Effe} = D_l + \frac{4\delta D_{b/i}}{L} \tag{4-73}$$

where D_l and $D_{b/i}$ follow Arrhenius type temperature dependence given by

$$D_l = D_l^0 e^{-\frac{Q_l}{kT}}$$
$$D_{b/i} = D_{b/i}^0 e^{-\frac{Q_{b/i}}{kT}} \tag{4-74}$$

and L is diameter of grain/phase size, it's value is estimated as 2 μm according to Ye et. al.(2003c).

Final calculation yields a value for D_{Effe} for Pb and Sn as

$$D_{Effe}^{Pb} = 2.307 \times 10^{-16} (m^2 / s)$$

$$D_{Effe}^{Sn} = 1.864 \times 10^{-15} (m^2 / s) \qquad (4\text{-}75)$$

respectively for Pb and Sn at temperature 373k.

From the diffusivity data presented above, the diffusivity of Sn is almost one order of magnitude larger than Pb at this temperature. In the analysis, the diffusivity of Sn will be used. The equilibrium vacancy concentration at a stress free state is reported as ${}^{C_{v0}}/_{C_a} = 3 \times 10^{-5}$ by Balzer and Sigvaldason (Balzer and Sigvaldason 1979) with $C_a = 3.69 \times 10^{22} / cm^3$ for pure tin.

Based on the relation of vacancy diffusivity and atomic diffusivity(Clement and Thompson 1995)

$$D_a C_a = D_v C_v \qquad (4\text{-}76)$$

at stress free state, D_v can be obtained as

$$D_v = 62.14 (\mu m^2 / s) \qquad (4\text{-}77)$$

Table 11 Effective charge number in the literature

	(Lee et al 2001)	(Lee and Tu 2001)	(Ye et al 2003a)

Temperature(° C)	120 °C	120 °C	100 °C
Current Density (A/cm^2)	$2x10^4$	$3.8x10^4$	$1.3x10^4$
Time (hrs)	324	39.5	37.5
*DXZ**	$2.16x10^{-11}$	$1.85x10^{-10}$	$5.62x10^{-10}$
*Z**	1.16	9.94	30.20

As pointed out by (Ye et al 2003b), thermomigration needs to be included in consideration when temperature gradient is on the order of 1000 $^0C/cm$. In this study *Z*=10* is chosen since it gives a better fit to the experimental data and simulation results..

4.3.3 Numerical Simulation

4.3.3.1 Samples Structure

The experimental tests of electromigration are conducted by (Ye et al. 2003a;Ye et al. 2003b;Ye et al 2003b) for flip chip modules produced at Motorola Lab. The schematic cross sections of test module and solder joints are shown in Figure 63. The under bump metallization (UBM) on silicon die side is electroless nickel (Ni). The diameter of the solder (Pb37/Sn63) joint is around 150 □*m* and the height is about 100 □*m*. The solder joints are encapsulated in the underfill between the silicon die and PCB. Among the modules tested, there are two different treatments of copper (Cu) plate surface: one with plated nickel barrier layer and one without.

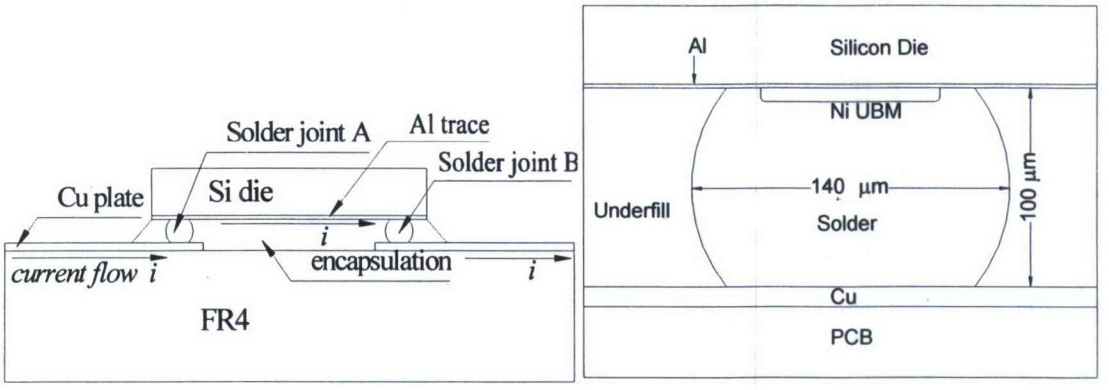

Figure 63 Cross Section of Test Module and Solder joints **(Ye et al. 2003a)**

4.3.3.2 Boundary Condition and Loading

Based on the structure of test module, plane strain element is used to simulate the solder joints. Also the boundary conditions used in simulation are,

a) Displacement boundary condition: All fixed at both sides for solder joints.

b) Diffusion boundary condition: Blocking boundary condition at both sides.

Blocking boundary condition for diffusion is defined because of a barrier layer of electroless Ni. On the Cu plate side, some modules do not have this Ni layer. These modules without Ni barrier layer will not be simulated due to the lack of experimental data to determine the right boundary condition.

Electrical current field is not uniform in solder joints. Due to the size difference with thin layer of aluminum trace and solder interconnections, the current density in the thin aluminum trace is at least one order of magnitude larger than in the solder. When the current is entering solder joint from silicon side, at the entering points, there will be current crowding. In order to take into account

that current crowding effect, a current density field is obtained first using electrical field analysis. This result will be used as an input for the next step of the analysis. Five different current density is simulated ranging from $0.2\times10^4 A/cm^2$ to $1.0\times10^4 A/cm^2$ (The current density is an average value assuming uniform distribution in solder joints). The current field simulation results are shown in Figure 64.

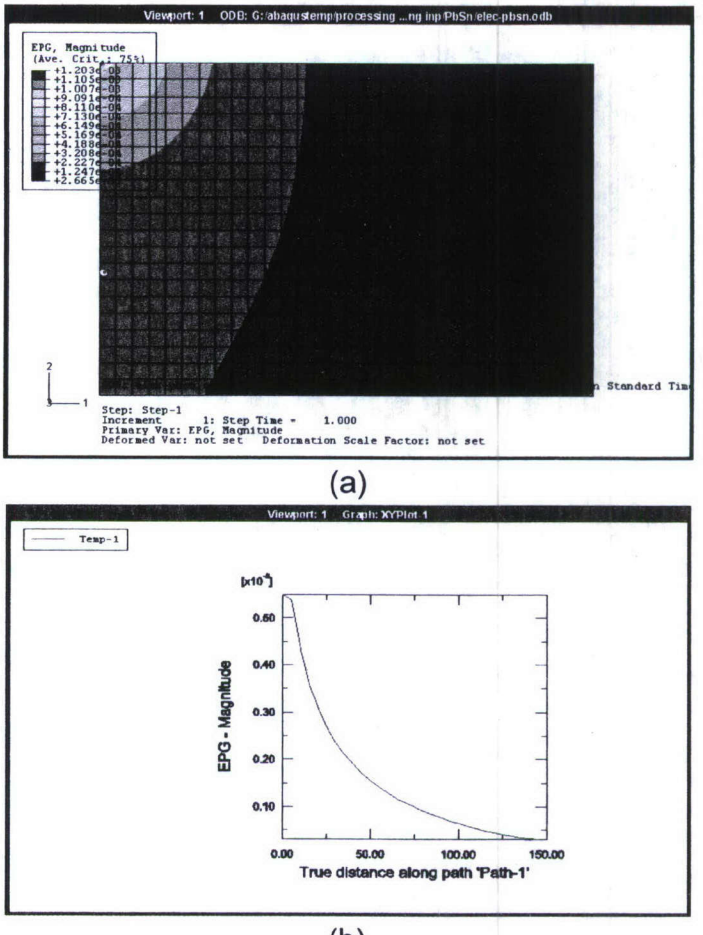

Figure 64 Current Field Simulation (a) Contour (b) Distribution along the Upper Edge (where EPG is electrical potential gradient)

4.3.3.3 Simulation Result and Analysis

Simulation results for current density of $0.2\times10^4 A/cm^2$ are shown in Figure 65. The concentration and spherical stress which are shown in Figure 65 (a) and (b) are corresponding to the blocking boundary condition and current density distribution. The largest value for vacancy concentration and spherical stress are in the upper left corner (where positive value is tension). On the other hand the lower right corner is compression zone. Plastic shear strain and equivalent plastic strain distribution after 100 hours stressing are shown in Figure 65 (c) and (d) respectively. There are two concentration areas for plastic shear stain and equivalent plastic strain. One is at the upper boundary close to the left side and the other is at left middle side of the joint. Both are due to the interaction of confinement of boundary and deformation caused by vacancy redistribution and generation. Damage as defined in (4-61) based on entropy production is shown in Figure 65 (e). In the damage calculation, the damage in the compression zone is set up to be zero and from Figure 65 (e) damage distribution shows the same profile as equivalent plastic strain and plastic shear strain. This means that the contribution of damage from plastic deformation is the dominant factor in the damage formulation. The total atomic flux divergence is the ratio between changes of atomic concentration and original atomic concentration. The total atomic flux divergence result is shown in Figure 65 (f). The most critical damage area is in the upper edge which is the silicon die side and solder interface. In order to identify the most critical damage location, vacancy concentration,

damage and total atomic divergence flux results for the upper edge are shown in Figure 66. Due to the boundary confinement, the biggest damage location is not at the corner but a little bit away form the corner position. The simulation results for this critical element are compared at different current density levels.

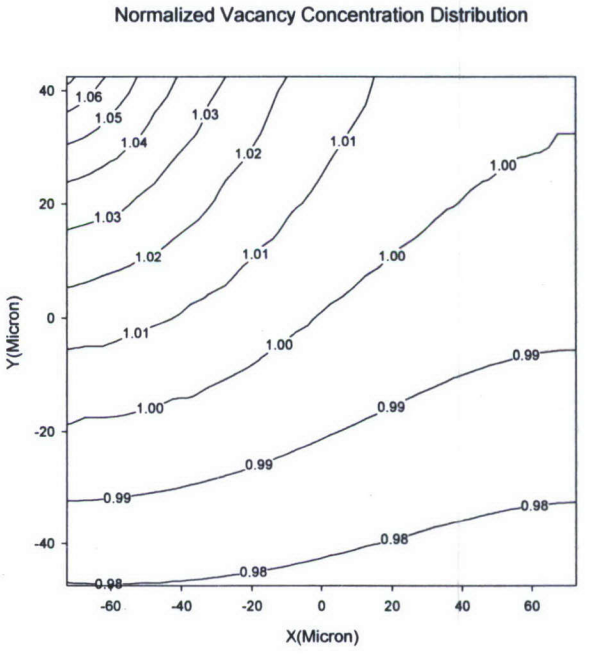

(a)

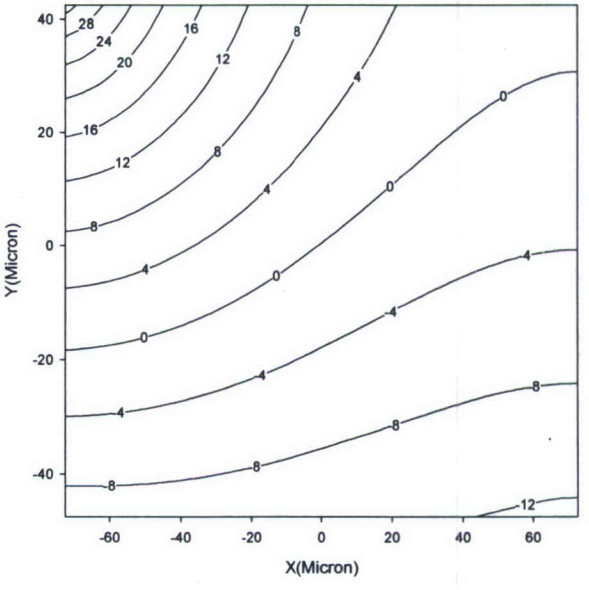

(b)

Plastic Shear Strain Distribution

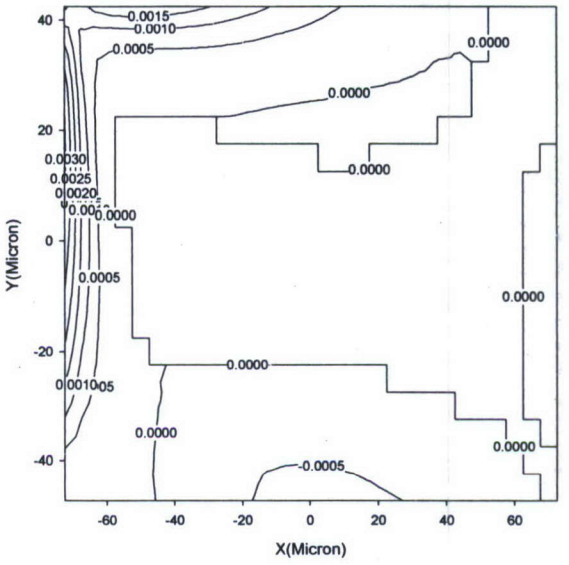

(c)

Equivalent Plastic Strain Distribution

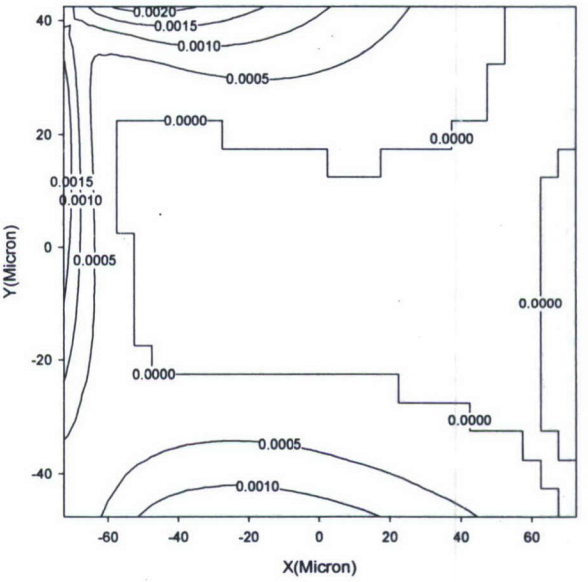

(d)

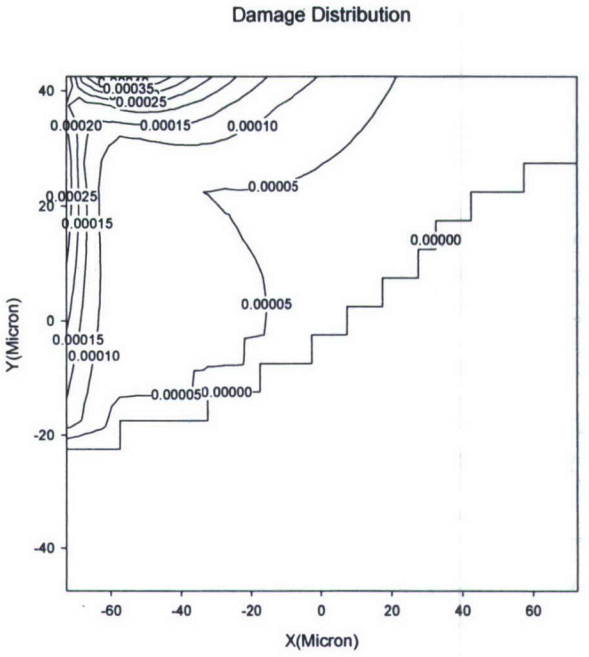

(e)

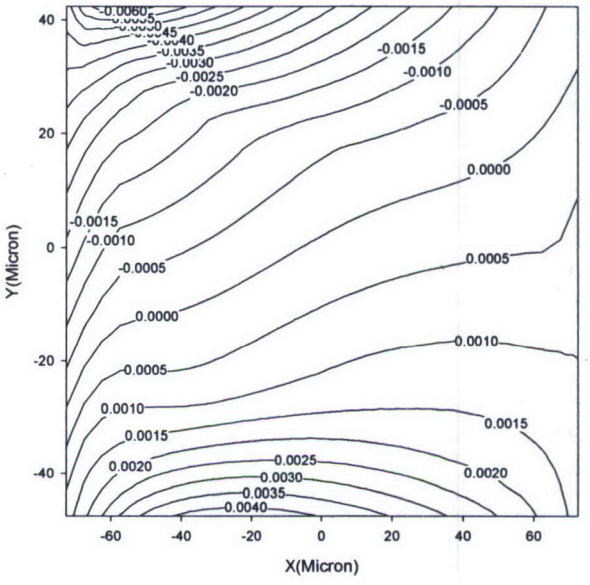

(f)

Figure 65 Simulation result at 100 hours for current density of $0.2\times10^4 A/cm^2$

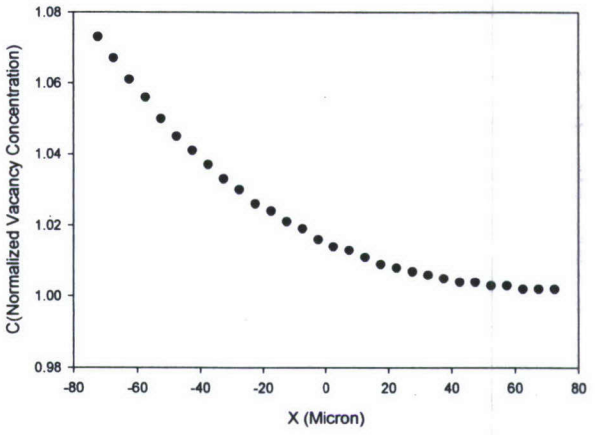

(a)

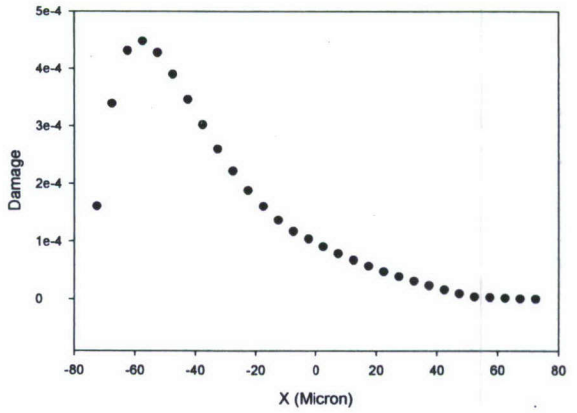

(b)

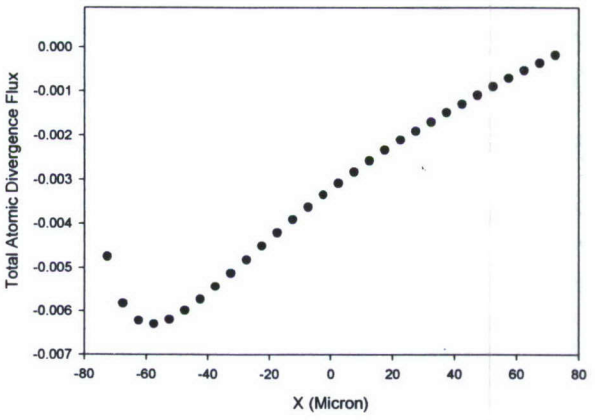

(c)

Figure 66 Simulation results for upper edge of solder joint at 100 hours for current density at $0.2\times10^4 A/cm^2$

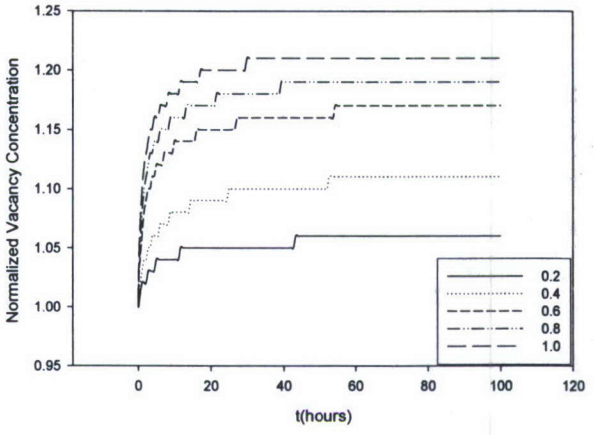

Figure 67 Normalized vacancy concentration evolution at different current density levels

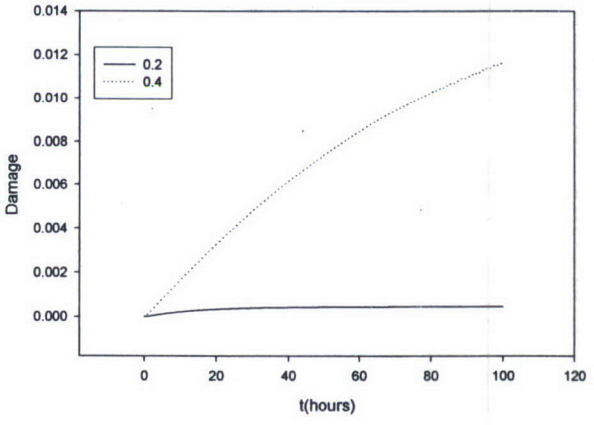

(a)

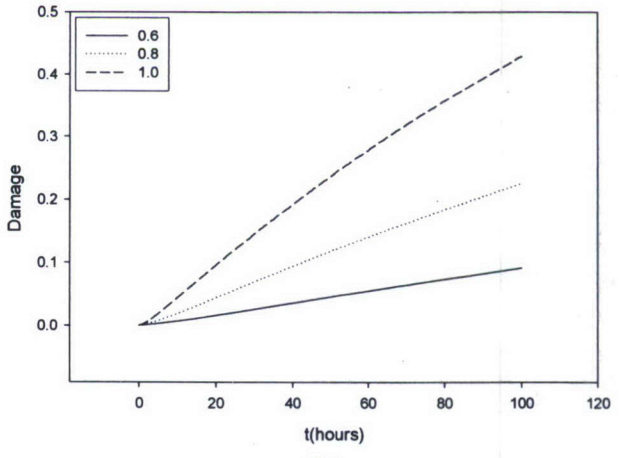

(b)

Figure 68 Damage evolution for different current density level at the most damage prone point

Figure 67 shows the normalized vacancy concentration evolution at most damage prone area for different density levels. The normalized vacancy concentration level will reach stable position at every different current density levels. Damage evolutions for the most critical point for different current density level are shown in Figure 68. Figure 68 (a) shows the damage evolution for two smaller current density levels and Figure 68 (b) shows the results for three higher current density levels. At low current density level, the damage will reach a steady level. This is due to the fact that spherical stress gradient and concentration gradient counter balance the electron driving force. At higher current density level, the counter balance forces can not resist electron wind force and after the counter balance forces reach a maximum value(when the normalized concentration stabilized), damage accumulation will continue until failure. At this stage, damage accumulation rate will be a constant and in Figure 68 (b), this constant rate of damage accumulation can be clearly seen. The steady state can be verified by vacancy flux at the critical point of solder joint, which are shown in Figure 69. For current densities at lower level, the flux is reaching zero after 100 hours of simulation. For higher current density (above or equals $0.6\times10^{4}A/cm^{2}$) levels, the flux is stabilized but not reaching zero after 100 hours simulation.

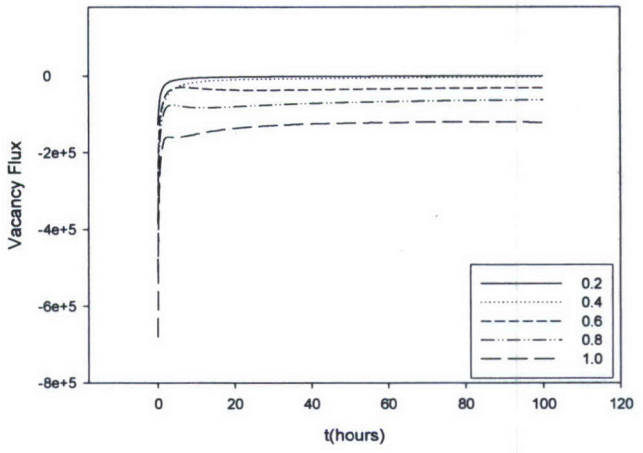

Figure 69 Vacancy flux at the critical point of solder joint for different current densities

The total atomic flux divergence results at the critical points are shown in Figure 70. The total atomic flux divergence can be viewed as a mass depletion ratio. Or in the damage terms, it can be seen as physical void ratio. From the simulations, at highest current density level, after 100 hours of simulation, the total atomic divergence is around 70 percents. This means the mass depletion ratio is very high and void nucleation will occur well before that. Comparing with the damage value shown in Figure 68, the values of damage and total atomic flux are very close to each other. Since the total atomic flux have a direct physical meaning (void ratio), this proves that our thermodynamics based damage formulation is very successful for representing the physical damage value. The total atomic flux divergence calculated here is based on the assumption of constant vacancy and atomic ratio, which may not be correct after mass depletion

occur at large amount. But at least it can be used as a semi quantitive index for damage evaluation due to its clear damage implication. Figure 71 shows the nonlinear stress strain relationship at critical point for current density at three high current density levels. The nonlinear isotropic hardening effect can be clearly seen from Figure 71. Also due to the difference of driving forces, larger forces will create larger strain rate and the rate sensitivity can be clearly seen from Figure 71. This proves that viscoplastic rate sensitivity has an important effect which is not presented in thin film materials, such as copper and aluminum.

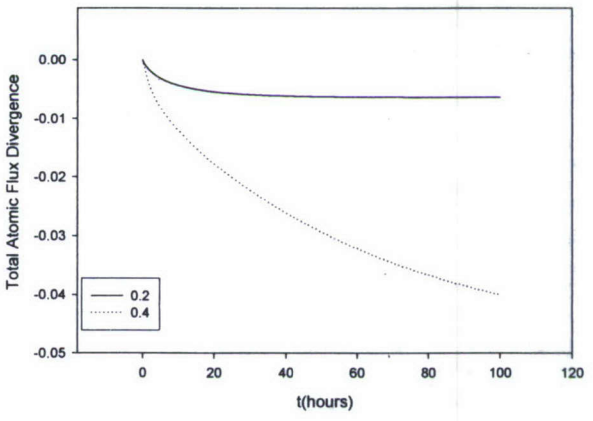

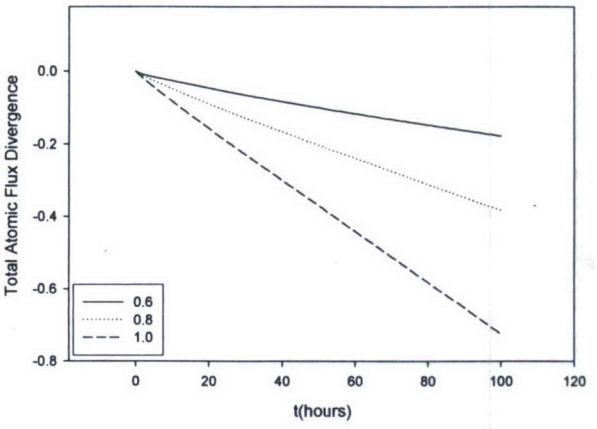

Figure 70 Total atomic flux divergence at the critical point of solder joint for different current densities

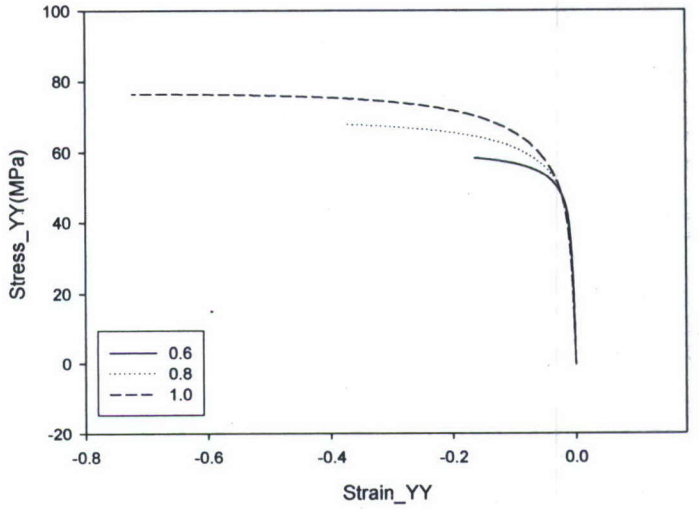

Figure 71 Stress and strain evolution

In order to determine the critical damage value for void nucleation, which is called incubation time, a first order polynomial linear regression method is used to determine the total time as a function of damage. This incubation time can be used as an index for total failure as shown by in situ void observation under high current density(Lin et al 2005). Since at higher current density the damage at later stage evolves linearly with time, a linear relation is reasonably accurate. According to the 95% confidence level linear regression results, the time needed to reach different critical damage value for three different current density levels (low current density is not considered since the damage will reach a stable value) is fitted, the function has the form as

$$t = A \bullet Damage \tag{4-78}$$

the parameter A is 1098.2,435.33,222.41 for current density level of $0.6,0.8,1.0\times10^4 A/cm^2$ respectively. The calculated value of t is in hours. Comparing the parameters with the ratio of corresponding current density, the time to reach critical damage is proportional to j^{-3} according to simulation results, which is in contrast with earlier reported data by Hua(2005). This is probably due to diffusion boundary conditions.

The experimental studies of eutectic solder joints result are presented at

Table 12. In order to utilized the experimental data for verification of the damage model and determine the critical damage value, a two parameter function fit is conducted using the Table Curve 3D software. The function is in the form like

$$t=\frac{a}{j^3}\exp(\frac{b}{T}) \tag{4-79}$$

where a and b is parameters to be determined by least square method and t is time to failure, j($10^4 A/cm^2$) is the current density, and T is temperature (K). This function is similar to Black's equation but the current density dependence is to the power of minus three instead of two. The reason for choosing current density dependence of power of minus three is that simulation damage result implicates that relationship. Utilizing the data in

Table 12, the value of a and b is determined to be 3.824E-4 and 4961.4 respectively. The detail results are listed in

Table 13.

Table 12 Experimental Results (Ye et al. 2003a)

Module Number	Current Density (10^4A/cm^2)	Temp. (K)	TTF Test (hours)
6	1.13	413*	61
14	1.2	428*	26
34	0.62	373	960
41	0.96	423	61
42	0.72	393	256
51	0.64	403	323

Table 13 Curve fitting of experimental results

Module	j	T	TTF	Predicted TTF	Residue	Residue%
1	1.2	428	26	23.952088	2.047912	7.876584
2	1.13	413	61	43.70169	17.29831	28.35789
3	0.96	423	61	53.651438	7.348562	12.04682
4	0.72	393	256	311.34605	-55.3461	-21.6196
5	0.64	403	323	324.08069	-1.08069	-0.33458
6	0.62	373	960	959.50163	0.498372	0.051914

According to the curve fitting results, at the temperature of 373K and current density level of $0.6, 0.8, 1.0 \times 10^4 A/cm^2$, the time to failure of experiments

prediction are 228.7, 446.6 and 1058.7 hours respectively. In equation(4-78), if we choose damage value as 1.0, the time to failure is 222.41, 435.33 and 1098.2 hours respectively which are very close to the experimental predicted values.

	$t=\frac{a}{j^3}\exp(\frac{b}{T})$	Simulation Result (D_{cr}=1)
$1.0\times10^4\,A/cm^2$	228.7	222.41
$0.8\times10^4\,A/cm^2$	446.6	435.33
$0.6\times10^4\,A/cm^2$	1058.7	1098.2

In finite element analysis, since the damage is incorporated into the mechanical degradation, the Young's modulus will decrease as damage increase, the relationship between damage and Young's modulus is as follows:

$$E' = (1.0 - D)E \qquad (4\text{-}80)$$

If the damage value reaches 1, the material will lose the ability of sustain any load and results in material total failure. The critical damage value of 1.0 is reasonable for predicting the time to failure. This damage value is depends on nominal current density at solder joint, current density distribution, material mechanical properties and temperature. For current density lower than $0.6\times10^4\,A/cm^2$, the time to failure is much larger than 1000 hours and this is also verified by the

experimental result(Ye et al 2004).

4.3.4 Conclusions and discussion

A damage model based on thermodynamics and continuum mechanics has been proposed and implemented into finite element simulation for solder joint under high current density loading. The simulation and comparison with experimental results verified the effectiveness of the damage model. A critical damage value of 1.0 is proposed according to the simulation result. This value fits with the experimental result very well.

According to the simulation and experimental results, below current density of $0.6\times10^4 A/cm^2$, the time to failure is much larger and does not follow Black's law. This is due to the fact that the counter balance forces can effectively eliminate electromigration driving force and create a stabilized state. Above this level of current density, the time to failure is inversely proportional to the power of three of current density (nominal current density value).

Current crowding effect is very clear in the simulation. A uniform current density of $0.8\times10^4 A/cm^2$ is applied to the same model and the comparison of the damage result and stress-strain relation between uniform current density and current crowding are shown in Figure 72. Although the nominal current density is the same in both cases, the damage evolution in current crowding case is much higher than uniform current density. The stress-strain curve clearly shows the rate

sensitivity of the solder material.

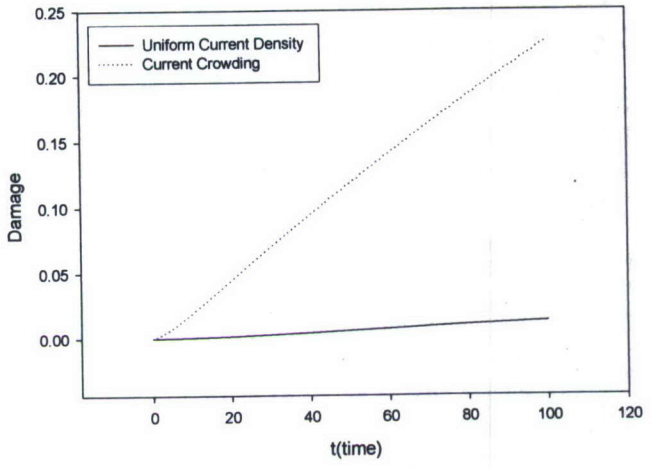

(a)

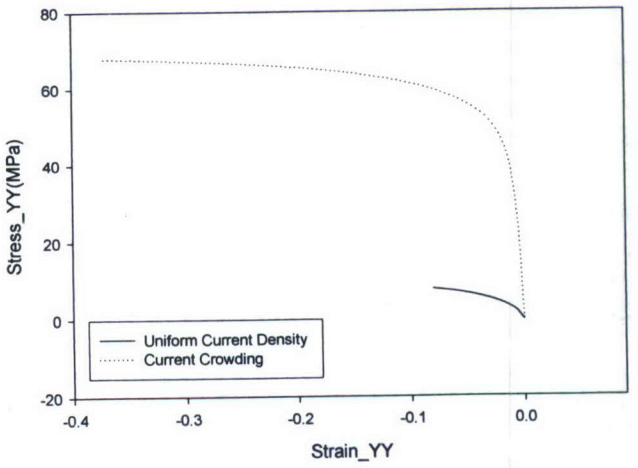

(b)

Figure 72 Comparison between current crowding and uniform current density

From the simulation, the current crowding effect seems to be very strong since the current density at the entrance is much bigger than nominal current density value. Current crowding depends on the thickness of the UBM. if the

thickness of the UBM increases, the effect of current crowding will be greatly minimized.

The damage formulation proposed here is a powerful tool and it can be combined with experiments to better predict time to failure. Also it can be used as a prediction tool for designing specific experimental set up and parameter study for preliminary concept design. The damage model used here based on previous successful application of thermal fatigue problems, this damage model has the capability of simulation of thermal effect combined with electromigration and thermomigration.

Chapter 5 Conclusions and Discussions

Equation Chapter 4 Section 1

5.1 Fundamental Contributions

This dissertation focused on the reliability of electromigration failure modeling using computational tools and continuum damage mechanics. The major contributions of this dissertation are summarized below:

1. A thermodynamic based continuum damage model is proposed based on physical failure mechanism. The biggest advantage of this proposed thermodynamic damage formulation is that its applicability is universal which allows combining diffusion and displacement induced failure effect, without need for any phenomenological potential surface.

2. A viscoplastic nonlinear isotropic/kinematic model based on previous work has been implemented using Abaqus user material subroutine and verified against the experimental results. Return mapping integration algorithm which is consistent with global Newton-Ralphson iteration scheme of Abaqus is used. This algorithm expedites the computational speed compared with Hinton and Owen

algorithm and it's generality makes it suitable for various other plasticity model implementations.

3. A displacement-diffusion coupled model is proposed which combined thermal effect and initial current field. The model is implemented using Abaqus user element subroutine and verified against the experimental results. Material plasticity is also considered in the models.

4. Damage is coupled into the displacement-diffusion coupled model and simulation has been performed to predict the damage of lead free solder interconnections.

5. It has been shown that diffusion boundary conditions can be more detrimental than current crowding.

5.2 Discussions

A general finite element treatment of electromigration caused diffusion problems which involve diffusion, displacement, material plasticity, thermal and electrical fields are presented in this dissertation. This general finite element treatment enables us to solve various boundary and initial condition problems which previous models fail to do. Thermal and electrical fields are obtained as predefined fields which can be obtained by Abaqus thermal-electrical coupled steady state simulation. The sequential analysis is reasonable since thermal and electrical fields can reach stability much faster than diffusion process thus can be treated unchanged during the long process of diffusion process which can take

from 100 hours to several thousands of hours. This will enables us to investigate thermal migration and current crowding effect through Abaqus simulation.

The boundary conditions here include diffusion boundary condition and displacement boundary condition. Usually solder joints and thin film are protected by an insulating layer which in solder joint case this layer might be intermetalic compound. This layer will form semi blocking or completely blocking boundary conditions. In the studies in the literature, blocking boundary conditions are usually assumed. But case study revealed that variable boundary condition effect should be considered in some cases. For example, in copper dual damascene structure, a very thin layer of Ta or TaN is used as a boundary layer. Experimental results show that different thickness of this layer will greatly affect the electromigration failure time. This is a clear proof that diffusion boundary conditions change will result In different failure time since the mechanical boundary conditions are not changed by this very thin layer of the structure. The simulations also verified this experimental result.

Current crowding which can take place in the interface of multiple layer of material or when there is abrupt change in geometry is an important factor especially in solder connections due to the packaging structure. The current in solder joint is delivered by a thin layer of Al or Cu tin film. When the current is passing from thin film to solder connection, due to abrupt geometry change , the current will concentrate at the corner of the entrance point. Combined with the

blocking boundary conditions in the interface, this will bring the worst combination of scenario. In analysis of copper dual damascene structure and solder connections, current crowding effects are taken into account and it was found that current crowding effect has a much bigger impact in solder connection than in copper dual damascene structure.

Material plasticity is considered in the proposed model. A viscoplastic time dependent material model with nonlinear isotropic/kinematic hardening is implemented using return mapping integration algorithm. This algorithm is consistent with Abaqus global Newton-Ralphson iteration scheme. This implementation makes this constitutive model versatile to accommodate various other plasticity models which based on J-2 yield conditions. The proposed algorithm is also very fast because is has a stable, implicit formulation regarding the time step. Numerical verifications are performed to compare with experimental results. The consideration of plasticity enables us to investigate plastic energy dissipation which is an important index used in our damage formulation.

A thermodynamically based continuum damage mechanics is coupled into the system. The coupling is based on equivalent strain concept. Similar damage mechanics model has been successfully implemented into low cycle fatigue failure prediction for thermal cycling of solder joints. Damage is defined as an internal state variable which represent material degradation. Simulations are

performed on multiple current density magnitudes and critical damage values which represent void nucleation are determined through the comparison with experimental results. At lower current density range, a stable state can be reached with the counter flow developed due to stress gradient and concentration gradient, while at high current density, a pseudo stability state can be reached and material will continue to degrade until final failure. A critical current density is proposed according to the above simulation and experimental result.

5.3 Suggestions for future work

Material parameter determination is limited by the limited time and equipment. Diffusion material properties such as diffusivity and effective charge number are obtained from literature and limited experimental measurement. As we know, stress gradient and concentration gradient will generate counter flow which will balance the diffusion caused by electron wind force. In measuring the effective chargeness number, this counter flow is not included which will makes the effective chargeness number smaller than it should be. For solving this problem, numerical simulation and experimental results should be utilized..

Diffusion boundary condition has great uncertainty. The interdiffusion at the boundary during the current loading needs to be investigated. Thermal effect is not taken into account in this dissertation although the model is capable of considering thermal gradient problem combined with electromigration. This is due

to the fact that electromigration in solder alloys needs more detailed work for verification. Once this verification process is finished, further implementation of thermal effects is then possible.

Void growth is not considered in the dissertation, which violate the continuum mechanics assumption. Void growth on continuum mechanics based on mesh deletion and regeneration will bring free surface singularity to the problem and makes solving the PDE very difficult. Although void nucleation time is considered as major part of time to failure, for some cases, void growth do dominant. In this situation, the damage parameters can be used as an indication of the total failure time.

Large deformation analysis should be consistent for very high current density problem.

References

Ainslie, N. G., D'Heurle, F. M., and Wells, O. C., "Coating, mechanical constraints, and pressure effects on electromigration," *Applied Physics Letters*, vol. 20, no. 4, pp. 173-174, 1972.

Ames, I., d'Heurle, F. M., and Horstmann, R. E., "Reduction of electromigration in aluminum films by copper doping (Reprinted from IBM Journal of Research and Development, vol 14, 1970)," *Ibm Journal of Research and Development*, vol. 44, no. 1-2, pp. 89-91, 2000.

Argon, A. S., Im, J., and Safoglu, R., "Cavity Formation from Inclusions in Ductile Fracture," *Metallurgical Transactions A-Physical Metallurgy & Materials Science*, vol. 6A pp. 825-837, 1975.

Armstrong, P. J. and Frederick, C. O., "A mathetical representatin of the multiaxial bauschinger effect," *G.E.G.B.Report RD/B/N731*, 1966.

Balzer, R. and Sigvaldason, H., "Equilibrium vacancy concentration measurements on tin single crystals," *Physica Status Solidi B: Basic Research*, vol. 92, no. 1, pp. 143-147, 1979.

Barnes, R. S., *Nature*, vol. 166 1950.

Basaran, C., Lin, M., and Ye, H., "A thermodynamic model for electrical current

induced damage," *International Journal of Solids and Structures*, vol. 40, no. 26, pp. 7315-7327, Dec.2003.

Basaran, C. and Yan, C. Y., "A thermodynamic framework for damage mechanics of solder joints," *Journal of Electronic Packaging*, vol. 120, no. 4, pp. 379-384, Dec.1998.

Basaran, C. and Tang, H., Nie, S. "Experimental Damage Mechanics of Microelectronics Solder Joints Under Fatigue Loading," *Mechanics of Materials*, vol. 36 1111-1121 2004.

Basaran, C. and Tang, H. "Implementation of Thermodynamics Framework for Damage Mechanics of Solder Interconnects in Microelectronic Packaging," International J. of Damage *Mechanics*, vol. 11 87-108 2002

Black, J. R., "Mass Transport of Aluminum by Momentum Exchange With Conducting Electrons," *Proc.6th Annual Symp.Reliability Physics IEEE Cat.7-15C58*, pp. 148-159, 1967.

Black, J. R., "Electromigration Failure Modes in Aluminum Metallization for Semiconuctor Devices," *Proceedings of the IEEE*, vol. 57, no. 9, pp. 1587-1594, 1969.

Blech, I. A., "Electromigration in thin aluminum films on titanium nitride," *Journal*

of Applied Physics, vol. 47, no. 4, pp. 1203-1208, 1976.

Blech, I. A. and Herring, C., "Stress Generation by electromigration," *Applied Physics Letters*, vol. 29, no. 3, pp. 131-133, 1976.

Blech, I. A. and Kinsbron, E., "Electromigration in Thin Gold Films on Molybdenum Surfaces," *Thin Solid Films*, vol. 25 pp. 327-334, 1975.

Blech, I. A. and Sello, H. RADC Tech. Rept. TR 66-31. 1965.

Ref Type: Report

Blech, I. A. and Sello, H. 5th Annual Symposum on Physics of Failure in Electronics, Columbus, Ohio. 1966.

Ref Type: Conference Proceeding

Blech, I. A. and Sello, H., "Physics of Failure in Electronics," in Shilliday, T. S. (ed.) *USAF Rome Air Development Center Reliability Series Proc. Vol. 5* Rome, NY: 1967, pp. 496-501.

Blech, I. A. and Tai, K. L., "Measurement of stress gradients generated by electromigration," *Appl.Phys.Lett.*, vol. 30, no. 8, pp. 387-389, 1977.

Bosvieux, C. and Friedel, J., "Electrolysis of metallic alloys," *Phys.Chem.Solids*, vol. 23 pp. 123-136, 1962.

Brown, A. M. and Ashby, M. F., "CORRELATIONS FOR DIFFUSION CONSTANTS," *Acta Metallurgica*, vol. 28, no. 8, pp. 1085-1101, Aug.1980.

Callister, W. Jr., *Materials Science and Engineering: An Introduction*, 4th ed. John Wiley & Sons, 1996.

Chaboche, J. L., "Constitutive equations for cyclic plasticity and cyclic viscoplasticity," *International Journal of Plasticity*, vol. 5, no. 3, pp. 247-302, 1989.

Chen, C.-M. and Chen, S.-W., "Electromigration effect upon the Sn/Ag and Sn/Ni interfacial reactions at various temperatures," *Acta Materialia*, vol. 50, no. 9, pp. 2461-2469, May2002.

Choi, W. J., Yeh, E. C. C., Tu, K. N., Elenius, P., and Balkan, H., "Electromigration of flip chip solder bump on Cu/Ni(V)/Al thin film under bump metallization," *52nd Electronic Components and Technology Conference 2002.(Cat.No.02CH37345).IEEE.2002, Piscataway, NJ, USA.*, pp. 1201-1205, 2002.

Chu, C. S. and Sorbello, R. S., "Relaxation-time dependence of the driving force in electromigration," *Journal of Physics and Chemistry of Solids*, vol. 52, no. 3, pp. 501-505, 1991.

Clement, J. J., "Reliability analysis for encapsulated interconnect lines under dc

and pulsed dc current using a continuum electromigration transport model," *J.Appl.Phys.*, vol. 82, no. 12, pp. 5991-6000, 1997.

Clement, J. J. and Lloyd, J. R., "Numerical Investigations of the Electromigration Boundary Value Problem," *Journal of Applied Physics*, vol. 71, no. 4, pp. 1729-1731, 1992.

Clement, J. J. and Thompson, C. V., "Modeling electromigration-induced stress evolution in confined metal lines," *J.Appl.Phys.*, vol. 78, no. 2, pp. 900-904, 1995.

Cocks, A. C. F., "On creep fracture by void growth," *Progress in Material Science*, vol. 27 pp. 189-244, June1982.

Das, A. K. and Peierls, R., "Force on a moving charge in an electron gas," *Journal of Physics C: Solid State Physics*, vol. 6, no. 18, pp. 2811-2821, 1973.

Decker, D. L., Weiss, J. D., and Vanfleet, H. B., "Diffusion of Sn in Pb to 30 kbar," *Physical Review B (Solid State)*, vol. 16, no. 6, pp. 2392-2394, 1977.

Duan, N., Scheer, J., Bielen, J., and van Kleef, M., "The influence of Sn-Cu-Ni(Au) and Sn-Au intermetallic compounds on the solder joint reliability of flip chips on low temperature co-fired ceramic substrates," *Microelectronics Reliability*, vol. 43, no. 8, pp. 1317-1327, Aug.2003.

Fiks, V. B., "On the Mechanism of the Mobility of Ions in Metals," *Sov.Phys.Solid*

State, vol. 1 pp. 14-28, 1959.

Fiks, V. B., "Dynamic (effective) charge of metal ions," *Fiz.Tverd.Tela*, vol. 6, no. 8, pp. 2307-2313, 1964.

Filippi, R. G., Wachnik, R. A., Aochi, H., Lloyd, J. R., and Korhonen, M. A., "The effect of current density and stripe length on resistance saturation during electromigration testing," *Applied Physics Letters*, vol. 69, no. 16, pp. 2350-2352, 1996.

Fischer, A. H., Abel, A., Lepper, M., Zitzelsberger, A. E., and Von Glasow, A., "Experimental data and statistical models for bimodal EM failures," *Annual Proceedings - Reliability Physics (Symposium)*, pp. 359-363.

Fisher, J. C., *J.Appl.Phys.*, vol. 22, no. 74, 1951.

Gall, M., Capasso, C., Jawarani, D., Hernandez, R., Kawasaki, H., and Ho, P. S., "Detection and analysis of early failures in electromigration," *Applied Physics Letters*, vol. 76, no. 7, pp. 843-845, 2000.

Gall, M., Capasso, C., Jawarani, D., Hernandez, R., Kawasaki, H., and Ho, P. S., "Statistical analysis of early failures in electromigration," *Journal of Applied Physics*, vol. 90, no. 2, pp. 732-740, July2001.

Gall, M., Jawarani, D., and Kawasaki, H., "Characterization of electromigration

failures using a novel test structure," *Materials Reliability in Microelectronics VI Materials Research Society Symposium Proceedings*, vol. 428 pp. Materials-86, 1996.

Gan, C. L., Thompson, C. V., Pey, K. L., and Choi, W. K., "Experimental characterization and modeling of the reliability of three-terminal dual-damascene Cu interconnect trees," *Journal of Applied Physics*, vol. 94, no. 2, pp. 1222-1228, July2003.

Gan, H., Choi, W. J., Xu, G., and Tu, K. N., "Electromigration in solder joints and solder lines," *JOM*, vol. 54, no. 6, pp. 34-37, June2002.

Gignac, L. M., Hu, C.-K., and Liniger, E. G., "Correlation of electromigration lifetime distribution to failure mode in dual Damascene Cu/SiLK interconnects," *Microelectronic Engineering*, vol. 70, no. 2-4, pp. 398-405, Nov.2003.

Gill, J., Sullivan, T., Yankee, S., Barth, H., and Von Glasow, A., "Investigation of via -dominated multi-modal electromigration failure distributions in dual damascene Cu interconnects with a discussion of the statistical implications," *Annual Proceedings - Reliability Physics (Symposium) 2002*, no. 02ch37320).

Gleixner, R. J., Clemens B.M., and Nix, W. D., "Void Nucleation in Passivated Interconnect Lines: Efffects of Site Geometries, Interfaces, and Interface flaws," *Journal of Materials Research*, vol. 12, no. 8, pp. 2081-2090, 1997.

Gleixner, R. J. and Nix, W. D., "An Analysis of Void Nucleation in Passivated Intercoonect Lines Due to Vacancy Condensation and Interface Contamination," *Materials reliability in microelectronics VI, San Francisco, CA, April 8-12 1996*, pp. 475-480, 1996.

Goods S.H. and Brown L.M., "The Nucleation of Cavities by Plastic Deformation," *Acta Materialia*, vol. 27 pp. 1-15, 1978.

Gupta, D., "Diffusion Process in Lead Based Solders Used in Microelectronic Industry," *Design & Reliability of Solders and Solder Interconnection*, pp. 59-64, Feb.1997.

Gupta, D., Hu, C. K., and Lee, K. L., "Grain boundary diffusion and electromigration in Cu-Sn alloy thin films and their VLSI interconnects," *Defect and Diffusion Forum*, vol. 143 pp. 1397-1406, 1997.

Gupta, D., Vieregge, K., and Gust, W., "Interface diffusion in eutectic Pb-Sn solder," *Acta Materialia*, vol. 47, no. 1, pp. 5-12, Dec.1998.

Gust, W., Mayer, S., Bogel, A., and Predel, B., "Generalized representation of grain boundary self-diffusion data," *Journal de Physique Colloque*, vol. 46, no. C-4, pp. 537-544, 1985.

Harrison, L. G., "Influence of dislocation on diffusion kinetics in solids with

paticular reference to the alkali halides," *Transaction of the Faraday Society*, vol. 57 pp. 1191-1199, 1961.

Hau-Riege, C. S. and Thompson, C. V., "Electromigration in Cu interconnects with very different grain structures," *Applied Physics Letters*, vol. 78, no. 22, pp. 3451-3453, 2001.

Hau-Riege, C. S., "An introduction to Cu electromigration," *Microelectronics Reliability*, vol. 44, no. 2, pp. 195-205, Feb.2004.

Herring, C., "Diffusional Viscosity of a Polycrstalline Solid," *Journal of Applied Physics*, vol. 21 pp. 437-445, 1950.

Herring, C., "Driving force for diffusion. Reply to comments," *Scripta Metallurgica*, vol. 5, no. 4, pp. 273-277, 1971.

Hoang, H. H., Nikkel, E. L., Mcdavid, J. M., and Macnaughton, R. B., "Electromigration Early-Failure Distribution," *Journal of Applied Physics*, vol. 65, no. 3, pp. 1044-1047, 1989.

Hu, C. K., Gignac, L., Liniger, E., Herbst, B., Rath, D. L., Chen, S. T., Kaldor, S., Simon, A., and Tseng, W. T., "Comparison of Cu electromigration lifetime in Cu interconnects coated with various caps," *Applied Physics Letters*, vol. 83, no. 5, pp. 869-871, 2003a.

Hu, C. K., Gignac, L., Liniger, E., and Rosenberg, R., "Electromigration in on-chip single/dual damascene Cu interconnections," *Journal of the Electrochemical Society*, vol. 149, no. 7, pp. G408-G415, 2002a.

Hu, C. K., Gignac, L., Malhotra, S. G., Rosenberg, R., and Boettcher, S., "Mechanisms for very long electromigration lifetime in dual-damascene Cu interconnections," *Applied Physics Letters*, vol. 78, no. 7, pp. 904-906, 2001.

Hu, C. K., Gignac, L., Rosenberg, R., Liniger, E., Rubino, J., Sambucetti, C., Domenicucci, A., Chen, X., and Stamper, A. K., "Reduced electromigration of Cu wires by surface coating," *Applied Physics Letters*, vol. 81, no. 10, pp. 1782-1784, 2002b.

Hu, C. K., Rosenberg, R., and Lee, K. Y., "Electromigration path in Cu thin-film lines," *Applied Physics Letters*, vol. 74, no. 20, pp. 2945-2947, 1999.

Hu, C.-K., Gignac, L., Liniger, E., Herbst, B., Rath, D. L., Chen, S. T., Kaldor, S., Simon, A., and Tseng, W.-T., "Comparison of Cu electromigration lifetime in Cu interconnects coated with various caps," *Applied Physics Letters*, vol. 83, no. 5, pp. 869-871, Aug.2003b.

Hu, C.-K., Mazzeo, N. J., and Stanis, C., "Electromigration in two-level bamboo grain structure Al(Cu)/W interconnections," *Materials Chemistry and Physics*, vol. 35, no. 1, pp. 95-98, Aug.1993.

Hua Ye, "Mechanical Behavior of Microelectronics and Power Electronics Solder Joints under High Current Density:Analytical Modeling and Experimental Investigation." PH.D. 2004.

Huntington, H. B., "Electro- and thermomigration in metals," *Diffusion, papers presented at a seminar of the American Society of Metals*, pp. 155-184, 1972.

Huntington, H. B. and Grone, A. R., "Current-induced marker motion in gold wires," *J.Phys.Chem.Solids*, vol. 20, no. 1/2, pp. 76-87, 1961.

Huynh, Q. T., Liu, C. Y., Chen, C., and Tu, K. N., "Electromigration in eutectic SnPb solder lines," *Journal of Applied Physics*, vol. 89, no. 8, pp. 4332-4335, 2001.

Johns, R. A. and Blackburn, D. A., "Grain boundaries and their effect on thermomigration in pure lead at low diffusion temperatures," *Thin Solid Films*, vol. 25, no. 2, pp. 291-300, 1975.

Kashyap, B. P. and Murty, G. S., "Experimental constitutive relations for the high temperature deformation of a Pb---Sn eutectic alloy," *Materials Science and Engineering*, vol. 50, no. 2, pp. 205-213, Oct.1981.

Kim, C. U., Morris, J. W. J., Genin, F. Y., and Fluss, M. J., "Influence of solute additions on electromigration in aluminum," *Materials Reliability in*

Microelectronics VI Materials Research Society Symposium Proceedings, vol. 428 pp. Materials-218, 1996.

Kirchheim, R., "Stress and Electromigration in Al-lines of Integrated-Circuits," *ACTA METALLURGICA ET MATERIALIA*, vol. 40, no. 2, pp. 309-323, 1992.

Kirchheim, R., "Modeling Electromigration and Induced Stresses in Aluminum Lines," *Mater.Res.Soc.Symp.Proc.*, vol. 309 pp. 101-110, 1993a.

Kirchheim, R., "Electromigration, models and atomistic interpretation," *Quality & Reliability Engineering International*, vol. 9, no. 4, pp. 287-293, July1993b.

Knowlton, B. D., Clement, J. J., and Thompson, C. V., "Simulation of the effects of grain structure and grain growth on electromigration and the reliability of interconnects," *Journal of Applied Physics*, vol. 81, no. 9, pp. 6073-6080, 1997.

Korhonen, M. A., Borgesen, P., and Li, C. Y., "Mechanisms of Stress-Induced and Electromigration-Induced Damage in Passivated Narrow Metallizations on Rigid Substrates," *Mrs Bulletin*, vol. 17, no. 7, pp. 61-68, 1992.

Korhonen, M. A., Bϕrgesen, P., Tu, K. N., and Li, C.-Y., "Stress evolution due to electromigration in confined metal lines," *Journal of Applied Physics*, vol. 73, no. 8, pp. 3790-3799, 1993.

Korhonen, M. A., Paszkiet, C. A., and Li, C. Y., "Mechanisms of thermal stress

relaxation and stress-induced voiding in narrow aluminum-based metallizations," *Journal of Applied Physics*, vol. 69, no. 12, pp. 8083-8091, June1991.

Kuschke, W. M. and Arzt, E., "Investigation of the stresses in continuous thin films and patterned lines by x-ray diffraction," *Applied Physics Letters*, vol. 64, no. 9, pp. 1097-1099, Feb.1994.

Lai, J. B., Yang, J. L., Wang, Y. P., Chang, S. H., Hwang, R. L., Huang, Y. S., and Hou, C. S., "A study of bimodal distributions of time-to-failure of copper via electromigration," *International Symposium on VLSI Technology, Systems, and Applications, Proceedings 2001*, no. 01TH8517).

Landauer, R., "Electromigration and spatial variations in metallic conductivity," *Journal of Electronic Materials*, vol. 4, no. 5, pp. 813-821, 1975.

Lane, M. W., Liniger, E. G., and Lloyd, J. R., "Relationship between interfacial adhesion and electromigration in Cu metallization," *Journal of Applied Physics*, vol. 93, no. 3, pp. 1417-1421, 2003.

Lee, T. Y. and Tu, K. N., "Electromigration of eutectic SnPb and SnAg3.8Cu0.7 flip chip solder bumps and under-bump metallization," *Journal of Applied Physics*, vol. 90, no. 9, pp. 4502-4508, 2001.

Lee, T. Y., Tu, K. N., Kuo, S. M., and Frear, D. R., "Electromigration of eutectic

SnPb solder interconnects for flip chip technology," *Journal of Applied Physics*, vol. 89, no. 6, pp. 3189-3194, 2001a.

Lee, T.-Y. T., Lee, T. Y., and Tu, K. N., "A Study of Electromigration in 3D Flip Chip Solder Joint Using Numerical Simulation of Heat Flux and Current Density," *Proceedings - Electronic Components and Technology Conference 2001, IEEE cat.n 01CH37220*, pp. 558-563, 2001b.

Li, B., Sullivan, T. D., Lee, T. C., and Badami, D., "Reliability challenges for copper interconnects," *Microelectronics Reliability*, vol. 44, no. 3, pp. 365-380, Mar.2004a.

Li, B., Sullivan, T. D., Lee, T. C., and Badami, D., "Reliability challenges for copper interconnects," *Microelectronics & Reliability*, vol. 44, no. 3, pp. 365-380, Mar.2004b.

Lin, M. and Basaran, C. Electromigration induced Stress Analysis using Fully coupled Mechanical and Diffusion Finite Element Analysis With Non Linear Material Properties . 2004a.
Ref Type: Unpublished Work

Lin, M. and Basaran, C. Electromigration induced Stress Analysis using Fully coupled Mechanical and Diffusion Finite Element Analysis With Non Linear Material Properties . 2004b.

Ref Type: Unpublished Work

Lin, Y. H., Hu, Y. C., Tsai, C. M., Kao, C. R., and Tu, K. N., "In situ observation of the void formation-and-propagation mechanism in solder joints under current-stressing," *Acta Materialia*, vol. 53, no. 7, pp. 2029-2035, Apr.2005.

Liniger, E. G., Hu, C. K., Gignac, L. M., and Simon, A., "Effect of liner thickness on electromigration lifetime," *Journal of Applied Physics*, vol. 93, no. 12, pp. 9576-9582, 2003.

Liu, C. Y., Chen, C., Liao, C. N., and Tu, K. N., "Microstructure-electromigration correlation in a thin stripe of eutectic SnPb solder stressed between Cu electrodes," *Applied Physics Letters*, vol. 75, no. 1, pp. 58-60, July1999a.

Liu, C. Y., Chen, C., and Tu, K. N., "Electromigration in Sn-Pb solder strips as a function of alloy composition," *Journal of Applied Physics*, vol. 88, no. 10, pp. 5703-5709, Nov.2000.

Liu, C.-L., Liu, X.-Y., and Borucki, L. J., "Defect generation and diffusion mechanisms in Al and Al-Cu," *Materials Reliability in Microelectronics VIII Materials Research Society Symposium - Proceedings*, vol. 516 pp. MRS, Warrendale, PA, USA-193, 1998.

Liu, R. F., Hu, C.-K., Gignac, L., Harper, J. M. E., Lloyd, J., Liu, X.-H., and

Stamper, A. K., "Effects of failure criteria on the lifetime distribution of dual-damascene Cu line/via on W," *Journal of Applied Physics*, vol. 95, no. 7, pp. 3737-3744, Apr.2004.

Liu, X.-Y., Liu, C.-L., and Borucki, L. J., "A new investigation of copper's role in enhancing Al-Cu interconnect electromigration resistance from an atomistic view," *Acta Materialia*, vol. 47, no. 11, pp. 3227-3231, Sept.1999b.

Lloyd, J. R., "Stress and electromigration," *Materials Research Society Symposium Proceedings*, vol. 391, no. Materials Reliability in Microelectronics V, pp. 231-242, 1995.

Lloyd, J. R., "Electromigration in thin film conductors," *Semiconductor Science and Technology*, vol. 12, no. 10, pp. 1177-1185, 1997.

Lloyd, J. R., "Electromigration in integrated circuit conductors," *Journal of Physics D-Applied Physics*, vol. 32, no. 17, pp. R109-R118, 1999.

Lloyd, J. R. and Clement, J. J., "Electromigration in copper conductors," *Thin Solid Films*, vol. 262, no. 1-2, pp. 135-141, June1995.

Lloyd, J. R. and Koch, R. H., "Study of Electromigration-Induced Resistance and Resistance Decay in Al Thin-Film Conductors," *Applied Physics Letters*, vol. 52, no. 3, pp. 194-196, 1988.

Lodder, A. and Brand, M. G. E., "Electromigration in transition metal hydrides: a finite-cluster-model study," *Journal of Physics F: Metal Physics*, vol. 14, no. 12, pp. 2955-2962, 1984.

Lubarda, V. A. and Benson, D. J., "On the numerical algorithm for isotropic-kinematic hardening with the Armstrong-Frederick evolution of the back stress," *Computer Methods in Applied Mechanics and Engineering*, vol. 191, no. 33, pp. 3583-3596, June2002.

Ma, Q., "High-resolution determination of the stress in individual interconnect lines and variation due to electromigration," *J.Appl.Phys.*, vol. 78, no. 3, pp. 1614-1622, Apr.2004.

McDowell, D. L., "A nonlinear kinematic hardening theory for cyclic thermoplasticity and thermoviscoplasticity," *International Journal of Plasticity*, vol. 8, no. 6, pp. 695-728, 1992.

Mehrer, H. and Seeger, A., "Analysis of the pressure dependence of self-diffusion with applications to vacancy properties in lead," *Crystal Lattice Defects*, vol. 3, no. 1, pp. 1-12, 1972.

Meyer, M. A., Herrmann, M., Langer, E., and Zschech, E., "In situ SEM observation of electromigration phenomena in fully embedded copper interconnect structures," *Microelectronic Engineering*, vol. 64, no. 1-4, pp.

375-382, Oct.2002.

Mishin, Y. and Herzig, C., "Grain boundary diffusion: recent progress and future research," *Materials Science and Engineering A*, vol. 260, no. 1-2, pp. 55-71, Feb.1999.

Morris, J. W., Kim, C. U., and Kang, S. H., "The metallurgical control of electromigration failure in narrow conducting lines," *Jom-Journal of the Minerals Metals & Materials Society*, vol. 48, no. 5, pp. 43-46, 1996.

Murray, J. L., "The Aluminum-Copper System," *International Metals Reviews*, vol. 30, no. 5, pp. 211-233, 1985.

Nah, J. W., Paik, K. W., Suh, J. O., and Tu, K. N., "Mechanism of electromigration-induced failure in the 97Pb-3Sn and 37Pb-63Sn composite solder joints," *Journal of Applied Physics*, vol. 94, no. 12, pp. 7560-7566, 2003.

Nie, S. and Basaran C. "A Thermodynamic Based Damage MEchanics Model for Particulate Composite" International J. of Solids and Structures Accepted (June 2006)

Neu, R. W., Scott, D. T., and Woodmansee, M. W., "Measurement and modeling of back stress at intermediate to high homologous temperatures," *International Journal of Plasticity*, vol. 16, no. 3-4, pp. 283-301, 2000.

Nogami, T., Nemoto, T., Nakano, N., and Kaneko, Y., "The Electromigration Lifetime Determined from the Minimum-Time to Failure in An Acceleration Test," *Semiconductor Science and Technology*, vol. 10, no. 4, pp. 391-394, 1995.

Oates, A. S., "Current density dependence of electromigration failure of submicron width, multilayer Al alloy conductors," *Applied Physics Letters*, vol. 66, no. 12, pp. 1475-1477, Mar.1995.

Ogawa, E. T., Ki-Don, L., Blaschke, V. A., and Ho, P. S., "Electromigration reliability issues in dual-damascene Cu interconnections," *IEEE Transactions on Reliability*, vol. 51, no. 4, pp. 403-419, 2002.

Olowolafe, J. O., Kawasaki, H., Lee, C. C., Klein, J., Pintchovski, F., and Jawarani, D., "Effect of interface layer on the microstructure and electromigration resistance of Al-Si-Cu alloy on TiN/Ti substrates," *Applied Physics Letters*, vol. 62, no. 19, pp. 2443-2445, May1993.

Onoda, H., Hashimoto, K., and Touchi, K., "Analysis of electromigration-induced failures in high-temperature sputtered Al-alloy metallization," *Journal of Vacuum Science & Technology B*, vol. 13, no. 4, pp. 1546-1555, July1995.

P.-C.Wang, "Topographic measurement of electromigration-induced stress gradients in aluminum conductor lines," *Appl.Phys.Lett.*, vol. 76, no. 25, pp. 3726-3728, June2000.

Park, Y. B. and Lee, D. W., "Effects of Ti and TiN underlayers on electromigration reliability of Al-Cu interconnects," *Materials Science and Engineering B*, vol. 87, no. 1, pp. 70-76, Oct.2001.

Park, Y. J., Andleigh, V. K., and Thompson, C. V., "Simulations of stress evolution and the current density scaling of electromigration-induced failure times in pure and alloyed interconnects," *Journal of Applied Physics*, vol. 85, no. 7, pp. 3546-3555, 1999.

Pecht, M. G., Agarwal, R., McCluskey, P., Dishong, T., Javadpour, S., and Mahajan, R., *Electronic Packaging Materials and Their Properties* New York: CRC Press, 1998.

Philbert, J., "Atom Movements-Diffusion and Mass Transport in Solids," *Les Editions de Physique*, 1991.

Prabjit, S. and Milton, O., "Tracer study of diffusion and electromigration in thin tin films," *Journal of Applied Physics*, vol. 56, no. 4, pp. 899-907, Aug.1984.

Rice, J. R. and Tracey, D. M., "On the Ductile Enlargement of Voids in Triaxial Stress Feilds," *Journal of Mechanics and Physics of Solids*, vol. 17 pp. 201-217, 1969.

Ross, C. A., "Stress and electromigration in thin film metallisation," *Materials*

Reliability Issues in Microelectronics Symposium.(MRS, Pittsburgh,PA 1991), vol. Symp. Proc. 225 pp. 35-46, 1991.

Rothman, S. J., *Diffusion in Crystalline Solids* Academic Press,New York, 1984, pp. 1-63.

Sarychev, M. E. and Zhinikov, Yu. V., "General model for mechanical stress evolution during electromigration," *Journal of Applied Physics*, vol. 86, no. 6, pp. 3068-3075, 1999.

Sasagawa, K., Hasegawa, M., Naito, K., Saka, M., and Abe, H., "Effects of corner position and operating condition on electromigration failure in angled bamboo lines without passivation layer," *Thin Solid Films*, vol. 401, no. 1-2, pp. 255-266, 2001.

Schaich, W. L., "Linear-response theory of the electromigration driving forces," *Conference Series - Institute of Physics*, vol. 30, no. Liq. Met., Invited Contrib. Pap. Int. Conf., 3rd, 1976, pp. 638-644, 1976.

Scorzoni, A., Neri, B., Caprile, C., and Fantini, F., "Electromigration in thin-film interconnection lines: models, methods and results," *Materials Science Reports*, vol. 7, no. 4-5, pp. 143-220, Dec.1991.

Seith, W., *Diffusion in Metallen; Platzwechselreaktionen* Berlin: Springer-Verlag,

1955.

Seith, W. and Wever, H., "A new effect in the electrolytic transfer in solid alloys," *Z.Elektrochem.*, vol. 57 pp. 891-900, 1953.

Shatzkes, M. and Lloyd, J. R., "A Model for Conductor Failure Considering Diffusion Concurrently With Electromigration Resulting in a Current Exponent of 2," *Journal of Applied Physics*, vol. 59, no. 11, pp. 3890-3893, 1986.

Simo and Hughes, *Computational inelasticity* New York: Springer, 1997.

Simo and Hughes, *Computational inelasticity* 2001.

Singh, N., Bower, A. F., Gan, D., Yoon, S., Ho, P. S., Leu, J., and Shankar, S., "Numerical simulations and experimental measurements of stress relaxation by interface diffusion in a patterned copper interconnect structure," *Journal of Applied Physics*, vol. 97, no. 1, pp. 013539-11, Jan.2005.

Solak, H. H., "Measurement of strain in Al-Cu interconnect lines with x-ray micropdiffraction," *J.Appl.Phys.*, vol. 86, no. 2, pp. 884-890, July2004.

Sorbello, R. S., "Pseudopotential based theory of the driving forces for electromigration in metals," *Journal of Physics and Chemistry of Solids*, vol. 34, no. 6, pp. 937-950, 1973.

Sorbello, R. S., "Basic concepts in electromigration," *Materials Research Society Symposium Proceedings*, vol. 225, no. Mater. Reliab. Issues Microelectron., pp. 3-13, 1991.

Sukharev, V. and Zschech, E., "A model for electromigration-induced degradation mechanisms in dual-inlaid copper interconnects: Effect of interface bonding strength," *Journal of Applied Physics*, vol. 96, no. 11, pp. 6337-6343, 2004.

Tang, H. and Basaran, C., "Influence of microstructure coarsening on thermomechanical fatigue behavior of Pb/Sn eutectic solder joints," *International Journal of Damage Mechanics*, vol. 10, no. 3, pp. 235-255, July2001.

Trattles, J. T., O'Neill, A. G., and Mecrow, B. C., "Computer Simulation of Electromigration in Thin-Film Metal Conductors," *Journal of Applied Physics*, vol. 75, no. 12, pp. 7799-7804, 1994.

Tu, K. N., "Electromigration in stressed thin films," *Physical Review B*, vol. 45, no. 3, pp. 1409-1413, 1992.

Tu, K. N., "Recent advances on electromigration in very-large-scale-integration of interconnects," *Journal of Applied Physics*, vol. 94, no. 9, pp. 5451-5473, Nov.2003.

Tu, K. N., Yeh, C. C., Liu, C. Y., and Chen, C., "Effect of current crowding on

vacancy diffusion and void formation in electromigration," *Applied Physics Letters*, vol. 76, no. 8, pp. 988-990, 2000.

Tu, K. N. and Zeng, K., "Reliability issues of Pb-free solder joints in electronic packaging technology," *Proceedings - Electronic Components and Technology Conference 2002*, no. 02ch3734-5), pp. -5.

Ueno, K., Suzuki, M., Matsumoto, A., Motoyama, K., Tonegawa, T., Ito, N., Arita, K., Tsuchiya, Y., Wake, T., Kubo, A., Sugai, K., Oda, N., Miyamoto, H., and Saito, S., "A high reliability copper dual-damascene interconnection with direct-contact via structure," *Technical Digest - International Electron Devices Meeting 2000*, no. 00CB37138).

Valek, B. C. and Bravman, J. C., "Electromigration-induced plastic deformation in Passivated metal line," *Appl.Phys.Lett.*, vol. 81, no. 22, pp. 4168-4170, Feb.2004.

Van Gurp, G. J., De Waard, P. J., and Du Chatenier, F. J., "Thermomigration in indium and indium alloy films," *J.Appl.Phys.*, vol. 58, no. 2, pp. 728-735, 1985.

van Gurp, G. J. and du Chatenier, F. J., "Measurement of thermomigration in thin metal films," *Thin Solid Films*, vol. 131, no. 1-2, pp. 155-162, Sept.1985.

Von Glasow, A., Fischer, A. H., and Penka, S., "Electromigration and stressvoiding investigations on dual damascene copper interconnects,"

Advanced Metallization Conference (AMC) 2001, pp. 433-440.

Wang, P. C., "Real-time x-ray microbeam characterization of electromigration effects in Al(Cu) wires," *Appl.Phys.Lett.*, vol. 78, no. 18, pp. 2712-2714, Apr.2001.

Wang, P. C., Cargill, G. S., III, Noyan, I. C., and Hu, C. K., "Electromigration-induced stress in aluminum conductor lines measured by x-ray microdiffraction," *Applied Physics Letters*, vol. 72, no. 11, pp. 1296-1298, 1998.

Wever, H. and Seith, W., "New results on the electrolysis of solid metallic phases," *Z.Elektrochem.*, vol. 59 pp. 942-946, 1955.

Ye Hua, "Mechanical Behavior of Microelectronics and Power Electronics Solder Joints under High Current Density:Analytical Modeling and Experimental Investigation." PH.D. 2004.

Ye, H., Basaran, C., and Hopkins, D., "Measurement of High Electrical Current Density Effects in solder joints," *Microelectronics Reliability*, vol. 43, no. 12, pp. 2021-2029, 2003a.

Ye, H., Basaran, C., and Hopkins, D., "Experiment Study on Reliability of Solder Joints under Electrical Stressing -Nano-indentation,Atomic Flux Measurement," *Proceedings of 2002 International Conference on Advanced Packaging and Systems, Reno, Nevada*, Mar.2002a.

Ye, H., Basaran, C., and Hopkins, D., "Mechanical Implications Of High Current Densities In Flip Chip Solder Joints," *Proceedings of ASEM International Mechanical Engineering Congress and Exposition, Orleans, LA,* Nov.2002b.

Ye, H., Basaran, C., and Hopkins, D., "Damage Mechanics of Microelectronics Solder Joints under High Current Densities," *International Journal of Solids & Structures*, vol. 40, no. 15, pp. 4021-4032, 2003a.

Ye, H., Basaran, C., and Hopkins, D., "Mechanical degradation of solder joints under current stressing," *International Journal of Solids & Structures*, vol. 40, no. 26, pp. 7269-7284, 2003b.

Ye, H., Basaran, C., and Hopkins, D., "Numerical Simulation of Stress Evolution During Electromigration in IC Interconnet Lines," *IEEE Transactions on Components and Packaging Technologies*, vol. 26, no. 3, pp. 673-681, 2003c.

Ye, H., Basaran, C., and Hopkins, D., "Pb Phase Coarsening in Eutectic Pb/Sn Flip Chip Solder Joint under Electric Current Stressing," *International Journal of Solids & Structures*, 2003d.

Ye, H., Basaran, C., and Hopkins, D., "Thermomigration in Pb-Sn solder joints under Joule heating during electric current stressing," *Appl.Phys.Lett.*, vol. 82, no. 8, pp. 1045-1047, Feb.2003e.

Ye, H., Basaran, C., Hopkins, D., and Cartwright, A., "Reliability of Solder Joints under Electrical Stressing -Strain evolution of Solder joints," *Proceedings from the 8th Intersociety Conference on Thermal and Thermomechanical Phenomena in Electronic Systems, San Diego, CA, 5-29-2002*, pp. 946-952, 2002c.

Ye, H., Basaran, C., and Hopkins, D. C., "Deformation of solder joint under current stressing and numerical simulation--I," *International Journal of Solids and Structures*, vol 41, 4939-4958,2004.

Ye, H., Basaran, C., and Hopkins, D. C., "Deformation of solder joint under current stressing and numerical simulation--II," *International Journal of Solids and Structures*, vol 41, 4959-49738,2004.

Ye, H., Basaran, C., and Hopkins, D. C., "Mechanical implications of high current densities in flip-chip solder joints," *International Journal of Damage Mechanics*, vol. 13, no. 4, pp. 335-345, Oct.2004.

Ye, H., Hopkins, D., and Basaran, C., "Measurement and Effects of High Electrical Current Stress in Solder Joints," *Proceedings of the 35th International Symposium on Microelectronics, Denver, Colorado*, pp. 427-432, Sept.2002d.

Ye, H., Lin, M., and Basaran, C., "Failure modes and FEM analysis of power electronic packaging," *Finite Element in Analysis and Design*, vol. 38, no. 7, pp. 601-612, 2002d.

Yeh, E. C. C., Choi, W. J., Tu, K. N., Elenius, P., and Balkan, H., "Current-crowding-induced electromigration failure in flip chip solder joints," *Applied Physics Letters*, vol. 80, no. 4, pp. 580-582, 2002.

Yeh, E. C. C. and Tu, K. N., "Numerical simulation of current crowding phenomena and their effects on electromigration in very large scale integration interconnects," *Journal of Applied Physics*, vol. 88, no. 10, pp. 5680-5686, 2000.

Park Y-J,., Vaibhav, K. A., and Carl, V. T., "Simulations of stress evolution and the current density scaling of electromigration-induced failure times in pure and alloyed interconnects," *Journal of Applied Physics*, vol. 85, no. 7, pp. 3546-3555, Apr.1999.

Zschech, E., Meyer, M. A., Grafe, M., and Schneider, G., "Challenges of electromigration Electromigration degradation mechanisms in copper dual-inlaid interconnects," *Materialpruefung*, vol. 46, no. 10, pp. 513-516, 2004.